UNIVERSITY OF GLASGOW

DOCTORAL THESIS

A versatile light-sheet microscope, platform for advanced 3D fluorescence imaging and research

Author:
Chiara GARBELLOTTO

Supervisor:
Dr. Jonathan M. TAYLOR

A thesis submitted in fulfillment of the requirements for the degree of Doctor of Philosophy

in the

Imaging Concepts Group
School of Physics and Astronomy

April 25, 2021

Declaration of Authorship

I, Chiara GARBELLOTTO, declare that this thesis titled, "A versatile light-sheet microscope, platform for advanced 3D fluorescence imaging and research" and the work presented in it are my own. I confirm that:

- This work was done wholly or mainly while in candidature for a research degree at this University.
- Where any part of this thesis has previously been submitted for a degree or any other qualification at this University or any other institution, this has been clearly stated.
- Where I have consulted the published work of others, this is always clearly attributed.
- Where I have quoted from the work of others, the source is always given. With the exception of such quotations, this thesis is entirely my own work.
- I have acknowledged all main sources of help.
- Where the thesis is based on work done by myself jointly with others, I have made clear exactly what was done by others and what I have contributed myself.

Chiara Garbellotto

January 2021

Research outputs

The PhD project presented in this thesis has produced the following research outputs:

Journal article:

- C. Garbellotto and J. Taylor, "Multi-purpose SLM-light-sheet microscope," Biomedical Optics Express 9, 5419-5436 (2018).

Conference proceedings articles and oral presentations:

- C. Garbellotto and J. Taylor, "Modified Gaussian light-sheet for tiled SPIM," presented at Focus on Microscopy 2019, London, UK.
- C. Garbellotto and J. Taylor, "Multi-purpose SLM-light-sheet microscope," presented at Photon 2018, Birmingham, UK.
- C. Garbellotto and J. Taylor, "Applying compressive sensing and computational imaging to light-sheet microscopy for improved 3D *in vivo* imaging," presented at Scottish Universities Physics Alliance (SUPA) annual gathering 2017, Edinburgh, UK.
- C. Garbellotto and J. Taylor, "Building a versatile SPIM microscope by integrating a spatial light modulator," presented at Biophotonics North 2016, St. Andrews, UK.

Conference posters:

- C. Garbellotto and J. Taylor, "Multi-purpose SLM-SPIM," presented at Light sheet conference 2018, Dresden, Germany.
- C. Garbellotto and J. Taylor, "From stars to Zebrafish: story of an astronomer who meets light-sheet microscopy," presented at EPSRC CDT in Intelligent Sensing and Measurement annual conference 2016, Glasgow, UK.

Abstract

Light-sheet microscopy has become one of the leading techniques for 3D *in vivo* imaging, thanks to its optical sectioning capability, its imaging speed and its reduced photo-damaging effects on the specimen. This work presents the SLM-SPIM, a Selective Plane Illumination Microscope (SPIM, a cylindrical-lens-based light-sheet microscope) with a phase-only Spatial Light Modulator (SLM) integrated into its illumination arm. The SLM is placed in a Fourier plane, and it can be used to move and modulate the light-sheet to perform a variety of existing imaging techniques for improving image quality, such as structured illumination, tiling, pivoting, autofocusing and pencil beam scanning. The SLM-SPIM configuration presented in this work has been designed to allow all of these techniques to be employed on an easily reconfigurable optical set-up, compatible with the OpenSPIM design. This work presents results obtained by applying the above mentioned imaging techniques on samples of fluorescent beads, zebrafish embryos, and optically cleared whole mouse brain samples, thereby demonstrating the flexibility and performance of the system.

This work also presents two innovative light-sheet modulations evaluated using the SLM-SPIM, which have been specifically designed to help reduce the effect of photobleaching and, more in general, to improve the system's light-efficiency.

The first light-sheet modulation proposed is specifically designed to be used while performing the imaging technique known as tiling, which makes it possible to obtain a more uniform illumination by moving the highest-resolution region of the light-sheet across the imaging field of view. The proposed light-sheet aims at better confining the illumination light, thereby helping reduce the undesired extra photobleaching generated by the sample over-exposure typical of the tiling implementation. The simulated and experimental results obtained so far suggest that the advantages of using the modified light-sheet over a traditional Gaussian light-sheet would only be minimal (minimal reduction of photo-bleaching of the sample for the same number of images acquired). Nevertheless, the results obtained trying this imaging technique on the SLM-SPIM also demonstrate how such a versatile, flexible system can be a very useful tool when wanting to develop and try new ideas and imaging techniques.

The second innovative imaging technique proposed involves the generation of a depth-modulated light-sheet array which can be used to perform more light-efficient (i.e. faster and less photodamaging) 3D imaging, following the principles of compressive sensing. This thesis presents simulated and experimental results obtained using this compressed imaging scheme to reconstruct the 3D image of sparse solutions of fluorescent beads suspended in agarose. The results obtained so far seem to suggest that, for samples which are sparse enough in the spatial domain, the proposed compressed scheme allows for a successful reconstruction of a 3D image of the sample using half (or less) of the light-sheet images normally required by the traditional plane-by-plane 3D imaging scheme.

Acknowledgements

My biggest thank you goes to my supervisor Dr. Jonathan M. Taylor, who has been a wonderful guide to me throughout my whole PhD, always finding the perfect way to challenge me while also being extremely patient and supportive. I will forever miss our meetings, which I always walked out of magically recharged and full of enthusiasm. I would also like to thank my second supervisor, Prof. Andrew Harvey, who has been a precious source of advice and inspiration and who has helped me make the best out of my PhD years.

I thank all my colleagues and friends from the Imaging Concepts Group, who have helped me so many times and in so many ways. It has been a pleasure and an honour to work with them. I would also like to thank my friends from the University of Glasgow Optical Society and all the other researchers and fellow PhD students that I have met and worked with during my PhD. They have all helped making my PhD such an enjoyable and enriching experience, and for that I am extremely grateful. I am also grateful to the EPSRC (Engineering and Physical Sciences Research Council), which funded my PhD.

Last but not least, I thank my family and friends in Italy, and those friends who have been my family in Glasgow, for their constant support an faith in me.

Contents

List of Figures

List of Tables

List of Abbreviations

DoF	**D**epth **o**f **F**ield
DSLM	**D**igital **S**canned Laser **L**ight-sheet **M**icroscope
FoV	**F**ield **o**f **V**iew
FWHM	**F**ull **W**idth at **H**alf **M**aximum
MIP	**M**aximum **I**ntensity **P**rojection
NA	**N**umerical **A**perture
PSF	**P**oint **S**pread **F**unction
SLM	**S**patial **L**ight **M**odulator
SPIM	**S**elective **P**lane **I**llumination **M**icroscope
WD	**W**orking **D**istance

Dedicated to my mum.

1 Introduction

1.1 Motivation

3D fluorescence imaging of live biological samples allows the study of their intact structure. Moreover, if the 3D imaging can be performed fast enough, it also makes it possible to monitor how the sample's structure changes with time. Light-sheet microscopes are a great tool for this. Their use of a sheet of light to illuminate the sample does two main important things: performs what is called *optical sectioning* and allows fast 3D imaging. *Sectioning* means dividing the 3D sample into a series of planes which are then imaged independently, and *optical* sectioning means doing it optically, *i.e.* without actually cutting the sample in slices. This way the sample can remain intact and, if needed, alive. The sheet illuminates a whole plane simultaneously, which means that each plane can be imaged with a single camera shot. A 3D image can then be obtained by stitching together a stack of 2D images taken at different depths inside the sample. Light-sheet microscopy is therefore faster than other 3D imaging techniques which also perform optical sectioning, like confocal microscopy, where each plane is instead imaged in a point-by-point fashion.

The strength of light-sheet microscopy lies in its unique geometry of sample illumination and imaging light collection: the light-sheet comes in from the side and illuminates a plane which is perpendicular to the optical axis of the detection arm. In the most basic design of a light-sheet microscope, the two arms (one for illumination and one for imaging) are physically independent, but their optimal specifications are linked. In order to have good optical sectioning, the sheet thickness and the imaging DoF (Depth of Field) must match. In fact, if the light-sheet excites fluorescence in parts of the sample that lie outside the DoF of the imaging arm, these are seen as out of focus, contaminating the image with an undesired blur.

Many researchers all over the world work to keep pushing the limits of light-sheet microscopy, to make it even faster and even gentler to the sample. To improve light-sheet microscopes, modifications to their most basic design have been (and keep being) developed, both on their illumination and their imaging side. Considering the illumination side of a light-sheet microscope, one can try and think of different, new ways in which the light-sheet can be shaped and moved in order to improve the quality of the final image. In a similar way, work can be done on the imaging side of the microscope, where the fluorescence exited by the light-sheet can be detected and combined in different ways, both optically and computationally.

This thesis mainly deals with the illumination side of light-sheet microscopes, and it presents a light-sheet microscope which was designed with the main aim of creating a simple yet versatile system which could be a useful tool for researchers working on advanced fluorescence imaging techniques. The microscope was named SLM-SPIM (Spatial Light Modulator Selective Plane Illumination Microscope), as it uses a Spatial Light Modulator (SLM) to move the light-sheet and modify its 3D shape.

Combining a simple and reconfigurable optical design with the versatility offered by the SLM, the SLM-SPIM can be used to test new ideas and innovative imaging techniques, sparing researchers the time and resources needed to build a new imaging system specifically designed for one single experiment. As discussed in this thesis, the SLM-SPIM was in fact used to test two new light-sheet designs: one which aims at enabling longer imaging of fast photo-bleaching samples, and one which can be used to perform faster and less photo-bleaching 3D imaging.

This thesis also discusses how the SLM-SPIM makes it possible to perform many existing imaging techniques which have been developed to improve image quality in a light-sheet microscope. With the SLM-SPIM, the choice of which imaging technique to apply can be made depending on the characteristics of the imaged sample and on the particular biological question one is trying to answer.

1.2 Thesis Layout

This thesis is organized as follows.
Chapter 2 introduces light-sheet microscopy. Chapter 3 describes the system designed, built and used throughout this research project and the optical simulations developed to help with the design of the system and with the experiment planning. Chapter 4 shows how the SLM-SPIM described in Chapter 3 can be used to perform many existing advanced light-sheet imaging techniques, while Chapters 5 and 6 describe how the system was also used to start developing innovative light-sheet designs. Chapter 7 contains general conclusions and a discussion of future works.

2 Light-sheet microscopy

2.1 Introduction

The world of biological research is constantly challenging new technological development, demanding for instruments and methods able to serve increasingly sophisticated research applications. In the field of biological imaging, technological advances such as the revolutionizing onset of fluorescence microscopy and the constant development of new and improved imaging techniques go hand in hand with the use of more biologically relevant model systems. Such systems (as for example tissue samples, three-dimensional cell cultures or whole model organisms) require to be imaged with minimal perturbations in order to preserve their physiological integrity as experimental models. Light-induced photo-damage and photo-toxicity can have quite a dramatic effect on function and health of live biological samples, and minimizing their exposure to excitation light is therefore fundamental, especially when wanting to study their natural development.

Light-sheet microscopes use an unique excitation-detection scheme which allows for fast 3D imaging with minimal exposure of the sample to excitation light (see Figure 2.1). As their name suggests, light-sheet microscopes use a sheet of light to illuminate the sample. The light-sheet makes it possible to selectively excite fluorescence within a restricted, thin section inside three-dimensional, fluorescence labelled samples; at the same time a detection arm aligned perpendicularly to the plane of the light-sheet is used to collect the excited fluorescence and produce a 2D image of the illuminated plane. A complete 3D image can be reconstructed by combining a set of 2D images acquired at different depths inside the sample. The illumination confinement provided by the use of a sheet-like illumination results in dramatically reduced photo-bleaching and photo-toxicity, allowing for long-term imaging of live, intact, biological samples. Fields that largely benefit from light-sheet microscopy therefore include developmental biology/embryology, neurobiology, drug discovery and plant biology.

This chapter provides an introduction to light-sheet microscopy, and is organized as follows. The rest of this introductory section continues with a more extensive discussion of the advantages that light-sheet microscopes give when compared to other types of fluorescence microscopes, but also their limitations (Section 2.1.1), followed by a brief summary of the history of light-sheet microscopy (Section 2.1.2). Section 2.2 contains the most relevant theoretical background needed to fully understand how light-sheet microscopes work, and treats the topics of Gaussian beam propagation (Section 2.2.1), image formation in a microscope (Section 2.2.3) and the physics of fluorescence and photo-bleaching (Section 2.2.2). Section 2.3 builds on the theory described in Section 2.2 and concludes the chapter with some practical considerations involved in the process of designing a light-sheet microscope.

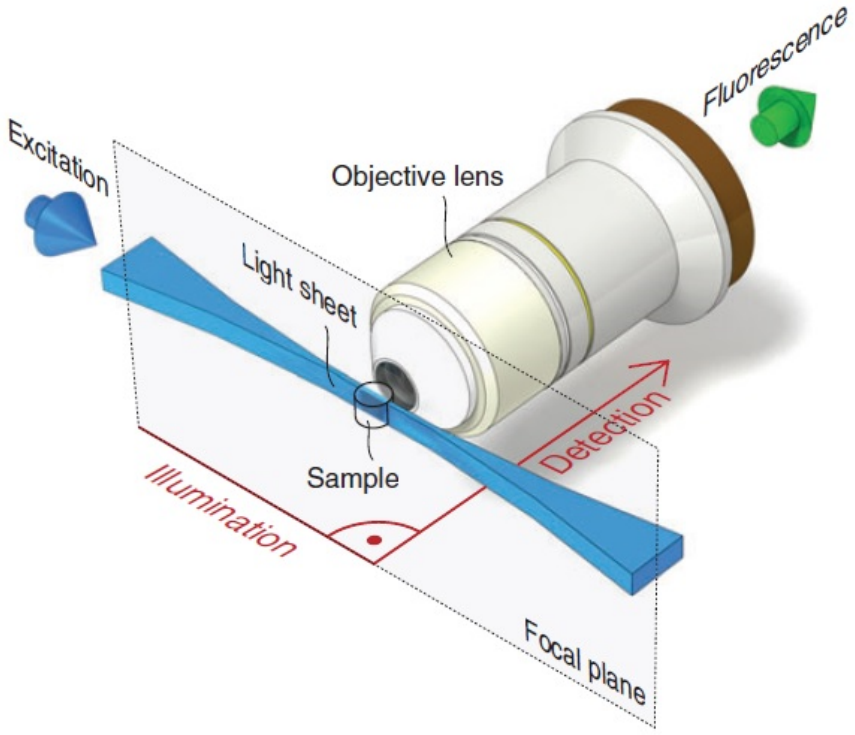

Figure 2.1: *Light-sheet microscopy illumination-detection geometry (figure taken from [1]). The illumination axis (blue arrow) is orthogonal to the detection axis (green arrow). The illumination optics is designed to illuminate a very thin volume around the focal plane of the detection objective, where the sample is placed. Only the sample's fluorophores that are on the illuminated plane get excited, an all the emitted fluorescence is collected by the detection optics and imaged onto a camera.*

2.1.1 Advantages and limitations

To understand what advantage light-sheet microscopy gives when compared to other fluorescence microscopy techniques, let us first introduce the epifluorescence microscope, which can in a way be referred to as the *standard* illumination-detection configuration of a fluorescence microscope. In an epifluorescence microscope light of the excitation wavelength comes from above the specimen (*epi-*, greek prefix for *over, on, upon*), is focused on it through the objective lens, and the fluorescence emitted by the specimen is then focused on the detector by the same objective lens, as shown in Figure 2.2.

Over the years, this technique has become increasingly powerful in terms of resolution, speed and penetration inside the sample, but its good performances are confined to thin (few μm) and transparent samples [2]. One of the reasons for this is that the illumination geometry causes the entire specimen thickness to fluoresce, while the microscope is focusing only at a specific depth (see Figure 2.3). The illuminated parts of the specimen that are out-of-focus emit fluorescence as do the in-focus ones, and their total fluorescence is collected, resulting in an image composed of the in-focus objects surrounded by a very blurred background. Considering that the DoF (the distance between the top and the bottom of the in-focus region of the specimen) of this kind of fluorescence microscopes is < 1 μm, even when viewing a specimen as thin as 5 μm around the 80% of the light collected on the detector may be coming from out-of-focus regions.

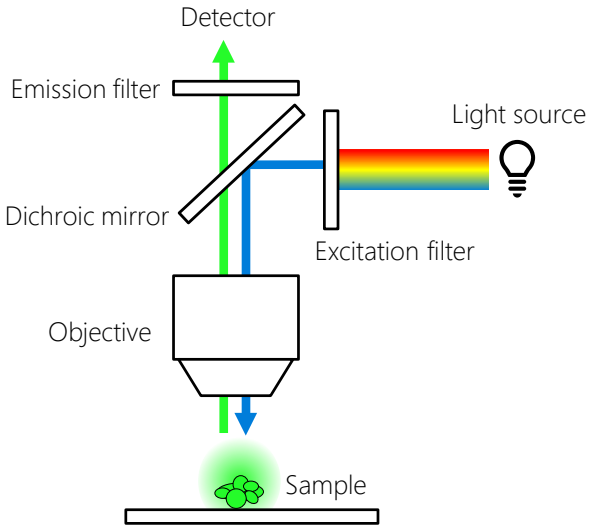

Figure 2.2: *Principles of an epifluorecence microscope. The excitation light (in blue in this figure) comes from above the sample and is focused on it through an objective lens. The fluorescence emitted by the specimen (in green) is focused on the detector by the same objective lens.*

Another problem of fluorescence images is scattering. Some of the fluorescence emission does not go directly into the objective lens, but is instead reflected, diffracted and refracted on its way there by other parts of the specimen, making altogether what can be called scattered light. Once finally collected, scattered light is then imaged on the position corresponding to its last point of scattering, instead of on the actual location of the fluorophore that emitted it. This problem increases when imaging deeper inside the specimen, which is why for thicker samples other techniques must be used, instead of epifluorescence microscopy, which are able to isolate and image a specific plane of the observed sample, performing what is called optical sectioning.

Thanks to their sheet-like illumination, light-sheet microscopes perform optical sectioning [3], which refers to the ability to isolate a clear image of a single plane inside a three-dimensional sample. The development of optical sectioning techniques like light-sheet microscopy has been fundamental not only to improve the performances of fluorescence microscopes in terms of resolution and thickness of the observable specimens, but also for the great impact they have had on 3D imaging of living organisms:
The most common way to reconstruct a three-dimensional image of a sample is to combine a stack of 2D images each representing a different plane inside the sample. To acquire this stack of images, the sample can be physically cut in slices, so that each slice can be imaged separately. This results in a set of clear, in-focus 2D images, each free of any out-of-focus background generated by other parts of the sample. When working with biological imaging though, physically cutting the sample modifies its natural condition and structure, inevitably limiting the relevance of the obtained observations, even more so when wanting to study dynamic or developmental processes. In this case the *slicing* procedure is instead better performed in an optical way, such that the different sections can still be imaged separately while the sample is left alive and intact.

Optical sectioning is not only performed in fluorescence microscopy, but also in other techniques, such as optical projection tomography [4], magnetic resonance

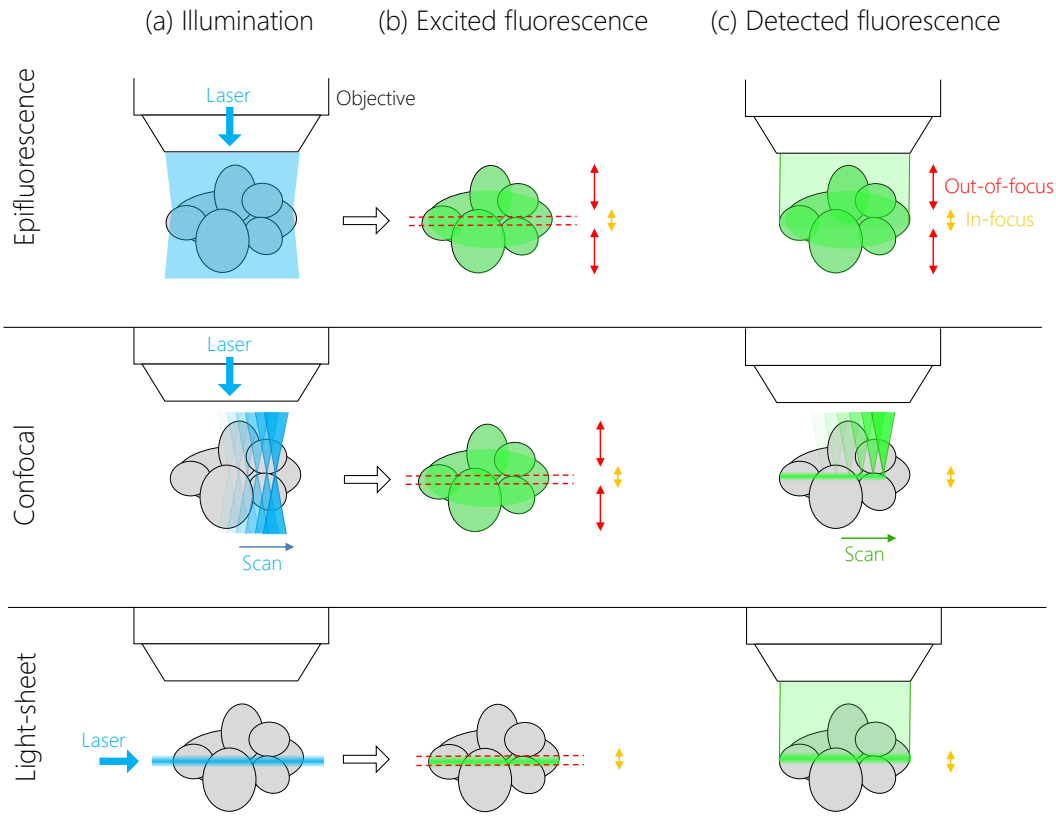

Figure 2.3: *This figure illustrates how three different types of fluorescence microscopes generate the image of a plane inside a three-dimensional sample. An epifluorecence microscope is illustrated in the first row, a laser scanning confocal microscope in the second, and a light-sheet microscope in the third. Column (a) shows how each of the three types of microscope delivers excitation light (in blue) to the plane of interest. Column (b) shows the fluorescence excited by the delivered illumination, and column (c) highlights what fluorescence is collected and effectively ends up in the image of that specific plane. In confocal microscopy, a tightly focused laser beam is scanned across the sample (a), and the sample is thereby exposed to high-intensity light not only in the plane of interest, but also above and below (b). A pinhole rejects much of the excited fluorescence and confines the image to the plane of interest (c). In light-sheet microscopy, a light-sheet illuminates the sample, from the side, within a thin slice (a). This allows to considerably reduce the overall photo-bleaching of the sample, since fluorescence is excited only on the plane of interest. All of the generated fluorescence is then collected and ends up in the final image (c).*

imaging [5] and optical coherence tomography [6]. Within the field of fluorescence microscopy, there are two main different ways of performing optical sectioning: illuminating the entire sample but limiting the detection to the desired volume, or illuminating only the plane of interest and detecting all the fluorescence it produces. The first approach, in which the whole sample is illuminated and the detection is limited to the desired volume, is realized in laser scanning confocal microscopy (LSCM [7], see [8] for an overview of the technique). In confocal microscopy a laser is scanned through the sample and the optical sectioning is achieved by refocusing the generated fluorescence light onto a pinhole. The pinhole selects only the in-focus light, and its size, which can be adjusted, determines the thickness of the section that is imaged. The image of each section is built up by sequentially collecting information from different points within that section. Some limitations of LSCM are the time needed to build up the final image, due to the scanning process, and photo-beaching, *i.e.* the fact that fluorophores lose their ability to fluoresce as they are illuminated,

which then sets a limit to the time over which the sample can be efficiently observed. The strong photo-bleaching effects caused by LSCM come from the fact that exciting a single spot with the laser light also inevitably illuminates the whole depth of the sample. This means that, while scanning just one plane to acquire its 2D image, the whole sample gets exposed to excitation light. Furthermore, the more planes are acquired the more the entire volume is illuminated and therefore subject to photo-bleaching. Performances of LSCM also degrade with the depth at which the optical sectioning is performed, and this technique is therefore usually used for samples of thickness up to 100 μm or for time-lapse dynamics experiments on surface tissue of relatively transparent embryos, such as those of the zebrafish [9].

Light-sheet microscopes instead perform optical sectioning in a different way: they excite fluorescence only where it is needed, *i.e.* on the plane that corresponds to the section one wants to image, and they collect all of the excited fluorescence at once, obtaining a 2D image of the section in a single camera exposure. Following this approach, every time a plane inside the sample is imaged, the rest of the sample remains unexposed to excitation light and therefore free of photo-bleaching and photo-damage effects. Light-sheet microscopy techniques are not the only ones that perform this type of optical sectioning, and another technique that limits the illumination to the desired volume is for example two-photon microscopy (see [10] for a review of the technique). Two-photon microscopy follows the same scanning principles of confocal microscopy but uses high-intensity infra-red laser pulse to excite fluorescence only in a small volume. Using longer wavelengths increases the penetration depth (up to 700 μm) with respect to confocal microscopy, at the cost of a reduced resolution. Another drawback is that the required high power laser increases, over time, photo-bleaching, photo-damage and also heating of the specimen. Light-sheet microscopy instead manages to selectively illuminate the area of interest but at the same time prevents the sample from excessive photo-damage.

Figure 2.3 illustrates the different illumination-detection schemes of an epifluorescence, a confocal microscope and a light-sheet microscope. In and epifluorescence microscope (first row of Figure 2.3), the excitation light illuminates the entire sample (Figure 2.3a), and therefore excites fluorescence in an entire 3D volume (Figure 2.3b). The same objective is used to collect the excited fluorescence, and the image of the in-focus plane therefore contains a diffused background generated by the out-of-focus fluorescence (Figure 2.3c). In confocal microscopy (second row), as the laser beam scans across the sample (Figure 2.3a), the whole sample again gets exposed to the excitation light (Figure 2.3b). The detection arm includes a pinhole which is used to reject out-of-focus light thereby confining the detection volume to a thin slice (Figure 2.3c). In light-sheet microscopy (third row), only a narrow volume around the focal plane is illuminated (Figure 2.3a), so that fluorescence is excited only in the plane that needs to be imaged (Figure 2.3c). The detection objective is used to simultaneously collect all the fluorescence coming from the illuminated plane (Figure 2.3c), which is then focused on the camera to create a sharp image of the plane, with reduced out-of-focus blurred. The biggest advantages in the use of light-sheet instead of confocal microscopy are therefore the much faster acquisition times and the significantly reduced photo-bleaching.

The classical light-sheet microscope uses a cylindrical lens to generate the light-sheet, and is commonly called SPIM (Selective Plane Illumination Microscope, more details on the origin of this acronym in Section 2.1.2). As it can be said for all other

light-sheet microscopes, SPIM's 2D snapshot acquisition and minimized light exposure of the sample makes it particularly well-suited for *in vivo* imaging. Despite this, SPIMs also suffer from a number of issues, including:

- Shadow artefacts: parts of the sample will absorb or scatter the side-launched light-sheet, generating dark stripes behind them, elongated parallel to the illumination direction.
- Scattering: when illuminating a plane inside the sample, light emitted by the excited fluorophores has to travel through sample tissue in order to be collected by the imaging objective, which means it inevitably undergoes some scattering on the imaging path. This results in undesirable out-of-focus background in the images, leading to reduced image contrast. Tissue scattering also affects the propagation of the light-sheet itself, resulting in even more out-of-focus light, in this case coming from out-of-focus fluorophores excited by the scattered light-sheet.
- Limited field of view: even in the absence of scattering, the illumination delivered by a Gaussian light-sheet is not uniform in thickness across the image FoV (Field of View). A Gaussian beam generates a light-sheet with a certain waist size (thickness of the light-sheet at its focus) and extent (Rayleigh length). This shape of the light-sheet results in an uneven illumination across the image FoV, with better optical sectioning around the beam waist, where the light-sheet is at its thinnest, and poorer optical sectioning (more out-of-focus excitation) at the sides of the image, which are generated by the thicker parts of the sheet.

A variety of modifications to the basic SPIM design have been proposed to tackle some of these issues, and similarly for the closely-related technique of DSLM (Digital Scanned Laser Light-sheet Fluorescence Microscopy [11]), where a light-sheet is synthesized by rapid scanning of a focused Gaussian beam. Shadows can be reduced by illuminating the sample from multiple directions [12, 13], and using Bessel [14–16] or Airy [17] beams instead of Gaussian beams permits a more uniform illumination across a larger FoV. One way to reduce the effects of scattering from tissue surrounding the imaged plane is to use a DSLM configuration (where a synthetic light-sheet is formed from a scanned Gaussian beam) in conjunction with a rolling confocal slit on the detection camera to reject scattered light [18]. Methods based on structured illumination, such as HiLo [19] and the method proposed in [20] which we refer to as the 3-phase method, can also help enhance image contrast by reducing the out-of-focus contribution. The technique known as tiling can be used to extend the limited FoV over which high-quality depth sectioning can be achieved, but still using a simple Gaussian beam to generate the sheet [21]. With tiling, each plane in the sample is imaged multiple times, each time with the light-sheet focused at a different lateral position in the FoV; the final image of the plane is then created by stitching together adjacent vertical stripes taken from the different images, each stripe containing only the part of the image generated by the thinnest part of the light-sheet.

Before going into more details on the theory and practicalities of light-sheet microscopy, let us open a parenthesis on a short summary of the history of this technique, which will help the reader get a better idea of the overall context.

2.1.2 Brief history of light-sheet microscopy

Light-sheet microscopy techniques have been used from long before their applications to fluorescence microscopy. The first published record of a microscope where a sheet of light was used to illuminate the sample from the side dates back to the beginning of the 20th century. In their article from 1903 [22], Zsigmondy and Siedentopf describe the microscope which they had named *Ultramikroskop* and used to observe gold particles. In the *Ultramikroskop* (Figure 2.4) the light from the Sun was collected and made pass through an horizontal slit to create a sheet of light, and the light scattered by the gold particles was viewed at 90 degrees from the illumination sheet.

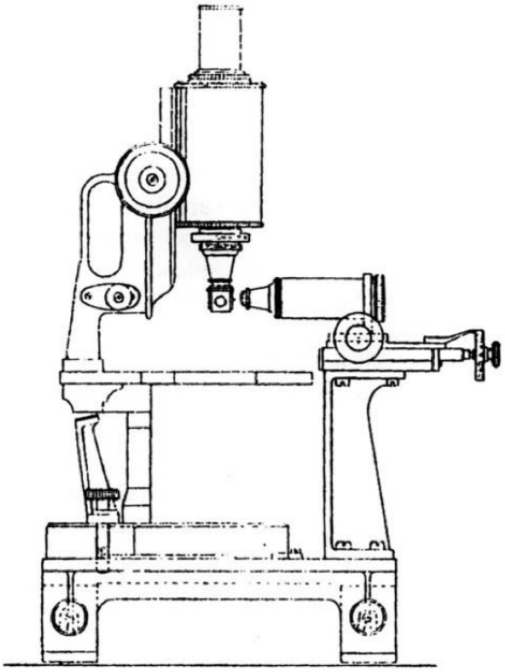

Figure 2.4: *Zsigmondy and Siedentopf's Ultramikroskop (Figure 3 from their initial paper [22]). The specimen holder was here attached to the objective of an upright microscope. The illumination objective was aligned at 90° to the imaging objective. Not shown in this image are the sunlight collector and the slit aperture which were aligned behind the illumination objective and used to form the light-sheet.*

A consistent further development of the light-sheet microscope, and its first application to fluorescence microscopy, only appeared several decades later. In 1993 Voie and colleagues published an article about the technique they had developed to investigate the 3D structure of guinea pig cochleas [23]. They called their technique Orthogonal Plane Fluorescent Optical Sectioning (OPFOS) and with it they were able to optically section whole fluorophore-stained and cleared cochleas. Their microscope (Figure 2.5) contained all the main elements which are present in current light-sheet devices: laser, cylindrical lens to create the light sheet, sample chamber, specimen clearing and staining for producing fluorescent optical sections and specimen movement to image different planes inside the sample.

In 2002, a few years after the OPFOS microscope, Fuchs *et al.* published their implementation of a thin laser light-sheet to image microbes with reduced background

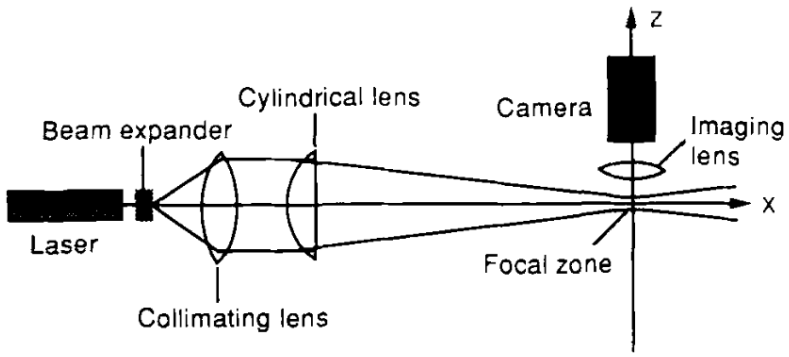

Figure 2.5: *Optical scheme of Voie et al.'s set-up to perform Orthogonal Plane Fluorescent Optical Sectioning (OPFOS)(Figure 2 from their 1993 paper [23]). This microscope contained all the main elements which are present in current light-sheet devices: laser, cylindrical lens to create the light sheet, sample chamber (not shown in this figure), specimen clearing and staining for producing fluorescent optical sections and specimen movement to image different planes inside the sample.*

illumination for oceanography [24]. In 2004 a Science article by Huisken *et al.* highlighted the usefulness of light-sheet microscopes for investigating embryonic development, reporting experiments on fruit fly embryos (*Drosophila Melanogaster*) and green fuorescent protein in muscle tissue of live Medaka fish (*Oryzias Latipes*) embryos [25]. The light-sheet microscope described by Huisken *et al.* brought the resolution of the OPFOS microscope (10 μm of lateral resolution and 26 μm of longitudinal resolution) to sub-cellular scales (up to better than 6 μm as deep as 500 μm inside the Medaka fish embryo). The frame recording speed reached by their system (10 frames per second) also allowed imaging of the heartbeat of the fish embryo that had previously been possible only in reduced heartbeat rate conditions. Figure 2.1 illustrates the typical illumination-detection geometry of such modern light-sheet microscopes, with one objective used to demagnify the light-sheet onto the sample and one objective used to collect the excited fluorescence.

Huisken *et al.* named their microscope Selective Plane Illumination Microscope (SPIM), an acronym which is nowadays used to refer to all light-sheet systems which use a cylindrical lens to generate the light-sheet. Over the years, in fact, light-sheet microscopes have evolved into many designs, which differ in terms of: light source used, light-sheet focusing techique, light-sheet inclination and properties, ideal specimen characteristics (such as size and scattering properties), freedom of movement of the specimen, FoV size, range of reachable depths inside the specimen, speed of data acquisition and processing, and more. A useful review of the most relevant existing light-sheet techniques can be found in [26] (see Table 2 therein for a direct comparison of the different techniques, with linked references) and [1] (Table 1).

Since 2004, light-sheet microscopy has been used in many applications, such as cell imaging [15], particle tracking [27] and neuronal imaging [28], and it has become a fundamental tool in non-destructive biological imaging [29, 30]. Modern light-sheet systems can reach an acquisition speed of up to hundreds of frames per seconds, have a lateral resolution which is primarily limited by the resolution of the imaging objective (usually $0.5 - 2$ μm) and an axial resolution which depends on the thickness of the light-sheet (usually $2 - 6$ μm).

2.2 Theory

This section summarizes the theoretical background useful to understand the three main physical processes involved in the formation of a light-sheet image: delivery of the excitation light to the sample in the form of a light-sheet (Section 2.2.1, referring to [31] for the theory of beam propagation), fluorescence emission from the illuminated parts of the sample (Section 2.2.2), collection of the excited fluorescence to generate an image (Section 2.2.3).

2.2.1 Gaussian beam propagation

A classical SPIM system uses a Gaussian beam to form the light-sheet. The sheet formed by collimating the light-beam using a cylindrical lens can be characterised by two main parameters: the size of its waist, which defines the maximum obtainable z-resolution, and its Rayleigh length, which defines the lateral extent of the region of the image characterized by good optical sectioning.
Consider a Gaussian beam propagating in a collimated fashion. Let z be the direction of propagation of the beam, and r the distance measured, in a transverse plane, from the central axis of propagation z. The light intensity profile of the collimated beam has a radial symmetry around the axis of propagation, meaning that it only depends on r. This dependence on r can be described by a Gaussian function (see p. 594 of [31]):

$$I(r) = I_0 e^{-2r^2/w^2}, \tag{2.1}$$

where I_0 is the intensity at the center of the beam ($r = 0$) and w is the beam half-width, defined as the value of r where the intensity falls to a value I_0/e^2 ($\simeq 0.14 I_0$). This means that most of the energy of the beam resides within an imaginary cylinder of radius w, as depicted in Figure 2.6.

When a Gaussian beam is focused (Figure 2.7), its intensity profile becomes dependent on z too, and Equation 2.1 becomes:

$$I(r,z) = I_0 e^{-2r^2/w(z)^2}. \tag{2.2}$$

The dependence of the beam half-width w on the position z along the axis of propagation (with $z = 0$ being the position of the focus) can be described as follows:

$$w(z) = w_0[1 + (\frac{\lambda z}{\pi {w_0}^2})^2]^{1/2}, \tag{2.3}$$

with w_0 being the beam half-width at $z = 0$, known as the beam waist. A practical measure of the divergence of a focused Gaussian beam is the distance over which its cross-sectional area doubles, or equivalently, the value of z for which $w(z) = \sqrt{2} w_0$. This distance is known as the Rayleigh range (z_R), and it follows from Equation 2.3 that:

$$z_R = \frac{\pi {w_0}^2}{\lambda}. \tag{2.4}$$

The smaller the waist w_0, the smaller the Rayleigh range z_R and the faster the beam diverges. For $z \gg z_R$ Equation 2.3 can be approximated as:

$$w(z) \approx w_0[(\frac{\lambda z}{\pi {w_0}^2})^2]^{1/2} \approx \frac{\lambda z}{\pi w_0}, \tag{2.5}$$

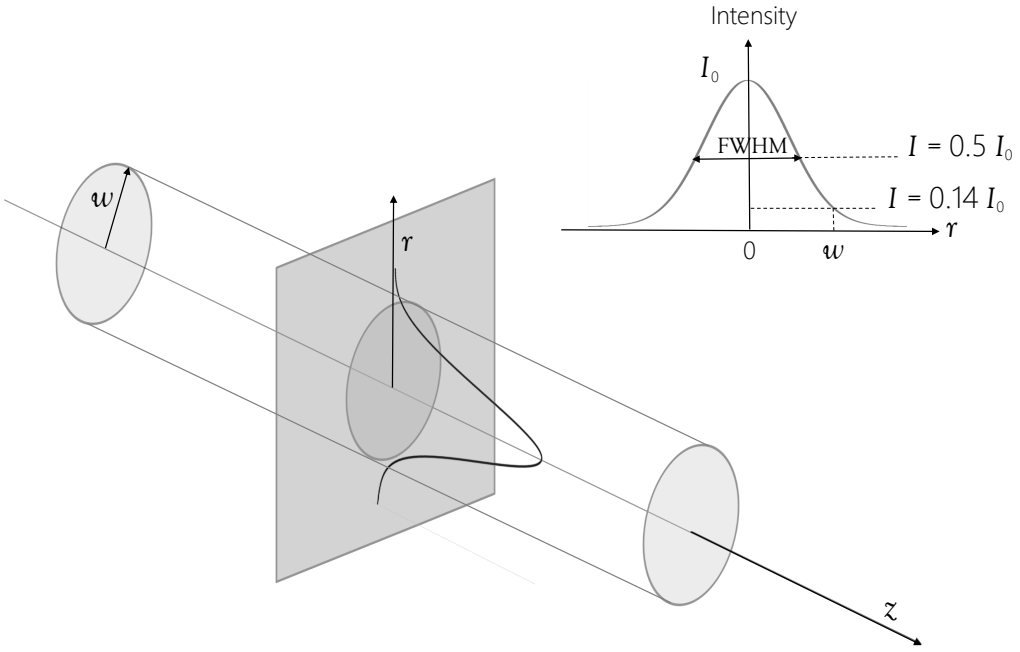

Figure 2.6: *Propagation of a collimated Gaussian beam. As the beam propagates along the direction z, its intensity profile only depends on r, the distance from the axis of propagation. The intensity profile along r has a Gaussian shape, with a maximum intensity I_0 at $r = 0$. Most of the energy of the beam resides within an imaginary cylinder of radius w, which is the beam half-width and is defined as the value of r where the intensity falls to I_0/e^2.*

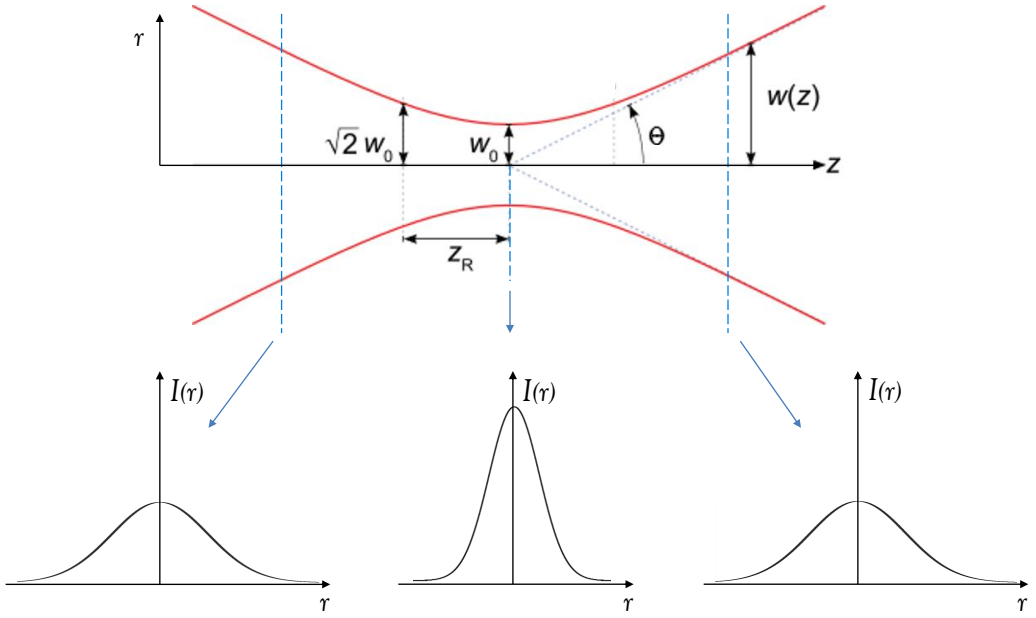

Figure 2.7: *Focused Gaussian beam. The intensity profile of the beam $I(r,z)$ depends both on the position along the axis of propagation (z) and the radial distance from it (r). The minimum beam width is called the beam waist w_0, while the Rayleigh range z_R is defined as the distance from the beam waist, along z, at which the beam width has diverged to a size of $\sqrt{2}w_0$.*

and since for $z \gg z_R$ the half-angular width of the beam (θ, in radians) approaches $w(z)/z$, a further approximation gives:

$$\theta \approx \frac{\lambda}{\pi w_0} \approx 0.32 \frac{\lambda}{w_0}, \tag{2.6}$$

which directly shows how the divergence rate of the beam increases for smaller values of the beam waist w_0.

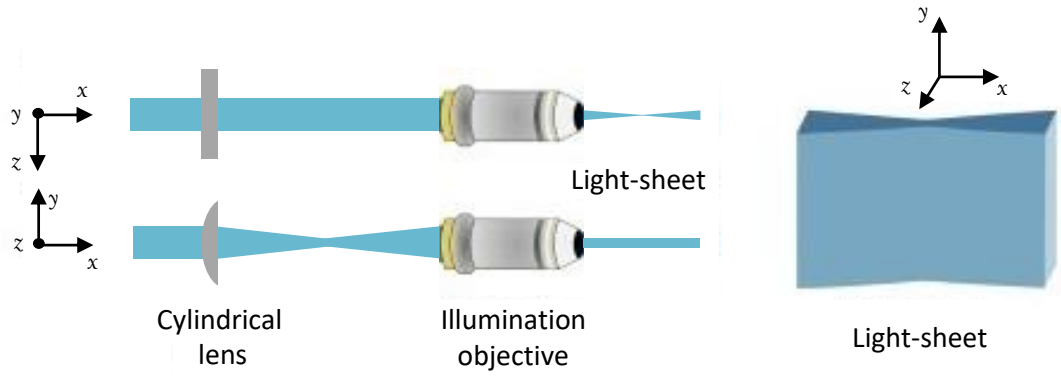

Figure 2.8: *In a SPIM, a cylindrical lens is used to focus a collimated beam in one direction. This figure shows two perpendicular views of a launching arm of a SPIM, showing how the cylindrical lens acts on the collimated beam coming in from the left, and how the objective de-magnifies and rotates the light-sheet generated by the cylindrical lens. The general convention in light-sheet microscopy is to name x the lateral direction in the images, y the vertical direction in the images, and z the direction parallel to the optical axis of the imaging arm of the microscope. These correspond to the axis of propagation of the light-sheet (x), the axis along which the light-sheet can be considered collimated (y) and the axis along which the light-sheet is focused (z).*

In a SPIM, the light-sheet is formed using a cylindrical lens, as in Figure 2.8. The cylindrical lens has optical power only in one direction, and it therefore transforms a collimated beam into a beam that is collimated in one direction and focused in the other. An objective is then used to de-magnify the light-sheet and direct it onto the sample. The beam divergence is linked to the numerical aperture (NA) of the objective focusing the beam by

$$\mathrm{NA} = n \cdot sin(\theta)\,, \tag{2.7}$$

where n is the refractive index of the medium. This, combined with Equation 2.6, gives

$$w_0 \approx 0.32 \frac{n\,\lambda}{\mathrm{NA}}. \tag{2.8}$$

Equations 2.7 and 2.8 show that a higher NA objective produces a thinner, but more quickly diverging light-sheet. In practice, the actual NA of an objective is decreased if only a portion of the rear aperture of the objective is filled by the incoming beam. The NA can be related to the physical properties of the objective in the following way:

$$\mathrm{NA} = \frac{d_{obj}}{2f}\,, \tag{2.9}$$

where d_{obj} is the used diameter of the objective lens, and f is its focal length. This means that, for example, if the beam only covers half of the back aperture of the

objective, the effective NA becomes 0.5 × NA, and the sheet waist doubles. In light-sheet microscopy the thickness of the sheet is usually specified using $2w_0$ or, more commonly, by its Full Width at Half Maximum (FWHM) (see Figure 2.6), with the relation between FWHM and w_0 being $w_0 = 0.849\times$ FWHM [32].

2.2.2 Fluorescence and photo-bleaching

The quality of an image can be assessed in different ways, and one of the qualities of a good microscopic image is its contrast, which quantifies the difference in brightness between what is interesting in the image (signal) and what is not (background, noise). Scientists working with microscopes have always put a lot of effort in the attempt to increase image contrast, and the discovery of fluorescent proteins in the early 1960s [33] made a big step forward in this direction, revolutionizing light-microscopy and becoming one of the most important tools at the service of biological imaging [34, 35].

In fluorescence microscopy the signal/background problem is tackled by labeling the desired cells, molecules, or even tissues with fluorescent molecules (fluorophores), so that the objects of interest become much brighter than the background. When fluorophores are illuminated they absorb the light, *i.e.* the energy, and later (nanoseconds) re-emit it producing what is called fluorescence emission. The emitted light has a different wavelength (typically longer) with respect to the absorbed one, and this is the property that makes fluorescence so powerful [36]: by using optical filters one can observe the fluorescence emitted by a sample without seeing the excitation light, thereby generating an image of the labelled parts only.

Let us see how fluorescence works in a bit more details. The phenomenon of fluorescence actually consists of two consecutive events. The first event is the absorption, by a fluorescent molecule (fluorophore), of one photon, which brings the fluorophore to and excited singlet state S^*. The second event is the relaxation of the fluorophore to the ground state S^0, with the emission of a photon, called fluorescent emission (Figure 2.9). A fluorophore in the excited state S^* can also transition into an excited triplet state T^* trough a radiationless process, and from there go back to the ground state S^0 with the radiation of a photon, which is in this case called a phosphorescent emission. In the linear regime (1-photon process), the density of absorbed photons (or excited fluorophores) per second, n_{1p}, depends on the fluorophore density n_0, the density of excitation photons and the probability each photon has of being absorbed. This probability can be characterized by the absorption cross section δ_{1p}, and depends on the wavelength of the photons and the material capability to absorb one photon. The density of excited fluorophores per second can therefore be written as

$$n_{1p} = \delta_{1p} n_0 \frac{I_\nu}{h\nu}\,, \tag{2.10}$$

where h is the Planck constant and I_ν is the intensity of the excitation laser at the photon frequency ν, so that $I_\nu/(h\nu)$ expresses the photon density. Generally, the excited molecule goes through different energy states before relaxing to its ground state emitting a photon, which is why the emitted photon is of a longer wavelength (less energy) than the absorbed one. The energetic difference between excitation and emitted photons is deposited on the sample, which may result in some damage (photodamage) through the production of heat. The efficiency of the fluorescence emission can be quantified by the quantum yield Φ, defined as the fraction of excited fluorophores that return to the ground state emitting one fluorescent photon. A low

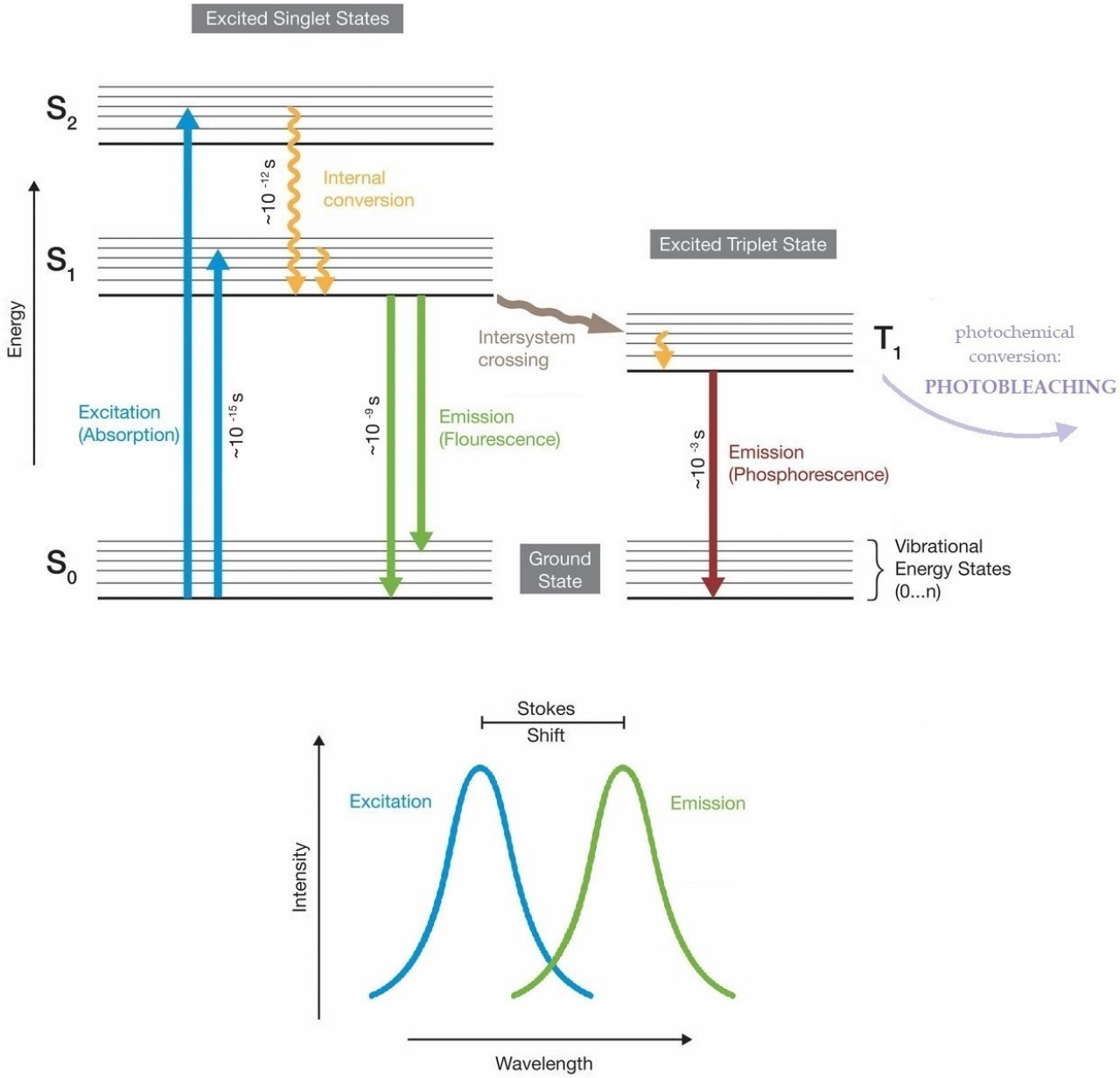

Figure 2.9: *Electronic energy level scheme illustrating linear fluorescence and the phenomenon of photo-bleaching. The absorption of a photon (blue arrows) sends the molecule into an excited energy state. The molecule goes back to its ground energy state by a combination of non-radiative relaxation (yellow wavy arrows) and the emission of a photon of longer wavelength than the absorbed one. The difference in wavelength between the absorbed and the emitted photons is called Stokes shift. If the photon emission comes from the relaxation of an excited singlet state it is called fluorescence (green arrows). If the excited molecule transitions to a triplet state before relaxing emitting a photon, the emission is called phosphorescence (red arrow). Moreover, the excited molecule might photo-bleach, which means that it undergoes a photochemical conversion and thereby looses its ability to fluoresce or phosphoresce.*

value of Φ means that the probability of photodamage is high. Using Equation 2.10, the number of photons emitted per second, Θ_{em}, for an interaction length l can be written as:

$$\Theta_{em} = \Phi \times n_{1p} \times S \times l = \Phi \times \delta_{1p} \times n_0 \times \frac{P}{h\nu} \times l\,, \tag{2.11}$$

where Φ is the quantum yield, S is the cross section of the laser beam and P is the excitation power, which is equal to $I_\nu \times S$. The fact that Equation 2.11 can be written as a function of the laser power, instead of directly depending on S, means that the value of Θ_{em} remains constant along the excitation laser beam, as long as the saturation state is not reached ($\Theta_{em} \ll n_0$). If the excitation beam is focused, the fluorescence will be more intense at the focus, where I_ν is higher, but since the area of the beam is smaller the number of emitted fluorescence photons will be the same as at any other section of the beam.

Photo-bleaching

Photo-bleaching is the phenomenon when a fluorophore loses its fluorescence due to damage induced by light. Molecules in the excited states S^* or T^* permanently lose their fluorescent capacity due to this dynamic process, thus irreversibly reducing the total amount of fluorophores in the ground state S^0 which may be excited. Photo-bleaching is an unwanted secondary effect, since it diminishes the amount of available fluorophores and, therefore, eliminates potentially useful information [37]. Photo-bleaching of a fluorophore or fluorescent sample is influenced by many factors, such as the chemical microenvironment in which the fluorophore is immersed, the presence of oxygen in the sample, and also the excitation radiation intensity, since high intensities imply high rates of photo-bleaching. This makes it difficult to find a general analytical model for the photo-bleaching process which would hold for all samples [38].

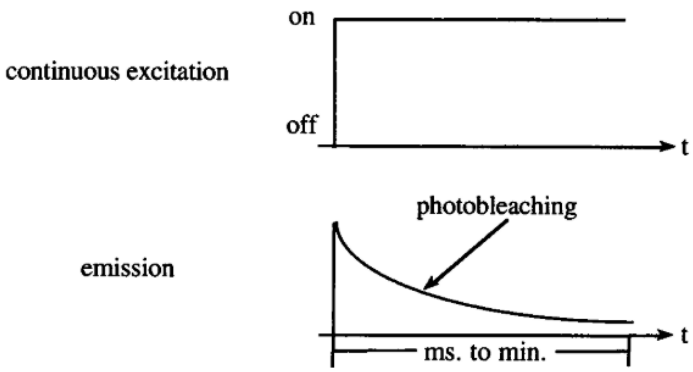

Figure 2.10: *Exponential decay of emitted fluorescence due to photo-bleaching caused by a continuous exposure to excitation light. Figure taken from Figure 2b of [39]. In fluorescence microscopy, photo-bleaching can be observed on the time scale of microseconds to minutes.*

Different types of photo-bleaching curves have been observed, and they generally present a negative exponential behavior [39] (Figure 2.10) that is modeled by a mono-exponential or multi-exponential curve. Equations 2.12 and 2.13 correspond to mono- and bi-exponential curves respectively, where $I(t)$ is the fluorescence intensity as a function of time t. The mono-exponential approach considers an homogeneous fluorochrome population with rate of photobleaching a and initial intensity I_0, while the bi-exponential models two different populations with rates b and c, and initial intensities $I_{0,b}$ and $I_{0,c}$ respectively:

$$I(t) = I_0 e^{-at} \tag{2.12}$$

$$I(t) = I_{0,b}e^{-bt} + I_{0,c}e^{-ct} \tag{2.13}$$

The topic of photo-bleaching will be discussed further in Chapter 5, where I present my attempts of modelling this process and try to see if I can observe a decrease in the photo-bleaching rate of the sample when using a different, special type of light-sheet.

2.2.3 Image formation

This section is dedicated to explaining the physical meaning of a few imaging terms which are used throughout this thesis, giving definitions and useful formulas for: diffraction limit, Airy disk, PSF (Point Spread Function), DoF (Depth of Field) and NA (Numerical Aperture).

The wave nature of light imposes a limit on the optical resolution of imaging systems, which describes its ability to reproduce fine details of an object. This limit is called the diffraction limit, and is a consequence of the interference that light waves experience as they propagate through an optical system. The result of this is that a point source of light is always reproduced, in the image, as a spot of a certain size. The pattern formed by a point source is known as the Airy disk (Figure 2.11a) and consists of a central bright spot surrounded by light circles of decreasing intensity. The intensity plot corresponding to the Airy disk is called the Point Spread Function, or PSF (Figure 2.11b).

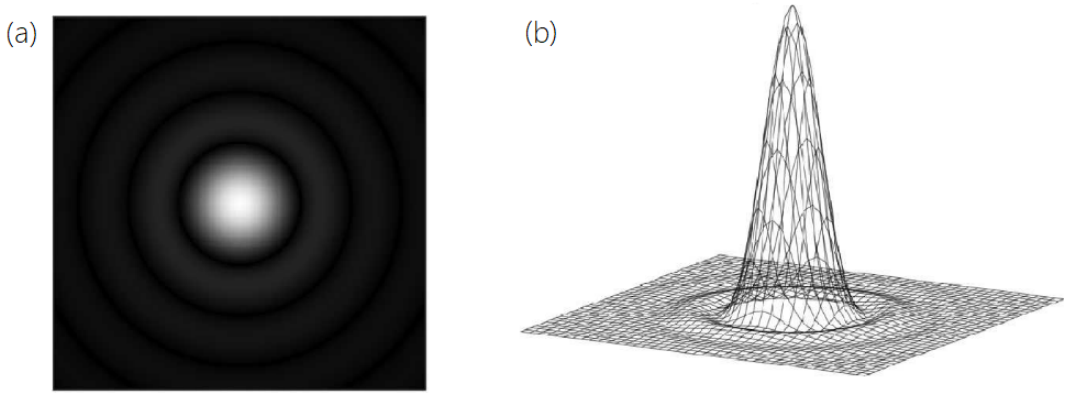

Figure 2.11: *Figure taken from [40]. Airy disk and relative PSF. Because of diffraction, a point source of light is reproduced as a blurry Airy disk (a) in the image of an imaging system. The surface plot of the Airy disk is called Point Spread Function (PSF)(b), and defines the optical resolution limit of the imaging system.*

The optical resolution of the imaging system can also be thought of as its ability to distinguish between two closely spaced Airy disks, and its therefore defined by the shape of its PSF. Two point sources are seen, in the image, as two PSFs. If the PSF of the system is very narrow, the two point sources can get very close to each other and still be resolved, *i.e.* recognised as being two distinct objects. In the 19th century, Ernst Abbe addressed the physics and mathematics of the PSF [41], and defined an equation that yields the smallest distance R over which 2 objects emitting light at a wavelength λ can be resolved:

$$R = \frac{\lambda}{2\ n \cdot sin(\theta)}, \tag{2.14}$$

where n is the refractive index of the medium and θ is half the angular aperture of the imaging lens, which together determines how much of a wave front can be captured. Equation 2.14 can be re-written in terms of the NA of the lens, which is defined as $\text{NA} = n \cdot sin(\theta)$:

$$R = \frac{\lambda}{2\ \text{NA}}\,. \tag{2.15}$$

Higher NA means better lateral resolution (smaller R). As illustrated in Figure 2.12, given a certain angular aperture (fixed θ), a medium of high refractive index (as for example immersion oil) will bend more light into the FoV of the objective lens, resulting in an increase of resolution. Equation 2.14 also shows that resolution increases as the wavelength decreases.

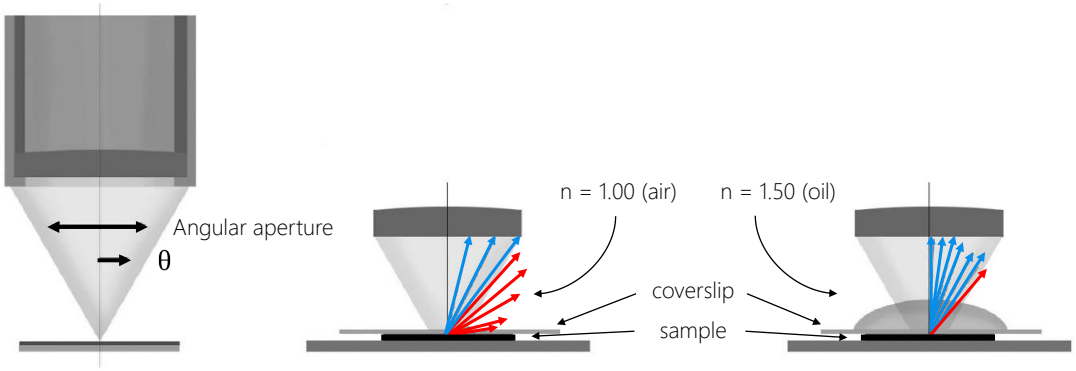

Figure 2.12: *Figure adapted from [40]. Illustration of the NA of an imaging lens, which can be defined as* $\text{NA} = nsin(\theta)$. *Both a large value of* θ *(half the angular aperture of the lens) and a high refractive index (n) have in fact the effect of increasing the amount of light from the specimen that the lens is able to capture (blue arrows).*

Lord Rayleigh gave a slightly different value for the resolution limit [42]: $R = 0.61\lambda/(n \cdot sin(\theta))$, which in practical applications only makes a small difference compared to Abbe's value of $0.5\lambda/(n \cdot sin(\theta))$. Both Rayleigh and Abbe defined it as the minimum distance at which two point sources can be in order for them to still be resolvable, *i.e.* distinguishable as two different objects. The difference in the resolution limit expressions given by the two scientists therefore simply comes from their different interpretation of what it means for two objects to be resolvable. Figure 2.13 illustrates the two different definitions for the resolution limit.

The resolution of an imaging system can also be quantified in the direction parallel to the optical axis (called axial or longitudinal direction) and is most often referred to as depth of field (DoF). Just as in classical photography, depth of field refers to the distance between the nearest and farthest object planes which are simultaneously seen as in focus. The term depth of *field* is used when talking about the object space, while depth of *focus* refers to the image space. In fact, even in the absence of aberrations, each point source generates a diffraction spot that actually extends above and below the image plane, and the above mentioned Airy disk only represents the 2D section of it across the intermediate image plane. Abbe's expression for the axial resolution is:

$$R_z = \frac{2\lambda}{(n \cdot sin(\theta))^2}\,. \tag{2.16}$$

Objectives commonly used in microscopy have an NA lower than 1.5, restricting the term θ in Equations 2.14 and 2.16 to less than 70 degrees (with new high-NA objectives closely approaching this limit). Using Abbe's Equations 2.14 and 2.16 one finds

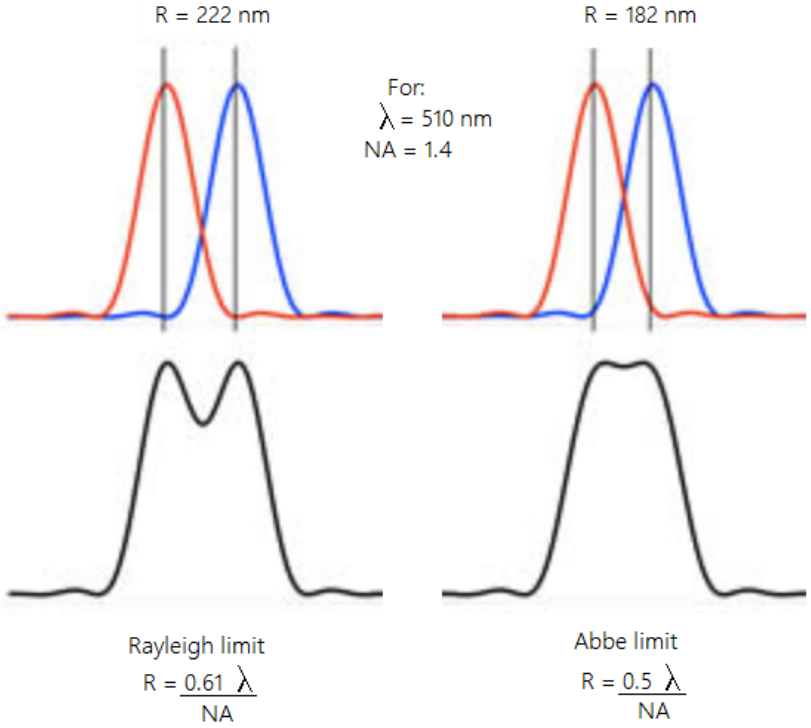

Figure 2.13: *Illustration of Abbe and Rayleigh's resolution limit definitions. According to Rayleigh, when two point sources are separated by a distance equal to the resolution limit, the first minimum of one Airy profile overlaps with the maximum of the second Airy profile (see first row in the figure), and the sum of the two profiles shows a distinct dip (second row). According to Abbe instead, at the diffraction limit only a much smaller dip is still discernible between the two main maxima of the Airy disks.*

that the theoretical resolution limit at the shortest practical excitation wavelength (approximately 400 nm) and with an objective having a NA of 1.40 is around 140 nm in the lateral dimension and approaching 400 nm in the axial dimension.

2.3 Practical considerations for light-sheet microscope design

A basic light-sheet microscope is made of an illumination arm (also called launching arm or excitation arm), a sample holder, and a detection arm (also called imaging arm). The role of the launching arm is to generate the light-sheet, and it is generally composed of a light source (laser), some optical components to collimate and expand the laser beam, some components to generate the light-sheet (a cylindrical lens, in the case of a SPIM), and an objective lens to de-magnify the light-sheet and focus it on the sample. The sample is mounted in front of the launching objective, usually attached to a set of translation stages which enable its precise placement. In light-sheet microscopes where the sample is imaged immersed in a medium, like water or glycerol, the sample is mounted inside a chamber which contains the imaging medium. The detection arm is generally composed of an objective lens, a filter to reject the illumination wavelength, a 2D detector array (*e.g.* a CCD or a sCMOS camera) and a lens which focuses the image onto the detector, which is called the tube lens.

The launching and detection arms of the light-sheet microscope are aligned at 90 degrees from each other, with the two objectives close to the sample. In case of dipping

objectives, these are immersed and/or sealed to the sample chamber. The different components used to build a light-sheet microscope should be chosen taking into account the interplay between the parameters of the components of the two arms, the size of the samples to be imaged and the desired FoV and resolution of the final images. In order to understand how to make these choices and where to start from, it is useful to start by studying the two arms of the microscope separately.

2.3.1 Illumination arm

As seen in Section 2.2.1, a light-sheet microscope uses a focused light beam to produce the excitation light-sheet. In the case of a Gaussian beam, its beam waist w_0 can be used to define the minimum thickness of the sheet, and can therefore be related to the sectioning ability of the microscope. In a first approximation, the beam waist w_0 can also bee linked to the axial resolution $R_{axial,ill}$ of the microscope, which can be expressed as $R_{axial,ill} = 2 \cdot w_0$. Using Equation 2.8 this becomes:

$$R_{axial,ill} = 2 \cdot w_0 = 2 \cdot \frac{n \cdot \lambda_{ill}}{\pi \cdot \mathrm{NA}_{ill}}. \tag{2.17}$$

In a similar way, the Rayleigh range z_R of the Gaussian sheet can be related to the FoV of the image by $\mathrm{FoV}_{ill} = 2 \cdot z_R$, which, using Equation 2.4 gives:

$$\mathrm{FoV}_{ill} = 2 \cdot z_R = 2 \cdot \frac{\pi \cdot w_0^2}{\lambda_{ill}}. \tag{2.18}$$

Conveniently, the FoV as defined by the previous equation is also equal to the FWHM of the axial intensity distribution (along x in Figure 2.14) of the Gaussian beam.

The previous equations start showing how the imaging parameters are linked to the size and shape of the light-sheet used: to image over a larger FoV one needs to increase the Rayleigh range of the excitation sheet, which can be achieved by lowering the NA of the launching objective. However, this will also reduce the optical sectioning capabilities, as the thickness of the generated sheet will also increase.

Depending on the application, truncated or *apertured* beams might be used instead of a Gaussian beam. It is therefore useful to find a more general definition for both resolution and FoV, without using parameters related to the Gaussian nature of the beam (see Chapter 5 for an example of the use of a non-Gaussian beam). As for Gaussian beams, the axial resolution of an image formed with apertured beams is related to their thickness at the focal position, which corresponds to the diameter of the Airy disk. Following Rayleigh's definition of the resolution limit $R = 0.61 \cdot \lambda/\mathrm{NA}$, the diameter of the Airy disk can be expressed as:

$$R_{axial,ill} = 1.22 \cdot \frac{\lambda_{ill}}{\mathrm{NA}_{ill}}. \tag{2.19}$$

Similarly, the FoV of the image will be related to the size of the main lobe of the focused beam in the axial direction (x- axis in Figure 2.14), which takes the form of a sinc^2 function:

$$\mathrm{I}(x) \propto \left(\frac{\sin(x)}{x}\right), \tag{2.20}$$

with $\mathrm{I}(x)$ being the intensity distribution of the focused beam along the x- axis. In this scenario, the distance D_x between zeroes of the sinc^2 function can be expressed

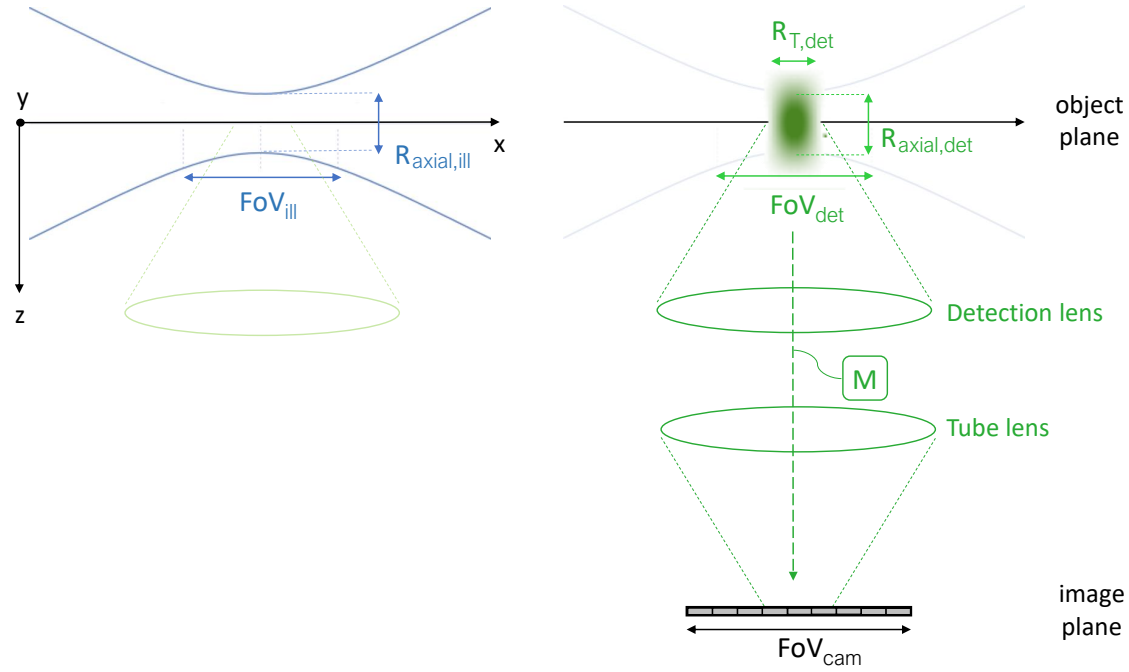

Figure 2.14: *Schematic of the illumination (on the left, in blue) and detection (on the right, in green) arm of a light-sheet microscope. The two arms are aligned at 90 degrees from each other, with the detection arm ending with the imaging sensor. The thickness and Rayleigh length of the light-sheet can be used to define $R_{axial,ill}$ and FoV_{ill}, respectively the axial resolution and the FoV provided by the light-sheet. The parameters of the optical components of the detection arm can be used to calculate the actual resolution (axial $R_{axial,det}$, and transversal $R_{T,det}$) and FoV (FoV_{det}) guaranteed by the detection arm. When building a light-sheet microscope, the aim is to chose the illumination and detection optics such that the resolution and FoV derived by the shape and size of the light-sheet match as well as possible those derived using the parameter of the detection arm. Moreover, one should take into account how R and FoV defined on the object plane map onto the image plane, since the size of the camera pixels and the size of the camera's total active area (FoV_{cam}) pose a limit to the transversal resolution and image FoV.*

in terms of λ_{ill} and NA_{ill} as [43]

$$\mathrm{D}_x = \frac{4 \cdot n \cdot \lambda_{ill}}{\mathrm{NA}_{ill}^2}, \tag{2.21}$$

but, as for Gaussian beams, the FoV can be defined as the FWHM of the central lobe of the sinc^2 function, and therefore be expressed as

$$\mathrm{FoV}_{ill} = \frac{1.78 \cdot n \cdot \lambda_{ill}}{\mathrm{NA}_{ill}^2}. \tag{2.22}$$

2.3.2 Detection arm

Following Rayleigh's definition, the transverse resolution of the detection arm can be expressed as:

$$R_{T,det} = \frac{0.61 \cdot \lambda_{em}}{\mathrm{NA}_{det}} \tag{2.23}$$

where NA_{det} is the NA of the detection objective and λ_{em} the fluorescence emission wavelength. Taking into account the same criteria (FWHM) as before, the axial resolution will be will be given by

$$R_{axial,det} = \frac{1.78 \cdot n \cdot \lambda_{em}}{\mathrm{NA}_{det}^2}. \tag{2.24}$$

The properties of the imaging sensor also play an important role in defining the final imaging properties, and a first important design consideration is that both the pixel size and the total active area of the imaging device need to be carefully adapted to the optical resolution and available FoV generated by the light-sheet, respectively. The maximum available FoV on the imaging device, FoV_{cam}, corresponds to the size of its active area, and can be expressed in terms of the pixel size and number of pixels as:

$$\mathrm{FoV}_{cam} = \mathrm{pixelsize}_x \cdot \#\mathrm{pixels}_x\,, \tag{2.25}$$

where $\mathrm{pixelsize}_x$ is the size of the pixels in the x- direction (lateral direction in the image), and $\#\mathrm{pixels}_x$ is the number of pixels in the same direction. FoV_{cam} corresponds, in the object plane, to a FoV_{object} equal to:

$$\mathrm{FoV}_{object} = \frac{\mathrm{FoV}_{cam}}{\mathrm{M}}\,, \tag{2.26}$$

where M is the magnification of the detection, given by

$$\mathrm{M} = \frac{f_{TL}}{f_{obj}}\,, \tag{2.27}$$

with f_{TL} being the focal length of the tube lens and f_{obj} the focal length of the imaging objective. When building a light-sheet microscope, one ideally wants the FoV generated by the light-sheet to match with FoV_{object}, the size in the object plane of the FoV offered by the imaging detector. Calling FoV_{ill} the FoV generated by the light-sheet as expressed by Equation 2.18 or 2.22, this ideal match can be written as:

$$\mathrm{FoV}_{ill} = \mathrm{FoV}_{object} = \frac{\mathrm{FoV}_{cam}}{\mathrm{M}} = \frac{\mathrm{pixelsize}_x \cdot \#\mathrm{pixels}_x \cdot f_{obj}}{f_{TL}}\,. \tag{2.28}$$

As regards the lateral resolution, according to the Nyquist sampling criterion we know that the maximum resolving power in the transverse direction on the camera, $R_{T,cam}$, can be expressed in terms of the pixel size as

$$R_{T,cam} = 2 \cdot \mathrm{pixelsize}_x\,. \tag{2.29}$$

In order to fully exploit the theoretical resolving power allowed by the optical components of the detection arm, one needs to make sure that the optical resolution limit $R_{T,det}$ as given by Equation 2.23 is not smaller than the one reachable by the detector. Expressing both quantities in sizes in the object plane, this constraint can be

formalized as:

$$R_{T,det} \geq R_{T,cam} = \frac{R_{T,cam}}{\mathrm{M}} = \frac{2 \cdot \mathrm{pixelsize}_x}{\mathrm{M}} \tag{2.30}$$

$$\frac{0.61 \cdot \lambda_{em}}{\mathrm{NA}_{det}} \geq \frac{2 \cdot \mathrm{pixelsize}_x}{\mathrm{M}} \tag{2.31}$$

$$\tag{2.32}$$

2.3.3 Matching illumination and detection parameters

Normally, the starting point for designing a light-sheet microscope is the size of the object to be imaged, which dictates the size of FoV_{ill}, the FoV that the light-sheet needs to illuminate. Having a desired value for FoV_{ill}, Equation 2.22 can be used to get a constraint on NA_{ill}, the NA of the illumination arm. Then, knowing the value of NA_{ill}, the thickness of the light-sheet can be determined by using Equation 2.19. The next designing step is relating the thickness of the light-sheet with the axial resolution of the detection system $R_{axial,det}$:

$$R_{axial,ill} = R_{axial,det}. \tag{2.33}$$

By using Equations 2.19 and 2.24 in the last equation, it is possible to find a very useful relationship between the illumination and the detection NAs:

$$\mathrm{NA}_{det} = \sqrt{\frac{\lambda_{em}}{\lambda_{ill}} \frac{1.78 \cdot n}{1.22} \cdot \mathrm{NA}_{ill}}\,. \tag{2.34}$$

However, in practice, fulfilling this equation is not always possible. In fact, an objective's NA, together with other parameters such as working distance (WD), magnification and so on, determines its physical size. Because of their size, once the two required objectives have been identified using Equation 2.34, placing them together in an orthogonal configuration might not always be possible, meaning that Equation 2.34 should be taken only as a guide line, and not as a hard constraint.

Once the NAs of illumination and detection objectives have been chosen, transversal and axial resolutions of the imaging system ($R_{T,det}$ and $R_{axial,det}$), can be calculated using Equations 2.23 and 2.24, respectively. Finally, once the transverse resolution is found, it can be used in 2.32 to find the magnification M and camera specifications needed to assure and adequate sampling of the images.

3 SLM-SPIM: flexible, versatile imaging platform

3.1 Introduction

In this chapter I introduce the SLM-SPIM, the microscope which I developed, built and used throughout my PhD. The system contains all the components typical of the basic SPIM microscope design: cylindrical lens to create the light-sheet, water imaging chamber, vertically mounted sample, motorized translation stage to move the sample, detection arm. The particular feature of this microscope's design is the addition of a Spatial Light Modulator (SLM) in its excitation arm, from which came its name SLM-SPIM.

While SLMs have previously been used for certain specific purposes in other light-sheet microscopes [17, 44, 45], we decided to propose a simple SLM-SPIM design which would be well-suited for applying a wide variety of different optical techniques, all on the same imaging platform.

A recent work, carried out in parallel to our own, presented the SSPIM (Structured SPIM [46]), a DSLM microscope incorporating an SLM which allows to shape the beam profile (Gaussian, Bessel, Airy, Lattice) and perform structured illumination and tiling (see Chapter 4 and Chapter 5 for more details on these imaging techniques). In contrast, in this thesis I present and discuss the use of a programmable SLM device in a more classical cylindrical-lens-based SPIM, such as the one used within the OpenSPIM design [47].

The present chapter contains all the relevant information about the SLM-SPIM design and operation. Section 3.2 introduces SLMs, describes the one used in the SLM-SPIM and explains its mode of operation. Section 3.3 describes the optical set-up and Section 3.4 the Matlab simulation tool which I developed to help with the system design, and I later also used to simulate experiments. Section 3.5 contains technical details regarding sample preparation and mounting and Section 3.6 summarizes the characterization of the microscope's light-sheet and imaging parameters. Section 3.7 closes the chapter with some brief conclusions.

Both this and the following chapter are based on our published article [48].

3.2 Spatial Light Modulators (SLMs)

SLMs are pixellated devices which can be used to modulate phase, amplitude or polarisation of an optical wavefront in two dimensions. An SLM consists of an address part and a light modulation part, which can be transmissive or reflective. Information is written onto the address part in order to change the optical properties of the light modulation part; the incoming light is modulated according to these changes,

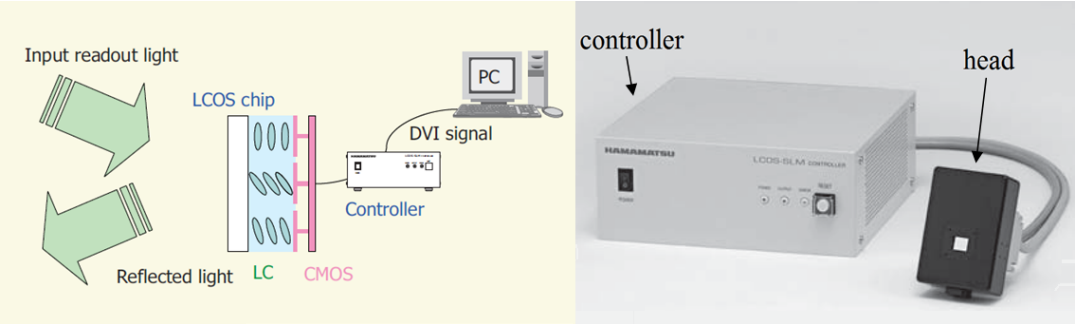

Figure 3.1: *Images taken from the Hamamatsu SLM instruction manual. Left: schematic explanation of our SLM's mode of operation. Right: Hamamatsu LCOS-SLM, series X13138. This SLM uses liquid crystals (LC) as the modulation material and an electric signal to modify their optical properties. The SLM head is connected to the control part, which is itself connected to a desktop computer with a DVI-D cable.*

resulting in an optical output that reflects the information written in the address part.

The versatility of SLMs has already been exploited in the field of optical microscopy [49], where they have been used for example as a Fourier mask in the imaging path [50, 51] or to control the light illuminating the sample [52]. SLMs have also already been used within SPIM systems, both on the imaging side (for example to correct for aberrations [44]) and in the excitation arm (for example to deliver structured illumination [45] or generate different light-sheets [17]).

The SLM used in the SLM-SPIM is the Hamamatsu LCOS-SLM (Liquid Crystal On Silicon Spatial Light Modulator), series X13138 (see Figure 3.1), which is an electro-optical liquid crystal SLM: it uses liquid crystals as the modulation material and an electric signal to modify their optical properties. Each pixel of the SLM head (pixel size 12.5 µm, for a total active area of 15.9 mm$\times$12.8 mm) can modify the phase of the incoming wavefront of a value between 0 and 2π. The SLM head is connected to the control part, which is itself connected to a desktop computer with a DVI-D cable. The SML head is thereby seen by the computer as a simple second monitor, and its phase modulation can be controlled by sending to it images in '.bmp' format: image pixel values from 0 to 256 are translated into light phase modulation from 0 to 2π. The exact input value that generates a phase modulation of 2π depends on the series of Hamamatsu LCOS-SLM and also on the laser wavelength. For the X13138 series and at 488 nm, this value corresponds to 138.

In the SLM-SPIM, the SLM is incorporated in the optical path of the excitation beam, and it is placed before the cylindrical lens, so that its active area is illuminated by a collimated beam of light, allowing for phase modulation of the wavefronts in 2 dimensions. The laser beam is expanded in order to cover as much of the active area of the SLM as possible, but without exceeding its size, to avoid spurious diffraction and reflections from the edges. A linear polarization filter is used to make sure that the polarisation axis of the laser beam is aligned with the liquid crystals of the SLM (axis perpendicular to the optical table), to assure the best phase modulation results. Two lenses and the cylindrical lens are used to conjugate the plane of the SLM to the back focal plane of the illumination objective (more details on the optical set-up in the next Section). Thanks to this conjugation, what the objective focuses (along one direction) on the sample corresponds to the Fourier transform of the phase-shift pattern displayed on the active area of the SLM.

3.3 Optical set-up

The optical set-up of the SLM-SPIM is illustrated in Figure 3.2 (optical scheme) and Figure 3.3 (picture), while Table 3.1 contains the details of the components and devices used. A second system, optimized for imaging cleared mouse organs immersed in glycerol, shares common laser launch optics and SLM with the water-immersion system, but has a separate final part of the excitation arm (final spherical lens, cylindrical lens and excitation objective), glycerol chamber, and a vertically mounted imaging arm. A picture of the glycerol system can be seen in Figure 3.4, a scheme in Figure 3.5, and the list of components in Table 3.1.

Different imaging techniques can be performed on both water- and glycerol-immersed samples, only requiring an easy adjustment of the SLM phase-patterns to switch between the two systems. In both water and glycerol systems a motorized stage is used to move the sample, so that 3D imaging can be performed by scanning the sample through a static light-sheet.

As shown in Figure 3.2, the water-immersion system also allows to easily switch between three slightly different optical configurations, each of which has a different positioning of the two lenses before the excitation objective (the cylindrical lens and the final spherical lens). Thanks to this, it is possible to choose between three light-sheets of different height and thickness (where the sheet's height and thickness correspond, in Figure 3.2, to its extent in y and z respectively). The three options also offer different conjugations between the plane of the SLM and the back focal plane of the excitation objective (further discussion below). The three possible light-sheets were profiled (see Section 3.6 for details), confirming the expected FWHM (at sheet waist) of ~ 2 μm for set-up 1, ~ 3 μm for set-up 2 and ~ 5 μm for set-up 3. The sheet height is ~ 4 μmm for set-up 1, ~ 2 μmm for set-up 2, and ~ 0.6 μmm for set-up 3.

As mentioned before, in the light-sheet launch path the cylindrical lens is placed after the SLM. Otherwise, with the SLM placed on a pupil or image plane after the cylindrical lens, a line would focus on the SLM, and phase modulation control would be possible only along one axis. The fact that the cylindrical lens has optical power only along one axis makes it impossible for the SLM (placed before it) to be conjugate to the pupil plane (or object plane) of the excitation objective in both horizontal and vertical axes simultaneously. What this consideration means in practice is that care is required in designing the light-sheet excitation arm to ensure that the SLM provides the degrees of freedom needed to manipulate the light-sheet as desired.

The SLM-SPIM's three interchangeable water-immersion set-ups offer different conjugations between the back focal plane of the excitation objective and the plane of the SLM, each of which is optimal for different families of applied beam shaping techniques. In a top-down view of the system design (Figure 3.2a), it can be seen that set-up 1 conjugates the SLM with the back focal plane of the excitation objective: the two lenses L3 and L4 are separated by the sum of their focal lengths, the SLM is at f_3 from L3 and the back focal plane of the objective is at f_4 from L4. However, because of the optical power of the cylindrical lens, when viewing the same set-up from the side (Figure 3.2b) the SLM is not conjugate to either a pupil or image plane. In contrast, set-up 2 gives the opposite situation and, in its side view, it conjugates the plane of the SLM with the focal plane of the excitation objective: L4 and the cylindrical lens are separated by the sum of their focal lengths and the back focal plane of the objective is at f_{cl} from the cylindrical lens. Set-up 3 gives a conjugation

Lenses	**L0:** achromatic doublet (Thorlabs, AC064-013-A-ML), $f = 13$ mm; **L1:** plano-convex, $f = 35$ mm; **L2:** plano-convex, $f = 100$ mm; **L3:** plano-convex, $f = 100$ mm; **L4:** plano-convex, $f = 100$ mm for set-up 1, $f = 50$ mm for set-up 2 and $f = 25.4$ mm for set-up 3; **CL:** cylindrical lens for set-up 1 and 2, $f = 50$ mm; **CL2:** cylindrical lens for set-up 3, $f = 80$ mm; **L5:** plano-convex, $f = 100$ mm;
Other optical elements	**BS:** beam splitter; **polarizer**: linear polarizer; **filter:** Green Fluorescent Protein (GFP) filter (central wavelength 525 nm); **obj1:** 10× Nikon Plan Fluorite Imaging Objective, 0.3 NA, 16 mm WD (Working Distance); **obj2:** 40× Nikon CFI APO NIR Objective, 0.80 NA, 3.5 mm WD;
SLM	Hamamatsu LCOS-SLM (Liquid Crystal on Silicon Spatial Light Modulator) serie X13138;
SLM head	**pixels:** 1272 × 1024; **pixel size:** 12.5 μm; **effective area size:** 15.9 mm × 12.8 mm; **fill factor:** 96 %;
SLM controller	**input signal:** DVI-D; **DVI signal format (pixels):** 1280 × 1024; **input signal levels:** 256; **DVI used frame rate:** 60 Hz;
Laser	OBIS coherent laser; **wavelength:** 488 nm;
Camera	XIMEA MD028xU-SY; **sensor active area:** 8.8 mm × 6.6 mm; **resolution:** 1934 × 1456, 2.8 Mp; **pixel size:** 4.54 μm; **frame rate:** 56.9 fps; **dynamic range:** 71.1 dB;
Glycerol system	Illumination arm, after the SLM, L3 and the pop-in mirror: **CL3:** cylindrical lens, $f = 60$ mm; **L6:** plano-convex, $f = 100$ mm; **obj3:** 5× ZEISS EC Plan-Neofluar Objective, 0.16 NA, 18.5 mm WD. Imaging arm: **L7:** plano-convex, $f = 150$ mm; **obj4:** 20× ZEISS Clr Plan-Neofluar Objective, 1.0 NA, 5.6 mm WD;

Table 3.1: *List of components used (with reference to Figure 3.2).*

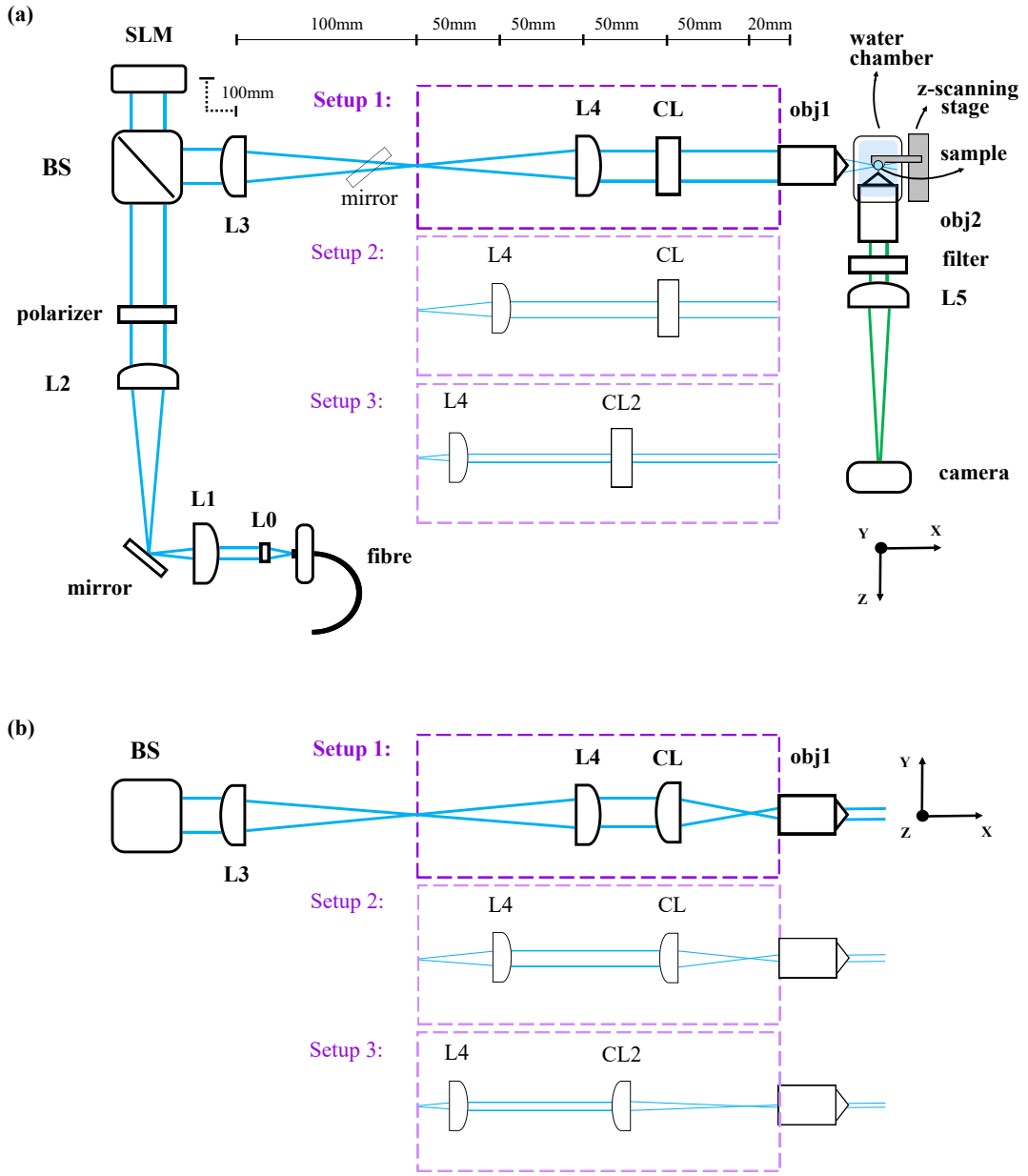

Figure 3.2: *Image taken from our publication [48]. Optical scheme of the SLM-SPIM, with a top view of the system in (a) and a side view of its excitation arm in (b) (see Table 3.1 for details of the individual components). Changing the position of the last two lenses before the excitation objective makes it possible to switch between three different set-ups, yielding different sheet heights and thicknesses, and change the conjugation of the SLM with the center of the FoV. (a) View of the SLM-SPIM from above. The cylindrical lens has no optical power in this plane. A mirror placed before the SLM (bottom left corner) permits adjustment of the vertical position of the light-sheet in the sample. A second mirror can easily be inserted after L3 and used to redirect the laser beam to the side (upwards in this figure), onto the second excitation arm (see scheme in Figure 3.5), which ends in the glycerol chamber. (b) Side view of the final part of the SLM-SPIM water-excitation arm, with its three different possible configurations.*

similar to the one of set-up 2, but was designed to give a good compromise between a perfect conjugation (achievable with the use of a cylindrical lens with $f_{cl} = 75$ mm, instead of the $f_{cl} = 80$ mm used on this set-up) and the combination of high flexibility in tilting the light-sheet and a high demagnification of the incoming beam

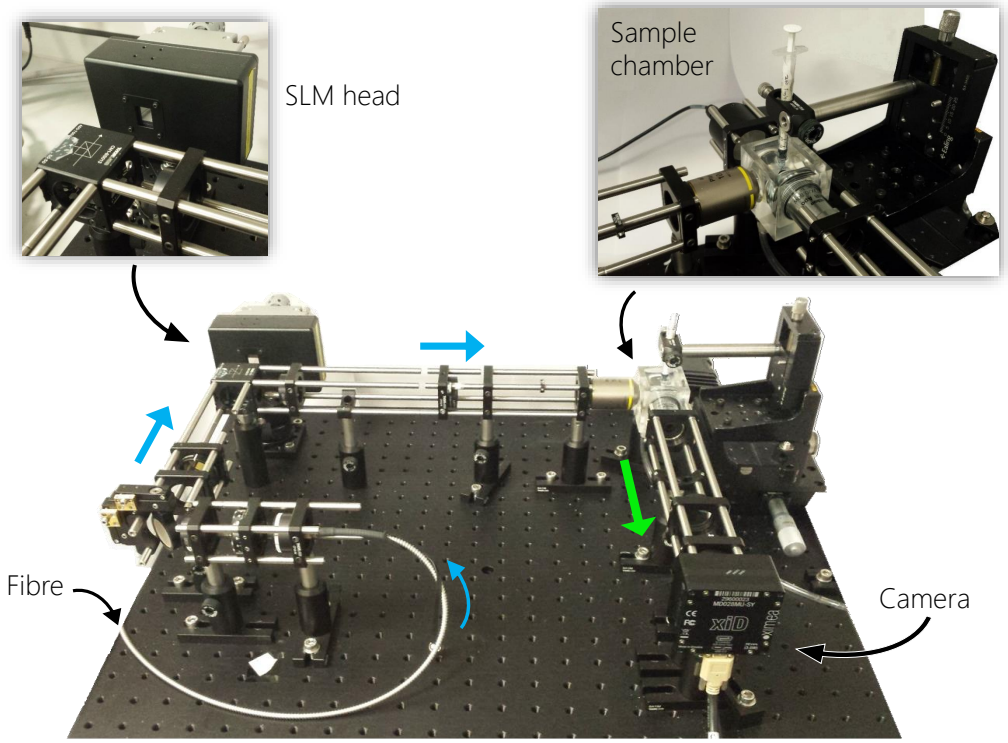

Figure 3.3: *Picture of the SLM-SPIM, with a zoom-in on the SLM head and the water chamber. The picture shows how a syringe is used to hang a sample vertically in the water chamber. Blue and green arrows show the direction of propagation of the excitation light (blue) and excited fluorescence (green).*

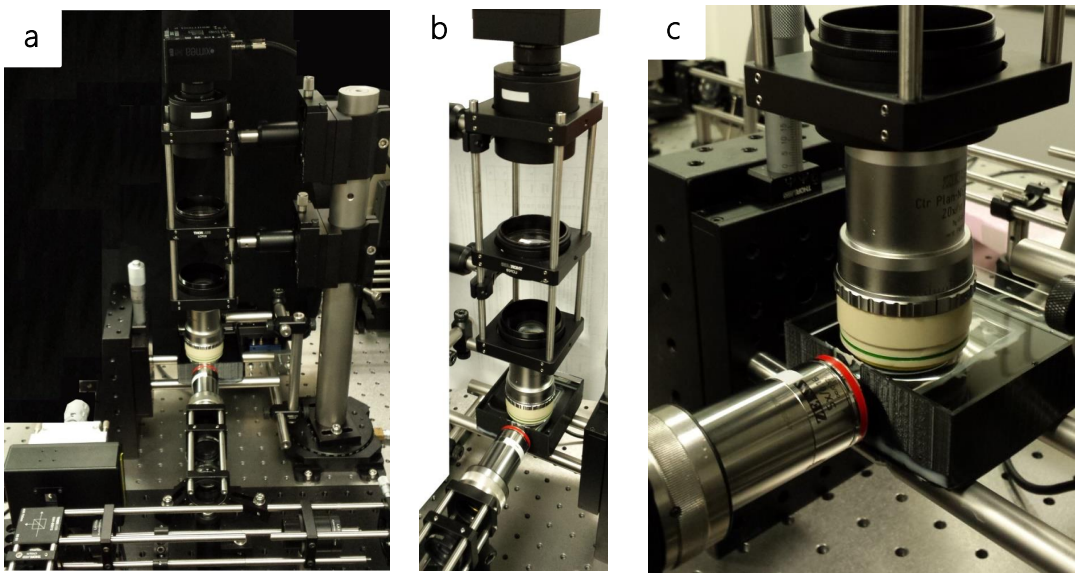

Figure 3.4: *(a) Picture of the Glycerol set-up. (b) Zoom-in on the glycerol excitation objective (horizontal on the table) and the vertical imaging arm. (c) Zoom-in on the excitation objective, the glycerol chamber and the glycerol-dipping imaging objective.*

(both of which are achieved using a longer f_{cl}), resulting in a light-sheet with thicker waist and longer Rayleigh length (see below for a more detailed discussion of these choices).

Most of the imaging techniques that we have so far implemented on the SLM-SPIM

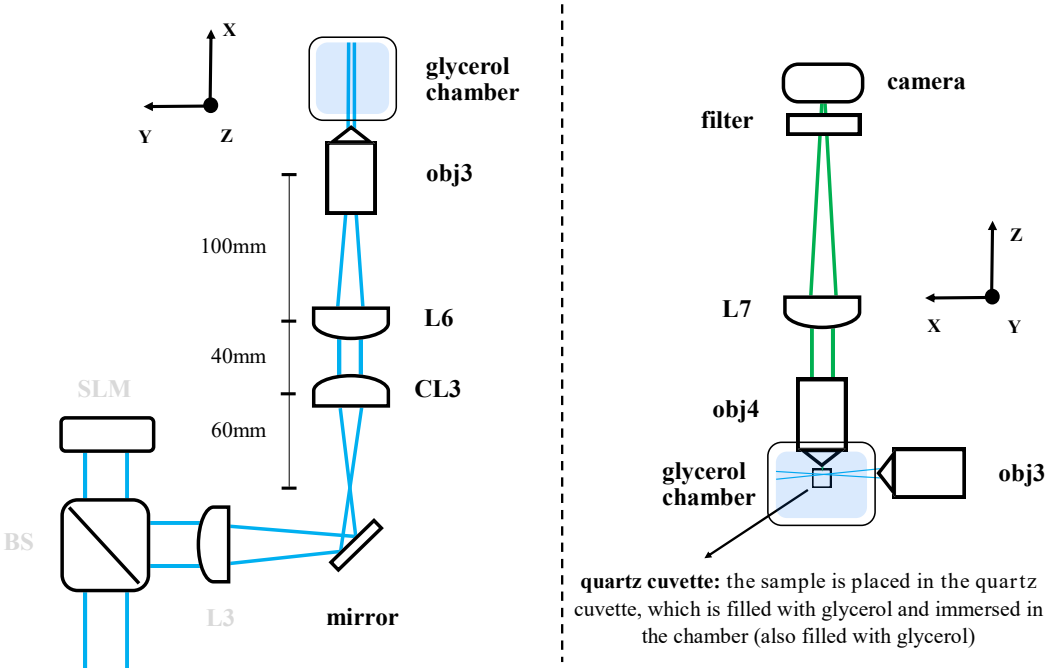

Figure 3.5: *Glycerol excitation (left) and imaging (right) arms (see Table 3.1 for details).*

can be performed using any of its three set-ups. Nevertheless, because of the different sheet height and thickness and SLM conjugation they provide, each of the three set-ups would be the preferred one for different imaging techniques. Set-up 1 gives the thinnest light-sheet at beam waist, and is therefore the best one to use for experiments such as the light-sheet tiling ones (described in Chapter 4, Section 4.2), where the only part of the light-sheet which is actually used to produce the final image is its central, thin waist. Instead, the conjugation of the SLM with the focal plane of the excitation objective generally makes set-up 2 the most appropriate for shadow suppression experiments (described in Chapter 4, Section 4.4). To suppress shadows in the image, the light-sheet is tilted in the sample plane, and the perfect conjugation of the SLM with the center of the FoV assures that the light-sheet does not shift vertically while being tilted (which would result in a change in image brightness dependent on the light-sheet tilt). Set-up 3 gives a thicker light-sheet, which also means a more even illumination across the FoV (longer Rayleigh length). This makes it a good choice for experiments such as the pencil beam scanning ones (described in Chapter 4, Section 4.3.3, where the light-sheet illumination is generated with a vertically scanned focused beam, and the use of a thicker but more uniform beam helps reduce the time needed to generate a homogeneously illuminated image of the entire FoV.

The choice of what set-up to use for a particular experiment should also depend on the characteristic of the sample to be imaged. Section 3.5 contains all the details about the samples imaged throughout this work, which for the water-immersion system are fluorescent beads and Zebrafish embryos. For normal SPIM images, and for the imaging experiments which could be performed with more than one of the three set-ups, these samples were always imaged using set-up 1. In fact, judging by the quality of the acquired images, I found the light-sheet generated by this set-up to be the most appropriate for these samples, with its vertically uniform illumination across the whole FoV and a 2 μm thick light-sheet waist. In Section 4.4 (shadow suppression experiments) of the following Chapter, I discuss an example situation

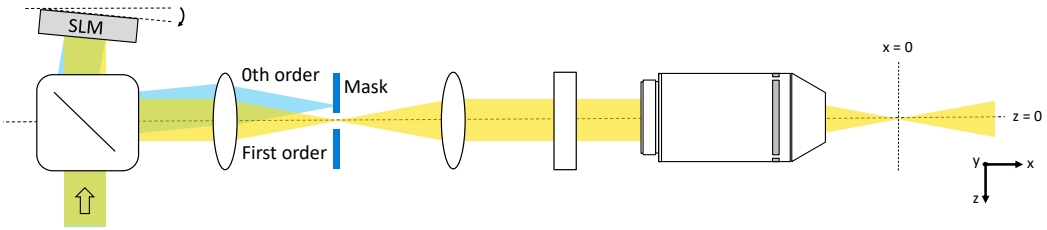

Figure 3.6: *Top view of the final part of the SLM-SPIM's excitation arm (sizes and distances not to scale), with a schematic explanation of the 0^{th} order blocking procedure. The 1^{st} diffracted order (yellow beam in the figure) is displaced from the 0^{th} order (light blue beam in the figure) by applying a constant phase tilt to the SLM, which is then physically tilted (and fixed) to bring the 1^{st} order back to the optical axis. The 0^{th} (and higher) orders are blocked by placing a slit mask elongated along y in the first focal plane after the SLM (blue mask in the figure).*

in which the type of sample strongly influences the set-up choice, further demonstrating the advantages of working with an easily reconfigurable system.

The SLM incorporated in the SLM-SPIM is used in a refractive mode. This means that most of the light modulated by the SLM is concentrated in the 1^{st} diffracted order, but some power is always lost in higher orders and in the so-called 0^{th} order (containing the specularly-reflected light that is not modulated by the SLM). In order to eliminate the 0^{th} order, a constant, horizontal phase ramp (phase tilt) is applied to the SLM, which displaces the 1^{st} order from the 0^{th} order. The SLM is then physically tilted (and fixed) such that the 1^{st} order is brought back to the optical axis, and the 0^{th} order is instead left to the side. A vertical (along y) slit mask placed in the first focal plane after the SLM is finally used to block the 0^{th} (and higher) orders (see Figure 3.6). When different phase patterns are applied to the SLM (to perform the different imaging techniques), the trajectory and structure of the 1^{st} order beam is altered slightly, but the addition of the constant phase ramp combined with the tilt of the SLM makes sure it always passes through the mask. This 0^{th} order masking method was applied for all the experiments presented in this work, also when using the SLM-SPIM for normal SPIM images, with a small difference only for the autofocusing experiments described in Section 4.5, where the masking procedure is conceptually the same but rotated of 90 degrees: the additional phase ramp is added vertically to the SLM, the slit mask is elongated along z and the SLM is tilted vertically.

A phase ramp with period p sends light of wavelength λ to the angle

$$\sin\theta_1 = \frac{\lambda}{p} \tag{3.1}$$

from the normal to the plane of the SLM. To displace the 1^{st} order along the z-direction, the phase ramp must be displayed horizontally on the SLM (*i.e.* with each row of the SLM representing the same phase ramp), with pixel values producing phase-shifts going from 0 to 2π (values from 0 to 138 in the input image, for excitation at 488 nm), with a period of p. The phase pattern applied to the SLM can be described by the following function:

$$\Phi(x,y) = \frac{2\pi x}{p} \bmod (2\pi)\,,$$

with x and y being the horizontal and vertical directions on the SLM's active area,

with ($x = 0$, $y = 0$) at its bottom left angle. A phase ramp with period p makes the 1^{st} diffracted order focus at a distance z_d from the 0^{th} order (at the focal plane of L3, the first lens after the SLM, where the mask is placed), which is related to the phase ramp period p by:

$$z_d = f_3 \cdot \sin\theta_1 = f_3 \cdot \frac{\lambda}{p}, \tag{3.2}$$

with $z_d = 0$ corresponding to the position of the focus of the diffracted 0^{th} order. For the 0^{th} order masking phase ramp, I decided to use a spatial frequency of 20 lines per millimetre (period $p = 4$ SLM pixels), which makes the 1^{st} order focus at a distance $z_d = 976$ μm from the 0^{th} order at the plane where the mask is placed. A smaller period size would displace the two foci even more, making the masking procedure less fiddly, with the minimum phase ramp period displayable on the SLM being $p = 2$ pixels (with for example one pixel giving 0 phase shift, the next one giving a phase shift of π, then 0 again and so on). One important thing to consider though, is that both the specific pattern displayed on the SLM for a certain experiment and the constant 0^{th} order masking phase ramp added to it have an influence on the overall diffraction efficiency of the SLM, defined as the ratio of the 1^{st} order intensity to the 0^{th} order intensity when no pattern is applied to the SLM. Keeping this in mind, I chose the period for the 0^{th} order masking phase ramp considering $p = 4$ pixels to give the best compromise between a big displacement of the 1^{st} diffraction order and a good diffraction efficiency, which I measured to be of ~ 60 % (at 488 nm), in accordance with the manufacturers specifications for our SLM model. In case of limited laser power availability, the overall diffraction efficiency could be increased by applying a lower-spatial-frequency phase ramp to the patterns ($p > 4$ pixels), at the cost of requiring greater care in the masking procedure, since the 1^{st} diffraction order would then be focused even closer to the 0^{th} order.

3.4 Optical simulations

I used Matlab to perform optical simulations which helped me in the process of designing the SLM-SPIM and implementing different imaging techniques on it. The code I implemented uses wave optics to simulate how a laser beam propagates through a series of optical elements (such as lenses and the SLM). The simulation operates in 2 dimensions: the initial beam is made propagate along the x-axis and the user is initially asked to choose between an $x-y$ or an $x-z$ simulation. Considering the x-axis of the simulation to be the direction of propagation of the laser beam along the SLM-SPIM's excitation arm means that the user is allowed to follow the propagation of the beam in a plane either parallel ($x-y$) or perpendicular ($x-z$) to the imaging FoV of the system. In order to make it possible to analyse the same set-up along both perpendicular views (running the simulation twice, once in $x-y$ and once in $x-z$), both the initial beam and all the optical elements are defined using 2 vectors of complex numbers, each representing the phase+amplitude profile of the element (or the light beam) along one of the two axes perpendicular to the beam's propagation axis (one vector for the phase+amplitude profile along y and one for the phase+amplitude profile along z). Once the user decides which of the two types of simulation to run (either $x-y$ or $x-z$), the simulation automatically selects the correct profile of the initial beam and of the optical elements placed in the optical path (either their y- or their z-profiles). Figures 3.7 and 3.8 show an example of an $x-z$ simulation. Figure 3.7 shows the inputs of the simulation, with the initial laser

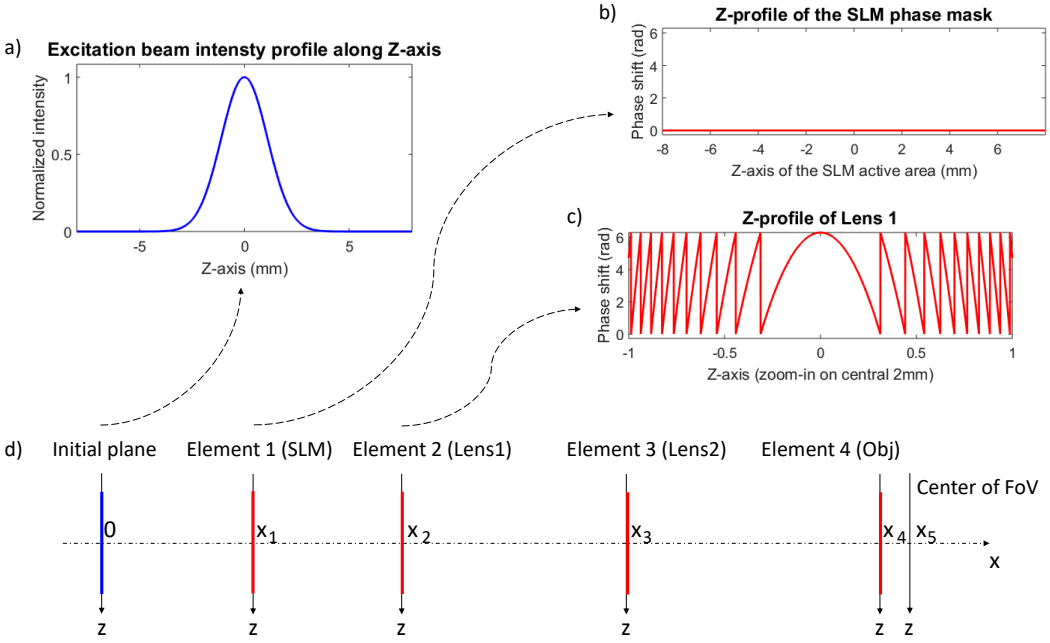

Figure 3.7: *Optical simulations inputs. In this example the user has chosen to run an $x-z$ simulation, with 4 optical elements positioned at x_1, x_2, x_3 and x_4 from the initial plane and the final FoV position at x_5 (beam propagating from left to right). (a) z-intensity profile of the initial laser beam. (b) z-phase profile of the first element, which in this case is set to be a phase-SLM with a flat, all-zeros profile (i.e. the SLM does not alter the phase profile of the incoming beam). (c) z-phase profile of the second element, which is set to be a lens.*

beam profile and the phase profile of four optical elements, placed at different positions along the x-axis. Figure 3.8 shows the outputs of the simulation: the intensity of the light field generated by the initial laser beam as it propagates through the optical set-up, intensity $x-z$ profile of the beam within the FoV of the imaging arm of the microscope (in this example forming a Gaussian light-sheet), and the z-intensity profile of the laser beam at the center of the imaging FoV.

At the beginning of the simulation, the user is asked to enter the following input parameters:

- resolution of the simulation, along y and z: default values set to $dy = dz = 0.125\ \mu$m;
- total size (along y and z) of the simulated light-field: default values set to $\Delta y = \Delta z = 16$ mm;
- initial beam profiles, in the form of two vectors of N_y and N_z complex numbers (one vector to use in the case of an $x-y$ simulation and one for an $x-z$ simulation, with $N_y = \Delta y/dy$ and $N_z = \Delta z/dz$). Example of the intensity component (amplitude squared) of a z-profile of the initial beam in Figure 3.7a;
- wavelength;
- series of optical elements: their positions along the propagation axis (x) and their phase+amplitude profiles along y and z. Example in Figure 3.7c and 3.7d;

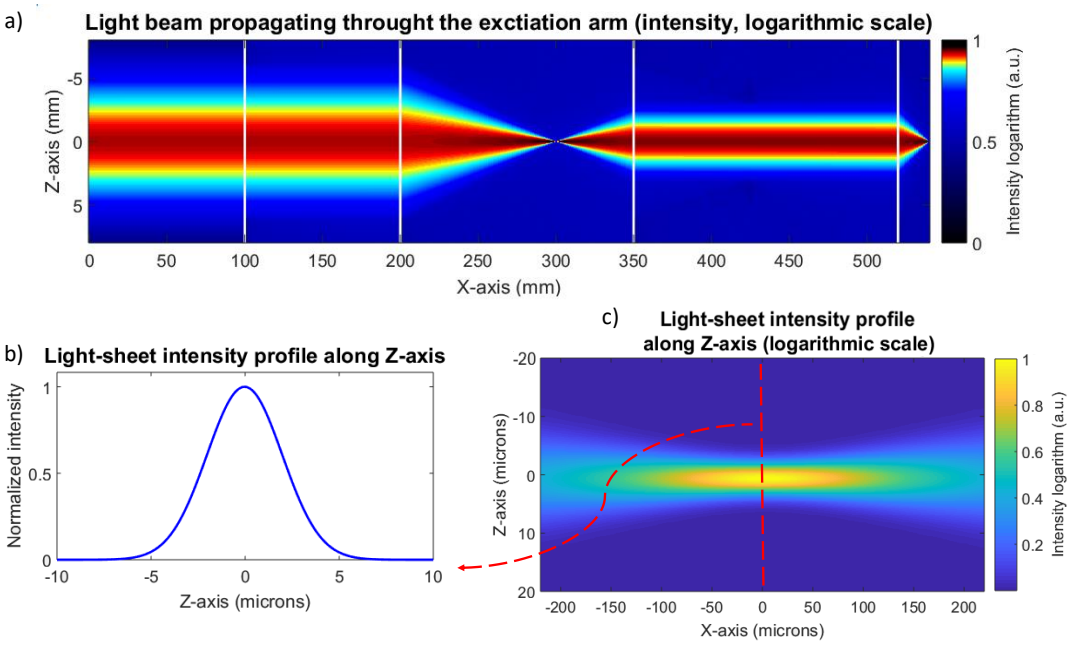

Figure 3.8: *Optical simulations outputs for the input system of Figure 3.7. (a) Simulated propagation of the initial laser beam through a series of optical components, which were chosen to replicate set-up 2 of the SLM-SPIM. The laser beam propagation goes from the initial plane at $x = 0$ to the center of the FoV of the imaging arm of the microscope. The intensity of the light-field is normalized to its maximum and plotted in a logarithmic scale, with the colorbar adjusted to highlight the details in the high intensity parts of the field. The positions of the 4 optical elements are highlighted with white lines. (b) z-intensity profile of the beam at the center of the imaging FoV (note that in this example the beam generates a light-sheet). (c) $x - z$ intensity profile of the beam within the FoV of the imaging arm, normalized to its own maximum and plotted in a logarithmic scale. The x-steps used for this simulation were $dx = 1mm$ for the path shown in (a) and $dx = 1\mu m$ for the path shown in (c).*

- if one of the optical elements is an SLM: its pixel size (along y and z), its number of pixels (in y and z), phase+amplitude profiles (along y and z). Example in Figure 3.7b;
- size, in the object plane, of the FoV of the imaging arm of the microscope (along $x - y$ and $x - z$) and distance between the center of the FoV and the last optical element of the excitation arm;
- size of the propagation steps along x: the user has to input the sizes of two different propagation steps, one (dx_1) which is used for the propagation from the initial plane ($x = 0$) to the last optical element, and one (dx_2) which is used from the last optical element to the right end of the FoV (beam propagating from left to right).

The final simulated light-field is generated by propagating the initial laser beam (defined by the 1-dimensional vector representing its phase and amplitude profile along y (or z) at $x = 0$) through the chosen set-up. The propagation of the light-field between two consecutive optical elements is performed using the following Fresnel approximation for the transfer function in free space (see Equation 4.1 - 8 of [53]):

$$\mathrm{H}(\nu_y) = e^{-jkd}\exp(j\,\pi\,\lambda\,d\,\nu_y^2)\,, \tag{3.3}$$

where H is a vector of N_y (or N_z) complex values representing the light-field at the

propagation distance d from the last optical element, and $\nu_y = k_y/2\pi$ is the spatial frequency in y, (or $\nu_z = k_z/2\pi$ in case of an $x-z$ simulation).

3.5 Samples

All the samples used in the water-immersion imaging system were mounted in a piece of FEP tubing (Fluorinated Ethylene Propylene, 1.3 mm ID $\times$ 1.6 mm OD, Adtech Polymer Engineering Ltd) inserted at the end of a syringe. FEP tubing has been shown to be a good choice for imaging samples in a water-immersion imaging light-sheet microscope [54]. The refractive index of FEP ($\sim$ 1.34) is in fact similar to the refractive index of water ($\sim$ 1.33), and it therefore assures minimal distortion both for the light-sheet which goes through the tube to get to the sample and for the excited fluorescence travelling through the tube before reaching the detector. The syringe was immersed vertically in the water chamber and attached to the translation stage using Thorlabs component. Figure 3.9 shows a syringe mounted in the water sample chamber, with a piece of FEP tubing attached to it, ready for imaging.

For calibration, alignment purposes, and some of the experiments which will be described in the following chapter, the FEP tube was filled with fluorescent beads (polystyrene beads, 0.2 μm, labelled with Dragon Green fluorescence, Bangs Laboratories Inc) embedded in a 1.5 % low melting point agarose solution (Agarose, High-EEO/Protein Electrophoresis Grade, Fisher Scientific).

The biological water-immersion samples used throughout this work were *ex-vivo* Zebrafish embryos (*Danio Rerio*), provided to us by Martin Denvir, Carl Tucker and team (Edinburgh University). The embryos used were 4-5 dpf (days post fertilisation), with the exact age specified within the description of each experiment. For imaging, the embryos were placed in a piece of FEP tubing filled with water. Without the addition of agarose in the tube to thicken the water, the embryo was left free to slowly sink to the bottom of the tube, where it settled, ready to be imaged. Since mounting the embryos in simple water is also a much simpler procedure compared to using an agarose solution, it was the technique chosen and used for all the experiments on fish embryos. The fish line used in our experiments was the Zebrafish nacre mutant (reduced pigment and therefore improved transparency). The Zebrafish used for heart imaging had the cardiac muscle labelled with green fluorescent protein (*myl7:eGFP*), while those used for imaging blood vessels had labelled internal walls of the heart and blood vessels (*flk1:GFP*). The *ex-vivo* fish specimens were preserved in formalin (10% Formalin solution, neutral buffered, Sigma-Aldrich). For the process of euthanasia, the fish were first anesthetized using a 167 mg/L tricaine solution (Ethyl 3-aminobenzoate, methanesulfonic acid salt, 98%, Acros Organics, Fisher Scientific), and then euthanised with a 1 g/L tricaine solution.

For the experiments in the glycerol-immersion imaging system, we used samples of mouse brain, which were cleared and provided to us by Andrew Tobin, Sophie Bradley and team (University of Glasgow). The samples were cleared following the CLARITY method [55]. For imaging, the sample was placed in a quartz cuvette (UV fused quartz glass, 3500 μL, 12.5 mm square outside dimension, 1.3 mm walls, Thorlabs part CV10Q3500F) filled with 85% glycerol, which was sealed making sure to eject any air bubble. The cuvette was then immersed in the chamber filled with 85% glycerol, and held horizontally underneath the dipping imaging objective. The 85% glycerol concentration was selected to match as well as possible the refractive indices of the cleared sample and the quartz cuvette ($\sim$ 1.46).

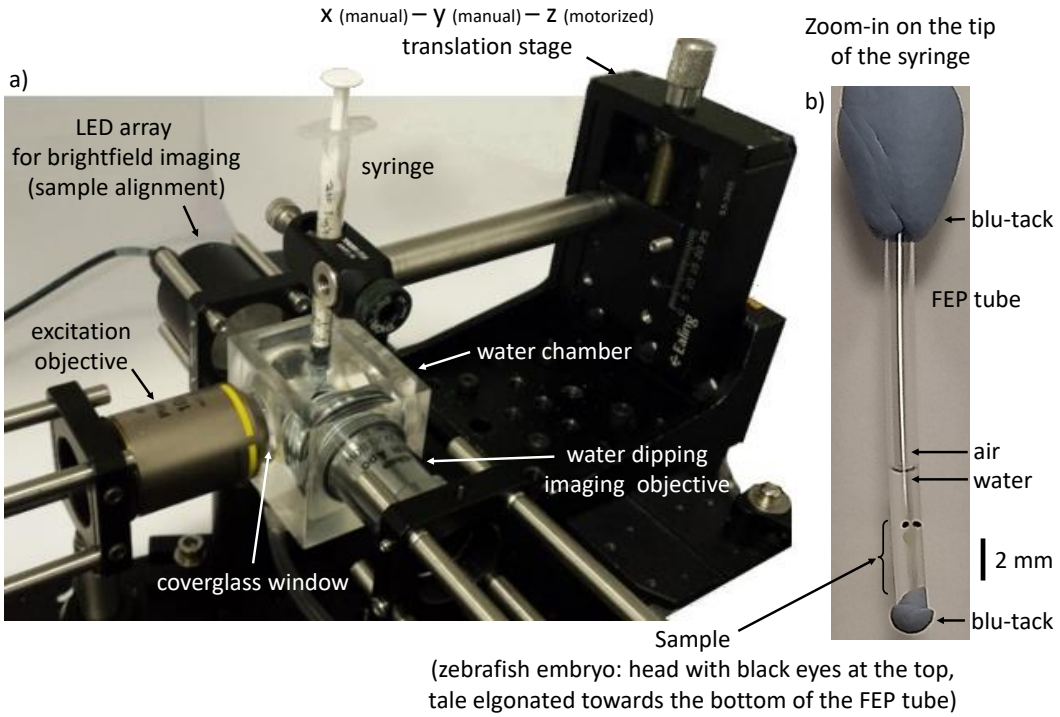

Figure 3.9: *(a) Picture of the sample chamber of the SLM-SPIM's water-immersion imaging system, with a sample mounted and ready for imaging. The sample is inside a piece of FEP tubing inserted at the end of a syringe, which is immersed vertically in the water chamber and attached to the translation stage using Thorlabs components. (b) Zoom-in on the piece of FEP tubing containing the sample, which in this picture was a zebrafish embryo. A piece of blu-tack (top) was used to attach the FEP tubing to the end of the syringe, and a small piece (bottom) was used to close the end of the FEP tubing which was immersed in the water.*

3.6 System characterisation

After assembling and aligning the SLM-SPIM, the system was characterized, both on its excitation and imaging sides. The results of this characterization are presented and discussed in the following two sections (Section 3.6.1 for the imaging side and Section 3.6.2 for the excitation side).

3.6.1 Imaging parameters

In the water imaging arm, the use of a 40× Nikon objective with a 100 mm tube should result in a 20× magnification. The magnification of an objective can in fact be expressed as:

$$M = \frac{F}{f}, \tag{3.4}$$

where M is the objective's magnification, F is the focal length of the tube lens and f is the effective focal length of the objective. For Nikon objectives, the given magnification is related to the use of a 200 mm tube lens, so that a 40× objective has an effective focal length $f = F/M = 200/40 = 5$ mm. When using a 40× Nikon objective with a 100 mm tube lens, the actual magnification can be calculated using Equation 3.4, which gives $M = F/f = 100/5 = 20$. With this magnification, the ∼8.8 mm × 6.6 mm active area of the camera used on the SLM-SPIM should give an

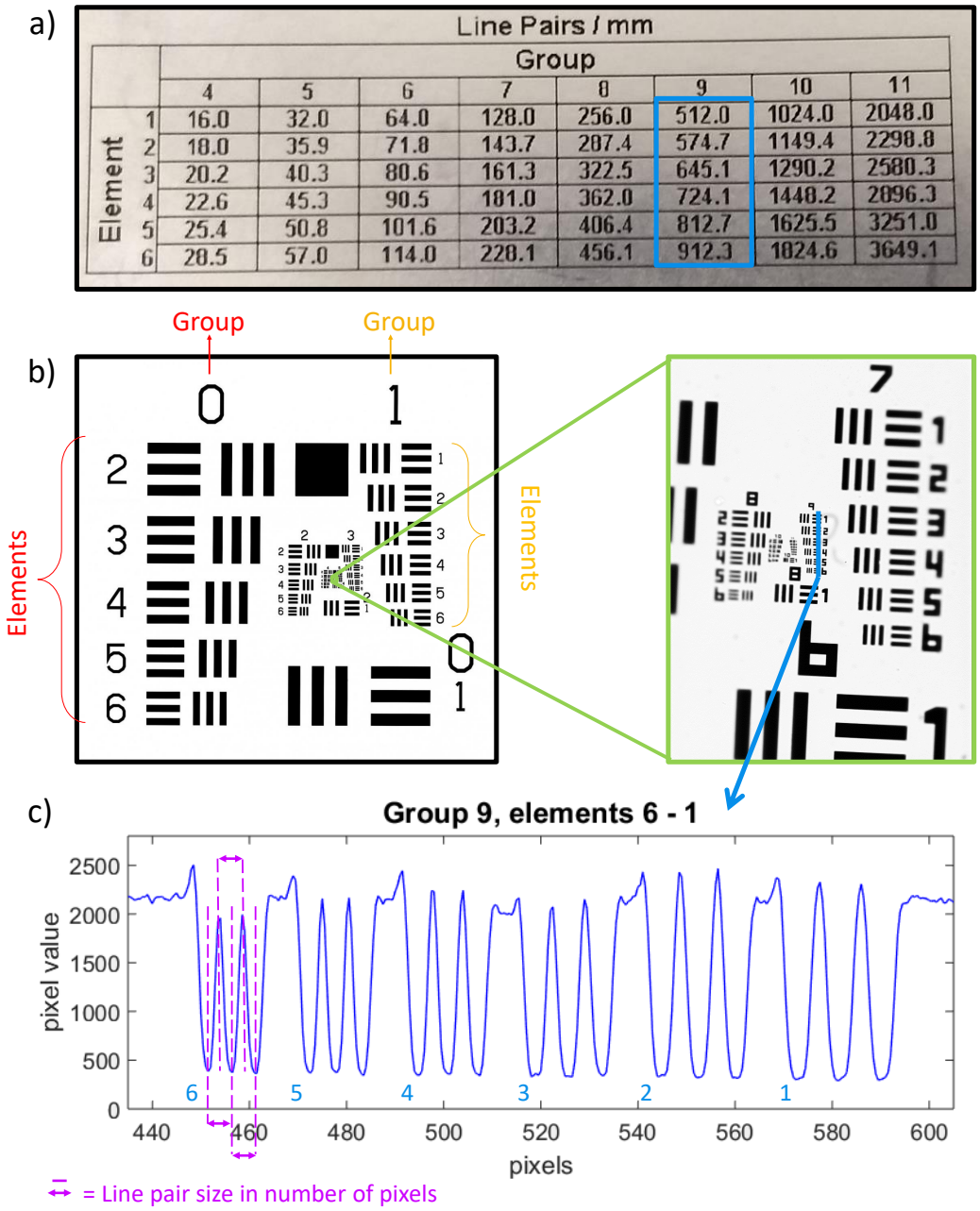

Figure 3.10: *Magnification check using the US air force target on the SLM-SPIM's water immersion imaging arm. (a) Table with values of lines per mm for each element of the target used. In blue the values relative to the elements of group 9 plotted in (c). (b) Entire target (archive image) and a zoom-in on one part of an image of the target taken with the water immersion imaging arm of the SLM-SPIM. (c) Plot of the column of the image which was analysed to check the actual magnification of the system. For each group, three measurements of the size of a line pair (in number of pixels) were taken and averaged (in magenta the distances measured for element 6). Each average line pair size was combined with the line/mm value given table (a) to find an estimate for the size of a pixel in microns. Each of the six values obtained for the pixel size was used to find one estimate for the magnification of the system M, and the six resultant values were averaged to give one single final estimate for M.*

imaging FoV of ~440 μm $\times$ 330 μm. The theoretical lateral resolution at λ = 0.525 μm is 0.4 μm (calculated as 0.61 $\times\lambda$ / NA for NA = 0.8). In the glycerol imaging arm, the combination of the 20$\times$ ZEISS objective and the 150 mm tube lens gives a

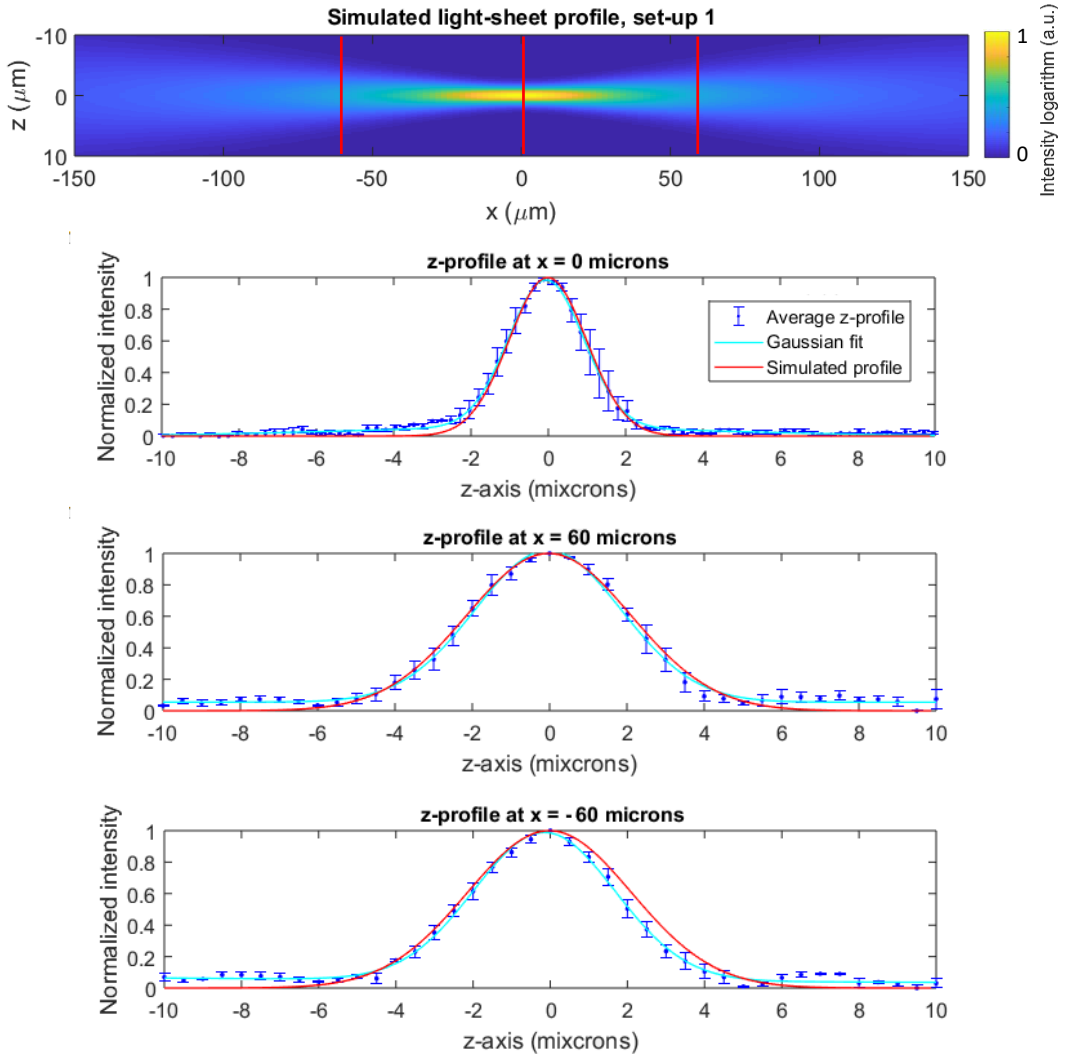

Figure 3.11: *Light-sheet profiling on set-up 1. A sample of fluorescent beads was scanned in z though the light-sheet with a step $dz = 0.5$ μm. Beads positioned at three different lateral positions in the image were used to extract the profile of the light-sheet at three different values of x : $x = -60$ μm, $x = 0$ μm and $x = 60$ μm (values referring to the object plane). The stack of images acquired was used to obtain a vector of values for each of the used beads (five beads for each of the three lateral positions), representing the variation of intensity of the light-sheet as the bead was scanned through it. Each value of a vector was obtained by selecting a square around the bead (in x and y, using the same square on each image of the stack) and summing the values of all the pixels inside the square. For each of the three lateral position, and average light-sheet profile was obtained by averaging the five vectors after normalizing each one of them to its own maximum. The three average profiles are here plotted together with their Gaussian fits, showing a good agreement with the profiles obtained from the simulations (red columns in the simulated $x - z$ light-sheet of the top image).*

magnification M = 18.18, an imaging FoV of ~490 μm $\times$ 370 μm (the magnification given for ZEISS objectives implies the use of a tube lens with focal length $f = 165$ mm). In this case the theoretical lateral resolution at λ = 0.525 μm is 0.3 μm (= 0.61 $\times \lambda$ / NA for NA = 1).

The actual magnification of both the water and glycerol imaging arms was checked by imaging a US air force target (see Figure 3.10). For the water imaging arm, the US air force target was attached to the end of a syringe using a piece of blu-tack, and the syringe was mounted inside the water chamber in the same way as for the water

light-sheet experiments. For the glycerol imaging arm. the target was placed at the bottom of the glycerol chamber (which was moved towards the imaging objective to put the target in focus). The measured magnifications were M = 20 for the water imaging arm and M = 18 for the glycerol imaging arm, values in good agreement with the theoretical ones. These values were obtained by analysing the 6 elements of group 9 of the US air force target used. For each of the 6 elements of the group, the size on the detector, in pixels, of a line pair (s_{pixel}) was estimated by averaging three measurements (in magenta in Figure 3.10c are the three distances measured for element 6). The real size, in microns, of a line pair can be calculated as $s_{\text{mic}} = 1000/a$, where a is the value of lines per mm given for that element (see table in Figure 3.10a). The size of a pixel in microns in the object plane ($p_{\text{mic,obj}}$) can be calculated as $p_{\text{mic,obj}} = s_{\text{mic}}/s_{\text{pixel}}$. This formula was used to find one value of $p_{\text{mic,obj}}$ for each element, which was then used to find an estimate for the magnification using the known size of a pixel in microns: $M_{\text{el}} = p_{\text{mic,real}}/p_{\text{mic,obj}}$ (where $p_{\text{mic,real}} = 4.54$ μm is the size of a pixel in microns, and M_{el} is the value for the magnification obtained analysing one of the 6 elements). The final estimate for the measured magnification was obtained by averaging the 6 values of M_{el}.

3.6.2 Light-sheet profiling

On the excitation side, the actual shape and size of the light-sheet was checked by imaging a sample of fluorescent beads while scanning it in z across the light-sheet. This method was used to check the shape of the z-profile of the light-sheet at different values of x (*i.e.* different distances from the sheet's focus), and it confirmed a FWHM (at sheet waist) of $\simeq 2$ μm for set-up 1, $\simeq 3$ μm for set-up 2 and $\simeq 5$ μm for set-up 3. Figure 3.11 shows as example the three experimental profiles extracted for the light-sheet of set-up 1 at positions $x = -60$ μm, $x = 0$ μm and $x = 60$ μm and how they compare to the simulated profiles for the same values of x.

3.7 Discussion and Conclusions

In this chapter I introduced the SLM-SPIM, the cylindrical lens based light-sheet microscope which I designed and built as the foundation of my PhD research project. The aim with this system was to build a light-sheet microscope which would be as versatile as possible and easy to use on both water- and glycerol-immersed samples. To help me in the process of designing such system, I developed a Matlab simulation tool (described in Section 3.4) which I later also used to simulate all the experiments discussed in the following chapters. The obtained system is a SPIM with an SLM integrated in its excitation arm, the option to image either in water or glycerol, and the possibility to quickly reconfigure the water imaging arm into three different optical set-ups. As discussed in Section 3.3, each of the three interchangeable water-immersion set-ups gives a slightly different light-sheet height and thickness, and a different conjugation between the back focal plane of the excitation objective and the plane of the SLM. Because of these differences, each set-up is optimal for a different type of applied beam shaping techniques, and can be chosen also depending on the specific characteristics of the sample. In the following chapters I will discuss how, thanks to the flexibility offered by the SLM and the reconfigurable optical set-up, the SLM-SPIM can be used to perform a variety of existing advanced light-sheet imaging techniques (Chapter 4), and as a tool to develop and trial new ones (Chapter 5 and Chapter 6).

As regards the imaging sample, this system was designed to be used mainly for Zebrafish imaging in the water chamber, and cleared mouse brain imaging in the glycerol chamber. Before performing the first imaging experiments on the system, I profiled the light-sheet and checked the imaging magnification, both on the water and glycerol imaging arms and for all three different water set-ups. The measured values were in good agreement with what predicted by the simulations and, as it will be seen in the next chapters, proved appropriate for their intended applications.

4 SLM-SPIM platform: implementing existing advanced imaging techniques

4.1 Introduction

This chapter illustrates the versatility of the SLM-SPIM introduced in the previous chapter, and its content is a re-adaptation of the *Results and Analysis* section of my and my supervisor's publication from 2018 [48]. The following sections showcase how I have been able to implement a variety of different imaging techniques, all on the same versatile SLM-SPIM microscope platform. Each section contains an introduction to one specific technique, an explanation of how it can be implemented on the SLM-SPIM, and experimental results to demonstrate the system performance. The set-up and sample used are specified within the description of each experiment. Section 3.5 can be consulted for more details on sample preparation and mounting, while in Figure 4.1 the reader is reminded of the three different optical set-ups which the system can be configured to.

4.2 Tiling for optical sectioning improvement

In a light-sheet microscope, the size of the light-sheet and the imaging parameters are carefully matched, taking into account the specific imaging application the microscope is intended for. This has already been mentioned in the previous chapters, in particular where discussing the design of the SLM-SPIM. Despite all the efforts that can be made to choose the most appropriate size of light-sheet for a system, there is always a trade-off one has to deal with, the one between light-sheet thickness and length. In fact, in the same way that a focused Gaussian beam generates a spot of a certain size and Rayleigh length (as discussed in Section 2.2), a light-sheet generated by a Gaussian beam is characterized by a certain thickness and length. Thinner sheets have shorter Rayleigh lengths, which means that they spread more rapidly as they propagate. If the light-sheet becomes thicker than the DoF of the imaging objective, some of the fluorescence it generates in the sample is seen as out-of-focus in the image. An ideal light-sheet would therefore keep a fixed, reduced thickness across the entire imaging FoV, and matching this thickness with the imaging DoF would guarantee good optical sectioning over the whole image.

Tiling, the technique discussed in this section, was specifically developed to work around this trade-off between light-sheet thickness and length [21, 56, 57]. The idea behind tiling is that the illumination delivered by an ideal thin and long light-sheet can be mimicked by a lateral scan of a thin, but inevitably short, light-sheet. This can be achieved by using only the thin part of the sheet for imaging, and move the sheet laterally to build up the image of the entire FoV (see Figure 4.2). Imaging can

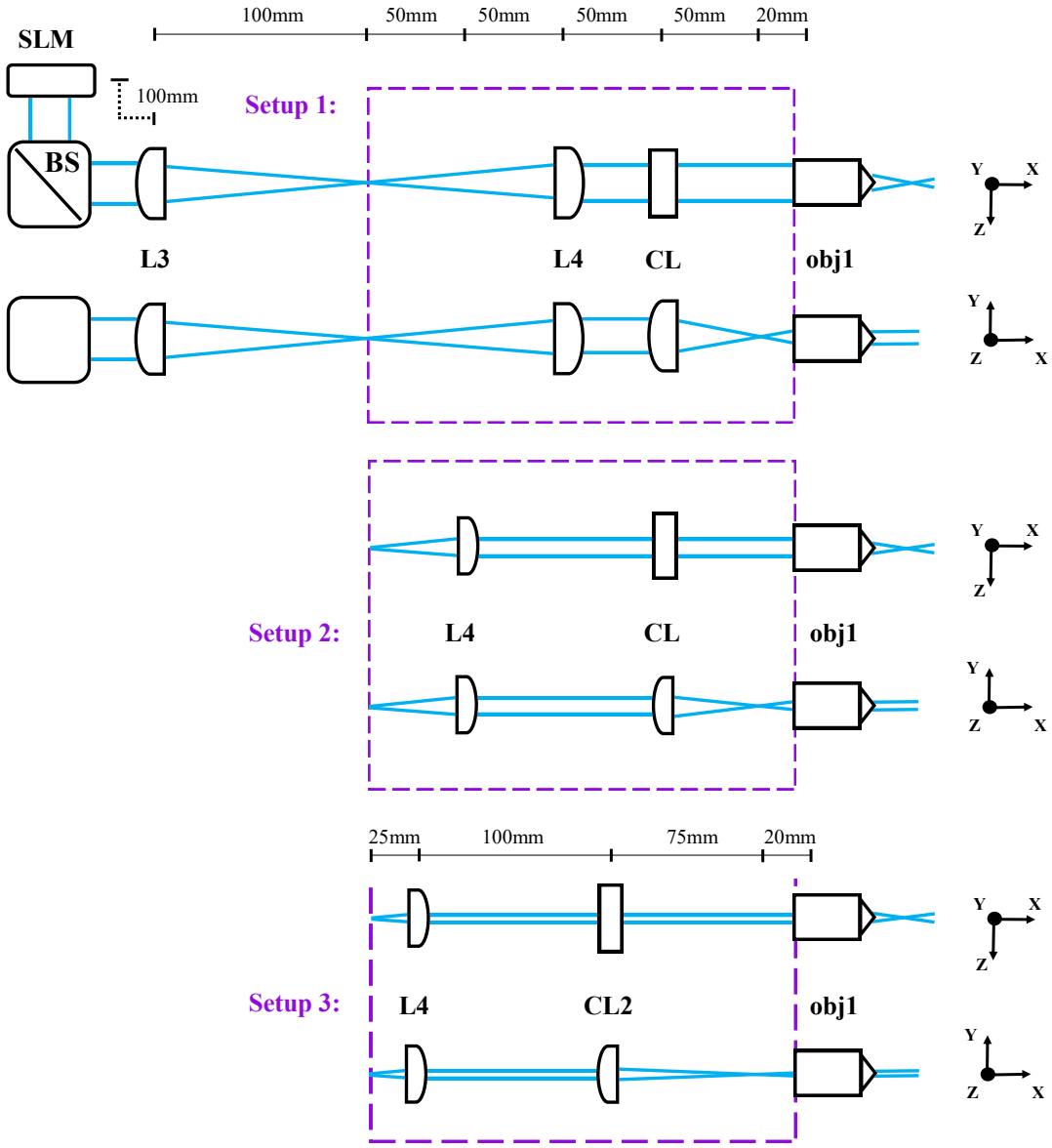

Figure 4.1: *Reminder of the three different optical configurations used on the SLM-SPIM for the experiments presented in this chapter. A top view and a side view of each of the three configurations of the microscope's excitation arm, with names of the components referring to the list in Table 3.1.*

be performed using a rolling shutter on the camera aligned with the position of the sheet waist [58], or by capturing entire images and creating the final image stitching together vertical stripes taken from the different images [21].

When using the tiling technique, each image plane is illuminated a number of times equivalent to the number of tiling positions, which means that, compared to imaging with a static light-sheet, the sample is exposed to extra excitation light, resulting in extra photobleaching and photodamage. Having to laterally scan the light-sheet also inevitably leads to slower imaging speed. To try and minimize these two main drawbacks of the tiling technique, the number of tiles, the thickness of the light-sheet and the total extent of its lateral scan should be carefully chosen considering the size of the region of interest within the FoV, the sample's photobleaching rate and the desired temporal and spatial resolution [57, 58].

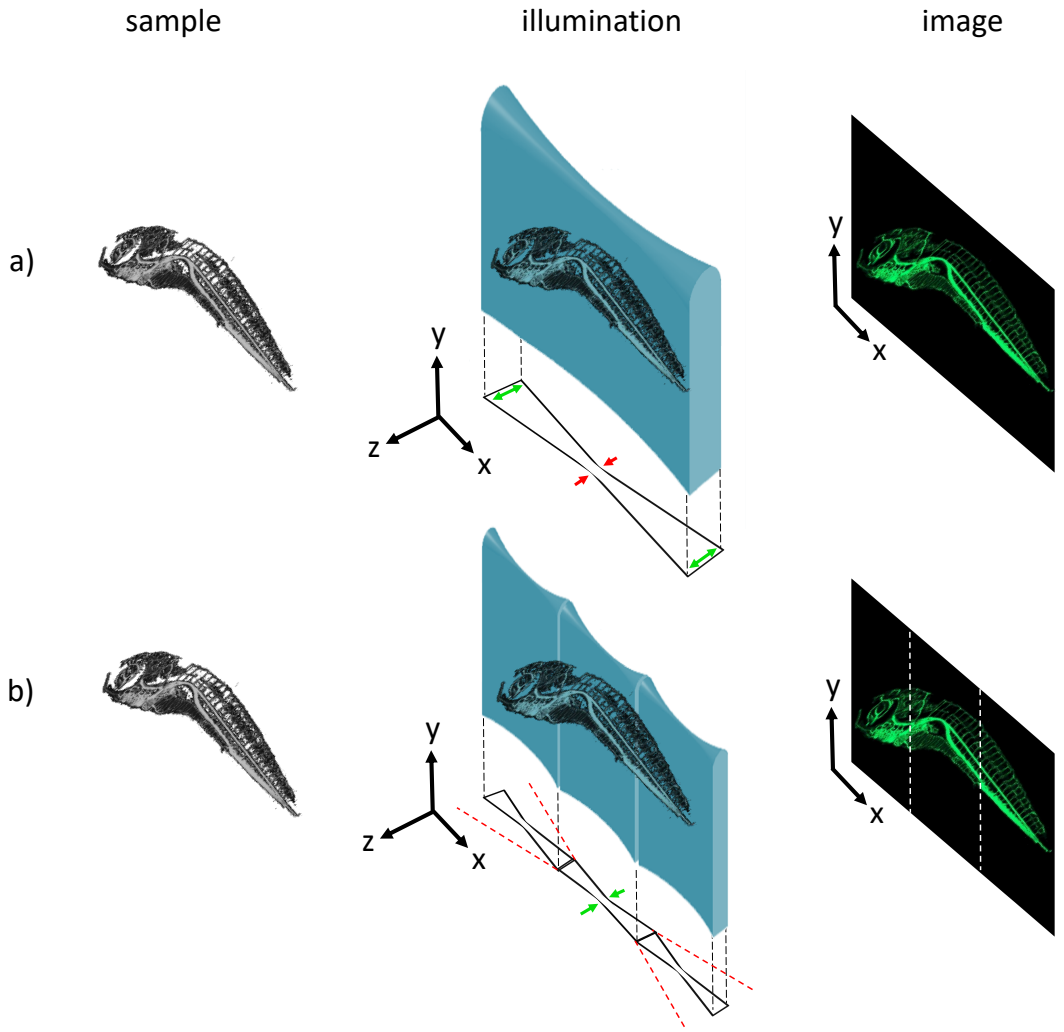

Figure 4.2: *Concept behind the tiling technique. (a) In a conventional light-sheet microscope the sample is illuminated with a Gaussian light-sheet, which is normally focused at the center of the imaging FoV. The thickness of the light-sheet is chosen in order to assure a good image quality across the whole FoV, which means trying to minimize out-of-focus fluorescence by making sure the light-sheet does not become much thicker than the imaging DoF towards the side of the FoV (green arrows). With a Gaussian light-sheet this is only possible at the expense of sacrificing the optical sectioning capability of the light-sheet waist (red arrows), i.e. making sure the light-sheet never becomes too thin. (b) To image the same sample over the same FoV using the tiling technique, the excitation beam is focused to generate a thinner light-sheet (green arrows), improving optical sectioning at the center of the image at the expense of generating more out-of-focus towards the sides of the FoV (red dashed lines). To work around this drawback, the thin light-sheet is tiled across the FoV (in this example in three positions), but for each position of the light-sheet only the fluorescence generated by its central, thinnest part is used to generate the final image of the entire FoV (to the right).*

4.2.1 SLM-SPIM implementation

To implement the tiling technique on the SLM-SPIM, the SLM can be used to apply a defocus to the excitation beam, generating a lateral displacement of the light-sheet focus in the imaging FoV. Such defocus can be obtained by displaying a quadratic phase function along the horizontal axis of the SLM (Figure 4.3a and 4.3b). The final, tiled image of a plane in the sample is generated by combining a set of images acquired with the light-sheet focused on the same plane but at different lateral positions within the imaging FoV (Figure 4.3c). Of each of the initial images, only

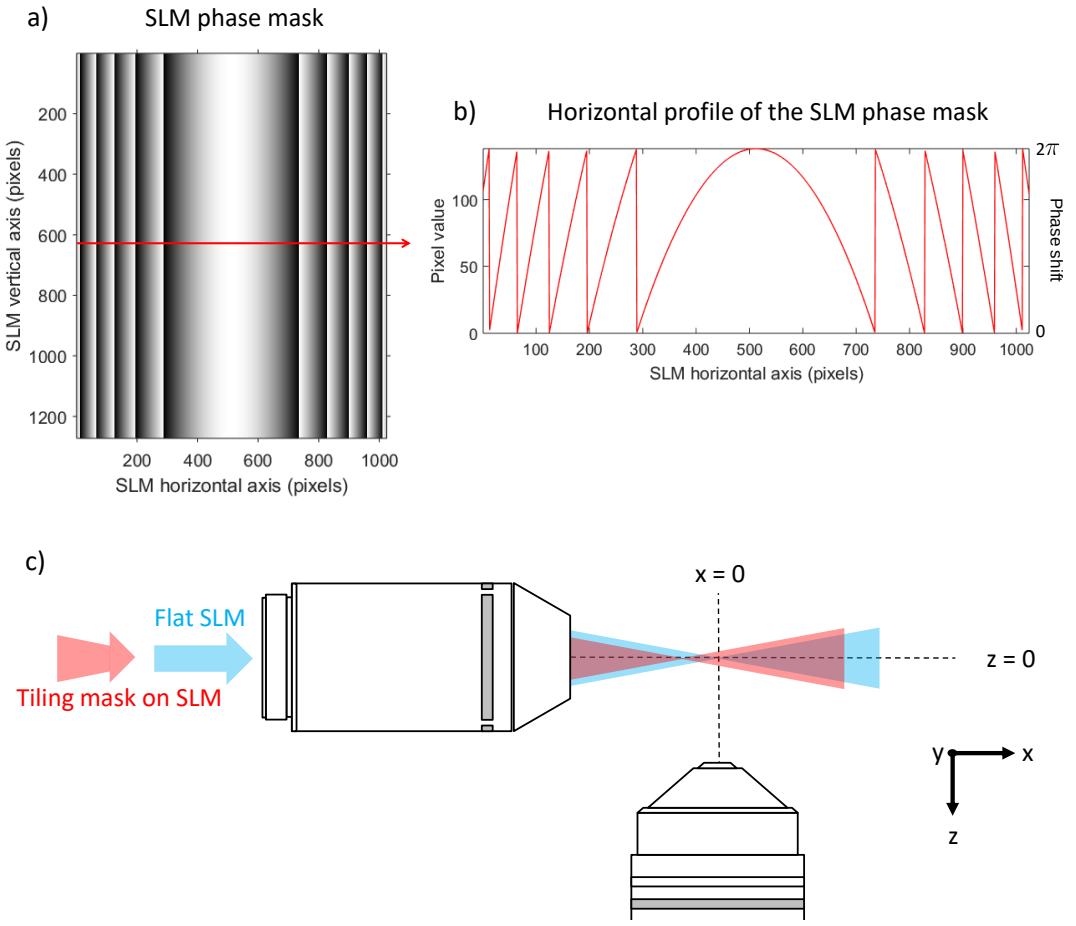

Figure 4.3: *(a) Example of a phase mask applied to the SLM to move the sheet's focus laterally within the imaging FoV. The pattern corresponds to a one-directional quadratic phase mask with values wrapped around the interval 0-138, with 0 in black and 138 in white (corresponding to the phase shift interval 0-2π). (b) Profile of one of the rows of the SLM phase mask (a). (c) Schematic explanation of what happens in the object plane when the phase mask (a) is applied to the SLM (sizes and distances not to scale): within a top view of the SLM-SPIM excitation arm, the collimated beam entering the excitation objective (in blue) is transformed into a slightly converging beam (in red), resulting in a lateral displacement of the sheet's focus within the imaging FoV (i.e. sheet focused at $x \neq 0$).*

a restricted vertical stripe is used to generate the final image, the one that overlaps with the position of the sheet waist. The SLM mounted on our system offers the flexibility to adjust the positions and number of tiles considering the sample's size and tolerance to excitation light. For example, if one is only interested in a small section of the entire FoV, the best thing to do is to restrict the tiling to the region of interest, minimizing both imaging time and sample exposure to excitation light. Results obtained using tiling on a sample of fluorescent beads suspended in agarose can be seen in Figure 4.4. The set-up chosen for these tiling experiments is set-up 1 (see Figure 4.1), which is the one that gives the thinnest light-sheet. As a suggestion for future works it would be interesting to mount a different camera on the SLM-SPIM and try and perform tiling using the rolling shutter more (the camera currently used does not have a rolling shutter mode).

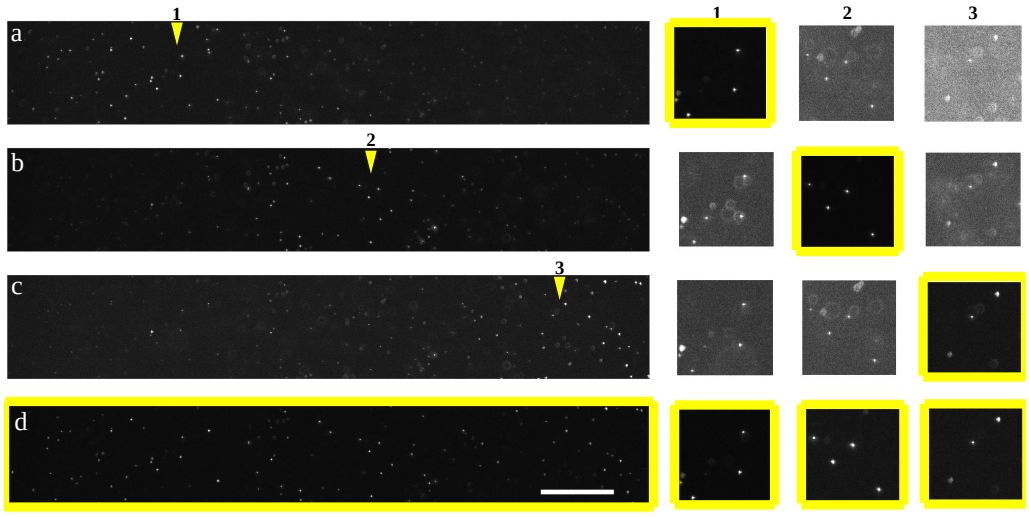

Figure 4.4: *Figure taken from [48]. Results of using the tiling technique on a sample of 0.2 µm fluorescent beads embedded in agarose. Images acquired using set-up 1 (see Figure 4.1). I acquired eight images of the same plane of beads, each with the light-sheet focused at a different lateral position in the FoV. Left: (a,b,c) same horizontal stripe taken from three of the eight images taken (only the second, fifth and eighth image are shown instead of the complete set of eight, for sake of clarity). In each stripe, the position of the light-sheet waist is indicated by the yellow arrowhead, and is characterized by brighter in-focus beads and fewer and dimmer out-of-focus beads. (d) Tiled image: this was obtained by combining, side by side, the vertical stripes corresponding to the position of the sheet waist in the eight images. Right: zooms on three different groups of beads visible in the image stripes on the left. Each column represents a different group of beads, each found at a different lateral location in the FoV (locations 1, 2 and 3). Each row shows how the same beads appear in the corresponding image on the left. Each of these zooms has been separately normalized to its own maximum value. Looking at one set of beads at a time (i.e. one column), notice the increase in relative amount of light illuminating out-of-focus features as the sheet's waist gets further away from the location of the beads. The tiled image (d) is created using only the parts of the images where most of the excitation light is concentrated on in-focus features, and gives good optical sectioning throughout the entire FoV. Scale bar: 50 µm.*

4.3 Structured illumination and pencil beam scanning for background reduction

In light-sheet microscopy, the selective illumination performed by the light-sheet is what makes it possible to achieve a good image contrast even when imaging a plane inside an intact 3D sample. Nevertheless, light-sheet images can still suffer from contrast degradation, mainly caused by scattering, which acts both on the incoming light-sheet and the excited fluorescence. In fact, as the light-sheets enters the sample, a certain amount of light gets scattered and ends up exciting parts of the sample which are outside the in-focus plane defined by the system's DoF. This fluorescence, excited by the part of the light which has been scattered, is ultimately seen as an out-of-focus signal in the image. Scattering from the sample tissue not only acts on the incoming light-sheet, but also on the excited fluorescence. Independently of where the fluorescence is coming from within the sample, it has to go through some more sample tissue before reaching the detector. The part of fluorescence that undergoes scattering on its way through the sample will contribute to a diffused fluorescence background in the image, resulting in a reduction of the image contrast.

In this section, I discuss two techniques which can be used in a light-sheet microscope to try and improve image contrast, namely structured illumination and pencil

beam scanning, and discuss how they can be implemented on the SLM-SPIM.

4.3.1 Structured Illumination

Different structured illumination techniques can be applied to light-sheet microscopy in order to achieve an improvement either in the contrast [59] or in the resolution [60] of the acquired images. In this section I discuss the implementation on the SLM-SPIM of one of the contrast enhancement structured illumination techniques, but as an idea for future works it would be interesting to try and perform one of the resolution enhancement techniques as well.

In order to improve image contrast, the used imaging technique needs to be able to discriminate the fluorescence coming from the in-focus plane from the specimen-related scattered background, making it possible to remove the out-of-focus light and thereby improve the contrast of in-focus structures [59]. Structured illumination techniques achieve this by using a modulated illumination, and taking advantage of the fact that the optical properties of a specimen affect the modulation pattern. Different structured illumination techniques require a different number of acquired images and a different mathematical procedure to extract the final, contrast enhanced image, but they all rely on the fact that the in-focus, non-scattered signal will be modulated according to the illumination pattern, while the specimen- and aberration-induced out-of-focus light will *lose* the modulation [19, 20, 61].

The technique I decided to try on the SLM-SPIM was first introduced and applied to widefield fluorescence microscopy [61, 62], and later applied to light-sheet microscopes [20, 59], and in this thesis I call it the 3-phase method. Following this approach, a single spatial frequency grid pattern is used to illuminate the sample, and the final contrast enhanced image is obtained by combining three different images taken using the same pattern but shifted by a precise spatial phase shifts of: 0, $2/3\pi$ and $4/3\pi$. The microscope images the pattern efficiently only on those portions of the object which are in focus. Instead, out-of-focus signal does not carry any trace of the pattern modulation and its contribution is similar in all the three images. By mathematically processing the three images, the grid pattern itself can be removed, together with all the non-modulated signal, to yield a final image with reduced out-of-focus background and hence enhanced contrast. The formula used to combine the three images $I_{1,2,3}$ is the following:

$$I = \frac{\sqrt{2}}{3}\left[(I_1 - I_2)^2 + (I_1 - I_3)^2 + (I_2 - I_3)^2\right]^{1/2}. \tag{4.1}$$

4.3.2 SLM-SPIM implementation

The 3-phase technique has been implemented on a DSLM microscope by fast time-modulation of the scanned beam [59], and in 2007 on a SPIM microscope using a grid-projection approach [20]. On the SLM-SPIM, the sinusoidal pattern needed to implement this technique can be generated by interfering two mutually-coherent light-sheets that propagate in the same $x-y$ plane, but at a different angle with respect to the optical axis of the illumination arm. These two light-sheets interfere in the sample plane and generate a light-sheet with sinusoidal modulation along y (Figure 4.5b). To generate the two interfering sheets, we display two opposite sawtooth patterns simultaneously on the top and bottom halves of the SLM, as in Figure 4.5a. As the beam diffracts off the SLM it is thereby split into two half-beams, propagating in the image plane ($x-y$ plane) but at two opposite angles α and $-\alpha$

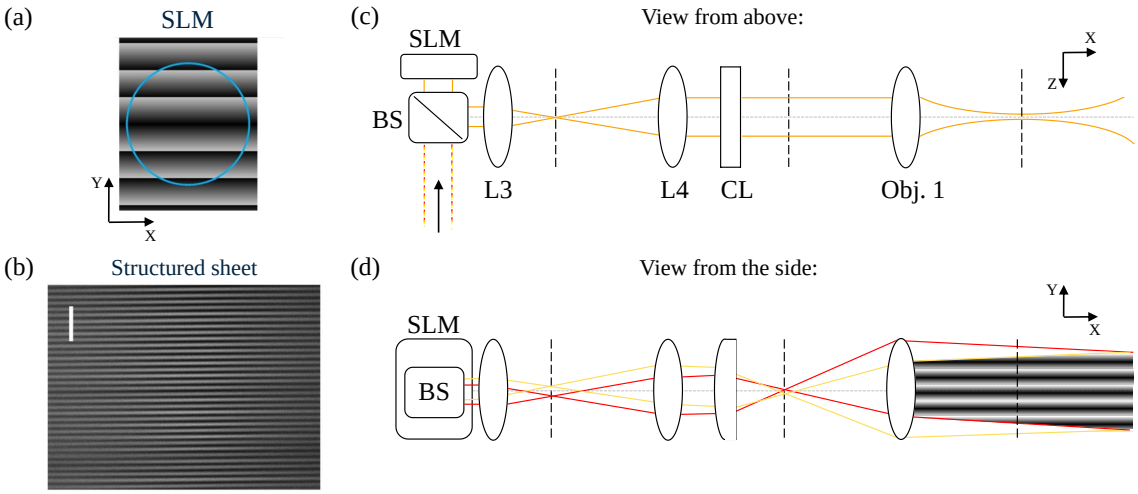

Figure 4.5: *(a) Pattern displayed on the active area of the SLM to create a sinusoidally modulated light-sheet; the blue circle indicates the footprint of the collimated input beam. (b) Experimental image of a modulated light-sheet obtained with our two half-beams interference method, imaged in aqueous fluorescein dye diluted in water, revealing an interference pattern with a period of* ~ 10 *µm (white to white); scale bar: 50 µm. (c) Schematic of the optical path (distances and sizes not to scale) of the light reflected off the SLM. The two beams follow the same optical path when viewed in an x-z plane, forming two co-planar light-sheets on the object plane. (d) In an* $x-y$ *view of the system, the two sheets propagate at different angles, generating an interference pattern along y in the object plane.*

from the optical axis of the excitation arm. When the two half-beams meet again and interfere in the sample plane, they generate the desired sinusoidal pattern (Figure 4.5b). The period Δy of the final illumination pattern is defined by the half angle α between the beams, which is in turn determined by the sawtooth period p on the SLM, following:

$$\Delta y = \frac{\lambda}{2 \cdot n \cdot \sin(\alpha)} = \frac{\lambda}{2 \cdot n} \frac{f_{obj} \cdot f_4}{f_{CL} \cdot f_3} \frac{p}{\lambda} = \frac{p}{2 \cdot n} \frac{f_{obj} \cdot f_4}{f_{CL} \cdot f_3}, \tag{4.2}$$

where f_3, f_4, f_{CL} and f_{obj} are the focal lengths of L_3, L_4, the cylindrical lens and the excitation objective respectively. In order to shift the illumination pattern by a desired phase (to perform the 3-phase method), the equivalent optical phase shift can simply be added to the pattern displayed on one of the two halves of the SLM. Figure 4.6 shows the results obtained using this structured illumination technique on the SLM-SPIM to image the heart of a formalin-fixed Zebrafish embryo specimen (4 days post-fertilization) expressing GFP fluorescence.

To quantify the improvement in image contrast obtained as a result of the out-of-focus background reduction, I calculated the standard deviation of the energy-normalized histograms [59] of the structured illumination (Figure 4.6c) and the normal light-sheet images (Figure 4.6b). This standard deviation can be calculated using the following formula:

$$\sigma_N = \sqrt{\frac{\sum_i \left(\frac{I_i - \bar{I}}{\sum I_i} \right)^2}{C - 1}}, \tag{4.3}$$

where C is the total number of pixels in the image, i ranges from 1 to C, I_i is the intensity value of the i-th pixel, $\sum I_i$ is the sum of all the pixels values in the image, and $\bar{I} = \sum I_i / C$ is the mean intensity value of the image. As more extensively explained

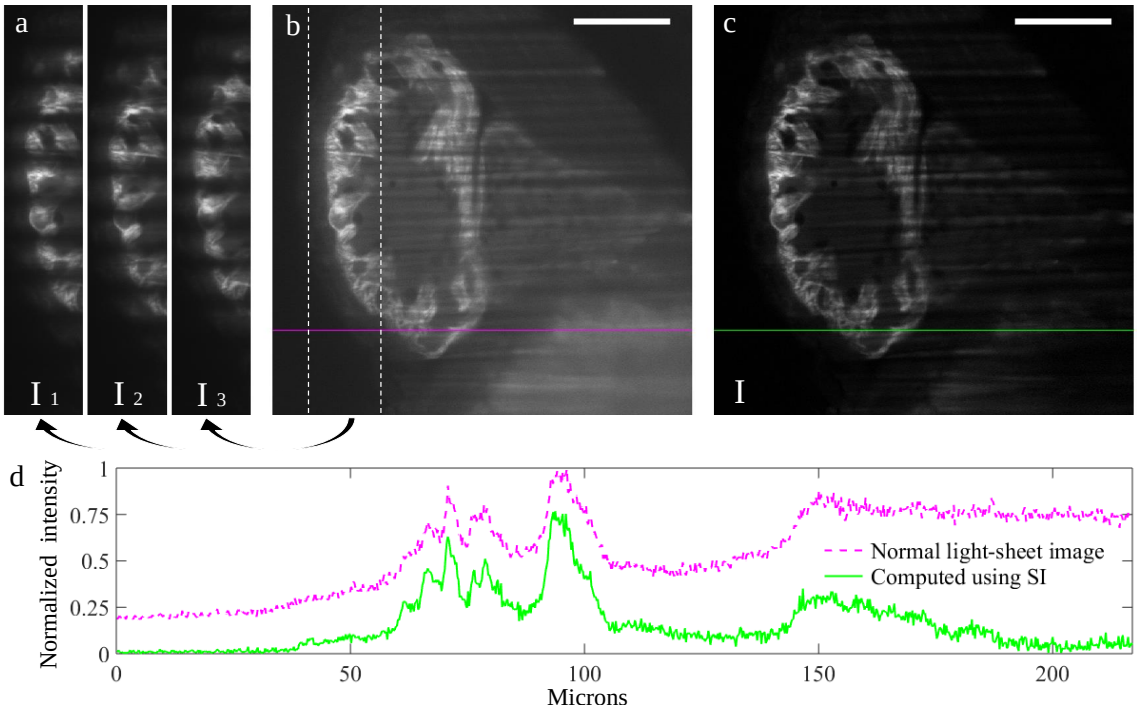

Figure 4.6: *3-phase structured illumination performed using set-up 1 of the SLM-SPIM. (a) Cropped views of the three images, $I_{1,2,3}$, taken with a modulated light-sheet (period = 20 µm on the sample plane). The sinusoidal pattern for the second and third images is shifted by a phase of $\frac{2}{3}\pi$ and $\frac{4}{3}\pi$ with respect to the pattern used for the first image. (b) Image acquired with a normal, non-modulated light-sheet. (c) Image obtained by combining I_1, I_2 and I_3 using Equation 4.1. (d) Intensity profile along the same row in images (b) and (c), to visualize the achieved background reduction and improved image contrast (values normalized to the global maximum of the two plotted lines). Scale bars: 50 µm.*

in [59], the ratio between the σ_N values of two images can be used to quantify the change in image contrast, with an higher σ_N value corresponding to a better image contrast. For the images shown in Figure 4.6b and 4.6c I calculated this ratio to be $\sigma_N(c)/\sigma_N(b) \sim 2.6$.

It should be noted that our approach to generate the two interfering light-sheets cannot be used with set-up 2 and 3. In fact, in the case of perfect conjugation between the SLM and the waist of the light-sheet (or almost perfect conjugation, with set-up 3) the desired interference appears only on one side of the imaging FoV. Instead, the mis-conjugation offered by the side view of set-up 1 moves the edge of the interference region to the side, allowing the two half-beams to interfere across the whole FoV. A possible alternative is to follow an approach analogous to the one used in [63]. The SLM is in that case divided into vertical stripes instead of into two halves, and the two blazed gratings displayed on alternate stripes. This method allows structured illumination experiments to be performed with all our three set-ups, but it gives rise to extra diffraction orders which reduce efficiency and, if not properly masked, increase out-of-focus excitation and bleaching. Masking these extra orders is possible, but we found that for the three main set-ups of the SLM-SPIM it requires a careful selection of stripe size and design and alignment of the mask, complications which can be avoided when following our suggested approach.

4.3.3 Pencil beam scanning (synthetic DSLM)

The same illumination delivered by a light-sheet can be obtained by scanning up and down (within the exposure time of the acquired image) a pencil beam (*i.e.* a beam focused along both directions y and z, as opposed to the light-sheet which is only focused along z). This technique is called Digital Scanned Laser Light-sheet Microscope (DSLM) [11, 64]. As mentioned in the introduction of Section 4.3, part of the fluorescence excited by the light-sheet (or by the scanned beam) inevitably undergoes some amount of tissue scattering before reaching the detector, resulting in diffused fluorescent background in the image, thereby reducing its contrast. Synchronizing the scan of a pencil beam in the illumination with a partial exposure of the detector on the imaging side can help reduce the contribution of this scattered light to the out-of-focus content of the resulting image [14, 18]. Such rejection of scattered light is referred to as confocal line detection, and can be performed by exposing, as the beam is scanned through the selected plane, only the rows of the detector that should be reached by the non-scattered fluorescence coming from the illuminated line of the sample (exposure method called *rolling shutter*, see Figure 4.7).

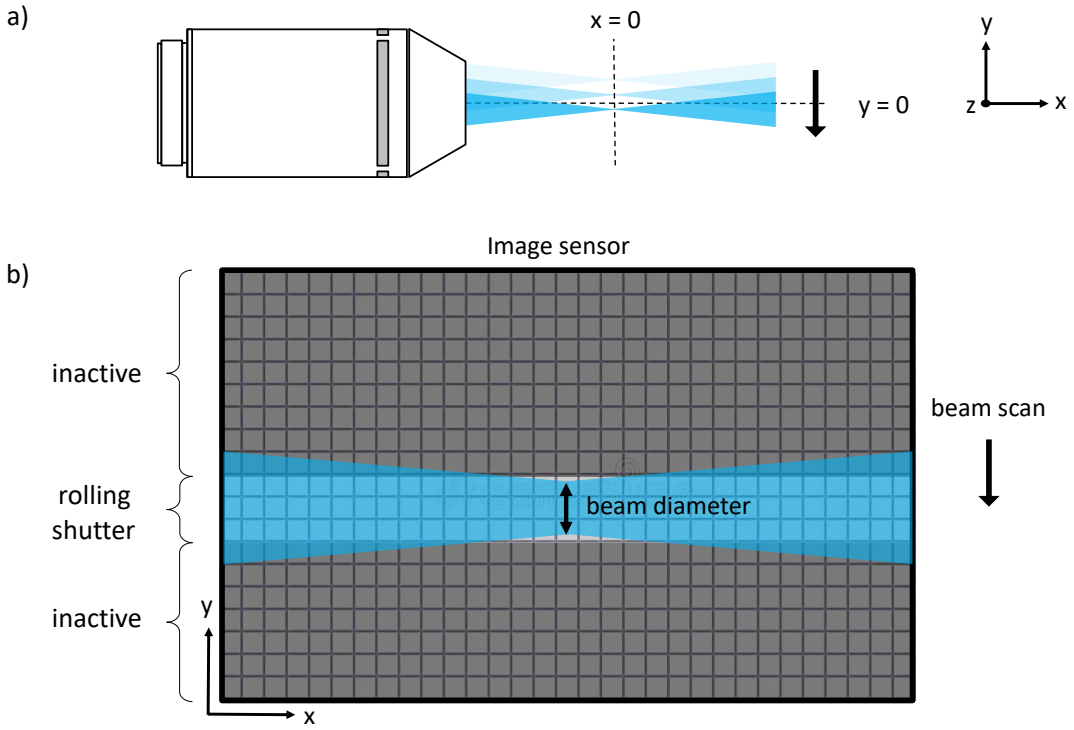

Figure 4.7: *Rolling shutter imaging mode to perform a confocal line detection. (a) The same illumination delivered by a light-sheet can be obtained using a beam focused along both x and z, scanning it across the FoV (i.e. across the y-axis, as shown in (a) and (b)) within the exposure time of a singe image capture. (b) Confocal line detection can be used in order to reject part of the scattered light, and it can be performed by synchronizing the vertical scan of the beam in the FoV with a vertical scan of an horizontal shutter on the detector. The shutter size should match the size (on the detector) of the laser beam, so that it exposes only the rows of the detector that should be reached by the non-scattered fluorescence coming from the region of the sample excited by the laser beam.*

One other way of performing this technique is by recording a sequence of full-frame images as the pencil beam is scanned across the FoV, and then create the final image by applying a synthetic confocal slit to each raw image (*i.e.* masking out all rows

except those where the pencil beam should have appeared). This post-acquisition confocal slit method is implemented for example in [14], where each image is multiplied by a smooth Gaussian mask centered and aligned with the illumination beam. In order for the mask to correctly select the desired part of each image, the position and inclination of the illumination beam needs to be known, either from previous calibration or from the acquired images. In fact, both implementations of the confocal slit technique (rolling shutter, and post-acquisition masking) require precise alignment and size-matching between the illumination beam and the detection line used. The disadvantages of the post-acquisition masking method, as opposed to the rolling shutter, are a reduction in speed and a less efficient data acquisition: many pixels are exposed (and their values are stored in images) even though they are later not used to form the final image.

4.3.4 SLM-SPIM implementation

On the SLM-SPIM we implemented the pencil beam scanning technique using the post-acquisition confocal slit method. By experimenting this method we developed an alternative way to process the raw images and achieve background rejection, obtaining a technique that combines the ease of a standard, full-frame acquisition with a simple and calibration-free post-processing procedure. Our imaging procedure consists of scanning the illumination beam across the entire FoV, acquiring a single full image for each position of the beam. We then combine these images into a 3D stack of size $n \times m \times i$, where $n \times m$ is the image size in pixels and i is the number of images taken. We obtain the contrast-enhanced image by simply computing the Maximum Intensity Projection (MIP) of the stack of images along its third dimension (dimension of size i).

To explain and justify this procedure, let us concentrate on how the intensity value of a single pixel changes as we scan through the stack of images. Let (x,y) be the position of the pixel in the image, and (x_s,y_s) its corresponding location in the sample plane, and assume we expect to detect some non-scattered signal from (x_s,y_s). The value of pixel (x,y) will be very low in the images taken with the pencil beam positioned far away from (x_s,y_s), somewhat higher as the beam gets closer to it and more scattered light reaches pixel (x,y), and it will be at its highest when (x_s,y_s) is directly in the path of the incoming beam. The Maximum Intensity Projection therefore gives, for each pixel (x,y), the intensity received by it in the image recorded with the illumination beam giving the best overlap with (x_s,y_s), the position in the sample that maps onto that pixel. And this is exactly what we wish to retain in our reconstructed image.

Acquiring entire images but then only retaining some pixel rows from each image is of course a relatively slow and inefficient way of implementing the pencil beam scanning technique. However, this shows how the flexible SLM-SPIM imaging system can easily be used to explore the feasibility of new imaging modalities, obtaining good pilot results without investing the time and effort needed to build and calibrate a high-speed dedicated rolling-confocal-slit DSLM system. Our post-processing approach based on a simple Maximum Intensity Projection also has the benefit of not requiring any calibration of the pencil beam position and orientation on each image plane.

In our implementation, the sample is illuminated by a regular 2D-focused beam, which we generate by displaying an opposing cylindrical lens phase function on the

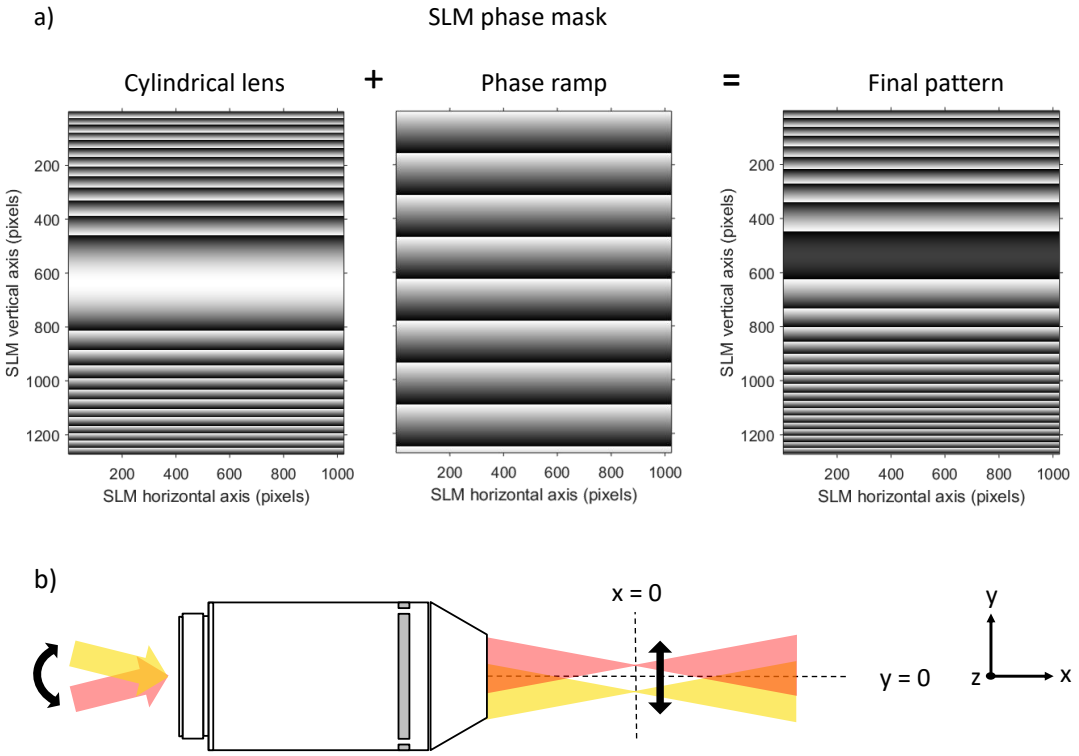

Figure 4.8: *(a) Example of a phase mask applied to the SLM to generate a pencil beam and move it vertically within the imaging FoV. The pattern corresponds to the sum of a quadratic phase function (i.e. a cylindrical lens pattern which undoes the effects of the physical cylindrical lens, turning the light-sheet into a beam focused along both x and z) and a linear phase ramp (which shifts the focus of the beam vertically in the FoV). The sum of these two functions results in a cylindrical phase function translated along y. (b) Schematic explanation of what happens in the object plane when the phase mask (a) is applied to the SLM (sizes and distances not to scale): within a side view of the SLM-SPIM water excitation arm (or top view of the glycerol arm), a collimated beam entering the excitation objective is transformed into a beam focused both along x and z, which is then scanned vertically to cover the entire FoV.*

SLM (see Figure 4.8). This corresponds to adding a quadratic phase function (defocus) along the vertical axis of the SLM, to undo the effects of the physical cylindrical lens (note that the same could be achieved by physical removal of the cylindrical lens from the system, combined with flat SLM). The result of this phase modulation is a beam which is focused in front of the launching objective along both y and z. The SLM is also used to scan the beam and sequentially illuminate, line by line, the entire in-focus plane. The phase function applied to our SLM is therefore the sum of the cylindrical lens pattern (to generate a focused beam) and a linear phase ramp (to vertically move the focus of the beam). In practice the combination of these two functions yields a cylindrical phase function that translates vertically on the SLM as the pencil beam is scanned (or laterally on the SLM, in case of our experiments with the glycerol set-up).

The improved contrast achievable using this technique is particularly valuable when imaging deep in highly scattering samples. To demonstrate this we decided to perform the pencil beam scanning technique on cleared whole mouse brain samples, with results shown in Figure 4.9. For these experiments I programmed the SLM to make the pencil beam translate with steps of 1.4 μm in the sample plane (corresponding to $\sim$6 pixels in the image, with the pencil beam having a FWHM of $\sim$ 25

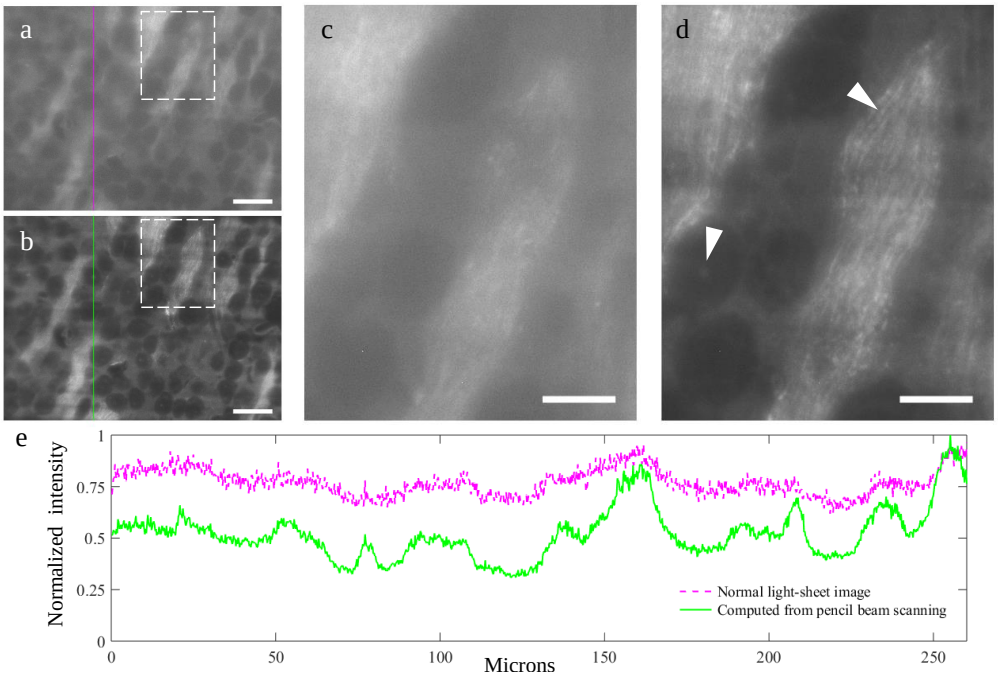

Figure 4.9: *Pencil beam scanning technique applied on a cleared whole mouse brain sample, imaged in glycerol. (a) Image acquired with a normal light-sheet. (b) Image generated with the scanning pencil beam technique, using our reconstruction procedure (based on a Maximum Intensity Projection) on a set of 200 raw images, each taken with the horizontal pencil beam focused at a different height in the sample plane. Scale bars: 50 µm. (c,d) Zoomed-in views of the dashed line rectangles in images (a,b), to highlight some of the faint features (left arrowhead) and fine structures (right arrowhead) revealed by the pencil beam scanning technique. Scale bars are here of 20 µm. (e) Cross section of the normalized intensity along the same column in images (a) and (b) (values normalized to the global maximum of the two plotted lines).*

pixels). A total of 200 images were taken to cover the region of interest shown in Figure 4.9 (1146×1556 pixels).

4.4 Pivoting for shadow reduction

Samples imaged with light-sheet microscope need to be transparent enough for the light-sheet to propagate through them. If a certain part of the sample instead strongly absorbs or scatters the excitation sheet, it generates a shadow which elongates parallel to the direction of propagation of the light-sheet. This type of shadow results in a distortion of the image, with loss of information. One way of reducing this effect is to combine illumination generated by light-sheets propagating at different angles [12, 13]. Figure 4.10 illustrates this technique, which is here referred to as light-sheet pivoting.

Shadow reduction by light-sheet pivoting is generally performed by continuously changing the angle of propagation of the light-sheet at a high speed ($>$ 1 kHz), to provide a range of illumination angles within a single image exposure. The way to practically achieve a tilt of the light-sheet depends on the specific arrangement of the optical components used to generate the light-sheet. Independently on how it is formed, a tilted light-sheet generated using a cylindrical lens maps onto a shifted line focus entering the back focal plane of the excitation objective (see Figure 4.10c).

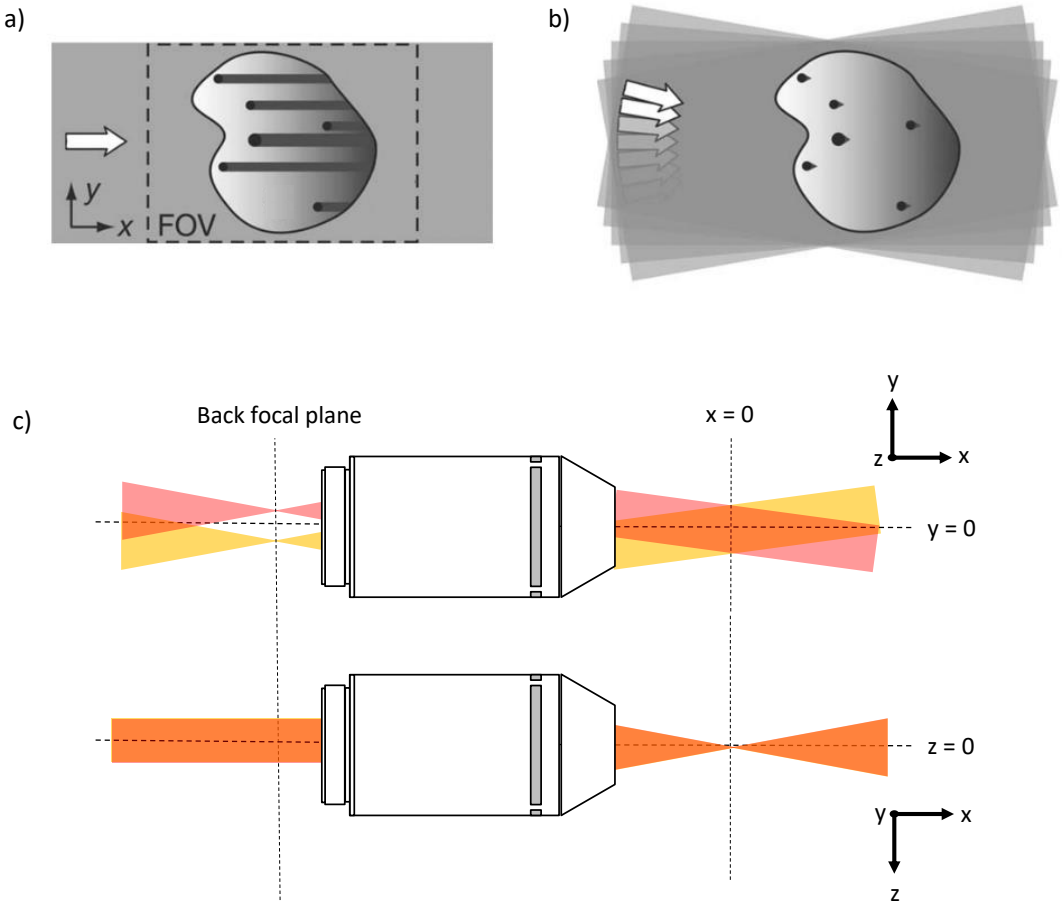

Figure 4.10: *Schematic explanation of how the light-sheet is tilted to reduce shadows. (a,b) Figures rearranged from Figure 1 of [12], visualizing how the shadows noticeable when using a normal light sheet (a) can be reduced by rapidly tilting the light-sheet within the imaged plane (b). (c) Side view (top) and top view (bottom) of the launching objective of the microscope (with sizes and distances not to scale) showing two light-sheets (in yellow and red) that propagate along two different directions but within the same plane in the sample (in this case plane $z = 0$). In an x-y view of the system (top row in the Figure), the light beams that generate the two light-sheets focus at two different heights at the back focal plane of the launching objective, while they appear as collimated and overlapped in an x-z view (bottom row in the Figure).*

4.4.1 SLM-SPIM implementation

On the SLM-SPIM, light-sheets with different propagation directions can be created by displaying different vertical sawtooth patterns (phase ramps) on the SLM (see Figure 4.11). A shadow-free image can be obtained by switching between the different light-sheets within the exposure time of a single image, in which case one important limiting factor to keep in mind is the update speed of the SLM, which for the one used in our system is 60 Hz. One other option is to record one image for each light-sheet inclination, and combine the different images post-acquisition. This second approach, despite being less efficient in terms of image acquisition/computing time, offers the flexibility to permit what we propose as an alternative and improved algorithm for combining the acquired images to obtain shadow suppression. As the image-combination approach proposed for the pencil beam scanning technique discussed in the previous section, the approach we propose here consists again in using the Maximum Intensity Projection.

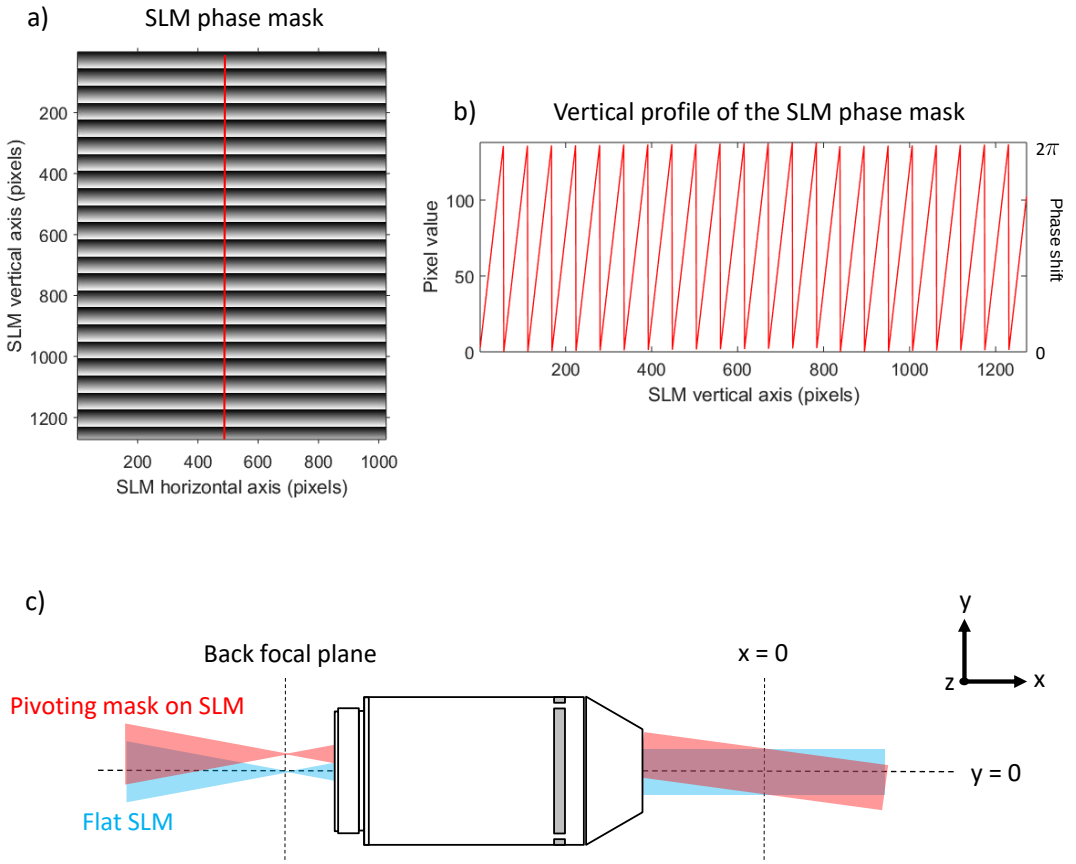

Figure 4.11: *(a) Example of a phase mask applied to the SLM to tilt the light-sheet while keeping it propagating along the same plane within the sample. The mask corresponds to a vertical phase ramp with values wrapped around the interval 0-138, with 0 in black and 138 in white (corresponding to the phase shift interval 0-2π). (b) Profile of one of the columns of the SLM phase pattern (a). (c) Schematic explanation of what happens when the phase mask (a) is applied to the SLM (sizes and distances not to scale). Within a side view of the SLM-SPIM launching arm, the beam generating a light-sheet which propagates along $y = 0$ (in blue) has a focus at $y = 0$ at the back focal plane of the launching objective; applying the phase mask (a) shifts this focus to $y \neq 0$ (in red), thereby changing the angle of propagation of the resulting light-sheet (within the same x-y plane).*

When the light-sheet is tilted through a range of different angles within a single image exposure, the resulting shadow-free image is generated from the sum of all the fluorescence excited by each light-sheet inclination. This technique can be replicated by computing the sum (or average) of a set of images acquired each with the light-sheet propagating at a different inclination. An alternative way of combining these images is to compute the Maximum Intensity Projection of the whole stack: for each pixel, the MIP compares the values assigned to that pixel on each image and only keeps the maximum one. This results in a final image where each pixel takes on the value from the raw image where that region was experiencing minimal shadowing. As it can be seen in Figure 4.12, the image obtained using MIP not only preserves a better image contrast when compared to the one obtained by averaging, but it also assures a more accurate representation of the true intensity profile across the image. In fact, computing the average of a set of images acquired with the light-sheet

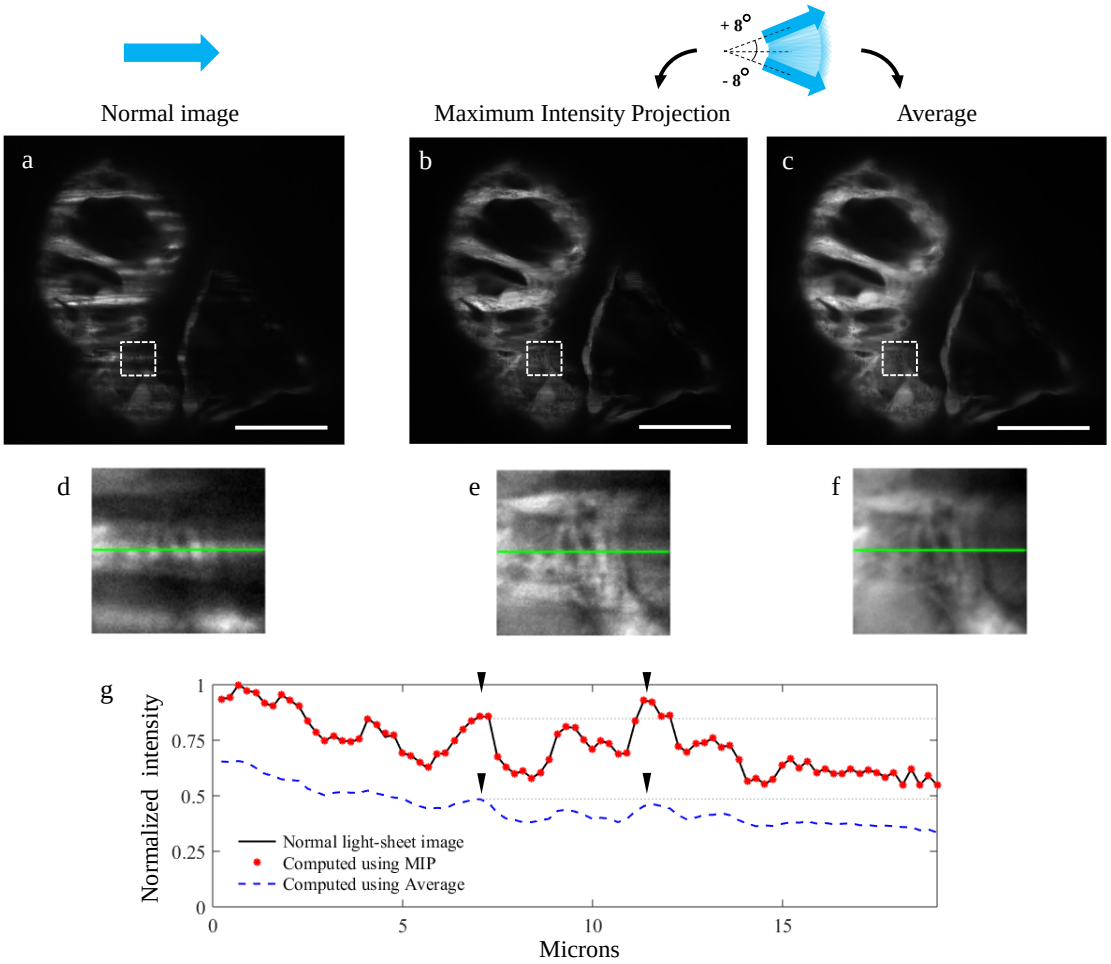

Figure 4.12: *Figure taken from [48]. Shadow suppression experiments using the light-sheet pivoting technique. (a) Normal light-sheet image of the heart of an ex-vivo Zebrafish embryo (euthanized at 4dpf, preserved in formalin). Images acquired using set-up 3 (see Figure 4.1). (b) Shadow-suppression image obtained using the Maximum Intensity Projection (MIP) method. The image was obtained computing the MIP of a stack of seventeen images, each acquired with the light-sheets propagating at a different angle, with the seventeen different angles equally spaced within ±8 degrees. (c) Shadow-suppression image obtained using the averaging method, generated from the same seventeen images used for (b). (d-f) Zoom-in of the dashed line boxes from images (a-c). Each image has been normalized to its own maximum value. (g) Intensity profile of the same horizontal line taken from the zoomed-in views (d-f). This intensity profile plot illustrates how, compared to averaging, the MIP preserves the original image contrast and a more accurate representation of the original intensity profile. Notice for example how averaging (dashed blue line) alters the relative intensity of the two peaks indicated by the two black arrowheads, making the right peak appear dimmer than the one on the left. These plots are normalized to the global maximum of the three plotted profiles. Scale bars: 50 µm.*

propagating at different angles results in an alteration of the true image intensity profile: parts of the sample which are well-illuminated in all the images (*i.e.* are not affected by shadows) are inherently seen as brighter than those that are only illuminated in some of the images. Using MIP on the other hand ensures that the final intensity of each part of the sample only depends on the intensity observed when that part is illuminated without obstruction, and not on the number of images which *agree* with that intensity value.

Figure 4.12 shows the comparison between a normal light-sheet image, with visible shadows, and the results obtained using the two alternative shadow suppression

algorithms: averaging, and our proposed MIP. For this experiment, seventeen images were acquired, with the light-sheet propagating at seventeen different angles, equally spaced within ± 8 degrees. Before combining the images, either with MIP or averaging, a rescaling was performed in order to account for the diffraction efficiency of the SLM, which varies depending on the angle of propagation of the 1^{st} diffracted order, with a higher tilt corresponding to a dimmer light-sheet (see following section for more details on this). An horizontal line was chosen from a region of the sample which, in the normal light-sheet image, is not affected by any shadows (green line in Figure 4.12d). The intensity profile along this line was plotted together with the intensity profile of the same line in the two images computed for shadow suppression. This comparison helps visualise how the averaging technique gives a decreased image contrast and also results in a distortion of the original intensity profile. The set-up used to perform these experiments is set-up 3 (see Figure 4.1). The reason for this choice are explained in the next section.

4.4.2 Set-up choice discussion

As discussed in Chapter 3, the SLM-SPIM allows to choose between three different set-ups for its excitation arm (see Figure 4.1), and the choice should be made taking into account both the type of experiment and the type of sample which is to be imaged. The shadow suppression experiments on *ex-vivo* Zebrafish embryo heart described in this section provide a good example of a situation in which the type of sample strongly influences the set-up choice. In fact, for the specific case of suppressing shadows in the Zebrafish heart, I decided to use set-up 3 instead of set-up 2, which would normally be the one we would recommend using for shadow suppression experiments on samples with finer shadows. Let us now discuss the reasons behind this in more detail:

The conjugation of the SLM plane with the center of the FoV is what makes set-up 2 the most appropriate set-up to be used for shadow suppression experiments, provided it can deliver a high enough tilt angle with high diffraction efficiency. As the SLM is used to send the 1^{st} diffraction order to different directions, it generates light-sheets that propagate at different angles but overlap entirely again on each plane conjugate to the plane of the SLM, as they do on the SLM itself. In the case of set-up 2, as the light-sheet is tilted using the SLM, its rotation in the sample plane happens around the center of the FoV, which is in fact conjugated to the plane of SLM. In set-up 1 the situation is different: the rotation of the light-sheet happens around a position that is to the side of the FoV, such that a tilt also corresponds to an undesired vertical shift of the light-sheet in the images. As the tilt angle increases, the bright central part of the Gaussian sheet shifts away (vertically) from the FoV, which is illuminated by less and less light.

There is however one other thing to consider: for shadow suppression the best results are obtained by using a large range of angles for the incoming light-sheets, particularly if thick shadows are present. In our system, a limit to the maximum achievable tilt angle is set by the SLM pixel spacing. By considering the magnification of the relay optics within our microscope, one can find the relation between the tilt angle of the light-sheet in the sample plane (θ_2) and the angle at which it originally propagates as it is diffracted off the SLM (θ):

$$\sin(\theta_2) = \frac{f_3 f_{\mathrm{CL}}}{f_4 f_{\mathrm{obj}}} \sin(\theta), \tag{4.4}$$

where f_3, f_4, f_{CL} and f_{obj} are the focal lengths of the four optical components which separate the SLM and the sample plane (see Figure 4.13), with f_{obj} being the focal length associated with the excitation objective. Assuming small angles, $\sin(\theta)$ can be approximated with λ/p to obtain:

$$\sin(\theta_2) = \frac{f_3 f_{CL}}{f_4 f_{obj}} \frac{\lambda}{p}, \tag{4.5}$$

where λ is the excitation wavelength (488 nm for the experiments discussed here) and p is the size of the period of the sawtooth pattern displayed on the SLM. This equation shows that the smaller the period of the sawtooth pattern on the SLM, the larger the angle at which the light-sheet generated by the 1^{st} diffracted order propagates. On the other hand, decreasing the sawtooth pattern period size also reduces the number of SLM pixels used for each period, and this coarser approximation of the ideal pattern results in a less efficient concentration of the diffracted light in the 1^{st} diffracted order, *i.e.* the resultant light-sheet is dimmer. Even for larger pixel periods, this varying diffraction efficiency means that larger-angle sheets will be somewhat dimmer, and prior to further processing we rescale each image to compensate for the different brightnesses of the light-sheets they have been generated with.

In order to obtain a sufficiently bright 1^{st} order, four SLM pixels was chosen as lower bound for the sawtooth period size. Using Equation 4.5 one can verify that a sawtooth period of four SLM pixels generates, with set-up 2, a light-sheet tilt angle of $\sim 3°$. For our experiments on the embryonic Zebrafish heart, I found that this maximum tilt angle was insufficient for good shadow suppression. With set-up 3, a period of four SLM pixels (50 μm) corresponds instead to a $\sim 8.8°$ tilt angle. For the wide shadows present in this specific samples, I found that the possibility to use a bigger range of light-sheet tilt angles was a more crucial factor with respect to having a perfect conjugation between SLM and FoV, and therefore decided to use set-up 3.

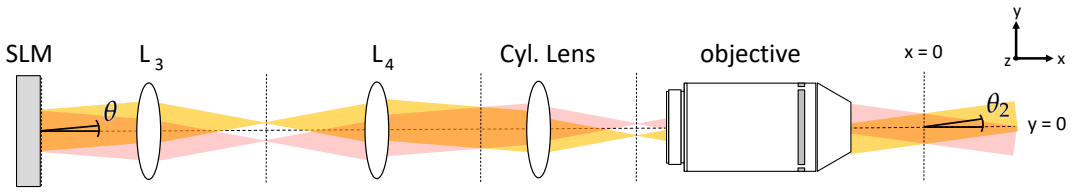

Figure 4.13: *$x-y$ schematic view of the excitation arm of the SLM-SPIM (sized and distances not to scale, beam splitter between the SLM and L_3 ignored for simplicity) with two co-planar light-sheets propagating at angles θ_2 (in yellow) and $-\theta_2$ (in red) with respect to the horizontal axis $y = 0$. A light-sheet that propagates with a tilt angle θ_2 generates from a beam which is diffracted off of the SLM with a certain tilt angle θ. The relation between the θ_2 and θ depends on the optical elements placed between the SLM and the object plane, and can be calculated using Equation 4.4.*

4.5 Automatic refocusing

On the SLM-SPIM, 3D imaging is performed by moving the sample through the light-sheet along the z-direction using a motorized translation stage. The camera acquisition is synchronized to the movements of the stage in order to acquire the

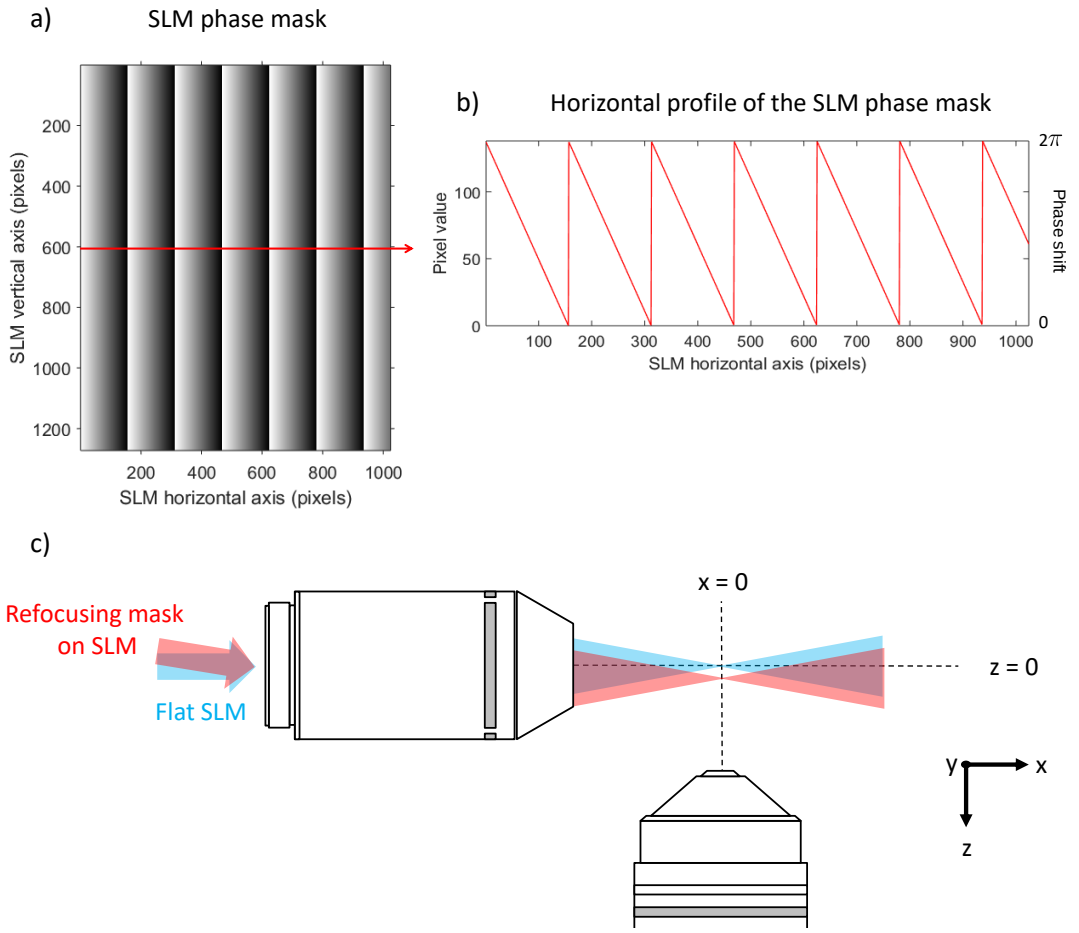

Figure 4.14: *(a) Example of a phase mask applied to the SLM to move the light-sheet in z, i.e. towards and away from the imaging objective. The pattern corresponds to a horizontal phase ramp with values wrapped around the interval 0-138, with 0 in black and 138 in white (corresponding to the phase shift interval 0-2π). (b) Profile of one of the rows of the SLM phase mask (a). (c) Schematic explanation of what happens in the object plane when the phase mask (a) is applied to the SLM (sizes and distances not to scale). Within a top view of the SLM-SPIM launching arm, the beam generating a light-sheet focused at ($x = 0, z = 0$) enters the excitation objective as a collimated beam propagating parallel to the z-axis (in blue); applying the phase mask (a) tilts the collimated beam and thereby shifts the focus of the light-sheet to ($x = 0, z \neq 0$) (in red).*

needed images at each different depth inside the sample. During the acquisition of a z-stack, the distance between the light-sheet and the imaging objective does not change, and the initial focus is therefore maintained. Nevertheless, it is very important, at the beginning of every imaging session, to check and eventually adjust the image focus. In the SLM-SPIM the light-sheet can be moved in z, *i.e.* towards and away from the imaging objective, by displaying a horizontal phase ramp on the SLM (see Figure 4.14). This offers a natural method for optimizing the position of the light-sheet to coincide with the focal plane of the camera, without having to move the imaging objective or the tube lens. Particularly for high-numerical-aperture imaging in thick samples, this optimization must often be performed on a per-sample basis, and even when moving to a different location in the sample.

I developed a MATLAB script to automatically adjust the light-sheet position and

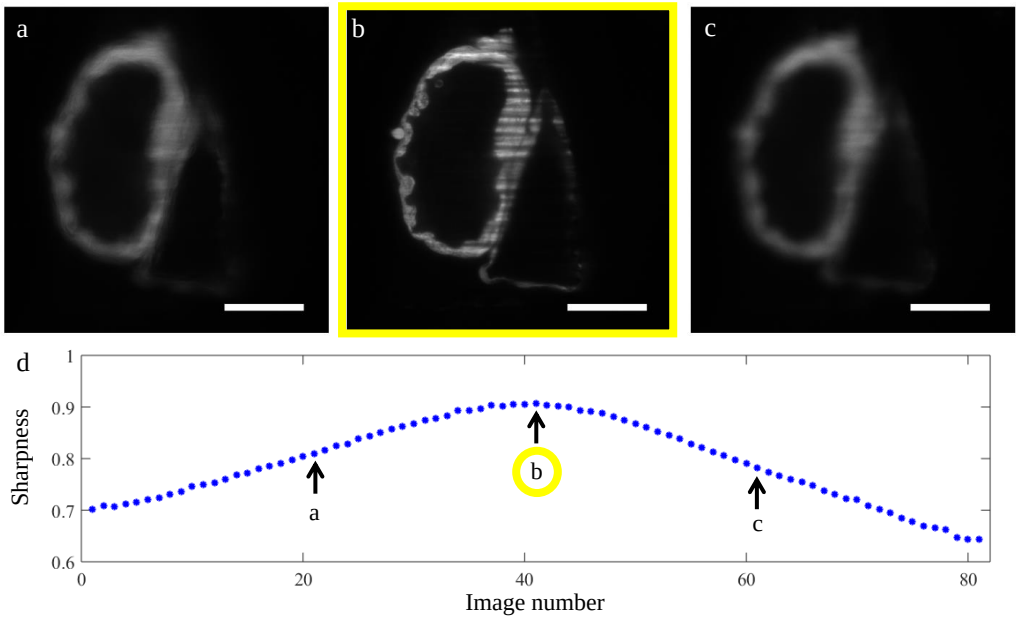

Figure 4.15: *Figure taken from [48]. Automatic refocusing experiment on ex-vivo 4dpf Zebrafish embryo's heart. Imaging performed using set-up 1 (see Figure 4.1). The sharpness metric used to find the position of best focus is the one expressed by Equation 4.6. The SLM was used to move the sheet in the z-direction with steps of 0.5 µm, for a total of eighty-one steps covering a range of 40 µm. At each step, one image was acquired. The motorized stage was used to make the sample move together with the light-sheet, so that the same plane inside the sample was imaged in each of the eighty-one images. (a,c) Two images taken with the light-sheet positioned in an out-of-focus plane. (b) Image identified by the sharpness analysis to be the one with best focus, indicating that it was taken with the light-sheet placed at the correct distance from the imaging objective. (d) Sharpness values, one for each of the eighty-one images, with the maximum value revealing the plane of best focus. To perform the refocusing in a quicker way, one could also take a smaller number of images and interpolate the sharpness curve to find the optimum focus. Scale bars: 50 µm.*

make it coincide with the plane of best focus. The automatic refocusing code performs the following steps:
First, the light-sheet is scanned over a certain range in z (chosen by the user) around its rest position (flat SLM), recording one image for each position of the light-sheet. During this scan, the sample is moved together with the light-sheet using the motorized stage, so that the relative position of the light-sheet with respect to the sample is fixed (*i.e.* the same plane inside the sample is imaged at each step, to ensure that any change in image contrast is purely due to the change in defocus of the same sample plane). The images are then automatically analysed, and the light-sheet (together with the sample) is moved to the position that yielded the image with best focus. To evaluate the quality of the focus of each image, I decided to use the sharpness metric proposed in [65] and used for adaptive optics on a SPIM in [66]. This metric quantifies the image focus through a measure of the ratio between the high and low spatial frequency content of the image, and is defined as follows:

$$S = \frac{\sum_{N_p} | \mathcal{F}[I(x,y)] |_{\text{masked}}}{\sum_{N_p} | \mathcal{F}[I(x,y)] |_{\text{unmasked}}}, \tag{4.6}$$

where $I(x,y)$ is the intensity at pixel (x,y), N_p is the number of pixels in the image,

and $\mathcal{F}$ represents the Fourier transform. The terms *masked* and *unmasked* refer to a rectangular mask which is applied to the 2D power spectral density of the original image ($\mathcal{F}[\mathrm{I}(x,y)]$). The mask sets to zero the central values of $\mathcal{F}[\mathrm{I}(x,y)]$, which represent the lowest spatial frequencies contained in the image. The sharpness value S is given by the sum of the absolute values of $\mathcal{F}[\mathrm{I}]_{\mathrm{masked}}$ divided by the the sum of the absolute values of $\mathcal{F}[\mathrm{I}]_{\mathrm{unmasked}}$ ($0 < \mathrm{S} < 1$). Moving away from the plane of best focus, the images become more blurred, which means that their high spatial frequency content decreases with respect to the low frequency content. As a result of this, the mask used to suppress the lowest frequencies has a stronger effect on $\mathcal{F}[\mathrm{I}]$, giving a lower value for S. The image with best focus is identified finding the maximum value of S (see sharpness plot in Figure 4.15). For the experiment presented in Figure 4.15 the sharpness metric was calculated suppressing all spatial frequencies below 0.009 μm^{-1} (in the sample plane), corresponding to a central mask of 11×9 pixels.

4.6 Discussion and conclusions

The results presented in this chapter show how the addition of a phase-only liquid crystal SLM to the illumination arm of a SPIM can give a versatile, flexible system able to deliver high quality images by applying a range of advanced light-sheet imaging techniques. Imaging fluorescent beads, Zebrafish embryos and optically cleared whole mouse brain samples, I demonstrated how the SLM-SPIM can be used to apply: structured illumination and pencil beam scanning techniques to reduce the out-of-focus content of the images; light-sheet pivoting to reduce the effect of shadows; light-sheet tiling to obtain a more uniform illumination across the imaging FoV and improve optical sectioning and automated focus optimization. New and computationally-undemanding image reconstruction methods based on the maximum intensity projection operation were also proposed. This modular system also gives the option to choose between three different light-sheets, allowing to select the sheet's thickness and height according to the characteristic of the sample and the imaging technique to be performed. While this chapter focused on how our system makes it possible to apply a range of different advanced imaging techniques on a single SPIM microscope, the next two chapters show how the SLM-SPIM also represents a great platform to explore combinations of multiple techniques and trial new ones.

5 Modified Gaussian light-sheet for photo-bleaching-reduced tiling

5.1 Developing new solutions using the SLM-SPIM platform

In the previous chapters I presented our SLM-SPIM and showed how it can be used to acquire conventional light-sheet images and also perform different imaging techniques which help improve image quality. As previously mentioned, the beauty of this system mainly lies in the flexibility offered by the SLM, which not only makes it possible to perform many existing imaging techniques, but can also be exploited to try and develop new ones. In this chapter and in the following one I describe the two main innovative light-sheet designs I have worked on using the SLM-SPIM, both of which aim at improving, each in its own way, SPIM's light-efficiency. The first one (topic of this chapter) consists of a light-sheet specifically designed to be used while performing tiling [21, 58]. Tiling (already introduced in Chapter 4) is an imaging technique which allows to obtain a more uniform illumination by moving the highest-resolution region of the light-sheet across the imaging FoV. The proposed new light-sheet aims at better confining the illumination light, to help reduce the undesired extra photo-bleaching generated by the sample over-excitation typical of the tiling implementation. The second innovative imaging technique (described in the following chapter) involves the generation of a z-modulated light-sheet which can be used to record 3D images in a more light-efficient way, following the principles of compressive sensing [67, 68].

5.2 Introduction

The imaging technique called tiling was already introduced in the previous Chapter 4 (Section 4.2), where it was shown how this technique can be performed on the SLM-SPIM. Let us now briefly recall how this technique works, what it can be used for and what its drawbacks are, which will lead to the presentation and discussion of our proposed modified light-sheet.

One limit to the optical sectioning capability of a light-sheet microscope is set by the trade-off existing between light-sheet thickness and length. The ideal light-sheet would stay thin across the whole imaging FoV, while light-sheets generated by a focused Gaussian beam only remain thin over the beam's Rayleigh length, which decreases together with the sheet's minimum thickness. Different light-sheets have been proposed and used, in combination with image deconvolution, to partly overcome this limit [15, 17, 69]. One other option to work around this physical limit is to use tiling, which involves moving the focus of a short, thin light-sheet across the imaging FoV while only effectively using the thin part of the sheet for imaging [21,

56–58]. This makes it possible to obtain good optical sectioning across a large FoV while using a simple Gaussian beam, and without involving any deconvolution. One disadvantage of using tiling, instead of performing a conventional "static-light-sheet" image capture, is the extra amount of excitation light each sample plane is exposed to as the light-sheet is swept across it to generate a single image. When dealing with samples which photo-bleach easily, the extra photo-bleaching caused by this extra illumination can considerably limit the amount of times the sample can be imaged before it completely bleaches. To partly solve this problem and thereby allow for the use of tiling for longer imaging of easily photo-bleached samples, we propose the use of a light-sheet that better concentrates the light within its waist (along the sheet's propagation direction), which is the only part of the light-sheet that tiling actually uses for imaging (see Figure 5.1). With the proposed light-sheet, the amount of excitation light which illuminates the sample without contributing to the final image is reduced, and so is the undesired extra photo-bleaching. Figure 5.1 illustrates the intensity profile of this type of proposed light-sheet and how it compares to the profile of a normal Gaussian light-sheet.

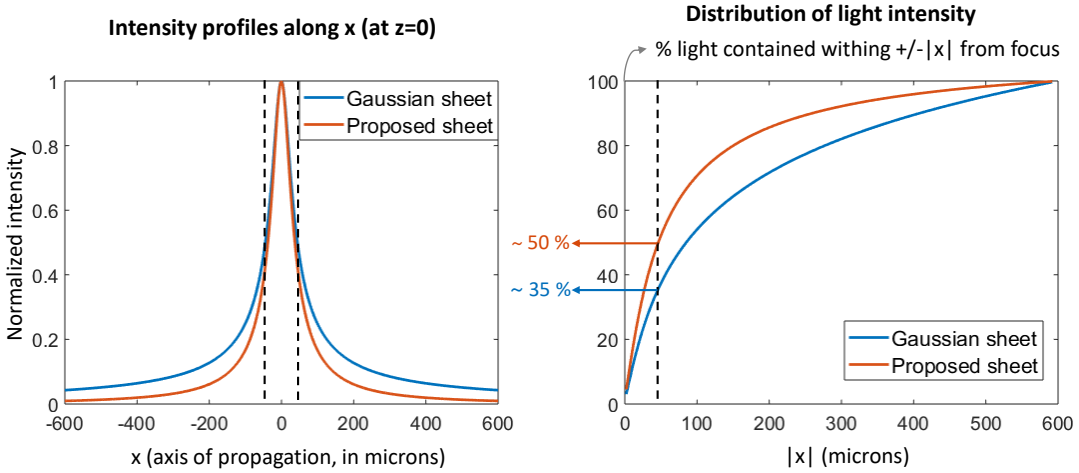

Figure 5.1: *Illustration of the x-intensity profile of a light-sheet which, when compared to a Gaussian light-sheet, better concentrates the light within its waist (along the sheet's direction of propagation). Left: On-axis normalized intensity profiles ($z = 0$, profiles along x-axis) of a Gaussian light-sheet (blue line) and one of our proposed modified light-sheets (red line). The dashed black lines delimit the length of the sheet waist along the x-axis, which extends for twice the Rayleigh range of the Gaussian beam ($-x_R \leq x \leq x_R$). Right: Distribution of the light intensity of the x-profiles shown on the left. For each of the two light-sheets, and for each value of $|x|$ along the x-axis, this plot shows the percentage of light intensity contained within a distance of $\pm|x|$ from the sheet focus (which is at $|x| = 0$). The percentage found for $|x| = x_R$ (dashed line) indicates the percentage of light intensity contained within the sheet waist (again, NB: only considering the x-intensity profiles at $z = 0$).*

A light-sheet with the type of x-intensity profile at $z = 0$ shown in Figure 5.1 can be obtained by masking the central part (along z) of the illumination beam which is focused to generate the light-sheet. On the SLM-SPIM, this can be done by applying a specifically designed phase mask to the SLM (see Figure 5.2). As a first step in order to define the exact profile of a light-sheet which can be generated using the SLM-SPIM and which could be used for photo-bleaching reduced tiling, I performed some simulations using the simulation tool described in Chapter 3 (Section 3.4). I divided the simulation process into four main steps, which are described in detail in the next section. After the simulations, I ran experiments on fluorescent beads, comparing the performances of the proposed light-sheets, in terms of photo-bleaching, against

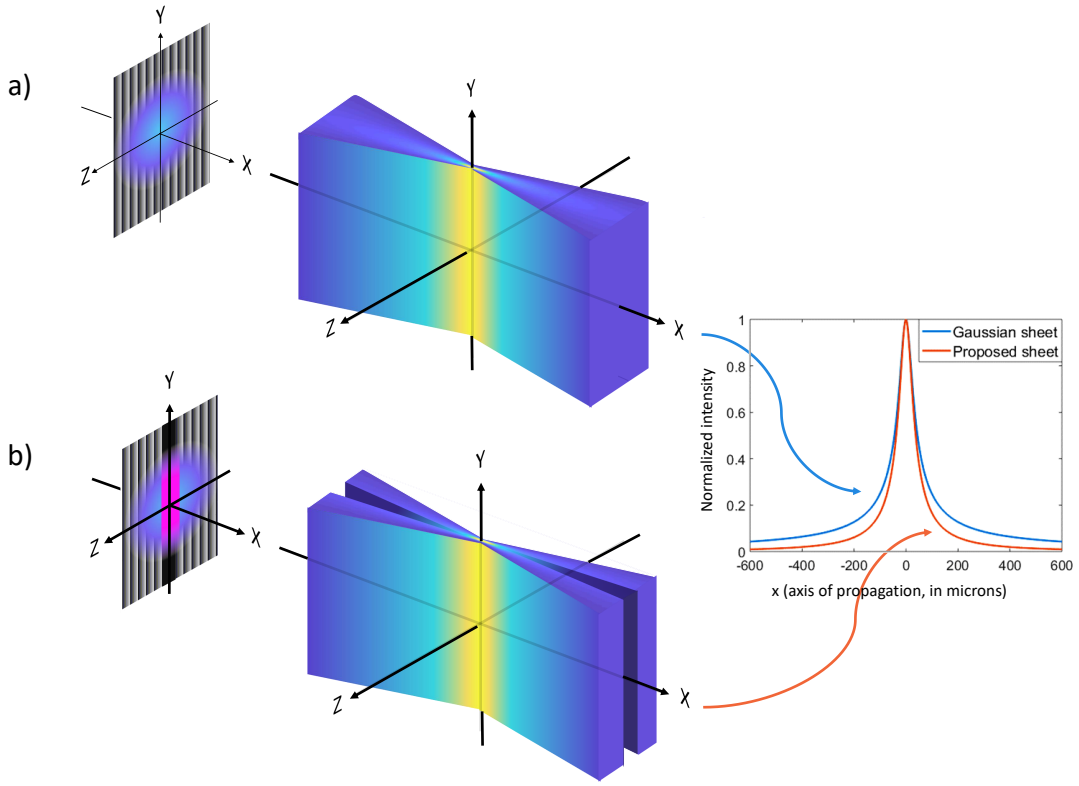

Figure 5.2: *Generation of a modified Gaussian light-sheet on the SLM-SPIM (only the SLM and the object plane shown, with light-sheet intensity profiles scratched, not simulated, just to give a general idea of their shape). As mentioned before, to perform experiments on the SLM-SPIM, a constant phase ramp is applied to the SLM and used to concentrate all the 1^{st} order diffracted light to one side (along z) of the 0^{th} order. The SLM is then physically tilted to use the 1^{st} diffraction order to create a final light-sheet focused at $z = 0$. (a) Generation of a normal Gaussian light-sheet: phase ramp on the SLM, Gaussian beam hitting the SLM (in blue) and Gaussian light-sheet focused at $z = 0$. (b) Generation of the modified Gaussian light-sheet with the intention of reducing photo-bleaching when used to perform tiling. To generate such light-sheet, the same constant phase ramp used for the creation of the normal Gaussian sheet is kept on the whole SLM active area except the central rows (around $x = 0$), where a flat pattern of 0 phase-shift is displayed. This kind of phase mask causes the central part of the beam (in magenta in the figure) to reflect together with the 0^{th} diffraction order. The SLM remains physically tilted as before, to make the final light-sheet (generated by the 1^{st} diffraction order) propagate along the $z = 0$ plane in the object plane, and to let the 0^{th} diffraction order (and now also the central part of the Gaussian beam) be blocked by a mask along the excitation arm of the system (see Figure 5.15 of Section 5.4 for further details on the phase masks used for this chapter's tiling experiments). On the right in the figure is a comparison between the x-intensity profiles at $z = 0$ of a normal and a modified Gaussian light-sheet (same profiles shown in Figure 5.1), which shows how the modified Gaussian light-sheet is characterized by a peak intensity (at $z = 0$) which decreases more rapidly with $|x|$, i.e. going away from the sheet's focus along the sheet's axis of propagation.*

the performances of a Gaussian sheet. The results of the performed experiments are presented and discussed in Section 5.4.

5.3 Simulations

I divided the simulation process into the following four main steps:

- Step 1: Simulate the proposed light-sheet and see how its shape changes depending on the shape of the SLM phase mask; use the results of this first simulation step to choose a range of possibly appropriate SLM phase masks to be used for tiling experiments;
- Step 2: Simulate the process of photo-bleaching;
- Step 3: Simulate the process of tiling the candidate light-sheets over a single fluorescent (and bleaching) plane and compare their imaging and photo-bleaching performances with those of a Gaussian light-sheet;
- Step 4: Simulate the process of tiling the candidate light-sheets over a sample of a certain thickness (*i.e.* made of more than a single plane) and compare their performances with those of a Gaussian light-sheet.

Before proceeding with the simulations, let me explain in a bit more detail what we want to achieve exactly with the new light-sheet:

Imagine imaging a certain 3D sample with a Gaussian light-sheet using the tiling technique. The 3D image is acquired as a series of planes, each imaged separately. To image each plane, the Gaussian light-sheet is swept (or stepped) laterally across the FoV, and the final image of the plane is made only of the fluorescence generated by the central (laterally), thin part of the sheet (ignoring scattering for now, see scheme in Figure 5.3). In order to image a developing process, this 3D imaging procedure is ran several times, generating an entire 3D image of the developing sample at different points in time. When photo-bleaching is an issue, confining the illumination, at each moment, to the part of the sample which is being imaged becomes particularly important, even more so if one aims at imaging the same 3D sample many times to capture its changes/development. In practice though, when using tiling, at each moment only a part of the light-sheet excites fluorescence that contributes to the final image, while a part of it excites fluorescence (and therefore bleaches the sample) without contributing to the final image. The light-sheet we are looking for aims at reducing the percentage of light which excites fluorescence that is not used for the final image, thereby producing the same final image while bleaching less the sample.

Let us now think of what happens under the effect of photo-bleaching. To simplify the situation, imagine dealing with a 3D sample made of fluorescent particles suspended in a non-fluorescent solution. Assume all the particles have the same initial brightness and size, bleach at the same rate and are homogeneously distributed within the 3D volume (in the preliminary experiments described in Section 5.4, this ideal sample is represented by fluorescent beads suspended in an agar solution). Consider imaging the same 3D volume over and over again, using tiling. For a certain level of photo-bleaching, each 3D image will be a bit dimmer than the one just before, meaning that its average brightness will be lower. In fact, every time the light-sheet illuminates a certain plane, it bleaches it by a certain amount, such that the next time that same plane is imaged it will fluoresce a bit less, generating a dimmer image. If the sample bleaches at a particularly high rate, one might even start noticing a brightness gradient within each 3D image, with each plane being, on average, a bit dimmer than the plane imaged just before it. This can happen if the planes are so closely spaced that while the light-sheet waist is being used to image a certain plane, its wider sides significantly illuminate other planes too, generating photo-bleaching. A third effect which might occur while using tiling on easily bleached samples is a lateral brightness gradient within each plane. Imagine the

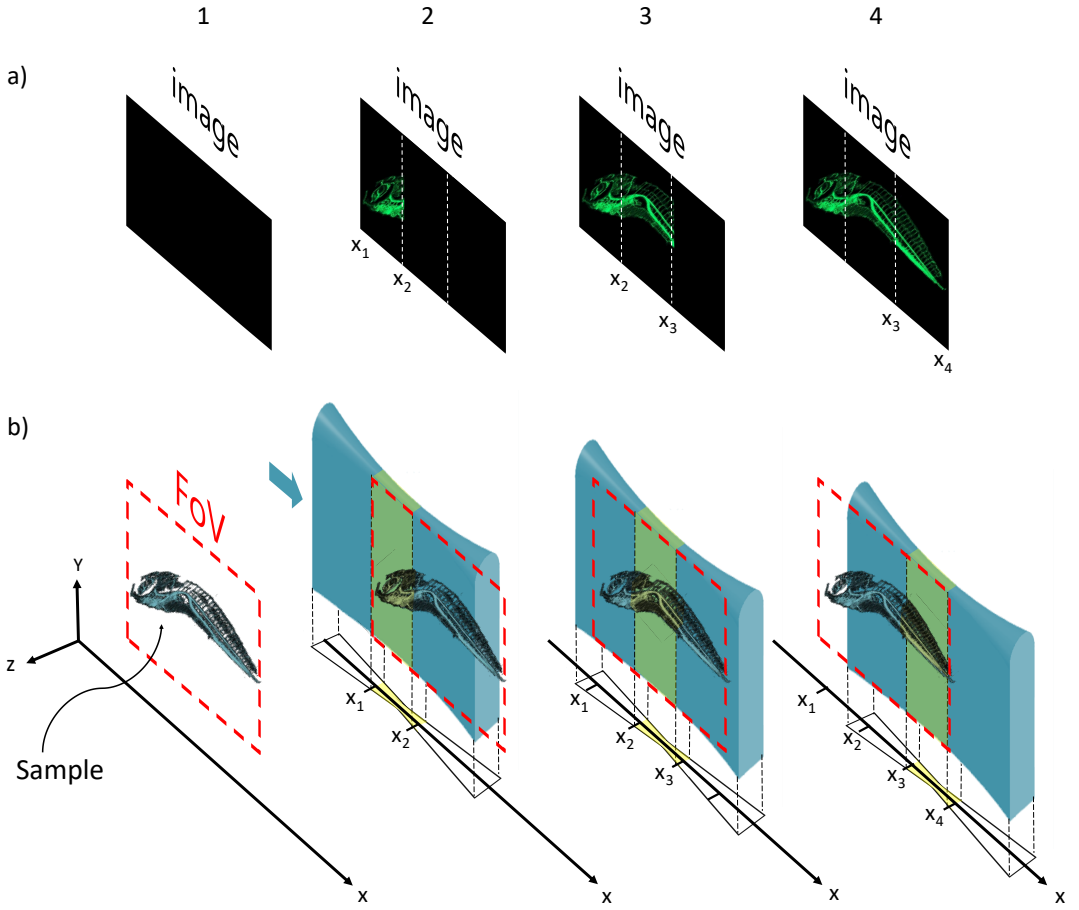

Figure 5.3: *Schematic of the procedure of imaging a plane using the tiling technique (in this case in a stepped mode). In this example the entire FoV (1) is imaged over three steps (2,3,4). The FoV is illuminated using a light-sheet which, in this case, illuminates the FoV propagating from the left to right (see arrow in step 2b). The FoV is divided laterally into three regions, and at each step the light-sheet is focused at a different lateral position within the FoV: its thinnest part (in green in the Figure) illuminates the left part of the FoV in the first step (region from x_1 to x_2), the central part of the FoV in the second step (region from x_2 to x_3), and the right part of the FoV in the last step (region from x_3 to x_4). Out of each imaging step, only the fluorescence excited by the thin part of the sheet is used in the final image (step 4a). This can be achieved by capturing an image of the entire FoV at each step, cropping to retain a vertical stripe out of each image and then combining those three stripes to make up the final image. Another option is to expose, at each step, only the part of the detector which corresponds to the position of the thin part of the sheet.*

sheet is scanned from left to right to perform tiling across a certain plane inside the sample. If the sample bleaches easily, every time the sheet waist is used to image a certain part of the plane, the sheet sides bleach parts of that plane which are to the left and to the right of the imaged part. Therefore, when the sheet-waist is moved to the right in the FoV to image another part of the plane, it illuminates fluorophores which have previously been bleached by a certain amount, and this effect increases as the light-sheet keeps being moved towards the right end of the FoV. The aim of the new light-sheet is to reduce these effects, allowing for longer (in time) and more accurate imaging of samples which are particularly sensitive to photo-bleaching.

5.3.1 Step 1: Light-sheet x- and z-profiles

As mentioned earlier, when compared to a Gaussian light-sheet, the type of light-sheet we want to generate must concentrate a higher percentage of its light within the sheet waist, which is the only part of the sheet actually used for imaging when performing tiling (green part of the sheet in Figure 5.3). In order to generate a light-sheet with this characteristic, we propose to mask the central part of the Gaussian beam which is used to generate the sheet. In practice, this could be done by placing a physical, opaque mask in front of the central part of the beam. On the SLM-SPIM, a phase mask can be displayed on the SLM to mimic the effects of a physical mask (more details on this in Section 5.4). Within the simulations, I simplified the situation by using the SLM as an intensity mask, *i.e.* giving its pixels the ability to modify the intensity of the incoming beam: to simulate the effects of a physical mask which blocks the central part of the beam, the SLM pixels hit by that part of the beam are used to set to 0 the intensity of the light hitting them. The SLM makes it possible and easy to change the size of the blocking mask [1], and Figure 5.4 shows the results of an example simulation of the formation of a light-sheet using a 250 μm wide mask on set-up 1 of the SLM-SPIM (with 250 μm corresponding to 20 SLM pixels).

Figure 5.5 shows how the simulated light-sheet x- and z-profiles change depending on the mask width. These x- and z-profiles can be used to get an indication of what SLM mask sizes could be the most appropriate for what we want to achieve. For the purpose of our tiling experiments, we are interested in the percentage of light contained within the sheet waist. When looking only at the on-axis x-profile of the light-sheets, Figures 5.5a and 5.5b suggest that the wider the masked central part of the beam the more appropriate the light-sheet seems to be for tiling purposes. In fact, when using the Rayleigh range of the Gaussian light-sheet as the x-boundary of the light-sheet waist, Figure 5.5b shows that wider masks generate light-sheets concentrating a higher percentage of their on-axis ($z = 0$) light within their waist.

While it is reasonable to assume that the sheet's intensity does not change much along the y-direction within the distances of interest (*i.e.* the height of the FoV in the object plane), it is certainly important to take into account how the light-sheet profile changes along the z-direction as the different masks are applied on the SLM. As shown in Figure 5.5c, the z-profile of the sheet's focus (*i.e.* at $x = 0$) changes depending on the width of the blocked part of the beam. As the blocked part widens, the central peak narrows and at the same time bigger and bigger side-lobes appear, which means that an increasing percentage of light moves away from the central (along z) peak. Figure 5.5d clearly shows how wider masks generate light-sheets which are, at $x = 0$, less confined along the z-direction. In general, we can consider that all the light which still falls within a thickness equal to the DoF of the imaging system contributes to an in-focus signal in the image, while the rest generates out-of-focus signal and therefore reduces the optical sectioning capability of the light-sheet. Also, thinking of samples which bleach easily, light moved away from the imaging DoF translates into an undesired extra excitation of the sample, which is instead what we are trying to reduce. To make this initial analysis scalable with the shape of the original Gaussian light-sheet and independent of imaging parameters such as the DoF, I decided to consider the amount of light confined within the z-width of the original Gaussian sheet waist (dashed red line in Figure 5.5d), and how it changes

[1] Note that from now on I use the terms *mask size* or *mask width* to refer to the width of the part of the SLM which is used to block the central part of the Gaussian beam.

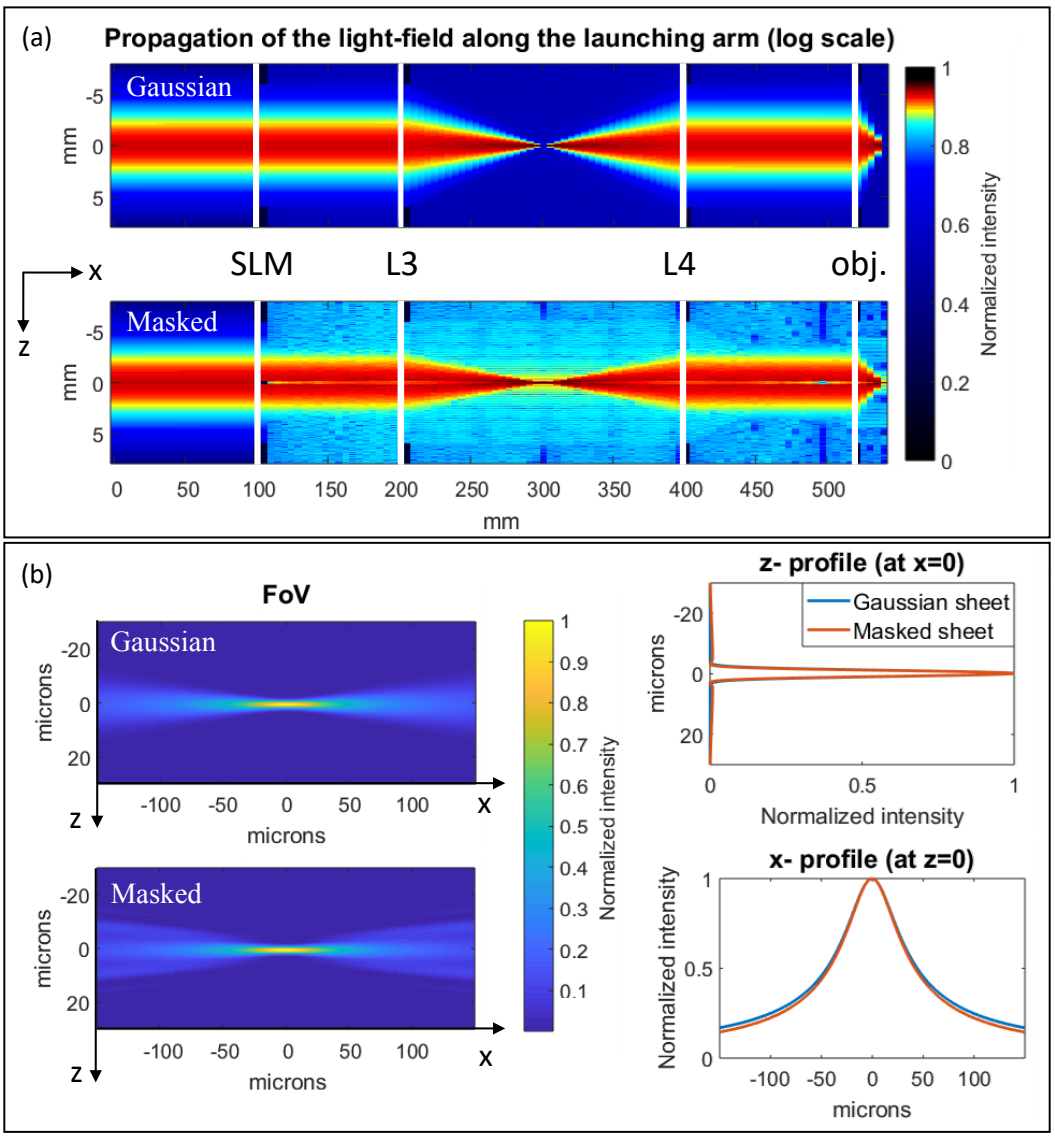

Figure 5.4: *(a) $x-z$ simulation of the formation of a light-sheet within set-up 1 of the SLM-SIM, using a normal Gaussian beam (top row) and masking the central part of the beam with a 250 µm wide mask, corresponding to 20 SLM pixels (bottom row). The mathematical model used to simulate the light propagation through the excitation arm of the SLM-SPIM is the one described in Section 3.4. In these simulations the SLM is used as an intensity mask to block the central part of the beam by making its central pixels turn to 0 the intensity of the light hitting them. The two fields (Gaussian and Masked) are each normalized to their own maximum, the intensity is plotted in a logarithmic scale but the colorbar is adjusted to highlight the details in the high intensity parts of the plots. The positions of the optical elements SLM, L3, L4 and excitation objective (see Table 3.1 for details on them) are highlighted with white lines. (b) $x-z$ view of the light-sheets generated in the FoV of the imaging arm by the propagations shown in (a). Left: $x-z$ intensity profiles of the Gaussian light-sheet (top) and the modified light-sheet (bottom), plotted in logarithmic scale, each normalized to its own maximum. Right: one-dimensional profiles of the intensity fields shown on the left: z-profiles at $x = 0$ (top) and x-profiles at $z = 0$ (bottom).*

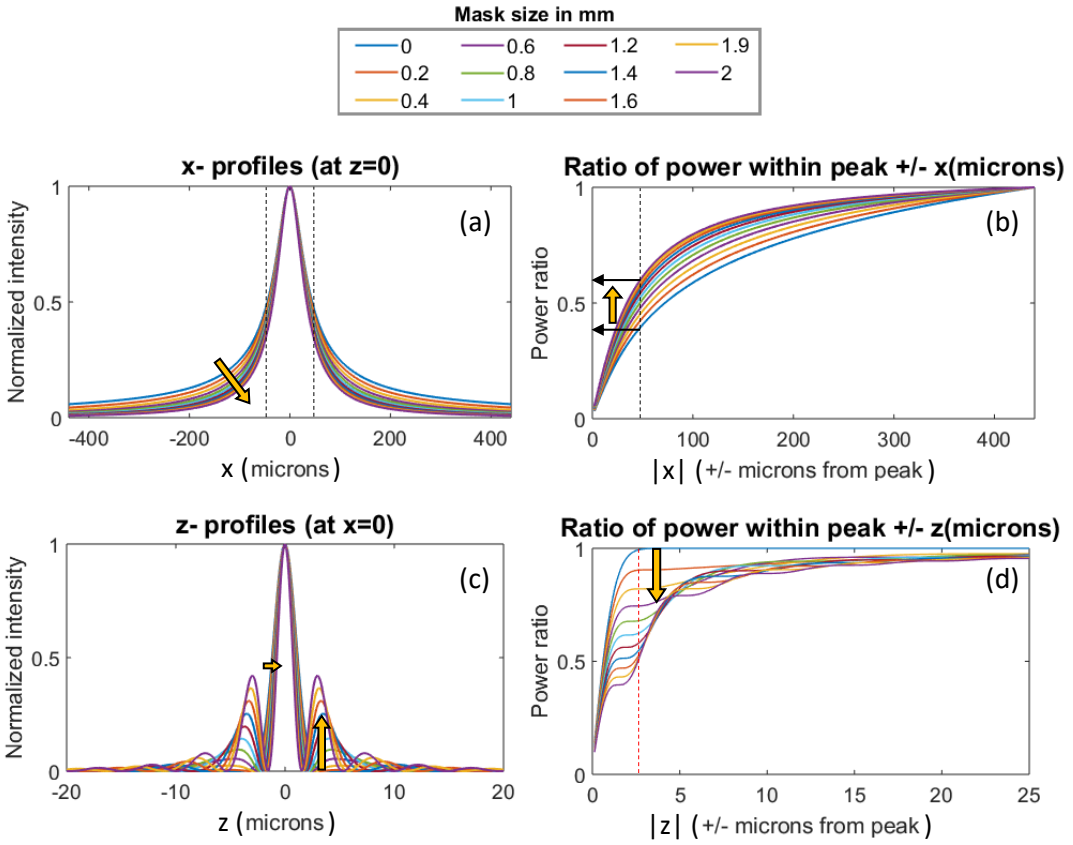

Figure 5.5: *First analysis of the simulated x- and z-profiles of modified light-sheets obtained by masking the central part of the Gaussian beam hitting the SLM using masks of different widths, between 0 (Gaussian light-sheet) and 2 mm. On each of the four plots of the Figure, the yellow arrows indicate what happens as the mask width increases. (a,c) One-dimensional intensity profiles, each normalized to its own maximum: x-profiles at $z = 0$ (a) and z-profiles at $x = 0$ (c). The simulated light-sheets cover a total of 880 µm in x and 50 µm in z. The dashed lines in (a) at $x = \pm x_R$, the Rayleigh range of the Gaussian beam, delimit the Gaussian sheet's waist. (b,d) Initial analysis of the distribution of the light intensity along the profiles plotted on the left. (b) For each distance $|x|$ in microns from the sheet focus (which is placed at $x = 0$), the plot shows the integral from $-x$ to x of the profiles plotted in (a), which corresponds to the sum of all the light-intensity contained by those x-profiles within a distance of $\pm x$ from their peak. Highlighted in black are values relative to $|x| = |x_R|$. (d) Same integration around the sheets' peaks as in (b), but here done along z, for the z-profiles plotted in (c). Dashed red line indicating the width of the main peak of the Gaussian profile.*

according to the size of the mask used. Figure 5.5d shows that, considering the z-profiles at $x = 0$, the amount of illumination confined within that z-range quickly decreases as the mask width increases.

These initial simulations and analysis of the x- and z-profiles suggest that to find the best modified light-sheet for tiling one needs to accept a compromise between the undesirable appearance of side lobes along the z-direction and a desirable confinement of the illumination within the sheet waist along the x-direction. Figure 5.5d can be used to set a lower bound to the amount of power a light-sheet z-profile needs to concentrate within the thickness (in z) of the original Gaussian sheet focus in order to be considered useful for low-bleaching tiling purposes. For example, it can be noticed that, when used on set-up 1 of the SLM-SPIM, some of the considered mask sizes generate light-sheets which concentrate less than 50% of their power at $x = 0$ within the original Gaussian focus (masks wider than $\sim$ 1.4 mm), which I decided to consider as an already quite stretched lower bound. For this reason, even if masks wider than 2 mm would make a more significant impact on the on-axis x-profile of the light-sheet (as shown in Figure 5.5a), I decided not to extend the range of mask sizes considered in these simulations any further than the 0-2 mm range I started with.

Once the range of possibly useful mask widths has been chosen, a second simulation step can be performed: a more quantitative evaluation of the possible advantages that, when used to perform tiling, each of the proposed light-sheet can provide with respect to the use of a normal Gaussian sheet. This analysis can itself be split into two separate steps, starting from the simplified case of only considering what happens when imaging a single $x - y$ plane over and over again, under the usual assumption that the beam profile is constant along y. This simplified situation is simulated and analysed in Section 5.3.3. As a following step, the complete $x - z$ profile of the beam is considered (Section 5.3.4), analysing what happens when using the modified sheets to image a volume of a certain z-thickness.

Before proceeding with these simulations, the next section describes the mathematical model used to simulate the process of photo-bleaching.

5.3.2 Step 2: Simulating photo-bleaching

As mentioned in Chapter 2 (Section 2.2.2), photo-bleaching takes place when a fluorophore loses its fluorescence ability due to damage induced by light. In fluorescence imaging, this loss of fluorescence corresponds to a loss of signal. The simplest model of photo-bleaching can be described as a single exponential decay:

$$I(t) = I_0 \, e^{-\gamma \cdot t} \, , \tag{5.1}$$

where $I(t)$ is the fluorescence intensity of the fluorophore at time t, I_0 is its original fluorescence intensity at time t_0 and γ is the photo-bleaching rate. For the simulations discussed in this chapter, photo-bleaching was modelled as a single exponential decay as follows:
First of all, I considered exposure time to be a constant, and I incorporated it to what I here call "intensity" and indicate with the letter i, which dimensionally therefore corresponds to an intensity (*i.e.* power per unit area) times time. Each point of the sample is assigned a value F_0 which defines its initial capability to fluoresce. When a fluorescent point is exposed to a certain amount of excitation light, expressed in terms of laser intensity i, its capability to fluoresce changes from F_0 to a value $F(i)$

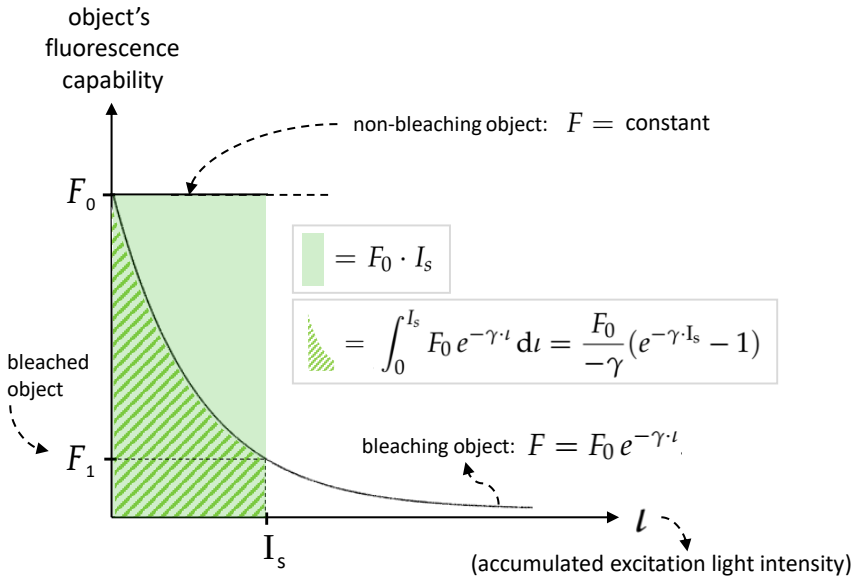

Figure 5.6: *In this chapter's simulations, photo-bleaching is modelled as a single exponential decay. Each point of a simulated sample is assigned a value F_0 which defines its initial capability to fluoresce. Consider a point in the sample which has been given an initial fluorescence capability F_0, and which is excited by a part of the light-sheet characterized by an intensity I_s. The image of this point is modelled as a point of fluorescence intensity equal to $F_0 \cdot I_s$ (uniform green area) in the case of a non-bleaching point, and $\int_0^{I_s} F\, \mathrm{d}i$ (dashed area) with $F = F_0 e^{-\gamma \cdot i}$ in the case of a point bleaching at a rate γ.*

which depends on the photo-bleaching rate γ assigned to that point. In the absence of photo-bleaching, the value F of a fluorescent point does not depend on how much that point gets exposed to excitation light ($F(i) = \text{constant} = F_0$). When excited by a part of the light-sheet characterized by an intensity I_s, a non-bleaching point with fluorescence capability F_0 simply produces a point image of fluorescence intensity $I_{image} = F_0 \cdot I_s$ (see Figure 5.6). Instead, when excited by the same part of the light-sheet, a point in the sample which has been given the same initial fluorescence capability F_0 but which bleaches at a rate γ bleaches to a value

$$F_1 = F_0\, e^{-\gamma \cdot \mathrm{I_s}}\,. \tag{5.2}$$

As depicted in Figure 5.6, such point produces a point image of fluorescence intensity I_{image} which is equal to the integral, from 0 to I_s, of the exponential curve $F(i) = F_0 e^{-\gamma \cdot i}$:

$$I_{image} = \int_0^{I_s} F_0\, e^{-\gamma \cdot i}\, \mathrm{d}i = \frac{F_0}{-\gamma}(e^{-\gamma \cdot \mathrm{I_s}} - 1). \tag{5.3}$$

5.3.3 Step 3: Tiling over a single plane

Before proceeding with the simulations, it is important to specify what is meant by the *advantage* that a modified Gaussian light-sheet might or might not provide when used for tiling, and how exactly I decided to quantify it. In the context of these simulations, an advantageous light-sheet is identified as follows:
The light-sheet in question and a Gaussian light-sheet are used to perform tiling; the percentages of light used and not used for imaging by each of the two sheets are calculated and compared: a light-sheet is considered advantageous for tiling if it gives a higher percentage of light used for imaging than a Gaussian sheet.

In this step of the simulations, I consider the simplified case of imaging a single, ideal, infinitely thin plane, which means that the light-sheets are here analysed only through their one dimensional (along x) on-axis ($z = 0$) intensity profiles. In order to accurately compare the different light-sheets it is useful to introduce an appropriate mathematical framework. Let us start with the coordinate system $x - y - z$ (lower-case letters, see Figure 5.7-left), where x is defined as the direction of propagation of the excitation light, y corresponds to the vertical direction in the light-sheet (the direction along which the excitation beam generating the light-sheet is not focused), and z the direction in which the light-sheet is focused. A second coordinate system $X - Y - Z$ (capital letters, see Figure 5.7-right) can be used to define the FoV in the object plane, which is represented by an infinitely thin plane ($\Delta Z = 0$, $Z = 0$) going from $X = 0$ to $X = FoV_{Xsize}$ ad from $Y = 0$ to $Y = FoV_{Ysize}$, where FoV_{Xsize} and FoV_{Ysize} are, respectively, the width and the height of the FoV in microns in the object plane. A third coordinate system $X_c - Y_c - Z_c$ can be used to define the FoV on the camera; this is oriented as the $X - Y - Z$ system with the only difference being that the size of the FoV scales according to the magnification which relates the object plane to the image plane.

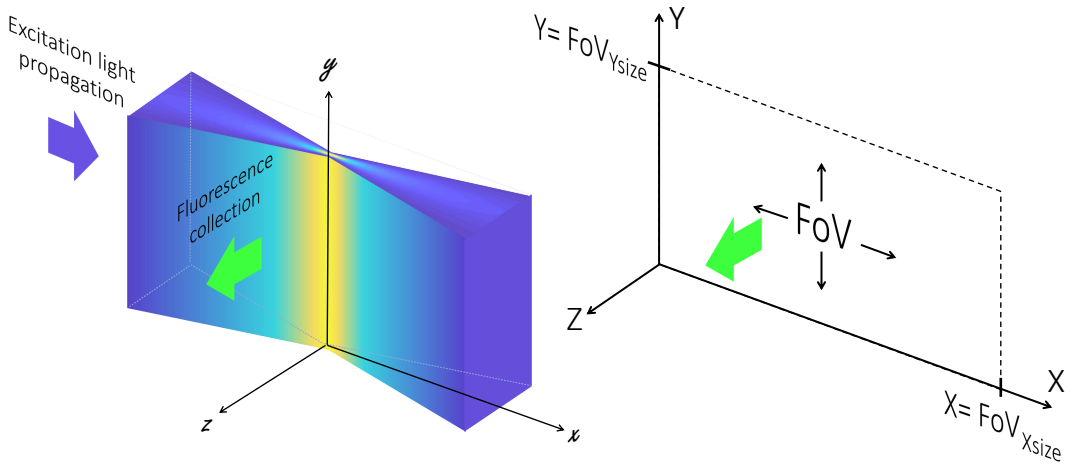

Figure 5.7: *Coordinate systems to define the light-sheet (left) and the FoV (right). Left: the light-sheet can be defined in a coordinate system $x - y - z$ (lower-case letters), where x is the direction of propagation of the sheet, y is the direction along which the light-sheet is not focused, and z the one in which it is focused. Right: a coordinate system $X - Y - Z$ (capital letters) can be used to define the FoV in the object plane, with X being the lateral direction in the FoV, Y the vertical one and Z the direction parallel to the optical axis of the microscope's imaging arm. The FoV is represented as an infinitely thin plane ($\Delta Z = 0$) at $Z = 0$ which goes, laterally, from $X = 0$ to $X = FoV_{Xsize}$, and vertically from $Y = 0$ to $Y = FoV_{Ysize}$.*

Let us now consider the case of imaging a single, infinitely thin plane performing tiling. Let $F(x)$ be the function describing the x-intensity profile of the light-sheet for $y =$ constant and $z = 0$, with the light-sheet's peak (the sheet's focus) at $x = 0$. For simplicity, let us assume that $F(x)$ does not depend on the value of y. When performing tiling using a rolling shutter on the camera, the sheet is smoothly scanned laterally across the FoV (along X) in the object plane, while at the same time a shutter aligned with the sheet waist is scanned across the FoV on the camera (along X_c). Let $\Delta x = 2a$ be the size in microns of the region of the light-sheet which is used for imaging, *i.e.* correspondent to a ΔX_c on the camera equal to the width of rolling shutter (Figure 5.8-left). Typically, the width of the rolling shutter is chosen to match the lateral extent of the sheet's waist, so that $2a = R_L$.

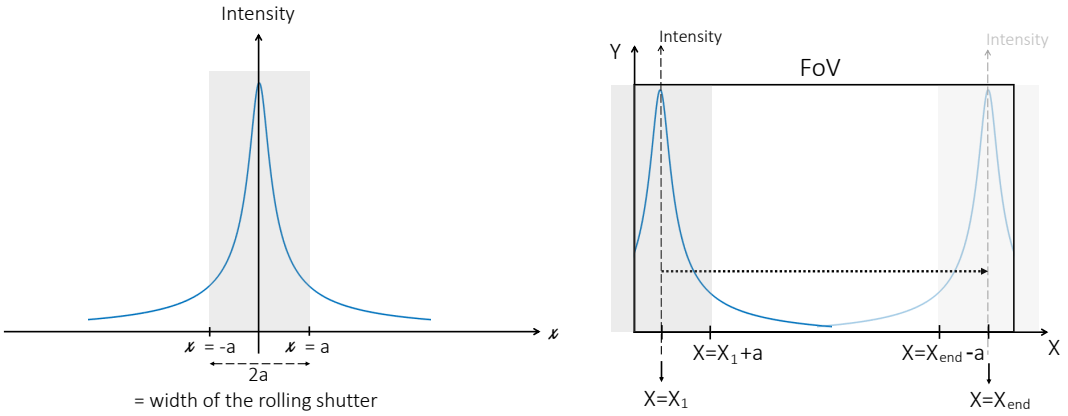

Figure 5.8: *Tiling a light-sheet over a single plane using a rolling shutter. Left: x-profile of the light-sheet for $z = 0$, with the sheet's focus at $x = 0$. As the light-sheet moves across the FoV, the rolling shutter moves across the detector, with its center always aligned with the sheet's focus ($x = 0$). The width of the rolling shutter on the camera can be mapped onto the $x - y - z$ coordinate system (gray band around $x = 0$ in the figure), where its width can be called $2a$. Right: To generate an image, the light-sheet is swept across the FoV, with its focus moving from a position $X = X_1$ to $X = X_{end}$. After a complete scan, all points in the FoV within $X = X_1 + a$ and $X_{end} - a$ have been exposed to the same amount of light coming from the area of the light-sheet aligned with the rolling shutter (from $x = -a$ to $x = a$).*

In the rolling shutter version of the tiling technique, the light-sheet is scanned across the FoV starting with the light-sheet focused at a certain lateral position in the FoV, X_1, and finishing at a position X_{end} towards the other end of the FoV (Figure 5.8-right). For a complete scan of the sheet from X_1 to X_{end} one can calculate: how much light each part of the FoV is illuminated with, how much of this light excites fluorescence that is used for imaging (*i.e.* is captured by the rolling shutter) and how much light excites fluorescence which is not used for imaging.

In this analysis, I make the following assumptions:

- the light-sheet is uniform along y;
- I simulate the FoV on the camera ($X_c - Y_c$) and the FoV on the sample ($X - Y$) using the same number of points but a different spatial resolution, which scales accordingly to the imaging system's magnification; I consider that fluorescence excited at a point X_p in the object plane does not undergo any scattering but simply gets collected at the geometrically corresponding point $X_{p,c}$ on the detector;
- as explained in step 2 of this simulations section, in the absence of photo-bleaching I consider fluorescence as being a linear process, *i.e.* the amount of fluorescence excited at a certain point in the FoV is directly proportional to the excitation illumination accumulated on that point. Instead, for photo-bleaching samples, I model photo-bleaching as a single exponential decay and assume that the rate of photo-bleaching γ is a constant that only depends on the sample.

For points of the FoV in the object plane ($X - Y$ reference system) which are within $X_1 + a$ and $X_{end} - a$ (Figure 5.8-left) the total amount of light used for imaging U (denoting *used* light) is a constant value that only depends on the light-sheet's profile $F(x)$ and on the half-size a of the rolling shutter used, and it can be calculated

as

$$U = \int_{-a}^{a} F(x)\mathrm{d}x\,. \tag{5.4}$$

Instead, the total amount of light not used for imaging W (denoting *wasted* light) also depends on the position of the point in the FoV (X_p) and on the start and end positions of the sheet's peak during its lateral scan (X_1 an X_{end}):

$$W = \int_{-(X_{end}-X_p)}^{-a} F(x)\mathrm{d}x + \int_{a}^{X_p-X_1} F(x)\mathrm{d}x\,. \tag{5.5}$$

As regards the lateral extent of the sheet's scan across the FoV, a reasonable thing to do is to start the scan with the light-sheet focused towards one side of the FoV, for example the left side, with its peak just far enough from the left edge to make the whole sheet waist be within the FoV from the very beginning of the scan: $X_1 = a$. In the same way, the scan ends when the sheet's focus is at a distance equal to a from the opposite side of the image: $X_{end} = FoV_{Xsize} - a$. To illuminate the FoV more uniformly one could decide to scan the sheet from $X_1 = -a$ to $X_{end} = FoV_{Xsize} + a$. This way the amount of excitation light used for imaging would be the same for all points in the FoV, *i.e.* Equation 5.4 would be valid for all points between $X = X_1 + a = 0$ and $X = X_{end} - a = FoV_{Xsize}$. One drawback of widening the scan range is the increased amount of light which illuminates the sample without being used for imaging. In fact, as from Equation 5.5, the amount of *wasted* light which excites point X_p in the FoV increases with the distance of X_p from both X_1 and X_{end}, which means that it is maximum for points at the center of the FoV and it increases as the scan widens.

As a first simulated experiment I decided to generate a Gaussian light-sheet using set-up 1 of the SLM-SPIM and scan it across the FoV ($FoV_{Xsize} = 440$ μm) using a rolling shutter size similar to the Rayleigh length of the sheet ($2a = 56$ μm). On the sensor, this would correspond to a rolling shutter width of $2a_{camera} = 2a \times M = 2a \times 20 = 1120$ μm, equal to $\sim$247 pixels, considering our camera pixel size of 4.54 μm. I set the scan to go from $X_1 = a(= 28\ \mu m)$ to $X_{end} = FoV_{Xsize} - a = 440 - 28 = 412$ $\mu m)$, with steps of 2 μm (equal to one data point, being 2 μm the x-resolution chosen for the simulations). I repeated the same simulation using a light-sheet generated by masking the 800 central microns of the illumination beam using the SLM, with the same values for a, X_1, and X_{end}. Figure 5.9 shows the simulated light-sheets and the distribution of excitation light resulting from their scan across the FoV, highlighting the amount of illumination generating excitation which does and does not end up on the final, tiled images (respectively U, blue curves, and W, magenta curves). Using what happens to a point at the center of the FoV as a reference (normalized intensity values highlighted in magenta and blue in Figure 5.9b), these simulations show that the total amount of light intensity which excites fluorescence that does not contribute to the final image (*wasted* illumination) is higher than the amount of light which excites fluorescence actually *used* for imaging, but the difference between the two decreases when using the modified light-sheet.

To better quantify the advantage which could be given by the modified light-sheets, I calculated how much the wasted excitation light is compared to the total light that the FoV is exposed to (Figure 5.10). The percentage of wasted excitation light plotted in Figure 5.10a was calculated by integrating the blue curve of Figure 5.9b to find the total amount of wasted excitation light accumulated in the whole FoV, dividing

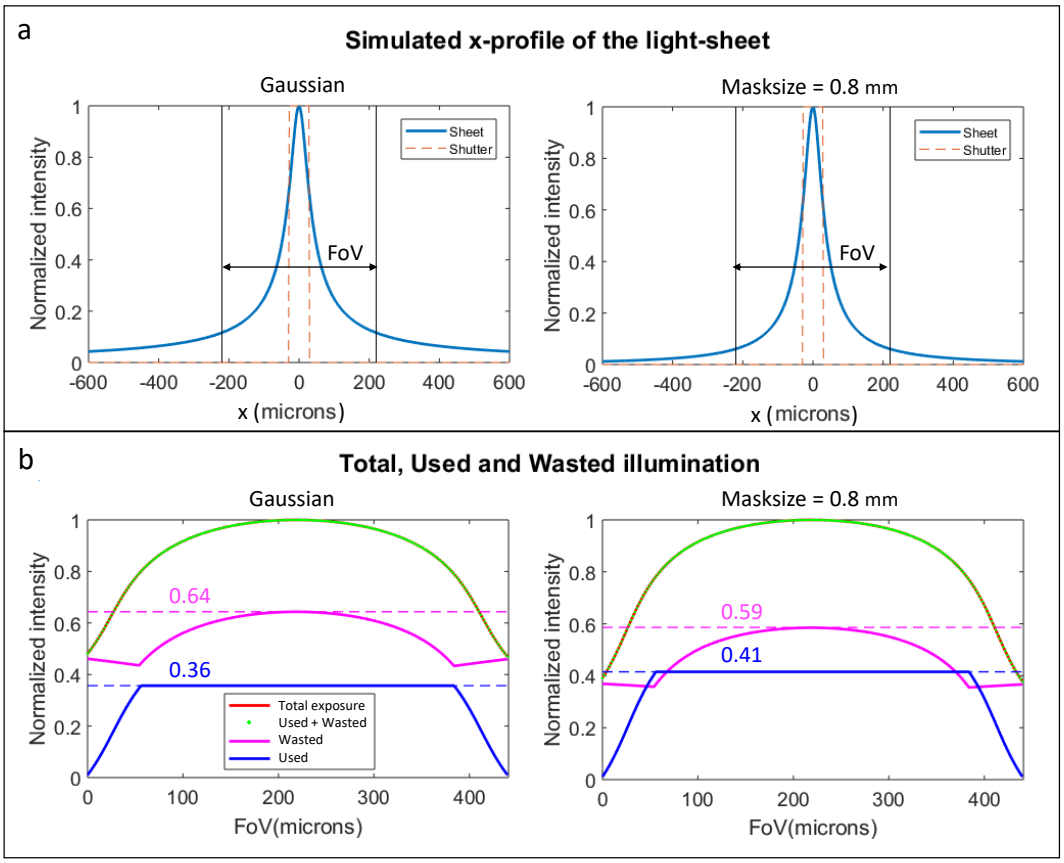

Figure 5.9: *Simulating tiling over a single plane using a rolling shutter. (a) x-profile of a Gaussian light-sheet (left) and a modified sheet (right) generated masking the central 800 µm of the Gaussian beam hitting the SLM. The simulated profiles extend over 1200 µm, and each of them was scanned over a 440 µm FoV (size indicated with two black lines in the plots, for reference). The size of the rolling shutter, in the object plane, was set to be* $2a = 56$ *µm (dashed red lines). (b) Excitation light intensity accumulated over the FoV within a complete tiling scan, using the Gaussian sheet (left) and the modified sheet (right). For each lateral position in the FoV (horizontal axis), these plots show: 1 (blue curve) - the sum of all the accumulated excitation light intensity generating fluorescence which is used for imaging, i.e. which is captured by the rolling shutter; 2 (magenta curve) - the accumulated excitation light intensity generating fluorescence which is not used for imaging; 3 (red curve) - the total amount of excitation light that position is exposed to. The green dotted curve is the sum of the blue and magenta curves, calculated only to verify that the sum of the used and wasted light equals the total light exposure (the green dots in fact cover the red curve). Within each plot, the three curves are normalized using the value correspondent to the total amount of excitation light intensity seen by the central point of the FoV. The values of used and wasted excitation light relative to that point are highlighted respectively with a blue and a magenta horizontal dashed line, and the corresponding normalized intensity value is highlighted with the same colors.*

this value by the integral of the red curve of Figure 5.9b (total exposure), and multiplying by 100. I did this same calculation for different shutter sizes (from 6 μm to 102 μm in the object plane) and different light-sheets (mask sizes going from 0 mm, for Gaussian light-sheet, to 2 mm). As expected, the percentage of wasted excitation light decreases as the shutter size increases, and to highlight the advantage given by the different mask sizes the curves of Figure 5.10a are plotted in Figure 5.10b after normalization to the curve relative to the Gaussian light-sheet.

There are a few things which should be considered while discussing the data shown

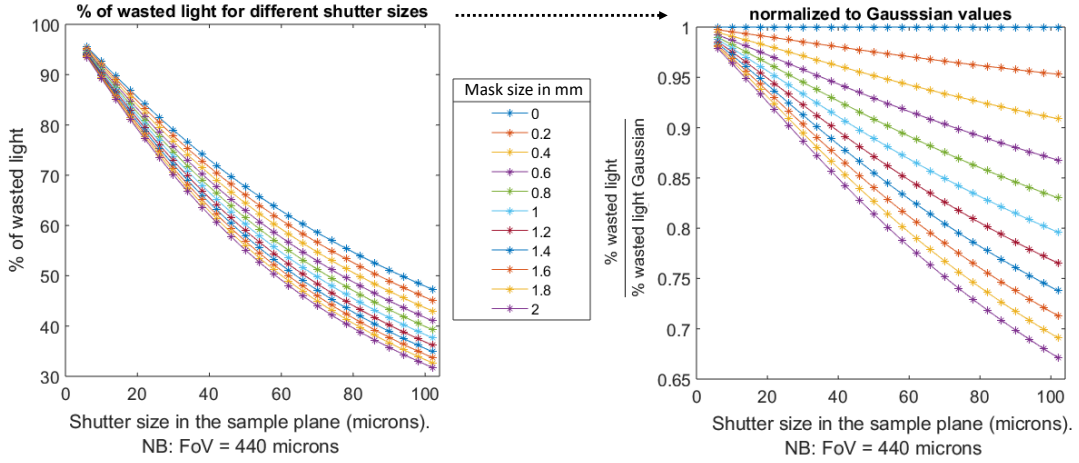

Figure 5.10: *Left: Percentage of excitation light accumulated on the whole FoV and then not used for imaging (wasted) with respect to the total excitation light delivered to the FoV, calculated for different shutter sizes (from 6 µm to 102 µm in the object plane) and different light-sheets, with mask sizes going from 0 mm (Gaussian light-sheet) to 2 mm. Right: Same values as in the left plot, but here normalized to values relative to the Gaussian light-sheet (0 mm mask curve).*

in Figure 5.10. First of all, while using a bigger shutter size reduces the amount of wasted excitation light, *i.e.* the amount of excitation light producing fluorescence which does not get to the sensor pixels activated within the shutter, it also decreases the optical sectioning capability of the tiling technique. A tiled image generated by a narrow shutter is in fact characterized by good, uniform optical sectioning across the whole FoV, but it is made of a small percentage of all the fluorescence which is excited by the light-sheet, since only the the fluorescence excited by a narrow part of the sheet's waist ultimately makes it through the narrow shutter. Instead, a wider shutter lets more of the excited fluorescence get to the sensor, but this extra fluorescence is excited by thicker parts of the sheet and thereby diminishes the optical sectioning of the final image. Overall, the choice of what size of shutter to use with respect to the x-extent of the sheet waist might depend on different factors, such as the amount of scattering observed in the sample (with narrower shutters decreasing the amount of scattering which ends up on the final image) and the sample's sensitivity to light (with samples which bleach easily the general idea is to try and make the most out of the excitation light which illuminates the sample, preferring in this case the use of wider shutters).

One other thing to keep in mind when looking at Figure 5.10b is that it analyses the ideal case of imaging and infinitely thin sample ($\Delta Z = 0$), and therefore considers only the on-axis ($z = 0$) x-profiles of the different light-sheets. In a real application though, an image of a single plane is formed by fluorescence coming from a section of the sample which has a certain thickness, which depends on the shape of the light-sheet but also on the optical specifications of the imaging arm of the microscope. What this means is that the analysis made so far does not take into account the three-dimensional shape of the different sheets, how it might influence the image quality and also a more accurate calculation of the actual amount of *used* and *wasted* excitation light. To try and get a more realistic picture of the situation, the next section discusses the case of simulating imaging a sample with $\Delta Z \neq 0$ and considering the $x - z$ shape of the light-sheets.

5.3.4 Step 4: Tiling over a three-dimensional sample

To deepen the analysis of the theoretical performances of the proposed light-sheets, we now need to consider their complete $x-z$ profile and what happens when they are used to image a sample with a Z-extent that goes beyond that of an infinitely thin plane. In this section, I keep making the assumption that the profile of a three-dimensional light-sheet does not vary significantly along y within distances comparable to the height of FoV of the imaging system, and I analyse a complete 3D imaging procedure using an $x-z$ (and $X-Z$ [2]) simulation. The aim of this final step of the simulations is the following: check if any of the candidate modified Gaussian light-sheets could be used to perform a tiling+Z scan of a 3D sample producing less photo-bleaching compared to what a Gaussian light-sheet would do, for a comparable amount of excited fluorescence ending up in the final tiled images. In order to make this comparison, I decided to use the following procedure:

- consider the $x-z$ profile of a Gaussian light-sheet and a fluorescence sample of a certain size in X and Z which bleaches at a certain photo-bleaching rate γ;
- move the light-sheet across the sample simulating a tiling scan (scan along X) plus a 3D scan (scan along Z) of the sample, considering that the sample bleaches as the light-sheet is scanned through it;
- repeat the tiling+Z scan on a new (i.e non-bleached) identical sample for each of the proposed modified Gaussian light-sheets, rescaling their intensity profile to make sure that the total amount of excitation light producing fluorescence which ends up in the final images is the same for all the light-sheets;
- use the total amount of bleaching experienced by the sample as a tool to compare the performances of the different light-sheets.

As one might have noticed, in the above description of the simulation procedure there is no actual imaging involved. I will explained in the following paragraphs how, with certain assumptions on the bleaching process and a proper rescaling of the light-sheet profiles, a useful comparison between the sheets' performances can be made without simulating the generation of any image.

The first element needed to perform these $x-z$ simulations is a simulated $x-z$ profile for each light-sheet. These profiles where obtained using the same code used in the previous sections, and Figure 5.11 shows, as an example, two of the obtained $x-z$ profiles, one for a Gaussian light-sheet and one for a sheet generated by masking the central 800 μm of the Gaussian beam illuminating the SLM. For this figure and also for the following ones of this section, I decided to only show results relative to the 800 μm-mask modified light-sheet, which is the one that I used for the actual experiments on the SLM-SPIM (reasons behind this choice explained in Section 5.4).

As expressed in the last point of the above list, the quantity I ultimately want to measure with these simulations is, for each different light-sheet, the total amount of

[2] Reminder: I introduced the two coordinate systems $x-z$ and $X-Z$ to explain how I modelled the tiling procedure in my simulations, where I needed to distinguish between the shape of a light-sheet (defined within the system $x-z$) and how the light-sheet moves across the FoV (defined within the system $X-Z$). Even though, when discussing tiling, the two systems are oriented in the same directions and both refer to sizes in microns in the object plane, I here keep using the coordinates $x-z$ when describing the shape of a light-sheet, and $X-Z$ to refer to the sample and the FoV in the object plane.

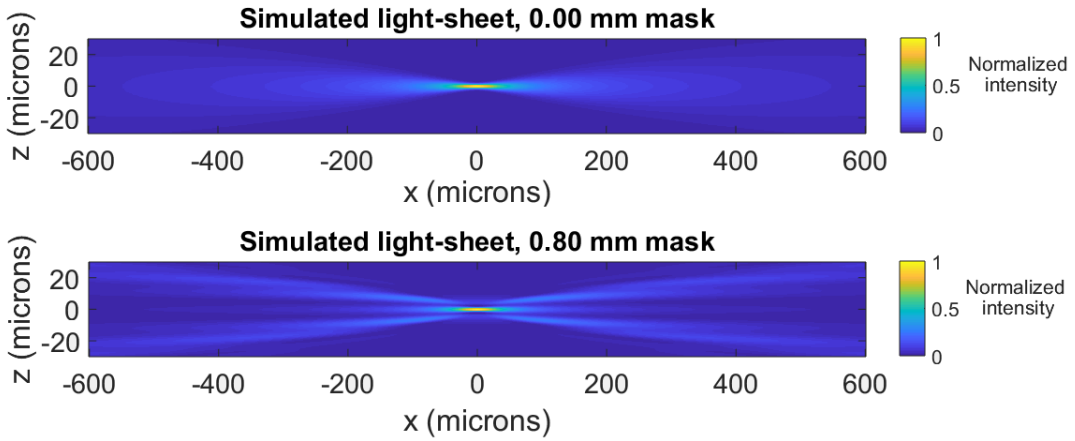

Figure 5.11: *Simulated $x-z$ intensity profile of a Gaussian light-sheet (top) and of a sheet generated by masking the central 800 μm of the Gaussian beam illuminating the SLM (bottom). The light-sheets are displayed using a logarithmic scale and each one is normalized to its own maximum. The simulated fields cover 1200 μm along x and 40 μm along z, with an x-resolution $dx = 2$ μm and a z-resolution $dz = 0.125$ μm.*

bleaching experienced by the sample after a complete tiling+Z imaging scan. When modelling photo-bleaching as explained in Section 5.3.2, the total amount of photo-bleaching experienced by a point in the sample only depends on how much excitation light that point is exposed to (expressed as the sum of all the excitation intensity the point is illuminated with) and on the sample's bleaching rate γ. To make my analysis independent of the sample's bleaching rate γ I decided to simply use the total exposure to excitation light as a measure of the resultant total photo-bleaching. When tiling a light-sheet over a certain volume, the total excitation light that each point in the sample is exposed to depends on many factors, such as the position of the point within the sample, the size of the FoV and the thickness of the sample with respect to the light-sheet, the extent of the sheet scan across the FoV, the X- and Z-steps used for the scan and the amount of time the light-sheet is kept in each position. As mentioned before, exposure time is not considered in this analysis, and I assume that the total amount of excitation light *seen* by a certain point in the sample simply depends on what parts of the light-sheet have illuminated it and how many times, but not for how long. As regards the dependence of the accumulated excitation light exposure on all the other parameters, I decided to try and analyse the situation in a way that would give and indication, more than an accurate estimate, of what kind of advantage the use of a modified light-sheet could give with respect to a Gaussian light-sheet, while also showing how the situation changes depending on the different factors. Figure 5.12 shows and example of the kind of map I obtained at the end of my analysis, in this case comparing the use of a Gaussian light-sheet with the use of a modified light-sheet generated with a 800 μm mask on the SLM. This map is meant to show if/how much/in what situation the considered modified light-sheet is expected to give an advantage over the use of a Gaussian light-sheet in terms of performing tiling giving a reduced sample exposure to excitation light (*i.e.* a reduced photo-bleaching) for the same amount of excited fluorescence used for imaging. In the following paragraphs I explain in details how this kind of map was generated and how to interpret it.

First of all, I decided to simulate the case of imaging samples of different sizes in Z, over FoV of different sizes in X. In terms of the lateral extent of the sheet scan, I only

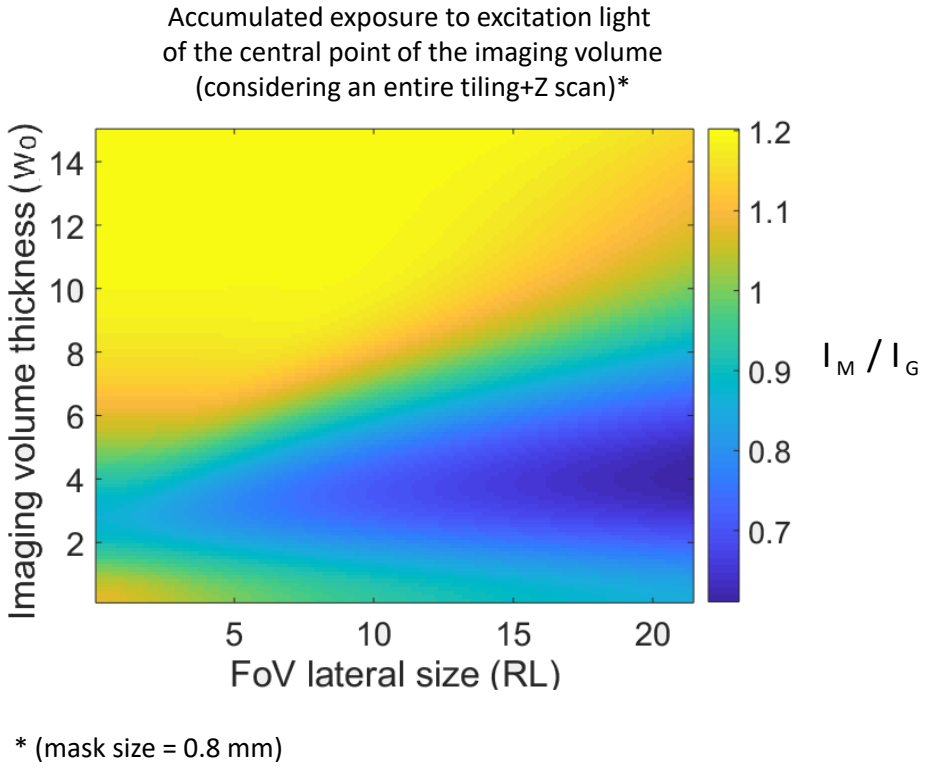

Figure 5.12: *Map of the possible advantages given by the use of a modified light-sheet for 3D imaging with tiling, expressed in terms of reduction of total excitation light exposure when compared to using a Gaussian light-sheet which excites the same amount of total fluorescence used for imaging. This map shows the results for a modified light-sheet obtained using a 800µm mask on the SLM. The map was generated considering the procedure of imaging a 3D sample tiling the light-sheet across the whole FoV (see main text for more details). For different values of imaging volume thickness and FoV lateral size (expressed in units of the original Gaussian sheet's Rayleigh length R_L and thickness W_0), the map shows the total amount of excitation light seen by the central point of the imaging volume when using a modified light-sheet (I_M), divided by the amount of excitation light seen by the same point when using a normal Gaussian light-sheet (I_G). Values < 1 in the map indicate that, for that FoV and sample thickness, using a modified light-sheet gives a reduction in the percentage of excitation light not used for imaging. The $x - z$ intensity profiles of the Gaussian and the modified light-sheet were in fact scaled in order to produce the same amount of fluorescence used for imaging (more details in the main text and in Figure 5.14. Because of this rescaling, the accumulated excitation light intensity values used for this map can be considered as a measure of the advantage given by the use of the modified light-sheet with respect to the use of a normal Gaussian light-sheet, considering as advantage the capability to excite (and therefore bleach) less the sample (i.e. lower values in the map indicating more advantage) while exciting the same amount of fluorescence which is used in the final 3D image.*

considered the general and somewhat realistic case of always tiling the light-sheet moving its focus from $X_1 = 0$ to $X_{end} = FoV_{Xszie}$. As regards the fluorescent bleaching sample, I simulated imaging a uniform fluorescent sample which extends in X and Z and bleaches at a certain rate γ as described in Section 5.3.2. For simplicity, I decided to only monitor what happens to the central point of the 3D imaged volume (central along X and along Z) during a complete $X - Z$ scan of the light-sheet. As for the X- and Z- scanning steps, I used steps of 1 data point in both directions (where with *data point* I refer to the resolution used for the simulation of the $x - z$ light-sheet profiles, so that $\mathrm{d}X = \mathrm{d}x = 2$ μm and $\mathrm{d}Z = \mathrm{d}z = 0.125$ μm). While choosing an X-step of 1 data point makes sense if one wants to simulate the case of performing

tiling using the the rolling shutter technique, using a 1 data point Z-step does not really replicate a real situation. In practice in fact, a Z-scan is performed by moving the light-sheet in Z by a certain amount between one plane and the next, and this amount depends on the Z-resolution of the imaging system, on the sheet's thickness and on the kind of details of the sample one wants to capture. I therefore decided not choose the value of dZ to accurately simulate a specific situation, but instead to chose a value that would make the analysis simpler and, even if less realistic, more general.

Figure 5.12 shows the results of a comparison between the use of a Gaussian light-sheet and a light-sheet generated with a 800 μm mask on the SLM. The intensity of the Gaussian and modified light-sheets used were scaled in order to produce the same amount of excitation light which is used for imaging (more details below). As mentioned before, such rescaling makes it possible to simply use the total amount of delivered excitation to compare the performances of the two light-sheets, without having to separately calculate the amount of used and wasted excitation light. For each FoV size and imaging volume thickness, the map in Figure 5.12 shows the accumulated amount of excitation exposure (expressed as an excitation intensity I_M) experienced by the central point of the 3D imaged volume ($X = 0.5 \cdot FoV_{Xsize}$, $Z = 0.5 \cdot \Delta Z$) after a complete tiling+Z scan of the modified light-sheet, divided by the amount of excitation exposure experienced by the same point when using a Gaussian light-sheet to perform the same tiling+Z scan (I_G). The size of the FoV and the thickness of the imaged volume are expressed in units of the Gaussian sheet's Rayleigh length R_L and thickness W_0, to make the analysis scalable with the shape of the initial Gaussian light-sheet.

The map in Figure 5.12 suggests first of all that, for a certain thickness of the imaged volume, the advantages given by the use of a modified light-sheet increase for wider tiling scans (*i.e.* wider imaged FoV). This can be explained going back to the shape of the x-profiles of the light-sheet (see for example those Figure 5.1). The modified light-sheets where designed to have a peak intensity at $z = 0$ which decreases faster with $|x|$ (*i.e.* going away from the light-sheet focus along the direction of propagation) with respect to a Gaussian light-sheet, and increasing the FoV over which the light-sheet is laterally tiled increases the impact that this difference makes on the final amount of excitation light not used for imaging. To image a very narrow FoV, almost only the central (along x) part of the light-sheet is needed, and using a Gaussian or a modified light-sheet does not make much difference. Considering the other extreme situation of imaging a very wide FoV, the lateral (along x) parts of the light-sheet make in that case a big contribution to the total excitation of the sample, and the fact that their intensity relative to the intensity of the sheet waist is smaller for the modified light-sheets than for a Gaussian light-sheet makes them excite much less fluorescence which is not used in the final image.

A second interesting thing to discuss using the map in Figure 5.12 is how, given a certain FoV size, the advantage of using a modified light-sheet changes depending on the thickness of the imaged sample. One can see that going from a volume thickness of 0 (ideal infinitely thin plane) to thicker volumes the values in the map first decrease, reach a lowest point around 3-4 W_0, and then increase again for thicker volumes. This suggests that, if one can hope to achieve a certain advantage from using a modified sheet to image a single plane, this advantage should be even more when imaging thicker samples, but only up to a certain thickness, beyond which the

possible advantage starts decreasing and at some point even turns into a disadvantage (values > 1 in the map). This trend can be understood looking again at the $x - z$ intensity profiles of the light-sheets (see Figure 5.13, a zoomed version of the $x - z$ profiles of Figure 5.11). By blocking the central part of the beam we are able to generate a light-sheet with a sheet waist (highlighted in red in Figure 5.13) similar to that of a Gaussian light-sheet, but whose intensity decreases faster going away from the sheet's focus (along the direction of propagation of the sheet, see red arrows in Figure 5.13). Nevertheless, all the light that contributes to the sheet waist must come from somewhere, and in the case of our modified Gaussian light-sheets a big contribution to that is given by the side-lobes (orange brackets in Figure 5.13). When one of these modified Gaussian light-sheets is used to perform a tiling+Z imaging of a sample, it only really gives an advantage over the use of a *normal* Gaussian light-sheet as long as the side lobes do not contribute much to the imaging procedure, which can only hold for samples within a certain thickness (see green bracket in Figure 5.13).

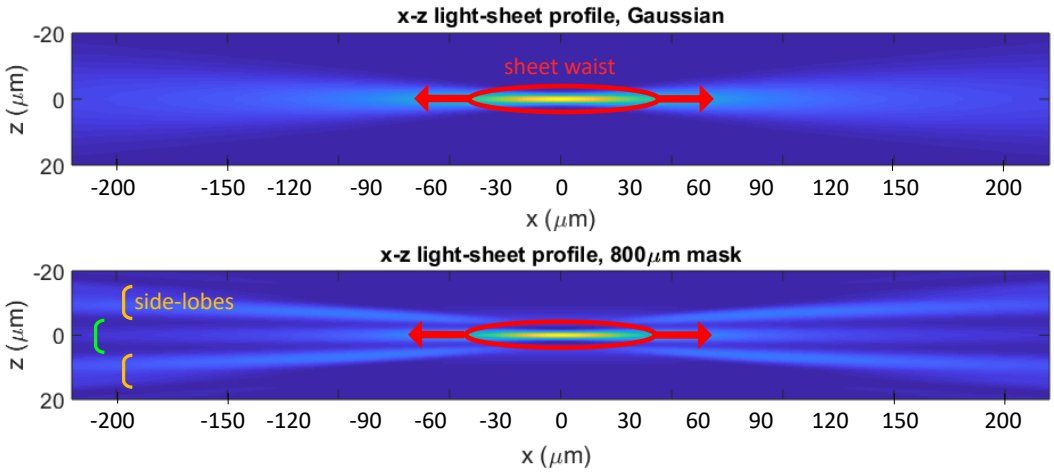

Figure 5.13: *Zoom-in on the central x values of the simulated $x - z$ intensity profiles of Figure 5.11. The modified light-sheet is characterized by a sheet-waist (circled in red) whose intensity decreases more rapidly than for a Gaussian light-sheet when going away from the sheet focus (red arrows). This kind of profile is generated by masking the central part of the incoming beam (green bracket). Because of this, in the modified light-sheet, a bigger percentage of the light contributing to the sheet waist comes from the side lobes (orange brackets), while in the Gaussian light-sheet every x profile (intensity profile, along z, for a certain value of x) has a single intensity peak at $z = 0$.*

One last thing left to explain in more detail about the simulations described in this section is the normalization procedure adopted to rescale the $x - z$ profiles of the modified light-sheets. The aim of this normalization is to assure that all the light-sheet would produce the same amount of excited fluorescence ending up in the final image. In order to do this, I considered that the fluorescence used for imaging is the one excited by the region of the light-sheet contained within the shutter size (along x) and the DoF of the imaging system (along z). For the simulations discussed in these sections (run for set-up 1 of the SLM-SPIM) I used a shutter size of 56 μm and a DoF of 1.75 μm, and normalized the $x - z$ profile of all the light-sheets (Gaussian light-sheet included) making the sum of all their intensity contained within these positions (see black squares in Figure 5.14) be equal to 100 (arbitrary units).

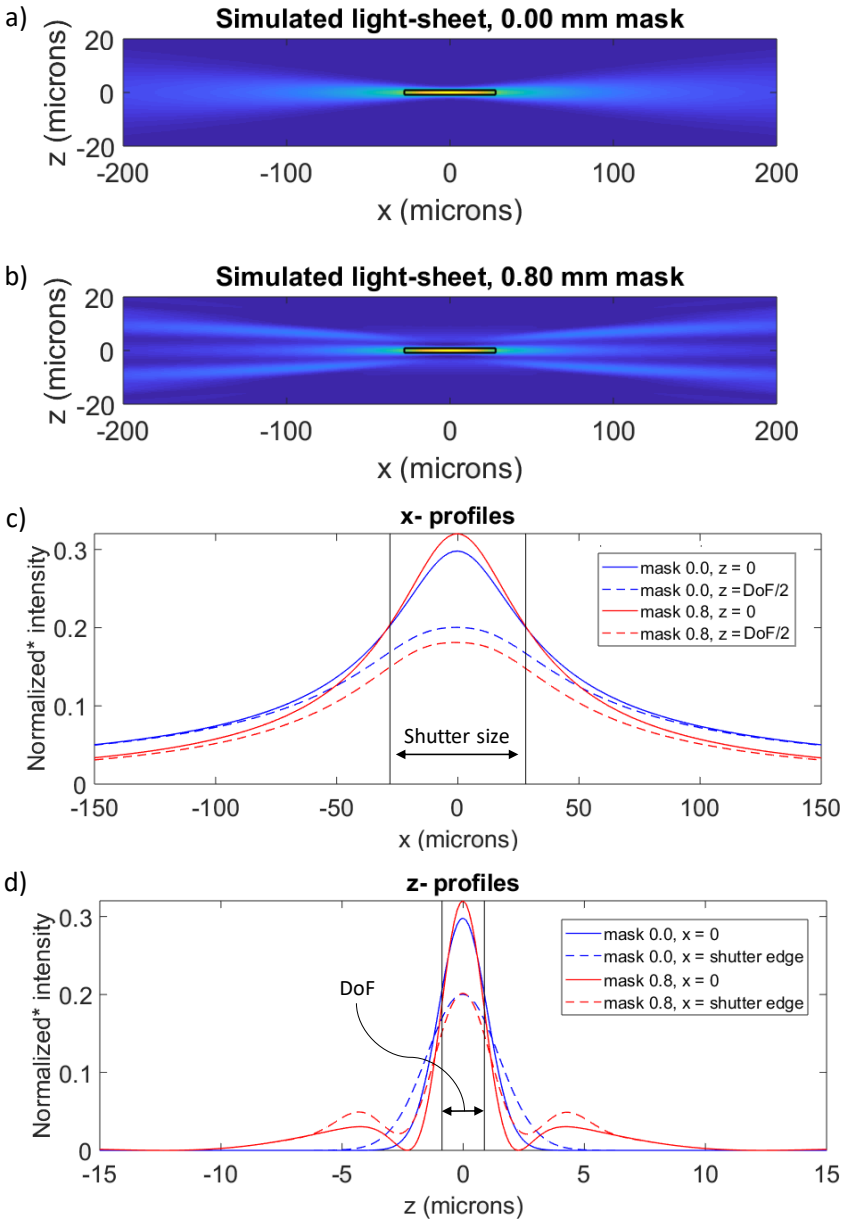

Figure 5.14: *Normalization of the $x-z$ intensity profiles used in the tiling+Z imaging simulations. (a,b) Simulated $x-z$ profiles of a Gaussian light-sheet (a) and a 800 µm-mask light-sheet (b), with a black square around the region used to normalize their intensity. The size of this region equals the chosen shutter size (56 µm for set-up 1) along x and the imaging system's DoF (1.75 µm) along z. (c,d) $x-$ and $z-$ intensity profiles of the two normalized simulated light-sheets shown in (a) and (b) for values of z equal to $\pm DoF/2$ (c) and x equal to $\pm ShutterSize/2$ (d) (i.e. equal to the limits of the region used for the normalization, highlighted with a black square in (a) and (b)). The normalization of the two $x-z$ intensity profiles in (a) and (b) was done by making the sum of all the intensity contained within $dx = DoF$ and $dz = ShutterSize$ equal the arbitrary value of 100.*

5.4 Experiments

5.4.1 Light-sheet characterization

Before performing the actual tiling experiments, I analysed the shape of the modified light-sheets generated using the SLM-SPIM (SLM phase-mask used described in Figure 5.15), and compared it with what the shape predicted by the simulations.

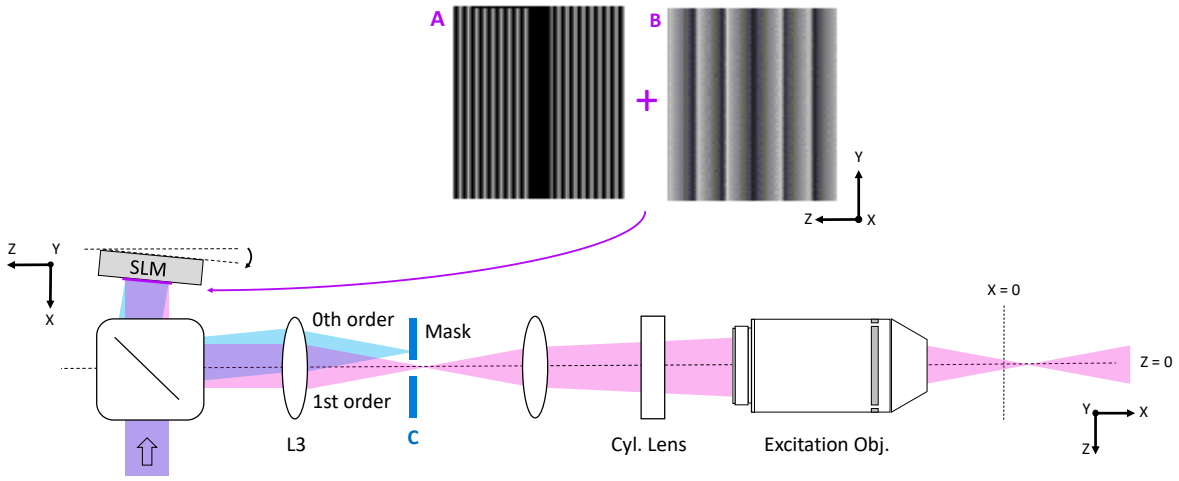

Figure 5.15: *Example of a phase-masks applied to the SLM of the SLM-SPIM to generate one of the modified Gaussian light-sheets and to use if for tiling experiments. These light-sheets can be created by masking the central part of the illumination beam. The phase-mask used to block the central part of the beam (A component of the SLM pattern in the Figure) works as follows: it concentrates the majority of the light hitting the SLM to a 1^{st} diffraction order, while leaving the central part of the beam reflect together with the 0^{th} diffraction order. The SLM is then physically rotated around its vertical axis (Y-axis) to let the 1^{st} diffraction order (pink rays in the Figure) be aligned with the optical axis of the illumination arm ($Z = 0$), and to make the 0^{th} order (light blue rays in the Figure) focus to a side ($Z \neq 0$). A physical mask (C) placed in the focal plane behind L3 is used to block the 0^{th} diffraction order (together with the light coming from the central part of the beam, and all the higher diffraction orders) and only let the 1^{st} order through. To use this light-sheet to perform tiling, the light-sheet can be focused at different lateral positions in the sample plane ($X \neq 0$) by adding a second pattern to the SLM (B component in the Figure), consisting of a quadratic phase function (defocus) along the horizontal axis.*

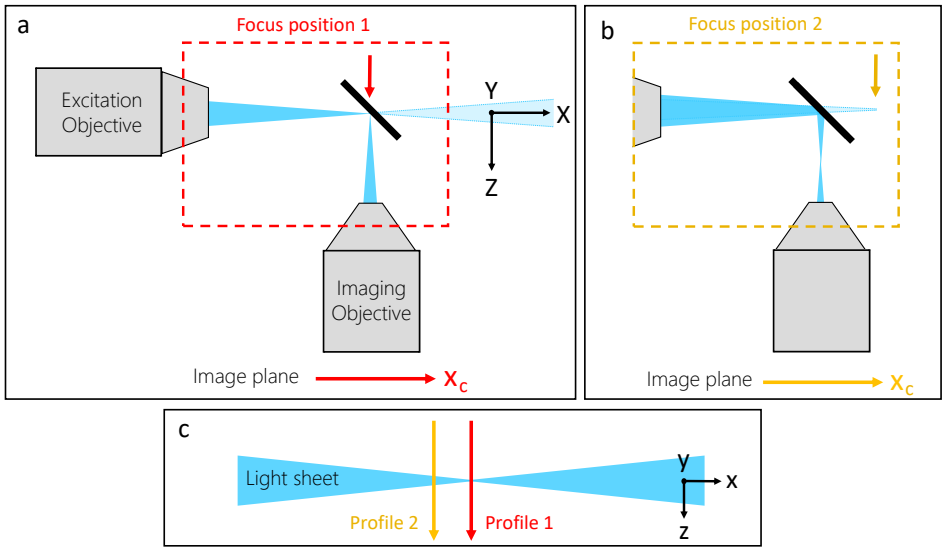

Figure 5.16: *Light-sheet profiling using a mirror. (a) The light-sheet is focused onto a mirror aligned at 45° to both excitation and imaging objectives. If placed at the correct distance from the mirror, the imaging objective focuses on the camera the $y - z$ profile of the light-sheet focus (with the z-axis of the sheet along the horizontal axis of the camera, X_c, and its y-axis along the camera vertical axis Y_c). (b) Using the SLM, the light-sheet can be focused to different positions along its axis of propagation, so that $y - z$ profiles corresponding to different values of x can be seen on the camera (c).*

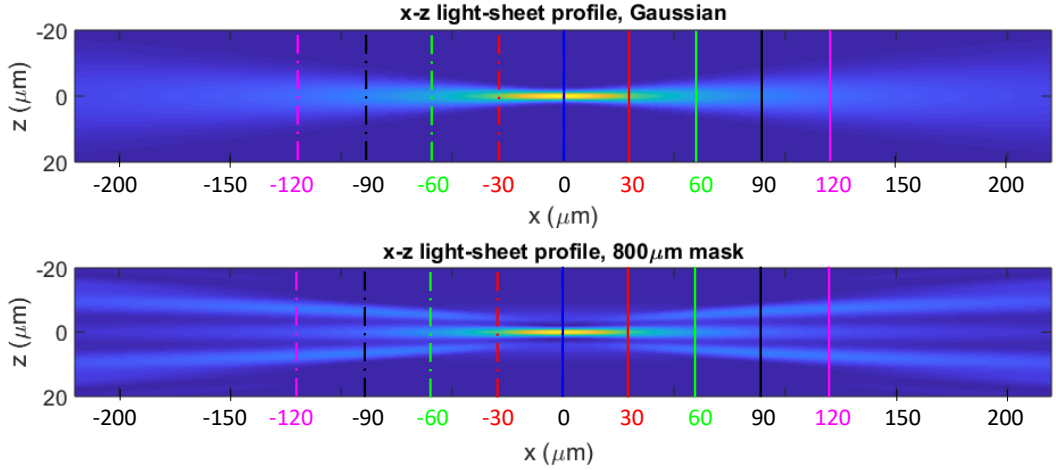

Figure 5.17: *Simulated $x-z$ intensity profile of a Gaussian light-sheet (top) and a light-sheet generated with a 800 μm mask on the SLM (bottom). The lateral extent of these light-sheets represents the width of the FoV of the SLM-SPIM, 440 μm. Using the 45° set-up of Figure 5.16, different $x-z$ profiles for each of the two light-sheets were imaged, for 9 different values of x, ranging from -120 μm to 120 μm (highlighted with different colors in the figure). The z-profiles relative to these x-values are plotted in Figures 5.18 and 5.19, each one together with its simulated counterpart.*

In order to profile the light-sheet along z, I mounted a mirror in the sample chamber, between the launching and imaging objectives, and aligned it to be at 45° to both objectives, as depicted in Figure 5.16. Removing the GFP filter from the imaging arm of the microscope, this set-up can be used to directly image a magnified $y-z$ section of the light-sheet on the detector. The SLM can be used to focus the light-sheet at different positions along its axis of propagation (such as focus positions 1 and 2 in Figure 5.16a and 5.16b), thereby focusing different $y-z$ sections of the light-sheet on the detector (Figure 5.16c). Using this method, I imaged the $y-z$ profile of a Gaussian light-sheet and the 800 μm-mask light-sheet for different values of x (see Figure 5.17). Integrating each image along the vertical direction (*i.e.* integrating the $y-z$ profiles along y) I obtained the z-profiles. A comparison between the experimental and simulated z-profiles is shown in Figure 5.18 for the Gaussian light-sheet and in Figure 5.19 for the modified light-sheet.

The experimental z-profiles of both light-sheets seem to successfully replicate the shape of the central peak predicted by the simulations, both in terms of the decay of its peak intensity going away from the sheet's focus (*i.e.* for increasing $|x|$), and of its width, which also changes with $|x|$. As regards the modified light-sheet, its experimental profiles (Figure 5.19) show the appearance of the expected side-lobes around the central peak, but their peak intensity does not agree with the simulations as well as the intensity of the main peak does. Also, some dimmer secondary lobes appear which are not predicted by the simulations. Some extra side-lobes can also be noticed in the Gaussian z-profiles, particularly at $x = 0$. From this qualitative comparison between the experimental and simulated profiles, it seems reasonable to expect that the light-sheets will perform more or less as expected when used for experiments over a single plane, where what counts is the variation of the peak intensity with $|x|$ and not the shape of the profiles along z. Instead, it is not straight forward to predict how much the difference between the simulated and observed shape of the light-sheets along z might influence their performances in tiling experiments on thicker volumes. Not being able to explain the origin of those extra

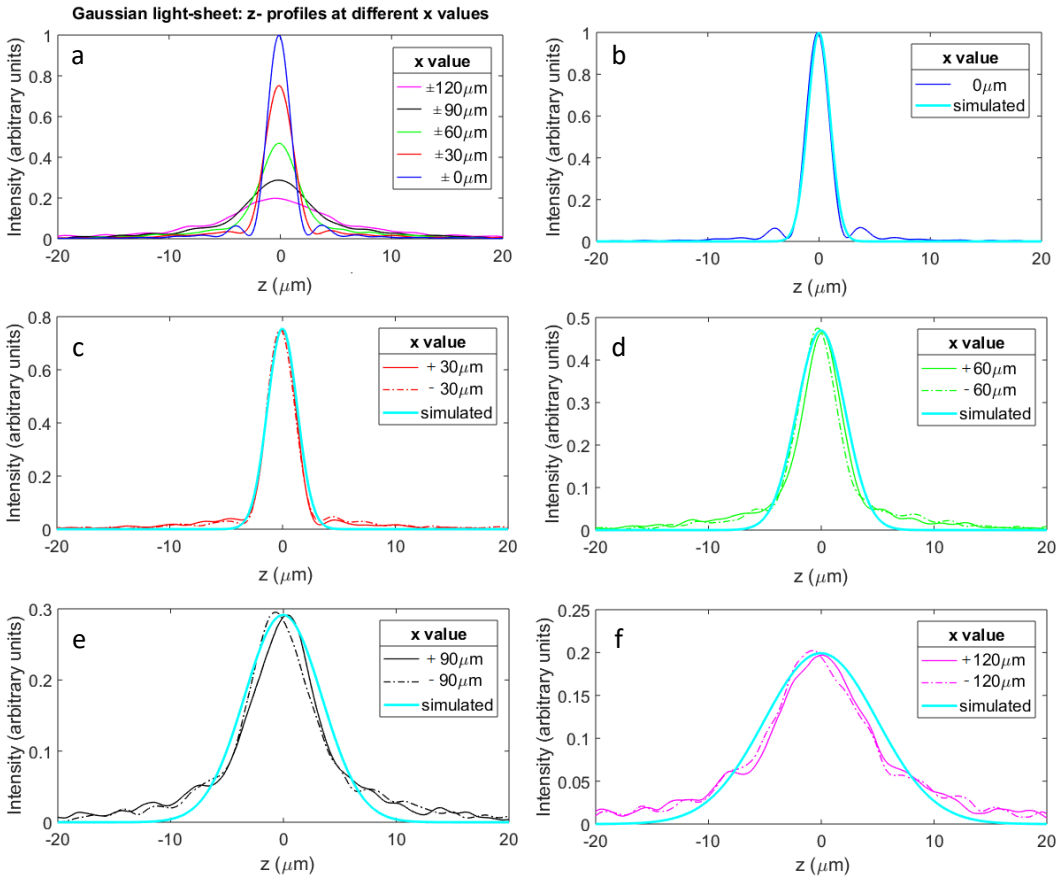

Figure 5.18: *Experimental z-profiles of a Gaussian light-sheet for different values of x (values shown in Figure 5.17).(b-f) These z-profiles where obtained by taking images of different $y-z$ sections of the Gaussian light-sheet with the method explained in Figure 5.16, and integrating each image along its vertical direction (corresponding to the sheet's y-axis). All the profiles are normalized to the peak value of the profile relative to $x = 0$ μm plotted in (b). Each pair of profiles (for $+x$ and $-x$) is plotted with the simulated z-profile obtained for that value of $|x|$ (simulated $+x$ and $-x$ profiles are identical). The simulated profiles are also normalized to the peak value of the simulated profile relative to $x = 0$ μm . Plot (a) shows, for each value of $|x|$, a z-profile obtained by averaging the profile relative to $+x$ with the one relative to $-x$, again normalized to the peak value of the $x = 0$ μm profile.*

side-lobes, nor to reproduce them successfully in the simulations, I decided to proceed and perform the experiments on a single plane, remembering that the observed discrepancies might be one of the causes of an eventual difference between the predicted and actual experimental results.

5.4.2 Sample

The sample used for the tiling experiments described in this section consisted of fluorescent beads (polystyrene beads, 2 μm, labelled with Dragon Green fluorescence, Bangs Laboratories Inc) embedded in a 1.5 % low melting point agarose solution (Agarose, High-EEO/Protein Electrophoresis Grade, Fisher Scientific). These beads were chosen because, unlike the other fluorescent beads used through this work, these are surface-labelled and they photo-bleach relatively fast when imaged with a laser power within the range currently available to the SLM-SPIM (0.5 - 100 mW). A piece of FEP tubing (Fluorinated Ethylene Propylene, 1.3 mm ID × 1.6 mm OD, Adtech Polymer Engineering Ltd) inserted at the end of a syringe was filled with the

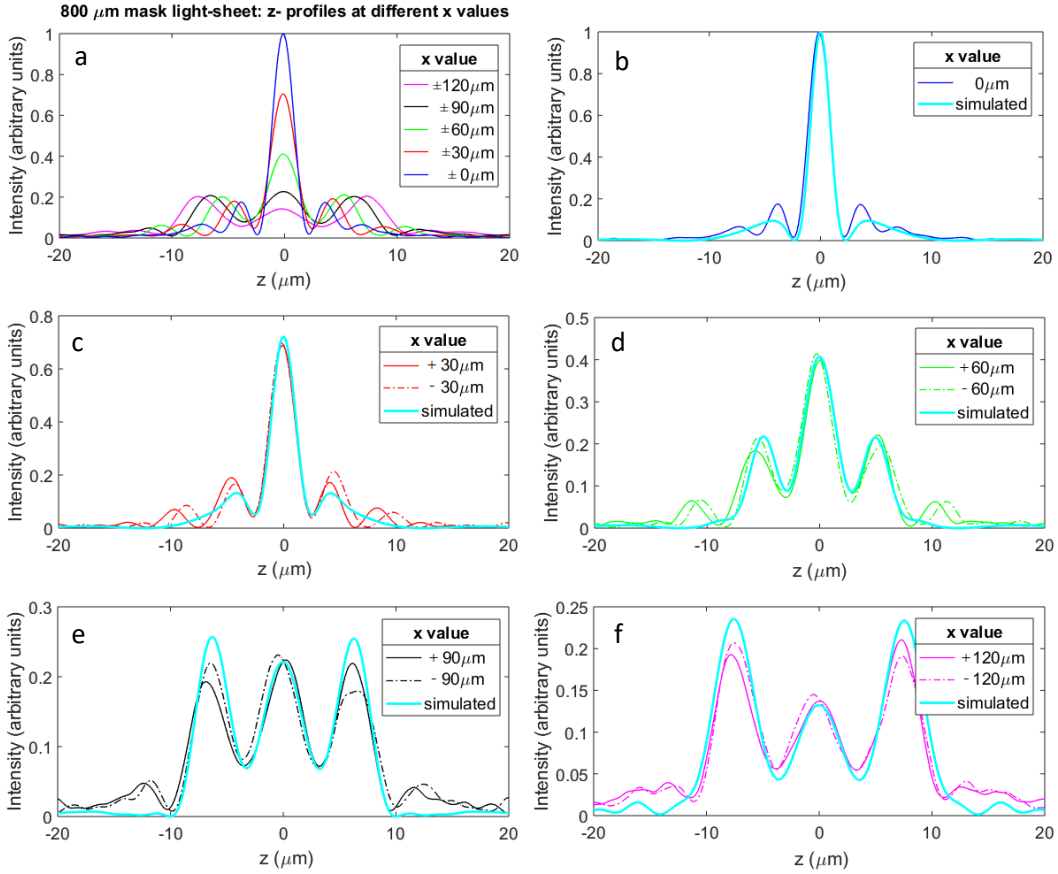

Figure 5.19: *Same plots as in Figure 5.18 but here for a light-sheet generated masking the central 800 μm mask of the Gaussian beam.*

beads+agarose solution; the syringe was immersed vertically in the water chamber and attached to the translation stage.

To make it easy to monitor the fluorescence of single, isolated beads, I decided to use a quite low concentration of beads (see example image in Figure 5.20). One complication when dealing with photo-bleaching though is that each bleaching object can only be used for one single repetition of one single experiment. What this means in the context of these tiling experiments is that the comparison between the the photo-bleaching caused by different light-sheets can not be done using the same fluorescent bead. In order to decrease as much as possible the dependence of the results on the choice of the observed bead (results might for example depend on the bead's size, position in the FoV or position in the FEP tube), I repeated more rounds of the same experiment (same size of imaged volume, tiling+Z scan parameters, light-sheet shape, laser and imaging parameters), each round on a different part of the FEP tube (*i.e.* imaging different beads). I then selected a few beads out of each round of imaging, making sure they were all located within the same area relatively to the imaged volume (all at the center of the FoV and on the central plane along Z). I extracted a photo-bleaching curve out of each of the chosen beads and combined the curves from all the beads to generate an average bead photo-bleaching curve for that experiment (more details on this procedure in Figures 5.20 and 5.21 and in the next section).

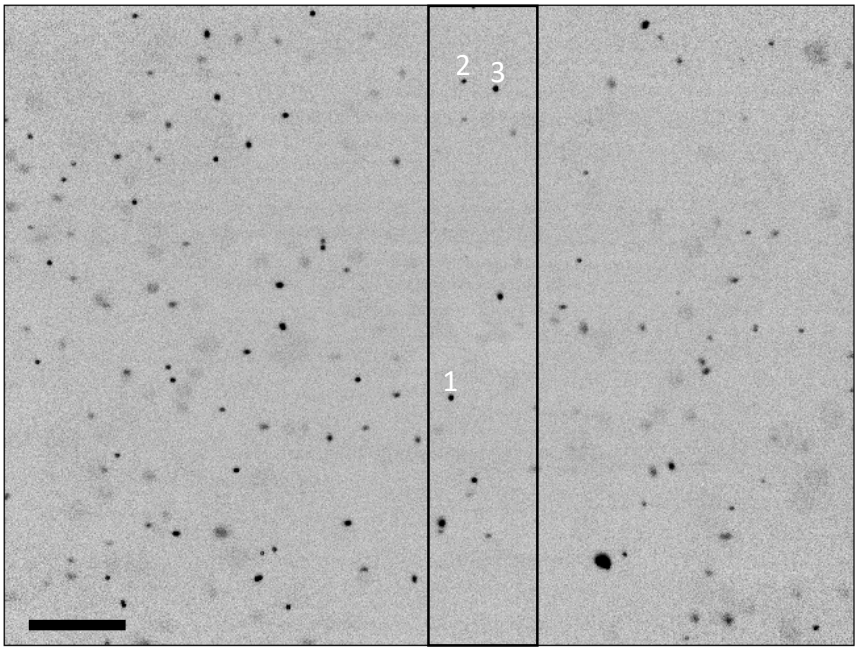

Figure 5.20: *Example of one of the images taken during one tiling experiment (inverted colors). This image is the 5th image of a single-plane tiling experiment (complete experiment consisting of 4 rounds, each made of* 30×8 *images). A Gaussian light-sheet was used to illuminate the sample (light-sheet coming in from the left), and the black rectangle shows the lateral position at which the Gaussian light-sheet was focused. The experiment consisted of imaging the same plane in a sample (fluorescent beads embedded in agar) for 30 times, each time tiling the light-sheet through 8 positions (8 tiles) across the FoV. This experiment was run for four rounds, i.e. on four different planes within the same FEP tube. The three numbered beads are the only ones selected to be analysed for this round of the experiment, and they were chosen because they are well isolated, in-focus and located within the light-sheet waist (see Figure 5.21 for a zoom-in on bead 1). A bleaching curve made of 30 values was created for each bead, extracting its fluorescence out of the 5th image of each of the 30 tiling scans. The three curves were then combined together with curves belonging to other beads, located in the same area of the FoV but selected from the other rounds of the same experiment, each one run with the same parameters but on a different plane within the same sample. Scale bar: 50 µm.*

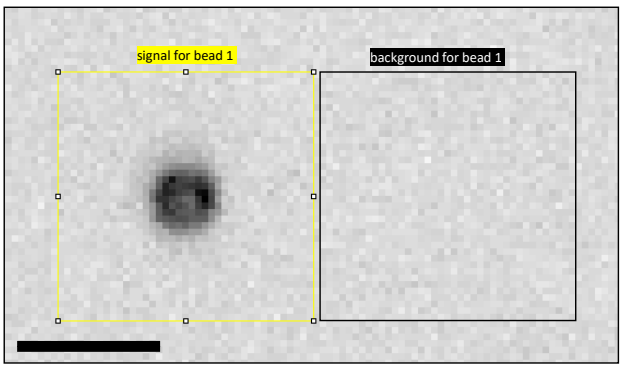

Figure 5.21: *Zoom-in on bead 1 of Figure 5.20. The fluorescence value of a bead in an image was extracted by summing all the light contained within an area surrounding the bead (yellow square) and subtracting a mean background value extracted from an area of the same size located close to the bead, to its right (black square). Scale bar: 5 µm.*

5.4.3 Tiling over a single plane

The first experiments I ran with the modified light-sheets consisted of repeatedly imaging a single plane within the sample tiling the light-sheet over the entire FoV, and comparing the photo-bleaching caused by a modified light-sheet with the one caused by Gaussian light-sheet. To simplify and speed up the experiments, the sheets were tiled in a stepped mode, instead of being smoothly swept across the FoV: the FoV was divided into 8 vertical stripes (8 tiles) so that each tiling scan was made of 8 images, each taken focusing the light-sheet at a different lateral position in the FoV for a time equal to the exposure time t_{exp} (focusing positions going from $X = FoV_{Xsize}/16$ to $X = FoV_{Xsize} \cdot 15/16$ with steps of $dX = FoV_{Xsize}/8$). The laser was pulsed and synchronized with the camera exposure. The intensity of the modified sheets was rescaled by using the same laser power but a different exposure time t_{exp} for each light-sheet. The calibration of t_{exp} was done using the non-normalized z-profiles acquired at $x = 0$ μm using the set-up described in the light-sheet characterization section and its Figure 5.16. These profiles had all been acquired using the same exposure time t_G (exposure time for the Gaussian light-sheet) and laser power. By comparing their peak intensities, each modified light-sheet was assigned a value $A = I_{MAX,G}/I_{MAX}$, where $I_{MAX,G}$ is the peak intensity of the Gaussian z-profile and I_{MAX} the peak intensity of the modified light-sheet. The value A was then used to find the correct exposure time t_{exp} for each light-sheet, calculating $t_{exp} = A \cdot t_G$, where t_G is the exposure time used for the Gaussian light-sheet. I verified that such rescaling of the exposure times made the different light-sheet excite the same amount of fluorescence around $x = 0$ by imaging a sparse sample of non-bleaching 0.2 μm fluorescent beads embedded in agarose, checking that the total fluorescence coming from a bead excited by the sheet's focus was the same for each light-sheet (using the same laser power but the rescaled exposure times).

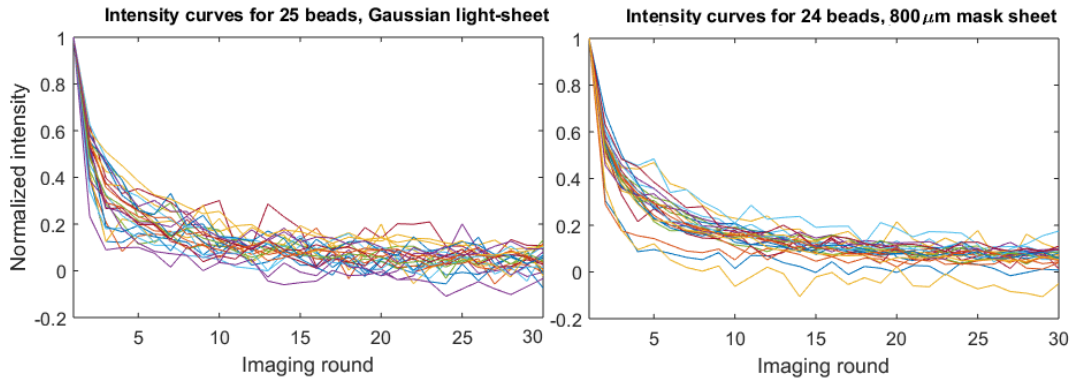

Figure 5.22: *Photo-bleaching curves for beads imaged with a Gaussian light-sheet (left) and a modified Gaussian light-sheet generated using a 800 μm wide mask (right). Each curve is normalized to its own maximum. All the analysed beads were located in the same area of the imaged FoV, but belong to 6 different planes of the same sample (3 planes for each of the two light-sheet).*

Figure 5.22 shows the bleaching curves extracted from 25 beads for the Gaussian light-sheet and 24 beads for a 800 μm-masked light-sheet. Each set of analysed beads contains a mix of beads taken from 3 different rounds of the same experiment. Each round consisted of 30 tiling scans of a single plane, and a different plane of beads was used for each of the three rounds. All the analysed beads were located within the same area of the FoV, the area illuminated by the sheet waist in the 5th image of the tiling scan. Each bleaching curve was normalized to its own maximum and, for

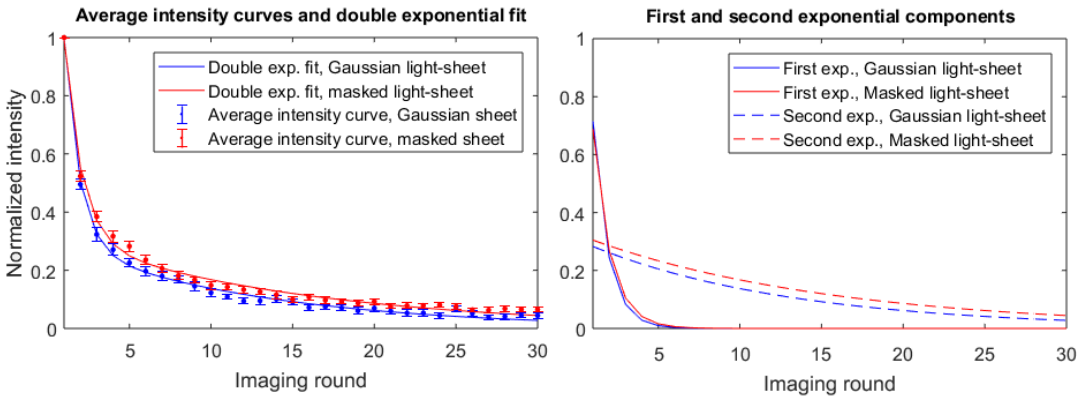

Figure 5.23: *Left: Mean photo-bleaching curves (blue dots for the Gaussian light-sheet, red dots for the modified light-sheet) obtained from the photo-bleaching curves plotted in Figure 5.22, with errors* $E_i = \text{std}(m_i)/\sqrt{N_b}$ *(blue and red bars) and double exponential fits of the form* $f = a_1 \cdot e^{\gamma_1 x} + a_2 \cdot e^{\gamma_2 x}$ *(blue and red lines). Right: The two exponential terms* $a_1 \cdot e^{\gamma_1 x}$ *(continuous lines) and* $a_2 \cdot e^{\gamma_2 x}$ *(dashed lines) of each of the two exponential fits* $f = a_1 \cdot e^{\gamma_1 x} + a_2 \cdot e^{\gamma_2 x}$ *plotted on the left graph (in blue for the Gaussian light-sheet and red the modified light-sheet).*

each of the two light-sheets separately, all the bleaching curves were combined to generate a mean bleaching curve. The two obtained mean bleaching curves are plotted in Figure 5.23-left, together with the error on the mean, which was calculated for the i-th point of each curve as $E_i = \text{std}(m_i)/\sqrt{N_b}$, where $\text{std}(m_i)$ is the standard deviation of the i-th point of the mean curve and N_b is the number of beads contributing to the mean value m_i.

In my simulations, I modelled photo-bleaching as a single exponential decay. If this was a good approximation of the actual photo-bleaching process, the experimental photo-bleaching curves would be well fitted by a single exponential function. Instead, as it can be seen in Figure 5.23-left, a double exponential is needed to obtain a satisfying fit of the experimental mean photo-bleaching curves. Each double exponential fitting function $f(x)$ is defined as $f = a_1 \cdot e^{\gamma_1 x} + a_2 \cdot e^{\gamma_2 x}$, and its two exponential components $e^{\gamma_1 x}$ and $e^{\gamma_2 x}$ are plotted separately in Figure 5.23-right.

I decided to isolate the first exponential term of the double exponential fit and use it to compare the experimental results to the simulated data. To generate the simulated photo-bleaching curves I replicated the imaging procedure actually used in the experiments: I simulated imaging 30 times a 440 μm FoV tiling a Gaussian light-sheet over 8 tiles and monitored the photo-bleaching experienced by a point located in the area illuminated by the sheet waist in the 5th tile. I chose the photo-bleaching rate γ so that the simulated photo-bleaching curve obtained for the Gaussian light-sheet would match the single exponential curve extracted from the experimental data. I repeated the same simulations for the modified light-sheet using the γ chosen analysing the Gaussian light-sheet data. I scaled the $x - z$ profiles of the two light-sheets used in the simulations so that their peak intensity was the same, which seemed to be the closest normalization to what I had done in practice to rescale the light-sheets for the experiments (procedure described above). The results of these simulations are plotted together with the experimental data in Figure 5.24.

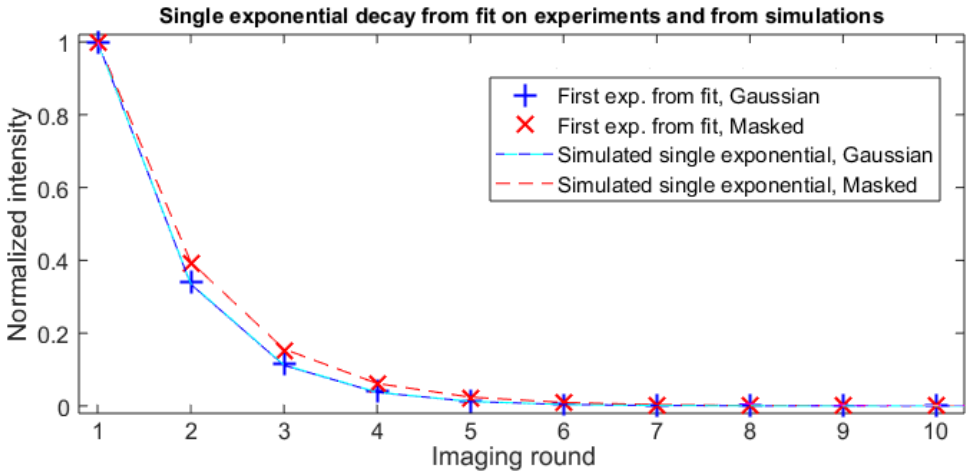

Figure 5.24: *Experimental and simulated photo-bleaching curves, zoom-in on the first 10 points, corresponding to the first 10 repetitions of the tiling scan on a single plane. First exponential term extracted from the double exponential fit to the data (blue + for the Gaussian light-sheet, red × for the modified light-sheet) plotted together with the simulated results (blue/cyan line for the Gaussian light-sheet, red dashed line for the modified light-sheet). The photo-bleaching rate γ used in the simulations was appositely chosen so that the simulated curve for the Gaussian case would fit the single exponential decay extracted from the experimental data.*

5.4.4 Tiling over a volume

With a second set of experiments I wanted to try and see if I could get a greater reduction of photo-bleaching when imaging a volume made of more than a single plane, as suggested by the photo-bleaching reduction map of Figure 5.12. I chose to try and tile the same modified light-sheet used for the single plane experiments (800μm mask), using the same number of tiles (8, for the 440μm FoV) but this time adding a Z-scan over a total volume of thickness $\Delta Z = 8\mu$m, imaging 17 planes spaced of $dZ = 0.5\mu$m. I decided to start by simulating this experiment to see what kind of photo-bleaching reduction I could hope to observe. In this case, the photo-bleaching curves were obtained by monitoring the fluorescence of a point placed at the center of the imaged volume, both along X ($X_{\text{point}} = 0.5 \cdot FoV_{Xsize}$) and Z ($Z_{\text{point}} = 0.5 \cdot \text{Volume}_{Zsize}$). To compare the photo-bleaching reduction to the case of imaging a single plane, the photo-bleaching rate γ was decreased and chosen to make the simulated curve generated using a Gaussian light-sheet match the one simulated for the single plane case. The results of these simulations are shown in Figure 5.25.

Unfortunately, the experiments run with these parameters were not successful, in the sense that each attempt gave a very different result, sometimes showing a minimal decrease of photo-bleaching when using the modified light-sheet, sometimes not showing any difference from using a Gaussian light-sheet, and sometimes instead even showing a slight increase in photo-bleaching.

I believe that one thing which might explain why the results I obtained do not agree with my simulations could be the difference between the actual shape of the light-sheets and their simulated shape, especially outside their central (along z) peak. On the other hand, from profiling the light-sheet I observed that the experimental light-sheets match well the simulated profiles around their central peak, which could explain why the experiments on a single plane agreed with my simulations. Nevertheless, if the main problem were the difference between the actual shape of the

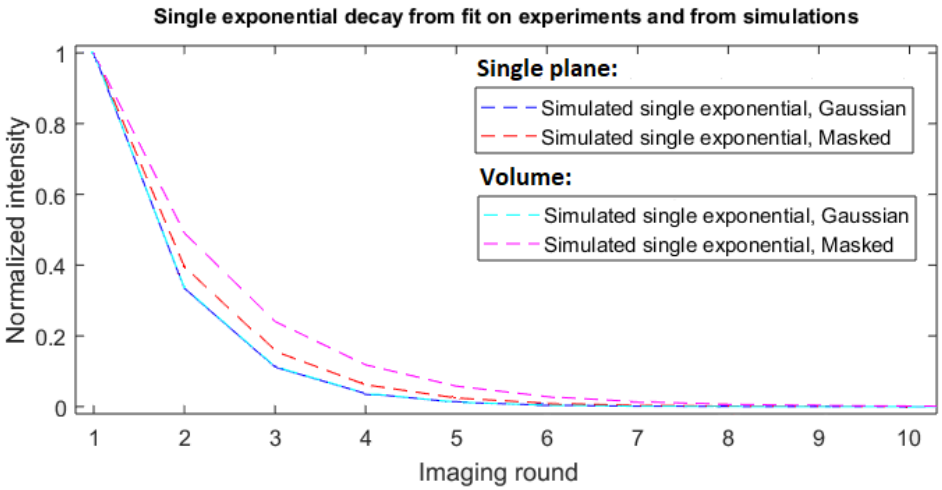

Figure 5.25: *Simulated photo-bleaching curves, zoomed-in on the first 10 points, corresponding to the first 10 repetitions of the tiling scan on a single plane (blue and red) and on a 8 µm thick volume imaged through 17 planes spaced of $dZ = 0.5$ µm (cyan and magenta). The photo-bleaching rate γ used for the simulations of the volume imaging was chosen so that the simulated curve for the Gaussian light-sheet case would coincide with the one simulated in the case of imaging a single plane.*

light-sheets and their simulated shape, I would expect to see similar results when repeating the same experiment. It is true that the real shape of the sheets might actually be a bit different from one experiment to the other (because I image a different plane in a different part of the sample and the tube), but I believe this difference should not be big enough to explain the level of variability I am seeing in the results.

5.5 Discussion, conclusions and future works

In this chapter I presented a modified Gaussian light-sheet which aims at decreasing photo-bleaching while performing tiling. I first discussed the Matlab simulations I performed (Section 5.3), which seemed to show that, when compared to the use of a normal Gaussian light-sheet, the proposed light-sheet could indeed help decrease photo-bleaching while performing tiling. I then presented the experimental results I obtained imaging a sample of fluorescent beads which photo-bleach relatively fast when imaged with a laser power within the range currently available to the SLM-SPIM (details on the sample in Section 5.4.2).

All the experiments I ran on a single plane within the sample resulted in a plot similar to the one in Figure 5.24, *i.e.* with the experimental photo-bleaching curve matching the simulated one. These experimental results served to confirm my simulations, and supported our hypothesis that the modified Gaussian light-sheet could indeed help decrease photo-bleaching when imaging a single plane many times using tiling.

On the other hand, the results obtained from experiments performed on thicker volumes (consisting of more than one plane along z) were not in good agreement with the predictions from my simulations. As mentioned at the end of the previous section, I believe that one thing which might be affecting these results might be the difference between the actual shape of the light-sheets and their simulated shape.

In order to check if this could be the problem, one could profile the sheets more precisely and then run the simulations using the profiled shape of the sheets.

One further suggestion I have for future works is to improve the photo-bleaching model used in the simulations. It is in fact known that the photo-bleaching is a complex process which can not be accurately represented by a single exponential decay [38]. This can also be noticed from the photo-bleaching curves I extracted from my experiments (see for example Figure 5.23), where the data could not be fitted to a single exponential curve. For simplicity, I have so far approximated the photo-bleaching process with a single exponential, but I believe that improving this model would make the simulations more realistic.

To conclude this chapter, I would say that the simulated results I presented in Section 5.3 suggest that the proposed modified sheet might help decrease photo-bleaching while performing tiling, but that the improvement would probably only be incremental. Data in Figure 5.25 can in fact be interpreted as follows: when imaging a sample many times performing tiling using a Gaussian light-sheet, the sample can be imaged only 2 times before it bleaches to a fifth of its original intensity, while using the modified sheet the same sample could be imaged only one more time before experiencing the same amount of photo-bleaching. Nevertheless, this can be seen as a good example of how useful it can be to have a flexible system such as the SLM-SPIM, which, together with a simulation tool can make it relatively straight forward to develop and evaluate new techniques and ideas.

6 3D illumination for compressive SPIM

6.1 Introduction

In this chapter I discuss the second innovative imaging technique which I worked on as part of my PhD project. The technique involves the use of a z-modulated light-sheet to record 3D images following the principles of compressive sensing [67, 68]. The chapter starts with a general introduction of the topics of 3D imaging and compressive sensing (below), to explain the motivations behind the developed imaging technique. Section 6.2 continues with a more detailed introduction to compressive sensing, and in Section 6.3 I discuss its application to 3D imaging with a light-sheet microscope. In Section 6.4 I describe the proposed imaging scheme in more details and discuss the simulations I performed before testing it on the SLM-SPIM. Section 6.5 describes the experiments I performed and Section 6.6 contains a discussion of the experimental results, some conclusions and ideas for future works.

The most common way to obtain 3D images with a microscope is to combine a set of 2D images of individual planes. As discussed and seen in the previous chapters, when operating in their traditional way, light-sheet microscopes acquire each 2D image in a single shot, making the 3D acquisition much faster than it is with other microscopes, such as, for example, confocal microscopes, where each 2D image acquisition requires a 2D scan of a single illumination spot. Light-sheet microscopes are also less photo-damaging than confocal microscopes, thanks to their confinement of the illumination light to the plane that is being imaged. High 3D imaging speed and low photo-damage are the two main features that made light-sheet microscopy become so popular in the life sciences, and they are also the two things that we believe could be improved even further by exploiting the principles of Compressive Sensing along the third direction (z-direction). In fact, a traditional light-sheet builds a 3D image from a set of 2D images in the same way as, for example, a confocal microscope: it images one plane at a time and then simply puts the acquired images one over the other. This way of performing 3D imaging involves what might seem to be an inevitable trade-off between imaging time, Signal to Noise Ratio (SNR) and light exposure of the sample, and this trade-off could be overcome by using a compressive scheme along the third direction of imaging. Let us look at these three aspects in more detail:

First of all: what is it that fundamentally limits a light-sheet microscope's 3D imaging speed? Assume one wants to reconstruct a 3D image of a sample that is 200 μm $\times$ 200 μm $\times$ 200 μm in size. For a required axial resolution of 2 μm, launching and imaging objective NAs need to be chosen so that the entire volume can be generated from a total of 100 planes, with spacing $\delta z = 2\mu$m, with each image representing a 200 μm $\times$ 200 μm $\times$ 2 μm section of the entire volume. In the simplest light-sheet

implementation the 100 images are acquired by moving the sample along the z direction with steps of $\delta z = 2$ μm. In order to reach high 3D imaging speeds one might instead keep the sample fixed while moving the light-sheet and the imaging objective together, at a fixed distance from each other: this option allows to avoid dealing with possible movement artefacts caused by moving the sample too fast. One could even decide to leave both sample and imaging objective fixed, and only move the light-sheet through the sample, using something else (like a tunable lens [70]) on the imaging side to make sure that the light-sheet stays in focus for the whole scan. Moreover, it has been shown how, for certain volume sizes, it is possible to overcome the refocusing issue by extending the imaging DoF using wavefront coding [71], and applying a proper post-acquisition deconvolution to the acquired images. What all of this means is that, depending on what kind of light-sheet set-up one is working with, one might be able to achieve the desired 3D imaging speed without being limited by sample moving artefacts, mechanical limitations of moving components, or updating speed of electronic devices used to move the light-sheet and/or refocus the image plane.
Nevertheless, there is a final aspect involved in posing a limit to a light-sheet microscope's 3D image acquisition speed: the SNR. The desired SNR dictates the exposure time needed for each image (giving a certain laser power), which sets a lower bound to the time needed to image each plane. To reduce the total 3D imaging time (= exposure time per plane $\times$ number of planes) the laser power could be increased, thereby shortening the exposure time needed for each image, but this leads to the discussion of a second topic worth mentioning here: photo-bleaching.

As already mentioned in Chapter 2 (Section 2.2.2) and Chapter 5 (Section 5.3.2), photo-bleaching and its relation to light dose delivered to the sample is unfortunately not a simple issue to discuss [38], and it is strongly dependent on the chemical characteristics of the sample and its conditions. When dealing with live samples, photo-bleaching can result in sample damage (photo-damage), a modification of the sample's development or even death. In the previous section, the process of photo-bleaching was simplified and treated as being linearly dependent on the excitation illumination. In reality tough, even at low excitation light intensities, photo-bleaching is more often not a simple linear effect [37, 39, 72], which means that increasing the laser power in order to use lower exposure times might not always be an ideal method to increase imaging speed.

In order to achieve faster 3D fluorescence microscopy without increasing photo-bleaching, we intend to explore a direction that, to the best of our knowledge, has not been extensively explored yet, but that we believe is promising. The first step in this direction involves letting go of the idea that to generate the 3D image of a volume made on N planes one needs to record N 2D images, one per plane. The theory of Compressive Sensing teaches us that a signal (in this case the fluorescence coming from a 3D biological structure) which is sparse in a certain domain (in this case the spatial domain) can be sampled by (and then reconstructed from) a number of samples that is much smaller than what suggested by the Nyquist sampling theorem [67, 73–75]. Applied to 3D imaging, what this is telling us is that with the correct illumination scheme and post-processing of the acquired images we could be able to capture the 3D structure of a sample by acquiring much fewer images than what we are used to with the traditional plane by plane acquisition process.

6.2 Compressive Sensing

Compressing Sensing (CS) is a novel sampling theory which states that, under certain conditions, the number of samples needed to sample a signal can be less than what suggested by the Nyquist-Shannon theorem [67, 76, 77]. Consider the task of sampling a signal (which could for example be an audio signal or an image) whose highest frequency is f. The Nyquist-Shannon theorem says that $2f$ is the lowest sampling frequency which allows to later reconstruct the original signal from the set of samples. CS instead suggests that a lower sampling frequency is permitted, it explains for what signals this is possible and how the measurements must be done in order to assure minimum information loss. This theory has clearly generated a lot of interest in many fields of research, since dealing with high-dimensional data is often computationally and logistically disadvantageous. In many cases, even when the signals are sampled according to the limit imposed by the classical sampling theory, the problems related to their size lead to the need for compression, which makes it possible to reduce the size of the recorded signals keeping the information loss/distortion limited.

One of the most popular techniques for signal compression is known as transform coding [78] and relies on the fact that many signals can be represented with sparse expansion in terms of a suitable basis. Once the signal is expressed in a basis in which it is sparse, a compression can be obtained by only storing the largest coefficients, and when reconstructing the signal the non-stored coefficients are simply set to zero. This is the principle behind many compression techniques such as MP3 and JPEG. This process of sampling and compression is usually done by acquiring the signal with a suitably high sampling frequency, computing the complete set of coefficients in the proper basis (the one in which the signal is sparse), encode the largest coefficients and discard all the others.

Consider now a digital camera which has millions of imaging sensors, the pixels, but eventually encodes a picture on a few hundred kilobytes. This process can be seen as a waste of resources, since a lot of the acquired information is thrown away during compression. The fundamental idea behind CS is to optimize this process: rather than sampling at a high rate and then compressing the sampled data, it suggests a way to directly sample the data in a compressed form, *i.e.* at a lower sampling rate, with the number of required measurement actually equal to the compressed size of the signal. Measurements in CS must be able to encode only the important information about an object, and they therefore need to be specifically designed for the signal of interest.

To illustrate the concepts of CS, let $X \in \mathbb{R}^N$ be the N-dimensional vector representing a discrete signal, in time or space. The process of sampling this signal can be expressed in terms of an N-dimensional sampling vector A_m and the resulting measured value Y_m:

$$Y_m = A_m X = \sum_{i=1}^{N} A_{m,i} X_i. \tag{6.1}$$

A series of M different measurements can therefore be expressed as the following system of linear equations:

$$Y_m = A_m X, \quad m = 1, \ldots, M, \tag{6.2}$$

or in a matrix-vector form as:

$$Y = \mathbf{A}X, \tag{6.3}$$

where $\boldsymbol{A}$ is the $M \times N$ sampling matrix that transforms the original N-dimensional signal X into the M-dimensional measured signal Y. The M rows of $\mathbf{A}$ are the M sensing vectors A_m which define the sampling scheme adopted. If these rows are, for example, discrete representations of Dirac delta functions, Y becomes a vector of values of X sampled at different points in time or space; if the rows represent M different sinusoids, like in the sensing modality used in MRI, Y becomes a vector of Fourier coefficients.
CS deals with the under-sampled case, that is when the number of samples M is smaller than the dimension of the signal N. System 6.3 becomes an under-determined linear system, with more unknowns than equations, which means that there is an infinite number of vectors X that satisfy it. This kind of under-determined sampling system is extremely common in many applications. For example, the number of sensors may be limited, or the measurements may be really expensive, or the sensing process may be so slow that only a few measurements are possible. Given this situation, two main theoretical questions arise: how should the sampling matrix $\boldsymbol{A}$ be designed in order to make sure that the relevant information of the signal X is preserved? Once the sampling has been performed, how can the original signal X be recovered from the measurements in Y? The theory of CS states that if the data vector X is sparse enough in a certain basis, it is possible to design a matrix $\boldsymbol{A}$ with $M < N$ that ensures that the original signal can later be reconstructed accurately and efficiently from Y. In order for this sampling process do be successful, two fundamental premises must be taken into account: sparsity and incoherence.

Sparsity Let vector $X \in \mathbb{R}^N$ represent a signal (for example a vectorized N-pixel image). Vector X can be represented through its expansion in an orthonormal basis (such as a wavelet basis) $\mathbf{\Psi} = [\Psi_1 \dots \Psi_N]$ as follows:

$$X = \sum_{i=1}^{N} \alpha_i \Psi_i, \tag{6.4}$$

where $\alpha_i = \langle X, \Psi_i \rangle$ are the coefficients of X in the chosen basis $\mathbf{\Psi}$. X and α are equivalent representations of the signal, with X in the time or space domain and α in the $\mathbf{\Psi}$ domain. The signal X is said to be K-sparse if only K coefficients α_i in Equation 6.4 are non-zero. Moreover, the signal is said to be compressible if in Equation 6.4 just a few α_i are large, and many more are small. If a signal is sparse (or even just compressible), it is possible to discard the smallest coefficients α_i without much information loss. Let X_s be the signal obtained by keeping only the K largest coefficients α_i, such that:

$$X_s = \sum_{j=1}^{K} \alpha_j \Psi_j, \tag{6.5}$$

where α_j with $j = 1, \dots, K$ are the K largest coefficients within the N α_i. Since $\mathbf{\Psi}$ is an orthonormal basis, $||X - X_s||_{l_2} = ||\alpha - \alpha_s||_{l_2}$, and if X is sparse then α is well approximated by α_s and hence the error $||X - X_s||_{l_2}$ is small [1].

[1] $||\cdot||_{l_2}$ denotes the l_2-norm, *i.e.* $||\alpha||_{l_2} = (\sum_{i=1}^{N} |\alpha_i|^2)^{1/2}$.

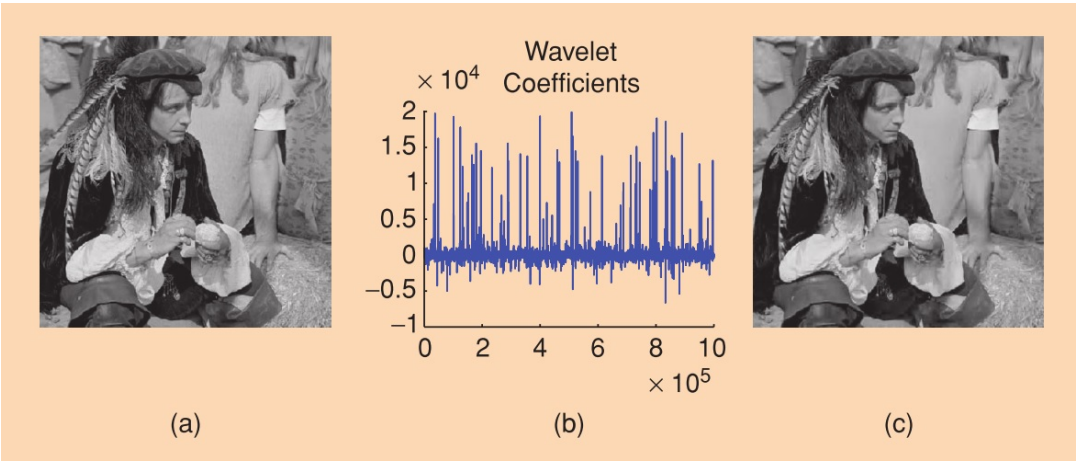

Figure 6.1: *This figure, taken from [80], is a good example on how compression successfully works for sparse signals. In (a) a megapixel image is shown, with pixel values going from 0 (black) to 255 (white). (b) shows the coefficients of the wavlet transform of the image: only few of them have a relevant value, while most of them are small. This set of coefficients is modified by setting to zero all the smallest ones, and keeping the original values of only the 25,000 largest ones; the image is then reconstructed from this new set of coefficients and is shown in (c): even when more than the 97.5% of the values of the wavelet representation of the image are thrown away, the reconstructed image still looks satisfyingly similar to the original one.*

An example of image compression can be seen in Figure 6.1, which shows how hardly noticeable the image loss can be when modifying an initial megapixel image (6.1a) by throwing away 97.5 % of its coefficients. As said before, signal sparsity is the principle that underlies most modern data compression techniques, and known compressive-type bases include for example 2D wavelets for images and localized sinusoids for music [79], but a greater innovation was introduced by CS and its sampling modalities. In fact, while normal data compression methods compute α from X and then encode the values and locations of the K most significant coefficients, CS acts in a non-adaptive way, namely in a way that does not require the knowledge of all the N coefficients α_i to determine the significant K ones. In order to make this possible, it is important that the two chosen bases, $\mathbf{\Psi}$ (the one in which the original signal is sparse) and $\mathbf{\Phi}$ (the basis of sampling waveforms) are highly incoherent.

Incoherence Two bases are incoherent if it is not possible to express any basis vector of one of them as a sparse linear combination of basis vectors of the other one. One fundamental condition for a compressive sampling and reconstruction scheme to work is that the two chosen bases $\mathbf{\Psi}$ (the one in which the original signal is sparse) and $\mathbf{\Phi}$ (the basis of sampling waveforms) must be highly incoherent. This means that while the signal of interest has to be sparse in $\mathbf{\Psi}$, the sampling waveforms need to be very dense in $\mathbf{\Phi}$. Formally, given the two orthonormal bases of $\mathbb{R}^N$, $\mathbf{\Phi}$ and $\mathbf{\Psi}$, their coherence is measured by the following parameter, which ranges between 1 and $\sqrt{N}$:

$$\mu(\mathbf{\Phi}, \mathbf{\Psi}) = \sqrt{N} \max_{1 \leq h,i \leq N} |\langle \Phi_h, \Psi_i \rangle|. \tag{6.6}$$

What μ does is measure the largest correlation between any two elements of $\mathbf{\Phi}$ and $\mathbf{\Psi}$: if $\mathbf{\Phi}$ and $\mathbf{\Psi}$ contain correlated elements, the coherence between them is large (approaching $\sqrt{N}$). One example of maximal incoherence is given by the classical sampling method in time or space, where the sampling basis $\mathbf{\Phi}$ is composed of the

Dirac functions and $\mathbf{\Psi}$ is the Fourier basis, which give a coherence value $\mu = 1$. The other extreme case is given by two identical bases, which are then maximally coherent and give $\mu = \sqrt{N}$. So, what is the importance of coherence? As expressed by Equation 6.1, each measurement corresponds to a projection of the signal vector on one element of the sampling basis[2], and the two bases being incoherent assures that each incoherent measurement captures a little bit of information about all the entries of the coefficient vector α. This means that incoherence optimizes the measurement process: by using incoherent bases fewer measurements are needed to capture the important information carried by the signal.

Once an appropriate sampling matrix has been chosen and the signal has been sampled, the challenge is then to be able to reconstruct the original N-dimensional signal from the M acquired measurements. The aim is to determine the sparsest representation α consistent with the measurements, and this corresponds to solving the following optimization problem:

$$\text{find } \min_{\alpha \in \mathbb{R}^N} ||\alpha||_{l_1} \quad \text{subject to } Y = \boldsymbol{A\Psi}\alpha\,, \tag{6.7}$$

where $||\cdot||_{l_1}$ denotes the l_1-norm ($||\alpha||_{l_1} = \sum_{i=1}^{N} |\alpha_i|$) and is used instead of the l_0-norm[3] to obtain computationally tractable optimization algorithms able to recover the exact solution.

Thinking of the case where X represents a vectorized image of N pixels, we know that images are in practice noisy and only approximately sparse. Compressed sensing algorithms in this real case therefore seek to recover the best approximation of X by finding the sparsest representation α subject to $Y \simeq \boldsymbol{A\Psi}\alpha$. The function of α minimized in Equation 6.7 may vary, depending for example on what type of noise is considered, and so do the constrains this function is subject to, giving a variety of different reconstruction algorithms to chose from when wanting to perform a compressive sensing experiment.

A fundamental theorem for CS, proven in 2006 by Candes and Romberg [79], relates the incoherence between the sampling basis and the basis in which the signal is sparse to the number of samples needed in order to assure that the signal reconstructed by Equation 6.7 is exact with very high probability. The theorem states that, if the original signal $X \in \mathbb{R}^N$ is K-sparse in the basis $\mathbf{\Psi}$ and the M measurements are chosen uniformly random in $\mathbf{\Phi}$, the reconstructed coefficients represent the original signal with high probability if

$$M \geq C \cdot \mu^2(\mathbf{\Phi}, \mathbf{\Psi}) \cdot K \cdot log(N)\,, \quad C > 0. \tag{6.8}$$

With this theorem, the importance of incoherence becomes clear: the lower the value of μ (small μ means incoherent pair of bases) the smaller the number of required measurements M. The lowest bound is found for completely incoherent bases, for which the number of needed measurements becomes of the order of $K \cdot \log(N)$. This is an important result, especially for strongly sparse big signals, like images, where the number of measurements then scales as the log of the number of pixels.

As said, the whole new sampling/reconstruction process proposed by CS had a big impact on different areas of research, and is developing in many applications, as

[2]Projection of vector X onto vector A_k: $\mathrm{P}_{A_m}(X) = \frac{\langle X|A_m\rangle}{\|A_m\|^2} A_m$.

[3]The l_0-norm of a vector corresponds to the number of non-zero elements of that vector.

for example MRI [81], astronomy [82], and analog-to-digital conversion [83]. The interest in CS techniques has developed in the optics world as well, and an important novelty in this field was brought by the demonstration, in 2008, of the so-called single-pixel camera [84]. In this case, the signal is the 2D image, which is classically sampled by N samples (the N pixels in the imaging CCD or CMOS) and later compressed with transform coding. Following the principle of CS, in the single-pixel camera the 2D detectors (pixels) are substituted with a single photon detector, and the image is reconstructed from $M < N$ measurements, where each measurement is taken by illuminating the scene with a random pattern and collecting the entire image with the single-pixel detector. In Gehm and Brady's article of 2015 [85], the possible utility of CS to electro-optic and infrared (EO/IR) applications was analysed, reporting various successful experimental results and discussing future challenges regarding the application of CS methods to EO/IR systems. Other applications of CS are for examples those on holography [86] and ghost imaging [87]. As regards microscopy, an optical-sectioning compressive sensing microscope was presented in 2010 [88], and developments have been made in application of CS techniques both to wide-field and confocal fluorescence microscopy [89, 90].

6.3 Compressive Sensing applied to light-sheet microscopy

All the applications of CS mentioned above, even those that ultimately deal with 3D images, have concentrated on exploiting the possible benefits that CS can bring to the acquisition and reconstruction of a 2D image. When applied to 3D imaging, these techniques apply CS to image a single plane inside the sample, but perform a traditional sampling along the third dimension (*i.e.* the image of a 3D volume made of N planes is reconstructed from N images of single planes). Instead, we would like to exploit the idea of a possible compressed sampling along the third dimension of a 3D image.

In the case of light-sheet microscopy, this dimension is the axial dimension (called the z-axis in a typical light-sheet coordinate systems) and the 3D structure to reconstruct is a fluorescent sample. In conventional light-sheet microscopy, the 3D image of a fluorescent sample is made of a set of N images, with the n-th image being the image of the n-th plane of the imaged volume (the plane at z_n along the z-axis). Using CS, the original volume can be reconstructed from $M < N$ images. In the specific case in which the dimension which is sampled in a compressed fashion is the axial dimension (*i.e.* the z-axis), the m-th image of the set of M images no longer represents the image of a single plane in z, but contains a linear combination of information coming from different planes.

Machine learning has been applied to 3D microscopy, developing image restoration methods which use neural networks to reconstruct 3D images requiring the acquisition of less images than the number of reconstructed planes [91, 92] . These imaging techniques are able to operate in the presence of a somewhat similar under sampling along the axial direction to the one proposed by the compressed imaging scheme discussed in this chapter, but, as for any machine learning technique, the quality of their reconstruction relies strongly on the similarity between the imaged sample and the training set used. Instead, the proposed z-compressed scheme relies on the much more general assumption that the 3D distribution of fluorescence in a biological sample is sparse in the spatial domain.

Consider a 3D sample imaged as a set of N planes following the conventional 3D imaging scheme. Let $z_i = z_1, \ldots, z_N$ be the axial coordinates of the N planes. For each (x,y) position in the sample (*i.e.* for each pixel of the acquired images), let $X_{(x,y)}$ be the vector of N values representing the fluorescence intensities at the N points (x,y,z_i) in the imaged volume. Assume the same 3D sample is imaged using a z-compressed imaging scheme, which allows to reconstruct the same volume (made of N planes) from a set of M acquired images. In this case, the compressed system that needs to be solved for each (x,y) position is:

$$Y_{(x,y)} = \boldsymbol{A}_{(x,y)} X_{(x,y)}, \tag{6.9}$$

where $Y_{(x,y)}$ is the vector containing the M intensity values acquired for pixel (x,y), and $\boldsymbol{A}_{(x,y)}$ is the $M \times N$ sampling matrix. The m-th row of the matrix $\boldsymbol{A}_{(x,y)}$ is an N-dimensional vector representing the z-profile (at (x,y)) of the illumination used to acquire the m-th image of the compressed set of images. If the laser power is calibrated so that the light dose received by the sample during the acquisition of the m-th image is less or equal to the light dose received during the acquisition of the n-th image of a plane-by-plane imaging scheme, acquiring $M < N$ compressed images means decreasing the amount of light delivered to the sample (*i.e.* less photobleaching), with respect to what happens when performing a plane-by-plane image acquisition. The amount of time necessary to acquire the images needed to reconstruct an entire volume also decreases, but at the expense of more post-processing required.

As we were at the early stages of our work on this, in spring 2017, an article was published which described a z-compressed scheme for light-sheet microscopy [68]. As I will discuss in more details in the following sections, the imaging scheme proposed by Woringer *et al.* differed from the one we had in mind on a few main aspects: the way to generate the illumination patterns suitable for the compressed sampling, the modality with which the illumination is delivered to the sample, and the way to deal with the focus adjustments required on the imaging side to be able to capture relevant and usable information within each compressed image.

The research challenges involved in the development of our compressive 3D light-sheet microscopy technique can be divided into three main areas:

- **Compressed sampling:** the chosen sampling matrix (matrix $\boldsymbol{A}$ in $Y = \boldsymbol{A}X$) needs to implemented experimentally, *i.e.* the illumination patterns required for the acquisition of the z-compressed images need to be physically produced. The work carried out with regard to this topic is presented and discussed in Section 6.5.1.

- **Signal reconstruction:** once the compressed images are acquired, the original signal needs to be recovered. The chosen compressed reconstruction algorithm was first tested trying to reconstruct a 3D sample from simulated compressed images. These simulations are described and discussed in Section 6.4.

- **Extended DoF:** each compressed image contains information coming from different depths in the sample. Ideally, all of this information should be seen as in-focus by the imaging objective. In a conventional light-sheet acquisition scheme though, the imaging DoF is matched with the thickness of the light-sheet (a few μm), which means that only a single plane at a time is seen as in-focus, the one illuminated by the light-sheet.
  In [68], the imaging DoF is matched to the thickness of the light-sheet and, in

order to make each image of the z-compressed set contain information from many planes, during each m-th image acquisition the light-sheet is scanned through the entire volume (together with the imaging objective, to maintain the focus).
With our z-compressed scheme we propose a different approach: for each image, the illumination is spread across a Δz that corresponds to the thickness of the entire 3D volume. Ideally, we would want a good lateral resolution (requiring a high imaging objective NA) and at the same time a DoF that covers that entire Δz (requiring a low imaging objective NA). In order to combine these two requirements, wavefront coding on the imaging arm can be used to extend the DoF of a high imaging objective. We decided to consider the addition of wavefront coding to the system as separate, final step (ultimately not tackled within the research project presented in this thesis, but added to the suggestions for future works), and proceeded by first developing the compressed scheme on our 0.8 NA imaging arm, working with its small DoF, and secondly try the same experiments on a separate imaging arm equipped with a 0.3 NA objective, which gave us a lower lateral resolution but a DoF of at least ~ 14 μm. The final step would then be to get back to the 0.8 NA imaging objective and use wavefront coding to extend its DoF and with that its z-compressed volume imaging ability.

6.4 Simulations

This section describes the simulation of the proposed z-compressed image acquisition and reconstruction process. The simulations were performed using Matlab and were divided into the following three steps:

- **Choice of measurement matrix**: define a matrix of size $M \times N$, with the M rows corresponding to M measurement vectors and N being the number of planes to sample and then reconstruct;
- **Compressed imaging and reconstruction**: considering a 3D object composed of a set of N planes, simulate a z-compressed acquisition scheme, generating a set of M 2D images of the object; from the simulated set of M images, reconstruct N planes using a compressed sensing reconstruction algorithm;
- **Evaluation**: compare the reconstructed object with the original one and also with its image obtained using a plane-by-plane imaging scheme.

6.4.1 Choice of measurement matrix

Making the assumption that our sample is sparse in the spatial domain, I decided to start by using a truncated Fourier matrix as measurement matrix $\boldsymbol{A}$. To create the truncated Fourier matrix I selected the first M rows (containing the M lowest spatial frequencies) of an $N \times N$ complete Fourier matrix. Such measurement matrix $\boldsymbol{A}$ is an $M \times N$ matrix, and its M rows represent the M illumination patterns which will be used in the z-compressed acquisition scheme. Using the same notation, a plane-by-plane imaging scheme would be represented by an $N \times N$ identity matrix I_N. The n-th row of I_N is in fact made of all zeros and has a 1 in the n-th column, representing the fact that to acquire the n-th image of the plane-by-plane imaging scheme only the n-th plane within the sample is illuminated.

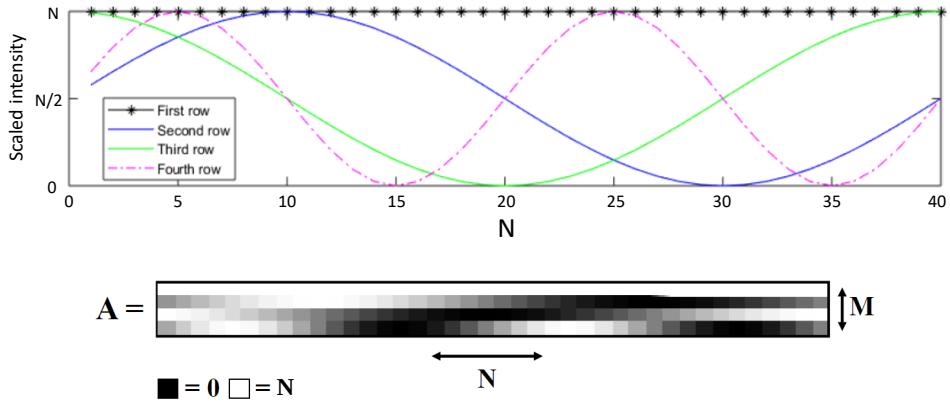

Figure 6.2: *Measurement matrix $\boldsymbol{A}$ used in the case of a 10× compression rate ($M = 4$, $N = 40$). Each of the M rows represents the z-profile of the illumination intensity used for the acquisition of one of the compressed images.*

To ensure that the total light dose received by the sample when using the compressed scheme is less or equal to the light dose received with a plane-by-plane imaging scheme, in my simulations I scaled the intensity of each row of $\boldsymbol{A}$ to values from 0 to $1/N$. To explain this rescaling, let us compare the light dose received by the sample in the case of plane-by-plane imaging and in that of z-compressed imaging. With the plane-by-plane scheme, the light dose received by a sample during the acquisition of the n-th image is all concentrated on the n-th plane (the n-th row of I_N has a 1 on the n-th column and 0 on every other column). The light dose delivered to the sample can therefore be expressed as

$$I_0 \cdot t_{exp} \cdot 1 = I_0 \cdot t_{exp} \,,$$

where I_0 is the laser intensity, and t_{exp} the exposure time. With the z-compressed scheme, the light dose received by the sample when acquiring the m-th image is spread over the entire volume, and its distribution across the N planes is defined by the profile of the m-th row of the measurement matrix $\boldsymbol{A}$. This light dose can be expressed as

$$I_0 \cdot t_{exp} \sum_{z=1}^{z=N} A_{m,z} \,.$$

By rescaling the intensity of each row of $\boldsymbol{A}$ to values from 0 to $1/N$, one assures that

$$I_0 \cdot t_{exp} \sum_{z=1}^{z=N} A_{m,z} \leqslant I_0 \cdot t_{exp} \cdot N \cdot \frac{1}{N} = I_0 \cdot t_{exp} \,,$$

which means that the light dose received by the sample when acquiring one of the z-compressed images it is equal or less than the light dose received for a single image of the plane-by-plane scheme. Therefore, for a z-compressed acquisition made of M frames, the total light dose delivered to the sample is always equal or lower than M/N times the total light dose delivered by a plane-by-plane acquisition of N planes. Figure 6.2 shows the measurement matrix used in the case of $N = 40$ and a 10× compression rate ($M = N/10 = 4$).

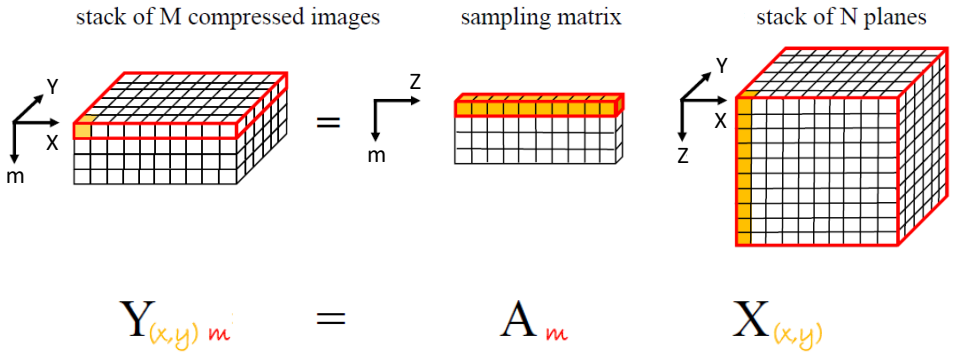

Figure 6.3: *Compressed system to be solved for each pixel (i.e. each position (x,y) in the imaged FoV). Consider the m-th simulated compressed image (in red, to the left). Each pixel (x,y) of this image (in yellow) is acquired by multiplying the m-th row of the sampling matrix (in yellow, in the middle) by the N-dimensional vector correspondent to the distribution of fluorophores in the sample at positions (x,y,z_i), $i = 1,\ldots,N$ (in yellow, to the right). This same operation is repeated for each position (x,y), to build up the entire m-th image. The illumination pattern (row of **A**) is then changed, and the same process is repeated to complete a set of M images. The fact that the sampling vector A_m is the same for each pixel of the m-th compressed image means assuming that the illumination patterns used do not depend on x and y.*

6.4.2 Compressed imaging and reconstruction

Given the measurement matrix $\boldsymbol{A}$, the z-compressed imaging scheme can be formalized as depicted in Figure 6.3: the value of pixel (x,y) of the m-th compressed image is generated by multiplying the m-th row of the measurement matrix $\boldsymbol{A}$ by the column vector of values (x,y,z_i), with $i = 1,\ldots,N$. The assumptions behind this formalization are the following:

- the same measurement matrix is used for every position (x,y), which means assuming that each of the illumination patterns described by $\boldsymbol{A}$ is constant across the imaging FoV;
- for simplicity, I assume the sample to be sparse in the spatial domain along the z-direction, without making any assumptions about its structure along x and y, nor considering the 3D imaging PSF of the system; following this, the reconstruction of the z-profile behind each (x,y) is treated as an independent compressive problem.

Following these assumptions, I decided to speed up the simulations by testing the compressed imaging scheme on a single x-z plane. For this purpose, I created a synthetic image representing one x-z section of a 3D sample, and named it **O** (object). I then simulated the plane-by-plane and the z-compressed imaging scheme following a similar procedure to the one explained in [68] (see Figure 6.4). To simulate a conventional plane-by-plane imaging scheme, I corrupted the image **O** with Poisson (P) and Gaussian (G) noise, given a certain SNR (SNR = 100 in the example of Figure 6.4), obtaining a plane-by-plane image $\boldsymbol{PbP}_{SNR} = P(\mathbf{O}) + G(\text{SNR})$. In parallel, I simulated imaging the same **O** using the z-compressed imaging scheme. In order to do so, I applied the measurement matrix $\boldsymbol{A}$ to **O** considering different values of M (*i.e.* varying the number of rows of $\boldsymbol{A}$), and subsequently applied Poisson and Gaussian noise as for the images generated with the plane-by-plane acquisition scheme: $\boldsymbol{C}_{M,SNR} = P(\boldsymbol{A}_M\mathbf{O}) + G(\text{SNR})$. I used these noisy compressed images $\boldsymbol{C}_{M,SNR}$ to reconstruct the original object, obtaining $\mathbf{RO}_{M,SNR}$ (Reconstructed Object). For the reconstruction, I

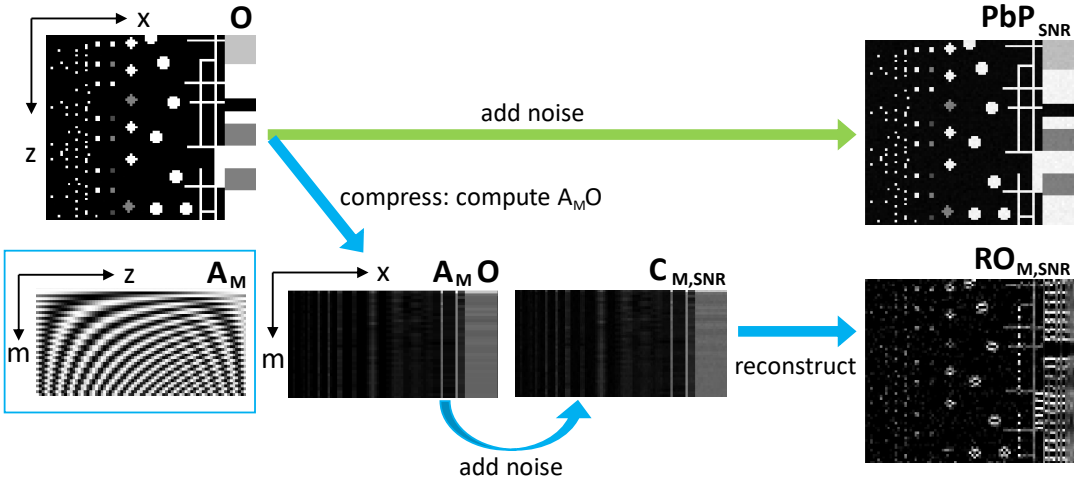

Figure 6.4: *Principle of the simulations: an x-z image is generated and used as the original object which needs to be imaged (**O**). Given a certain SNR (in this case SNR = 100), a noisy plane-by-plane image ($\boldsymbol{PbP}_{SNR}$) is generated by adding Poisson and Gaussian noise to **O** (green arrow). In parallel (blue arrow), the original object **O** is compressed along the z-axis by sampling it using matrix $\boldsymbol{A}_{\boldsymbol{M}}$ (with, in this case, $M = N/2$). The set of M compressed images ($\boldsymbol{A}_{\boldsymbol{M}}\boldsymbol{O}$) is then corrupted with noise as done for the plane-by-plane images, to obtain a noisy, compressed set of M images ($\boldsymbol{C}_{\boldsymbol{M,SNR}}$). The compressed images are decompressed to obtain a reconstruction of the original object, $\boldsymbol{RO}_{\boldsymbol{M,SNR}}$.*

used the l_1-magic library developed by Romberg and Candes in 2005 [93]. The implementation I chose is the one that tries to solve the following problem (called *basis pursuit*):

$$\min||x||_{l_1} \text{ s.t. } y = Ax, \tag{6.10}$$

i.e. tries to find the vector x with the smallest l_1-norm which explains the observations y. This l_1-magic implementation solves problem 6.10 by using the Newton method inside a so-called primal-dual algorithm, a second-order method. I repeated this procedure for different values of SNR, computing the standard deviation of the Gaussian noise as the mean of the non-zero pixels of the original image **O** divided by the desired SNR.

6.4.3 Evaluation

Figure 6.5 shows the results obtained running the simulation with SNR = 100 and, for the compressed scheme, compression ratios k = 2, 5, 10, 20. In order to be able to see how the reconstruction behaves in different scenarios, I generated an original object **O** which contains features of different sizes and regions (columns) characterized by different levels of sparsity. From this figure it can already be noticed how, even at the lowest compression ratio k = 2, regions of low spatial sparsity (right side of the object) are not well reconstructed. On the other hand, columns characterized by high sparsity (along z) are well reconstructed for a low compression ratio (regions highlighted in yellow in Figure 6.6a), and the quality of their reconstruction appears to deteriorate quite fast as the compression ratio increases (see Figure 6.5 and the plot of Figure 6.6b).

Figure 6.6 helps looking at these results into more details, showing a zoom-in on a region of the original object **O**, and comparing it to the same region taken from the object reconstructed from a set of $M = N/2$ compressed measurements (compression ratio $k = N/M = 2$). In Figure 6.6a, areas of high spatial sparsity are highlighted in

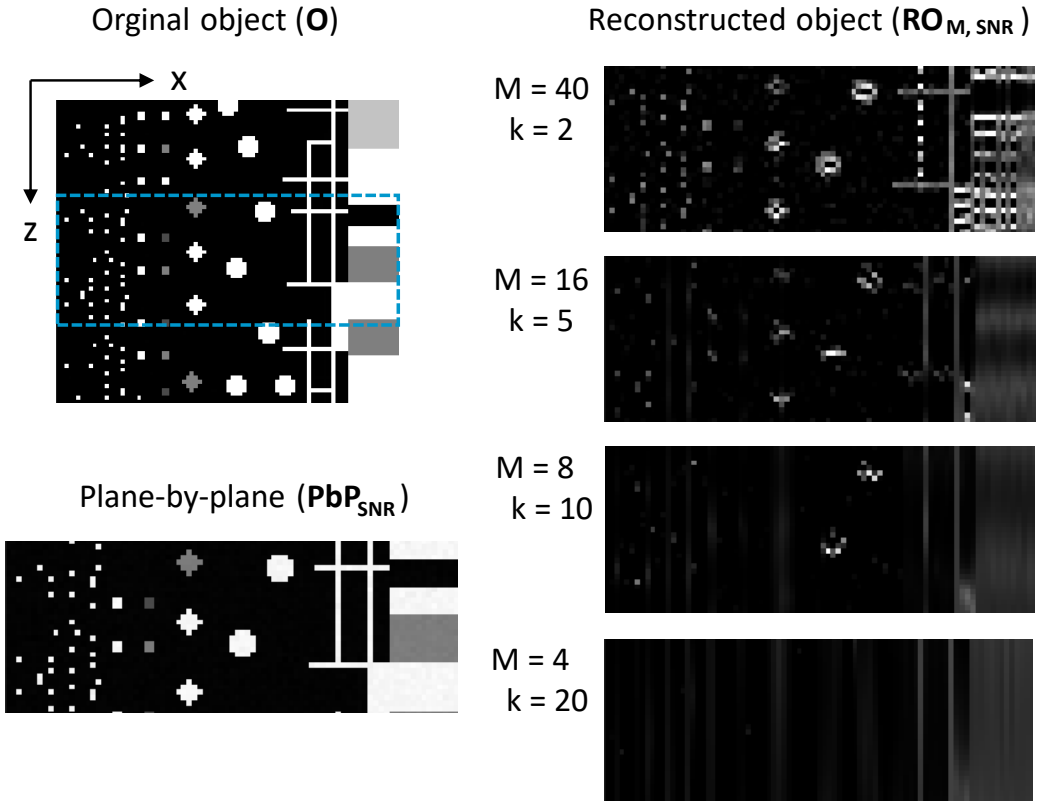

Figure 6.5: *Results of the simulations obtained using SNR = 100 and, for the compressed scheme, compression ratios k = 2, 5, 10, 20. Top left: original object* ***O****, containing features of different sizes and regions (columns) characterized by different levels of sparsity. Bottom left: plane-by-plane image the object (zoom in on the region of the in the original object highlighted in blue). Right: compressed reconstruction of the object for different compression ratios (zoom in on the same region of the original object, increasing compression ratio from top to bottom).*

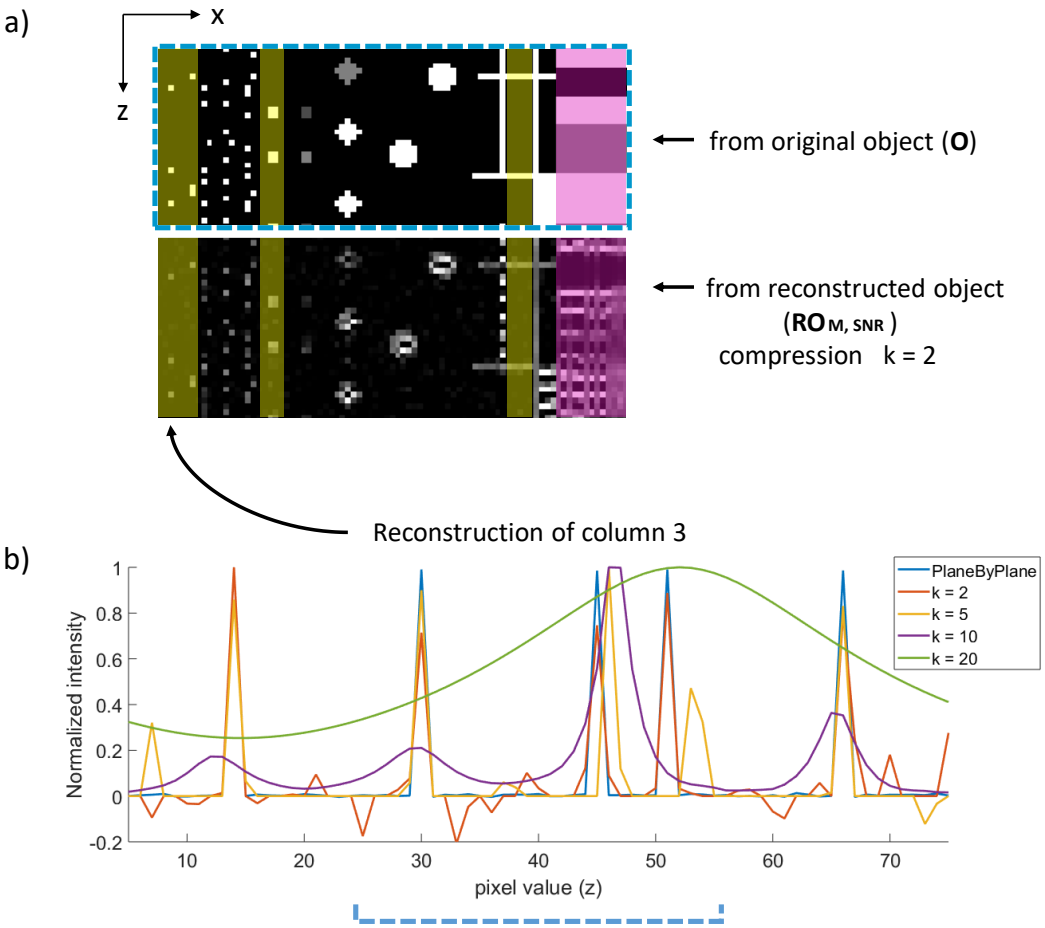

Figure 6.6: *Analysis of the simulation results. (a) Visual comparison between a region of the original object* ***O*** *and the same region taken from the object reconstructed from a set of M = N/2 compressed measurements (compression ratio k = N/M = 2). In pink a region of low sparsity (sparsity along z, vertically in the image) and in yellow regions of high sparsity. (b) Plot of the third column of the plane-by-plane image and of each of the 4 compressed reconstructed objects (each with a different compression ratio). The dashed blue line along the horizontal axis of this plot shows the interval of values visible in the region of the object shown in (a). The third column of the object contains 3 small features (5 in total, but only 3 within the region selected for this figure), and they are visible as 3 white dots along the third column of pixels in (a) and 3 sharp peaks in the plane-by-plane plot in (b).*

yellow, and areas of low sparsity in pink. By looking at this figure, it can be seen more clearly how for a compression ratio $k = 2$ the small features in the yellow areas are well reconstructed, while the big features in the pink area are reconstructed as a series of lines. A similar effect can also be noticed in the region of medium sparsity, at the center of the object, where the white circles and squares are reconstructed with a striped profile. As a suggestion for future works, it would be interesting to investigate on what exactly is causing this effect in the reconstruction, which I speculate could be a result of the reconstruction algorithm *forcing* some level of sparsity on the reconstruction.

For the first experiments with this compressed image acquisition scheme on the SLM-SPIM, I decided to image sparse samples of small fluorescent beads, and I therefore decided to look into more details at the simulated reconstruction of the sparse region of the object. Figure 6.6b contains a plot of the third column of values of the plane-by-plane object together with a plot of the same column taken from each of the compressed reconstructed objects (one column plotted for each k, with $k = 2, 5, 10, 20$). This column contains a series of small objects (white dots), each of which is seen by the plane-by-plane imaging scheme as a sharp peak in z (blue plot in Figure 6.6b). It can be noticed that, for $k = 2$, all the peaks are reconstructed in the correct positions (red plot), while for $k = 5$ two peaks are not reconstructed correctly (yellow plot). For higher compression ratios the peaks start becoming much smoother, and close by peaks seem to start being recognized by the reconstruction algorithm as one single object (see the single smooth peak for $k = 20$).

Overall, these simulations seem to suggest that, at least if the sample is a 3D sparse distribution of small objects, the proposed set of illumination patterns should allow for a successful reconstruction with a compression ratio $k = 2$. Following these suggestions, I decided to start the experiments on the SLM-SPIM by imaging a sparse sample of fluorescent beads embedded in agarose, acquiring a number $M = N/2$ of images using the above described illumination patterns. A subset of the $N/2$ acquired images can later be used to try and reconstruction the same 3D sample at a higher compression ratio.

6.5 Experiments

6.5.1 Measurement matrix generation

To perform the experiments on the microscope, the chosen measurement matrix needs to be translated into a set of light patterns. The truncated Fourier matrix discussed in the simulation section corresponds to a series of sinusoidal intensity patterns of different periods. Woringer *et al.*, who have used this type of matrix as measurement matrix [68], generated the sinusoidal intensity variations along z by modulating the intensity of a thin light-sheet (generated with a lattice light-sheet microscope [69]) during its z-scan. They performed a z-scan of the light-sheet within each single camera exposure, and scanned the imaging objective together with the light-sheet in order to keep it in focus. Our aim is instead to try and generate the desired illumination simultaneously across the whole imaging volume. The main advantage of this approach is a reduction of the maximum laser intensity experienced at any time by any point in the sample. Consider in fact a compressed image acquired with an exposure time t_{exp} using a light pattern which is spread simultaneously across the whole imaged volume (our suggested approach), and which illuminates a point P with a laser intensity I. Following the illumination approach

suggested by Woringer et al [68], point P would be illuminated only for a small fraction of t_{exp}, which means that to obtain the same fluorescent signal the point would need to be illuminated with a much higher laser intensity.

To create the desired light patterns, I used a technique similar to the one used to create the structured illumination patterns described in Chapter 4 (Section 4.3.1). In the structured illumination case, the interference is generated using two light-sheets that propagate on the same plane but in two slightly different directions, resulting in a structured light-sheet which is confined in z, propagates along x and has a sinusoidal profile along y (see Figure 6.7a). Instead, the illumination patterns needed for the Fourier matrix extend over a Δz bigger than the thickness of a normal light-sheet (tens of microns instead of a few microns), covering the entire volume that one is trying to image (and later reconstruct) in a compressed way. The z-axis is also the direction along which we want these illumination patterns to have a sinusoidal intensity profile. This sort of z-oriented structured illumination can be generated by interfering two collimated beams which propagate at opposite angles with respect to any $x-y$ plane [63], as depicted in Figure 6.7b. Similarly to the structured illumination case, the period of the interference pattern can be changed by modifying the angle between the two interfering beams.

In order to generated the desired interference patterns using the SLM-SPIM's reflective phase-only SLM, I followed the approach proposed by Judkewitz *et al.* in their 2014 article about axial standing-wave illumination frequency-domain imaging (SWIF) [63]. Using a reflective phase-only SLM, they turned a collimated beam into two beams interfering in the sample plane creating a series of illumination patterns modulated along the z-direction (see Figure 6.8). In their case, the generated illumination patterns were used to encode the axial profile of the sample in the Fourier domain. The SLM patterns Judkewitz *et al.* used to generate the two interfering beams are made of two interlaced blazed gratings (one for each of the two interfering beams): the SLM active area is dived into stripes (in my experiments I used a stripe width of 4 pixels) and the two blazed gratings are displayed alternately on every other stripe (see example pattern in Figure 6.8). The interference period can be controlled by changing the period of the blazed gratings (*i.e.* the angle between the two interfering beams), and the whole interference pattern can be shifted along the z-direction by adding a phase-shift to one of the two gratings.

The spacing between the interference fringes of the final pattern (δz) is related to the half angle α between the two beams by

$$\delta z = \frac{\lambda}{2 \cdot n \cdot \sin(\alpha)},$$

where n is the refractive index of the medium and λ is the wavelength of the laser. As the above formula suggests, in order to obtain high frequency patterns one needs to increase the angle α between the two interfering beams. On our system there are a few factors limiting the maximum angle α achievable. First of all the angle α is linked to the size of the period of the blazed grating displayed on the SLM, with a big α corresponding to a short period. The size of the SLM pixels therefore sets a first limit to the maximum achievable α, with the minimum period size corresponding to 3 SLM pixels. Secondly, as discussed in Chapter 4, smaller periods of the SLM patterns result in a decreased amount of light concentrated in the 1^{st} diffraction order, which leads to a dimmer final pattern. After evaluating the experimental quality of different interference patterns (more details in Section 6.5.3), I decided to consider

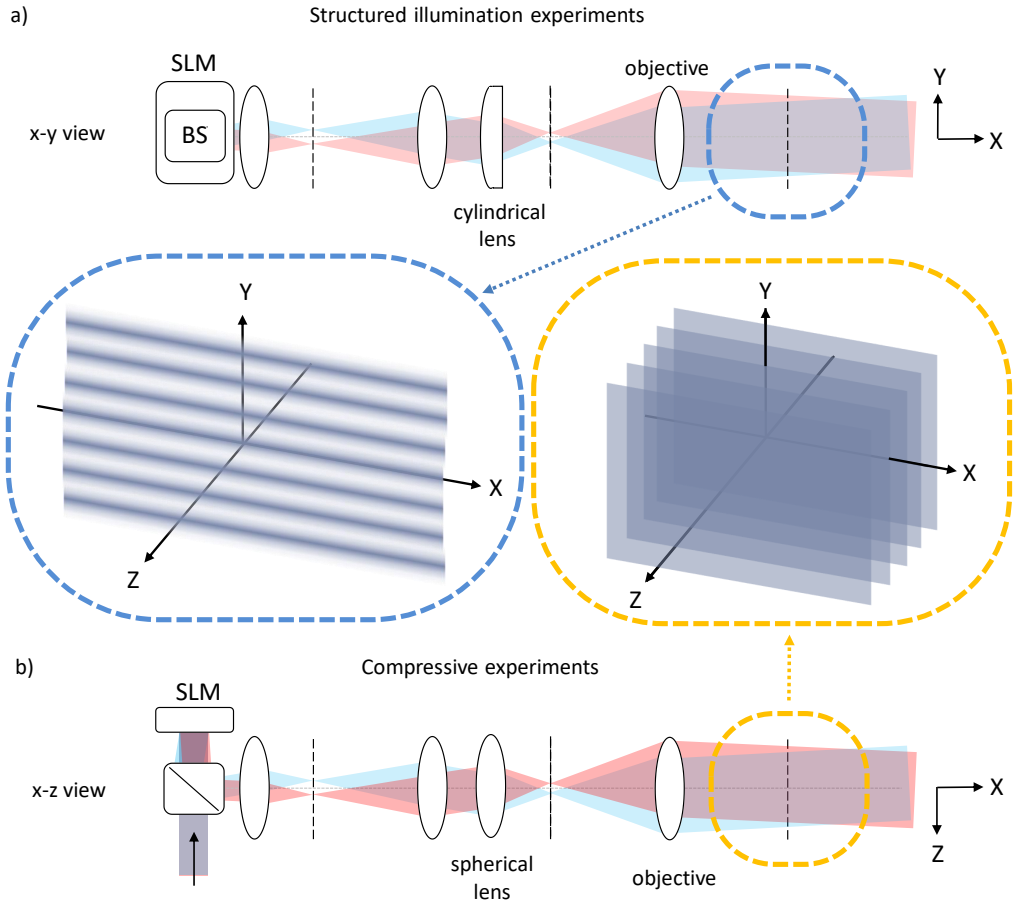

Figure 6.7: *Scheme of the final part of the SLM-SPIM's launching arm illustrating the formation of a structured light-sheet (a) to be used for structured illumination experiments (described in Chapter 4, Section 4.3.1), and a structured volume-illumination (b) which can be used for compressive volume imaging. The structured light-sheet (blue dashed zoom in the Figure) generates from the interference of two light-sheets (blue and red light-sheets in (a)) which propagates on the same $x-y$ plane but at two slightly different angles; the period of the interference pattern of the final light-sheet depends on the angle between the two interfering light-sheets. On the SLM-SPIM, the light-sheet that comes out of the excitation objective can be turned into a collimated beam by replacing the cylindrical lens of the SLM-SPIM with a spherical lens. In a similar way to what is done to generate a structured light-sheet, the SLM can be used to split the beam into two beams and make them propagate along two slightly different directions (b). The two beams focus onto two points at the back focal plane of the launching objective, and if these two points are located at the same value of y but at two different values of z (as in (b)), the final beams will generate a structured illumination characterized by a sinusoidal intensity profile along the z-direction (visualised as a series of illuminated planes in the orange dashed zoom in the Figure).*

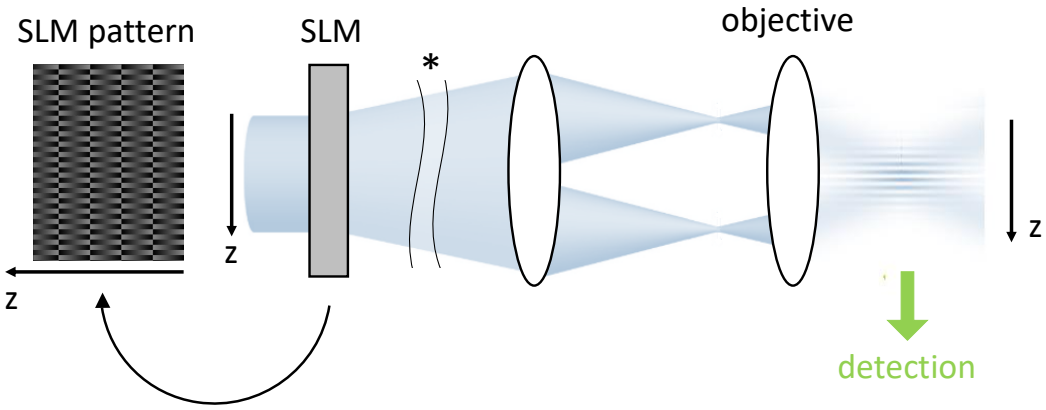

Figure 6.8: *Illustration of how the patterns for the compressive experiments can be generated following the technique presented by Judkewitz et al. in 2014 [63]. This scheme illustrates the same situation as the one depicted in Figure 6.7b, but simplifies the optics (missing parts synthesized by '*' and reflective SLM depicted as a transmissive element) and shows an example SLM phase mask (left). In order to generate a volume illumination with a sinusoidal intensity profile along the z-direction, the SLM is divided into stripes (in my experiments I used a stripe width of 4 pixels), and two blazed grating are displayed alternately on every other stripe. The two gratings split the beam into two beams which focus at different values of z at the back focal plane of the excitation objective, generating the desired interference pattern onto the sample.*

3 μm to be the minimum spacing δz between the interference fringes of the final pattern achievable with our system. The measurement matrix $\boldsymbol{A}$ used in the experiments presented in this chapter is made of 61 patterns (maximum $M = 61$), with interference periods going from 90 μm to 3 μm, with the first pattern corresponding to uniform illumination. A full Fourier matrix with minimum pattern period equal to 3 μm allows to reconstruct a 90 μm thick volume with a z-resolution of 1.5 μm ($M = N = 61$). These patterns were therefore initially designed to image a volume of a total z-thickness of 90 μm, and compare its reconstruction with a reference 3D image of the same volume acquired using a plane-by-plane scheme made of a total of 61 images ($N = 61$), for a z-resolution of 1.5 μm. For my first experiments, I instead decided to image the 90 μm using a plane-by-plane scheme made of a total of 121 images ($N = 121$), for a z-resolution of 0.75 μm, and compare this reference volume with the reconstruction obtained using the 61 patterns of $\boldsymbol{A}$, considering that the maximum value of M I could test for was $M = 61 = N/2$ (minimum compression ratio $k = N/M = 2$).

As mentioned before, in the proposed z-compressed scheme, each image pixel (*i.e.* each (x,y) position on the imaged volume) is treated as an individual CS system to solve, with all the CS systems sharing the same measurement matrix $\boldsymbol{A}$. Knowing the exact shape of the illumination patterns (rows of $\boldsymbol{A}$) used in the compressed image acquisition is fundamental, and in the case of the chosen interference patterns it means knowing their amplitude (*i.e.* peak-valley intensity difference), period size (*i.e.* fringe spacing) and phase shift (*i.e.* position of the fringes along z). The characterization of the illumination patterns is described in Section 6.5.3, while the next

section introduces the two set-ups used for the CS experiments performed on the SLM-SPIM.

6.5.2 Set-up

The set-up used for the first compressive experiments performed on the SLM-SPIM is illustrated in Figure 6.9. This set-up is almost identical to set-up 3 of the SLM-SPIM (see Figure 3.2), apart from the use of a plano-convex lens with f = 75 mm in place of the cylindrical lens with f = 80 mm used in set-up 3. Substituting the cylindrical lens with a plano-convex lens turns the light-sheet into a collimated beam, and the choice of using a focal length of 75 mm was made to get as close as possible to a 4f-relay system (referring to Figure 6.9: the second lens after the beamsplitter should have f = 25 mm to make a 4f-relay system with the f = 75 mm lens, and f = 25.4 mm was the closest I could get to that). The imaging parameters for this set-up are the same as for the water experiments presented in Chapter 4: FoV $\simeq$ 440 μm $\times$330 μm, lateral resolution at $\lambda = 0.525$ μm of $\simeq$ 0.4 μm (calculated as $0.61 \times \lambda/\text{NA}$ for the 0.8 NA imaging objective), magnification = 20, DoF $\simeq$ 2 μm (calculated as $1.78 \cdot n \cdot \lambda_{em}/\text{NA}_{det}^2$, following formula 2.24 used for the axial resolution of the 0.8 NA detection arm).

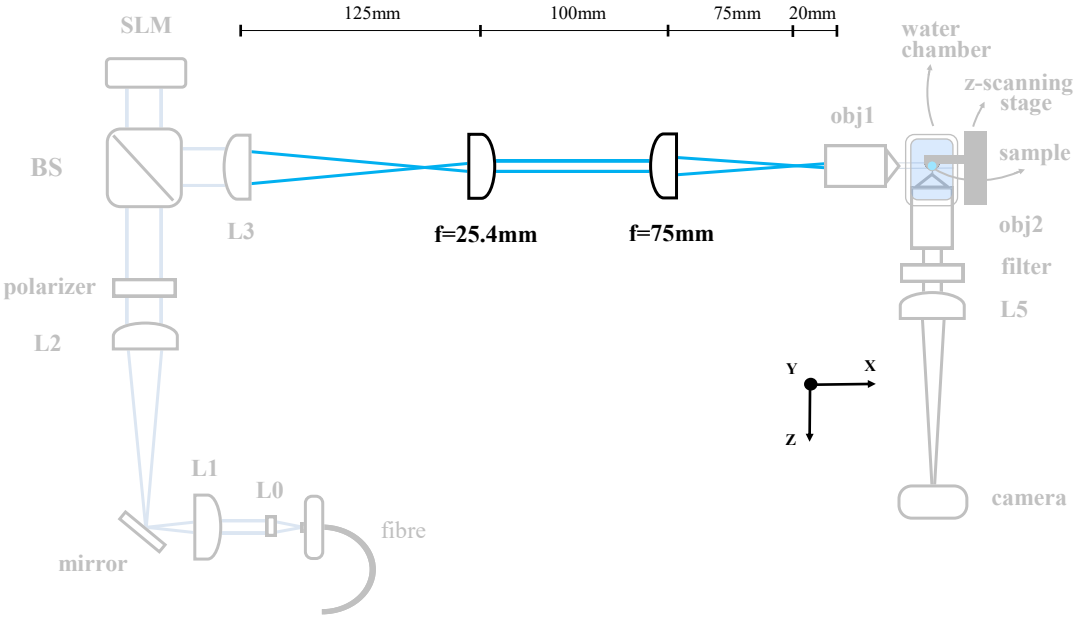

Figure 6.9: *Set-up used for the first round of compressive experiments. This set-up is almost identical to set-up 3 of the SLM-SPIM (see Figure 3.2), apart from the use of a plano-convex lens with f = 75 mm instead of the cylindrical lens with with f = 80 mm used in set-up 3.*

Figure 6.10 illustrates the set-up used for the second round of compressive experiments. This set-up, which I from now on refer to as the 0.3 imaging NA set-up, shares the laser expanding elements and the SLM with all the other set-ups described so far. Inserting a mirror after the first lens following the beam splitter (top right mirror in Figure 6.10) makes it possible to switch to this set-up without having to move any of the components of the rest of the system. I designed the illumination arm of this set-up so that a given SLM mask would generate the same final interference pattern on this set-up and on the 0.8 imaging NA set-up described above (refer

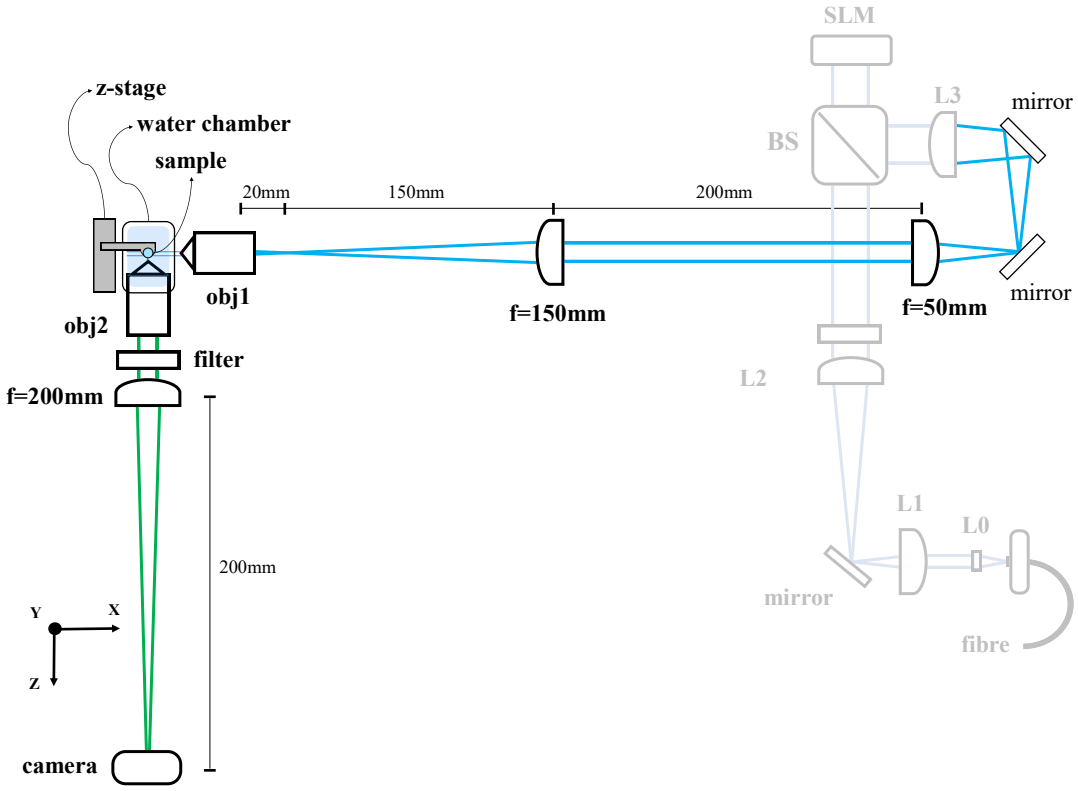

Figure 6.10: *Set-up used for the second round of compressive experiments. The illumination objective used on this set-up is identical to the one mounted on the 0.8 NA imaging arm (10× Nikon Plan Fluorite Objective, 0.3 NA, 16 mm WD (air)), while on the imaging side this set-up uses a lower NA imaging objective (10× Nikon CFI Plan Fluorite Objective, 0.3 NA, 3.5 mm WD, water dipping) which gives a much higher DoF (theoretical DoF increased from* $\simeq$ *2 µm for the 0.8 NA imaging objective to* $\simeq$ *14 µm for the 0.3 NA imaging objective). The camera and the filter are also identical to those used in the higher NA set-up.*

to the caption of Figure 6.10 for details on the optical components used). By this I mean that an SLM mask designed to generate, on the 0.8 imaging NA set-up, an interference pattern with a certain spatial frequency can be used on the 0.3 imaging NA set-up to generate an interference pattern with the same spatial frequency. The 0.3 NA imaging objective used in this set-up, the camera (which is the same camera used on the 0.8 NA detection arm), and the 200 mm tube lens give the following imaging parameters: FoV $\simeq$ 880 µm ×660 µm, lateral resolution at $\lambda = 0.525$ µm of $\simeq$ 1 µm (calculated as $0.6 \times \lambda / NA$ for the 0.3 NA imaging objective), magnification = 10, DoF $\simeq$ 14 µm (calculated as $1.78 \cdot n \cdot \lambda_{em}/\mathrm{NA}_{det}^2$, following formula 2.24 used for the axial resolution of the 0.8 NA detection arm).

6.5.3 Pattern characterization

In order to check the shape of the 61 illumination patterns that the chosen measurement matrix **A** is made of, I generated them in the water chamber of the 0.3 imaging NA set-up and imaged their z-profile using a mirror mounted in the chamber (mirror aligned at 45 degrees to both the illumination and imaging optical axis, as depicted in Figure 6.11a). Removing the fluorescence filter from the imaging arm, the $y-z$

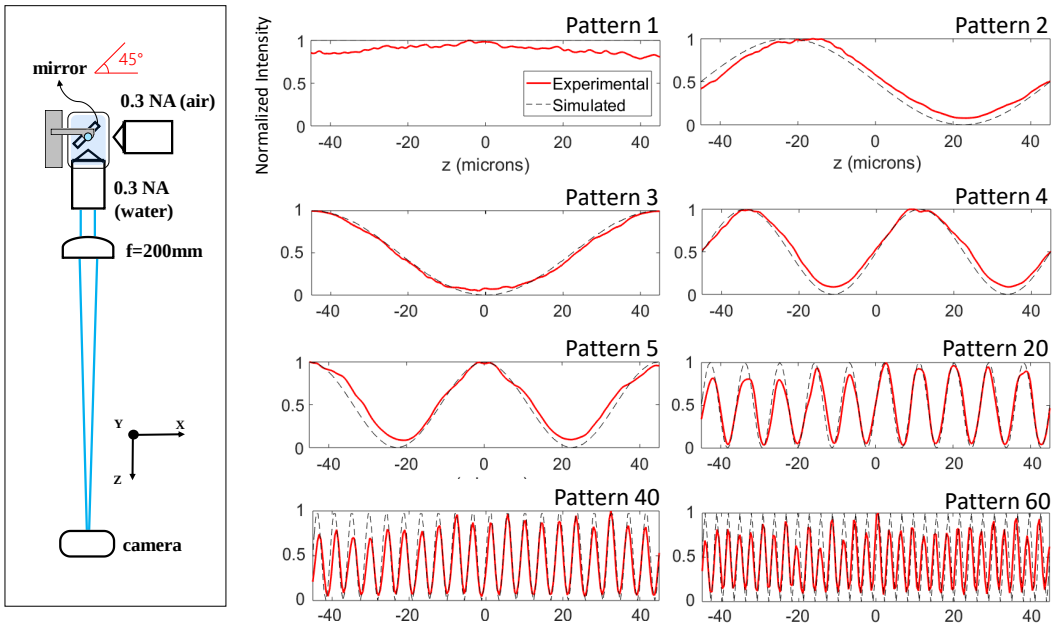

Figure 6.11: *Characterization of the illumination patterns used for the compressive experiments. Left: Set-up used to analyse the z-profiles of the illumination patterns (only showing the components between the excitation objective and the camera). A mirror was mounted inside the chamber of the 0.3 imaging NA set-up and aligned at 45 degrees at the intersection of the excitation and imaging optical axes. The mirror reflects the patterns generated in the chamber and makes it possible to image their $y - z$ profile directly onto the camera. Right: 8 plots showing the central 90 microns of the z-profiles of 8 of the 61 illumination patterns (experimental z-profiles in red and corresponding simulated z-profiles in black/dashed). Each experimental z-profile was obtained by summing 100 rows of the image obtained for that pattern (yellow rectangle in Figure 6.12). The simulated profiles were set to have intensities from 0 to 1 and the experimental z-profiles were plotted after normalization to their own maximum.*

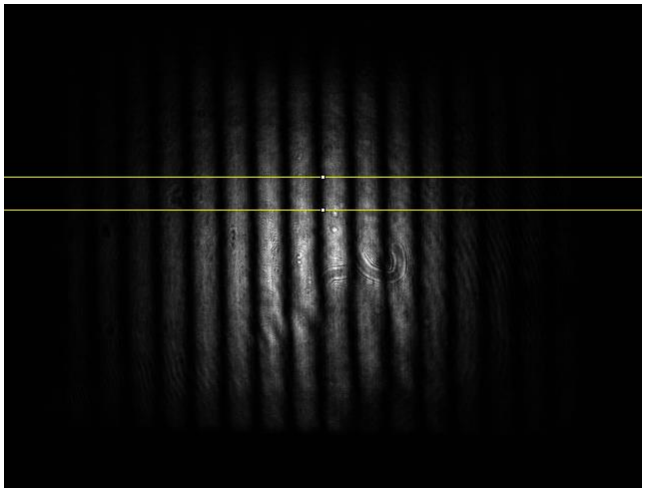

Figure 6.12: *Example of one of the images acquired to analyse the experimental z-profile of the patterns used for the compressive experiments (in this case the Fourier pattern with spatial frequency 45 µm). This image was taken using the profiling set-up described in the main text and illustrated in Figure 6.11a, and the yellow rectangle highlights the 100 rows which were summed to extract the z-profile of the pattern (some example z-profiles are plotted in Figure 6.11.*

profile of the patterns can be imaged directly onto the camera, with the z axis projected along the horizontal direction of the image (see example image in Figure 6.12).

Figure 6.11 shows the central 90 microns of the z-profiles of 8 of the 61 illumination patterns. Each of the plotted z-profiles was obtained by summing 100 rows of the image obtained for that pattern (yellow rectangle in Figure 6.12). This integration was done to reduce the distortions of the profiles generated by imperfections of the mirror and reflections from small particles in the water (distortions clearly noticeable in the example image of Figure 6.12).

As it can be seen from the profiles plotted in Figure 6.11, the experimental patterns seem to match well with their corresponding simulated profiles, both in terms of their period (distance between the peaks) and their phase (z-position of the peaks). On the other hand, as the frequency of the patterns increases, the contrast (peak to valley intensity difference) seems to degrade and it also starts showing some variability from peak to peak.

For the compressive reconstruction, I used the theoretical shape of $\mathbf{A}$, *i.e.* the simulated profiles shown in Figure 6.11, but with their intensity normalized to go from 0 to $1/N$. For this reason, I expected every difference between the simulated and experimental profiles to affect (decrease) the quality of the reconstruction. In order to improve the quality of the reconstruction, one could try and see if it is possible to make the shape of the experimental patterns coincide better with their simulated version which is used for the reconstruction. A second option could be to characterize the experimental patterns more precisely and change the matrix used for the reconstruction to make it represent better the actual shape of the patterns used for imaging. While discussing possible ways to improve the match between the patterns used for the reconstruction and those used for imaging, it should be noted that the profiles plotted in Figure 6.11 are each normalized to its own maximum. Before the normalization, I could observe a relative difference between the actual maximum intensity of the patterns. This difference could be used to either adjust their maximum intensities to the same value (by rescaling the laser power used for each pattern) or rescale the rows of $\mathbf{A}$ to match the observed relative values.

Another aspect which I find worth discussing here is the overall shape of the imaged z-profiles: Figure 6.11 shows only the central 90 μm of the z-profiles, but, as it can be seen from Figure 6.12, over a bigger z-extent their intensity is actually modulated by the Gaussian envelope of the original laser beam. Since this modulation is not significant within a z-range of 90 μm, I decided not to take it into account when building the matrix $\mathbf{A}$ used for the reconstruction. It should also be noted that on this set-up (and even more so on the 0.8 imaging NA set-up), features that are outside a z-range of 90 μm are seen so out-of-focus by the camera that they only contribute to a diffused background in the acquired images. In fact, a drop in the intensity of the patterns beyond the z-range that one is trying to reconstruct can only help improve the quality of the acquired images (and therefore reconstruction). Ideally, the illumination should be confined within the z-range of the reconstruction, especially when using a sample which extends in z beyond that reconstruction z-range. On our set-up, it would be interesting to try and confine the illumination along z using a rectangular slit at the back focal plane of the excitation objective.

The pattern of Figure 6.12 also shows the presence of a Gaussian intensity envelope along the y direction, which I decided not to incorporate to the matrix $\mathbf{A}$ used for the reconstruction. In this case I expected this difference between the vectors used for the reconstruction and the shape of the patterns used for imaging to affect the relative brightness of points reconstructed at different y-positions in the FoV, with the center (in y) of the volume appearing brighter than the rest, following a similar

modulation to the one observed on the experimental patterns. This effect could be corrected by incorporating the observed y-intensity modulation to the theoretical patterns used for the reconstruction.

6.5.4 Imaging NA: 0.8

For the initial experiments I decided to image a sparse sample of 0.2 μm fluorescent beads suspended in agarose (in a FEP tube mounted to the tip of a syringe, as done for the experiments described in the previous chapters). The aim of these experiments was to see if the proposed compressive imaging scheme is able to reconstruct the correct z-position of the beads. When imaging beads which are smaller than the z-resolution of the reconstructed volume (which is 0.75 μm), the z-position of a bead should be identified by a sharp peak in the z-intensity profile of the reconstructed volume at the (x, y) position of the bead.

The DoF given by the 0.8 NA imaging objective is $\simeq$ 2 μm, which means that I expected only beads located within a $\Delta z \simeq 2$ μm to appear as completely in-focus in the set of compressive images. Beads seen with a certain degree of out-of-focus should be reconstructed as disks located at a certain position in z, while I expected extremely out-of-focus beads to only contribute to a diffused background.

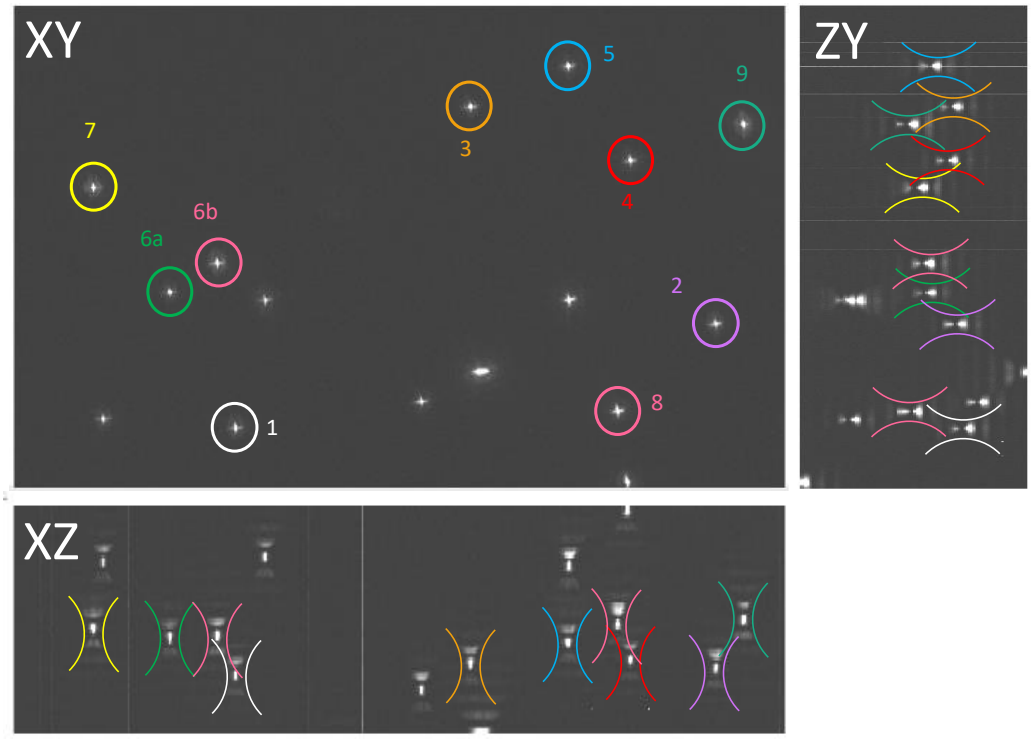

Figure 6.13: *Maximum Intensity Projections (along z,x and y) of a z-stack of a sample of 0.2 µm fluorescent beads suspended in agarose. The stack was acquired with a z-step of 0.5 µm while using a 3 µm interference pattern to illuminate the sample. I extracted the z-position of 10 beads (circled) and also used this dataset to confirm that the interference pattern used showed a period size of 3 µm (visible in the $x-z$ and $z-y$ projections). I named two of the beads 6a and 6b because they are located at the same position in z.*

As a first step, I took a z-stack of the bead sample, which I needed as a reference to compare the real position of the beads in z with the positions reconstructed using the

compressive imaging scheme. To acquire the z-stack, I moved the beads through the sample using a z-step of 0.5 μm, but, instead of using a cylindrical lens to generate a light-sheet, I acquired all the images of the stack using the 3 μm interference pattern to illuminate the sample. This dataset served a double purpose: to check the relative position of the beads within the sample and to check whether the size of the finest interference pattern still matched its theoretical value of 3 μm, even when generated within the FEP tube. Figure 6.13 shows the maximum intensity projections (along z,x and y) of the acquired z-stack. I selected 10 beads within the imaged volume (circled beads in Figure 6.13) and extracted their relative z-positions (more details on this below), while using the $x-z$ and $z-y$ projections of the z-stack I confirmed that the interference pattern used showed a period size of 3 μm.

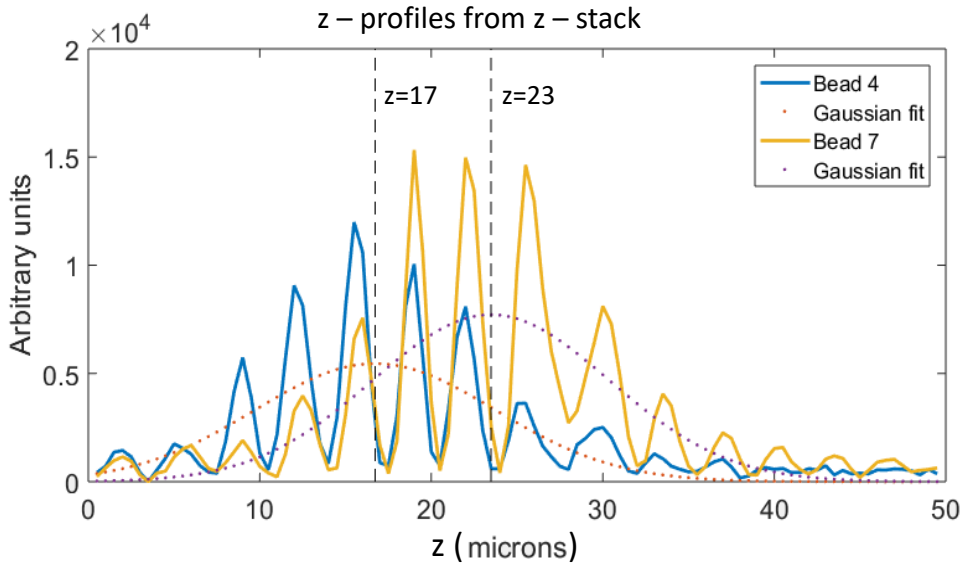

Figure 6.14: *Extraction of the z-positions of the beads from the z-stack acquired while illuminating the sample with the 3 µm interference pattern. The plot shows two of the ten z-profiles extracted from the z-stack (one z-profile for each of the ten selected beads). Each z-profile was generated by selecting a small square (in x and y) around the position of a bead, and, for each image of the z-stack, summing all the values within the square. Each z-profile was fitted with a Gaussian curve (dotted lines) to find the position of the bead (dashed lines indicating the center of the fitted curves, ±0.25 µm). These z-profiles also reveal the 3 µm interference pattern used as illumination during the z-scan.*

In order to find the relative z-positions of the selected beads, I extracted from the z-stack one z-profile for each bead. Each z-profile was generated by selecting a small square (in x and y) around the position of the bead, and, for each image of the z-stack, summing all the values within the square. In Figure 6.14 I plotted the z-profiles extracted for two of the ten selected beads (blue and yellow curves). These z-profiles reveal the 3 μm interference pattern used as illumination during the z-scan. It can also be noticed that, as the sample is moved along z, the amount of light hitting the selected squares increases as the bead gets into focus and then decreases as it goes out of focus again. In fact, as the bead goes out of focus, more and more of the fluorescence coming from it hits the detector outside the selected square. To find the z-position of each bead I fitted each z-profile with a Gaussian curve (dotted lines in Figure 6.14), and identified the position of the bead with the center of the Gaussian fit (dashed lines in Figure 6.14). In doing this, I rounded the center of the Gaussian curves to the closest half micron, so I assigned the position of the beads an uncertainty of ± 0.25 μm. I found the total distance between the first and the last of the selected beads to be 11 μm.

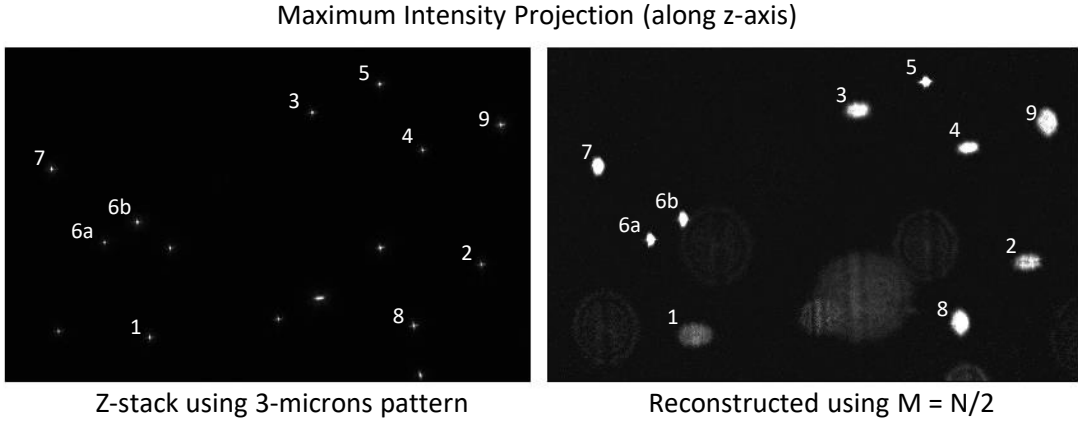

Figure 6.15: *Left: Maximum Intensity Projection, along z, of the $x-y$ region of the z-stack which contains the 10 selected beads. Right: Maximum Intensity Projection of the same $x-y$ region, but this time of the volume reconstructed from a set of compressive images (shown as over-saturated to make the out-of-focus beads visible). The reconstructed volume is made of 121 planes, with a z-resolution of 0.75 μm, for a total z-range of 90 μm, and was reconstructed using a set of 61 compressive images (N = 121, M = 61).*

As a second step I performed the compressive imaging. First, I repositioned the sample in z to have the 10 chosen beads as in focus as possible. Then, I acquired a set of compressive images using the 61 illumination patterns described in the previous sections (M = 61), and reconstructed the original volume (made of N = 121 planes spaced of 0.75 μm, for a total reconstructed z-range of 90 μm) using the chosen compressive reconstruction algorithm (described in Section 6.4.2). Figure 6.15 shows the maximum intensity projection, along z, of the $x-y$ region of the volume which contains the selected beads (MIP of the z-stack on the left and MIP of the reconstructed volume on the right, with the second one shown as over-saturated to make the out-of-focus beads visible). Figure 6.16 shows the maximum intensity projection of the reconstructed volume only, but with the z-direction color-coded, and arrows along the colorbar indicating the real z-position of the beads (as extracted from the z-stack). The bottom plot of Figure 6.16 illustrates the same data in a different way. In order to generate the profiles plotted in Figure 6.16 I selected a square (in x and y) in the reconstructed volume around each of the 10 selected beads and integrated over x and y to get a single vector of N = 121 values for each bead; the plot in Figure 6.16 shows the 21 central values of the 10 obtained vectors. The peaks in the plot indicate the z-positions where the beads were reconstructed at, and the vertical dashed lines indicate the z-positions extracted from the z-stack (in grey the ± 0.25 μm uncertainty which I assigned to the extracted z-positions).

The plot in Figure 6.16 shows that some of the beads were reconstructed at the correct position in z: beads 1, 4, 5, 6b, 7 and 8 show a peak at their z-position extracted from the z-scan ± 0.25 μm. On the other hand, bead 9 was reconstructed a bit too close to bead 8 (peak of bead number 9 outside the ± 0.25 μm range from its z-position extracted from the z-scan), while beads 2, 3 and 6a are not reconstructed as a sharp peak in z even though they seem to be reconstructed at the correct positions along z.

By looking at the reconstructed z-profiles of beads 2, 3 and 6a, plotted in Figure 6.16, I noticed that the central peak possibly seemed to be missing because of a too low

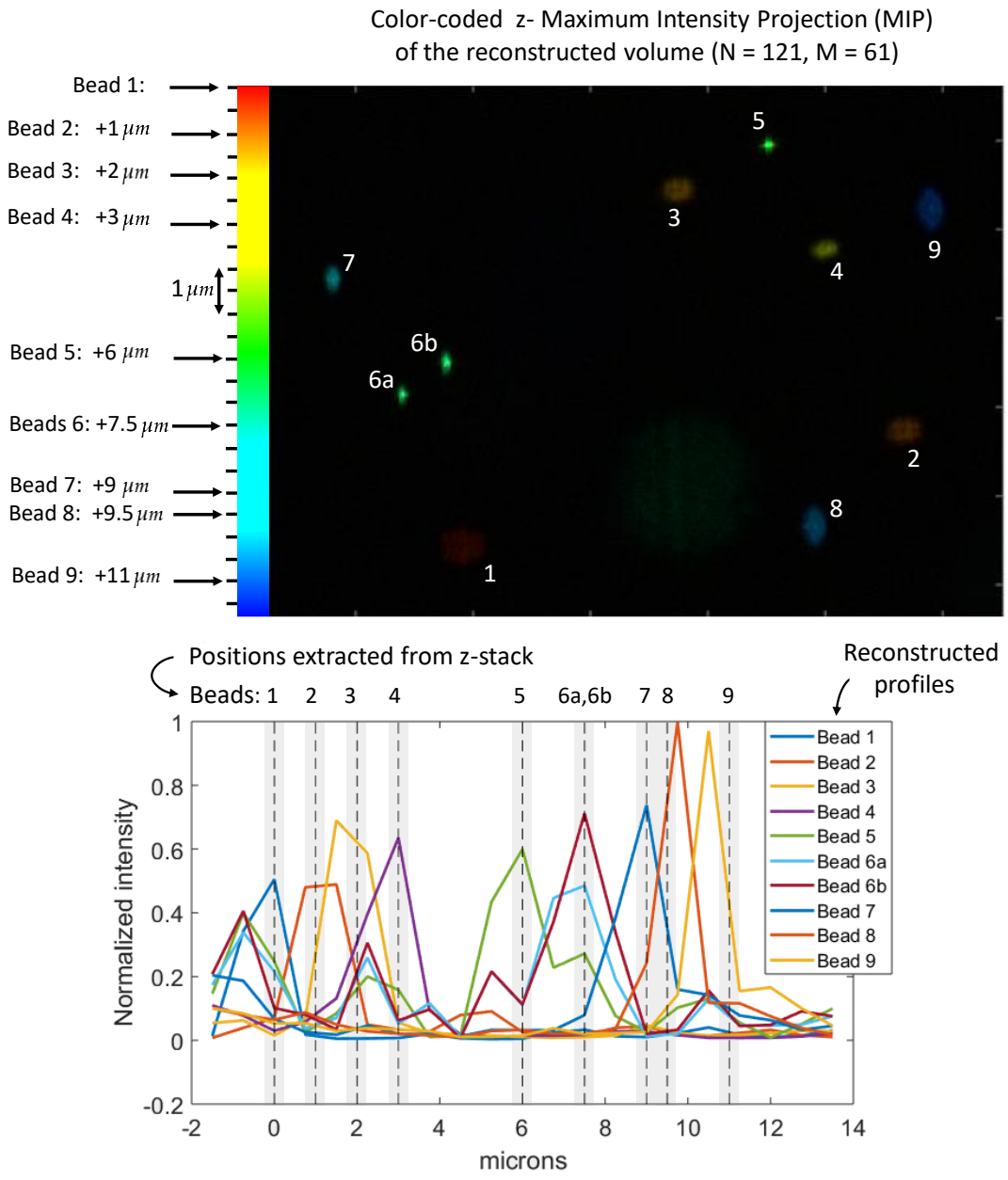

Figure 6.16: *Top: Maximum Intensity Projection of a compressive reconstruction of the volume of beads (same as on the right side of Figure 6.15: volume made of N = 121 planes, with z-resolution of 0.75 μm, reconstructed from M = 61 compressive images). In this MIP the z-direction is color-coded, and arrows along the colorbar indicate the z-position of the beads extracted from the z-stack. Bottom: Different visualization of the reconstructed z-positions of the same 10 beads. Each plot in this figure was obtained by selecting a square in x and y, in the reconstructed volume, around the position of a bead, and integrating over x and y to get a single vector of N = 121 values (only the 21 central values are shown in this figure). The 10 plotted z-profiles are all normalized to a global maximum (peak of bead 8). The vertical dashed lines indicate the relative position of the beads along z, information which was extracted from the z-stack (in grey the ±0.25 μm uncertainty which I assigned to the estimated z-positions). The peaks in the plots indicate the z-positions where the beads were reconstructed at.*

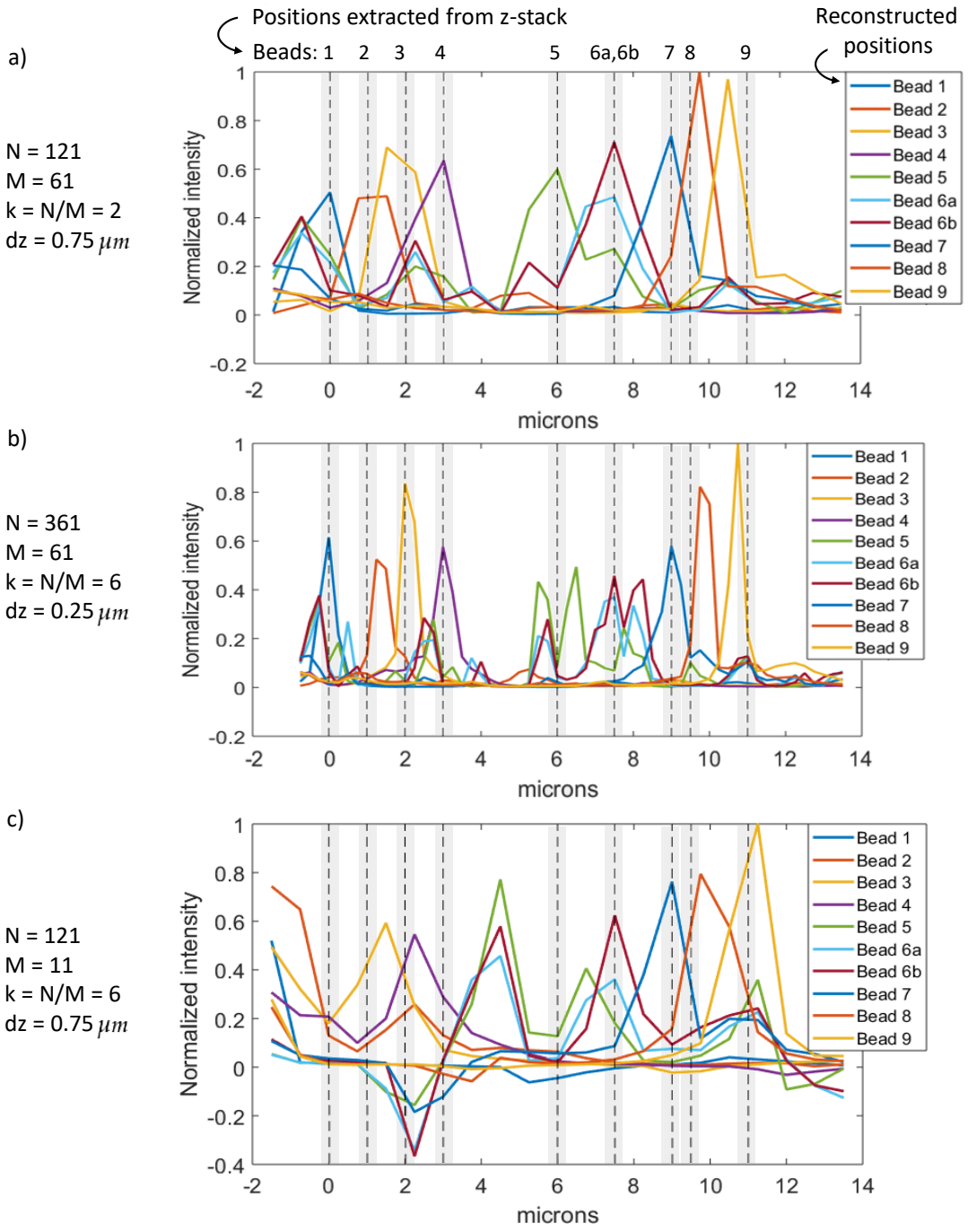

Figure 6.17: *This figure shows 3 examples of different reconstructions of the same volume of beads, initially imaged through 61 compressive images. The z-profiles of the same 10 beads are shown in each plot (z-profiles normalized to the global maximum, different for each of the three plots). (a) Same plot as in Figure 6.16: 121 reconstructed planes (N = 121), z-resolution of 0.75 μm, total reconstructed z-range equal to 90 μm, M = 61 compressive images used, compression ratio N/M = 2. (b) 361 reconstructed planes (N = 361), z-resolution of 0.25 μm, total reconstructed z-range equal to 90 μm, M = 61 compressive images used, compression ratio N/M = 6. (c) 121 reconstructed planes, z-resolution of 0.75 μm, total reconstructed z-range equal to 90 μm, M = 11 compressive images used (corresponding to the 11 patterns with lowest spatial frequencies), compression ratio N/M = 6. The vertical dashed lines indicate the positions of the beads along z, which I extracted from the z-stack (in grey the ±0.25 μm uncertainty which I assigned to the z-positions).*

z-resolution. A reconstruction of the same volume with a higher z-resolution is obtainable from the same set of z-compressed images by reconstructing with a higher compression ratio: same M (number of compressed images) but bigger N (number of reconstructed planes within the same total z-range) means bigger compression ratio k ($k = N/M$). Figure 6.17 compares the z-profiles of Figure 6.16 (obtained with $k = 2$ and shown again in Figure 6.17a), with the z-profiles obtained from a reconstruction of the same total z-range but with a higher z-resolution (Figure 6.17b: same number M of initial compressed images, more planes reconstructed, $k = 6$). Figure 6.17c also shows the results obtained by reconstructing the same number of planes as in Figure 6.17a (same final z-resolution), but using fewer compressed images (lower M), to make the compression ratio be the same as for the results shown in Figure 6.17b ($k = 6$).

The z-profiles plotted in Figure 6.17b show that, when reconstructing at a higher z-resolution, sharper peaks appear at the correct positions for beads 2 and 3. On the other hand, the peaks for beads 5, 6a and 6b appear degraded with respect to the lower resolution (and lower compression ratio) reconstruction of Figure 6.17a: the peaks are split into two adjacent peaks, separated by a dip. A similar effect can be noticed in Figure 6.17c, which shows z-profiles extracted from a reconstruction run at the same compression ratio as for Figure 6.17b, but with a lower z-resolution (same as in Figure 6.17a). In Figure 6.17c, the peaks for beads 5, 6a and 6b appear split into two peaks in a similar way to what shown in Figure 6.17b, but with the two peaks for each bead further apart from each other. Also, differently to what shown by Figure 6.17b, in Figure 6.17c the peaks of some of the beads do not seem to be centred at the correct z-positions any more (beads 1, 2, 3 and 4).

The results shown in Figure 6.17 confirm that, as expected, a higher compression ratio results in a poorer reconstruction (beads reconstructed at the wrong z-position or peak split into two adjacent peaks). By looking at these results, I was left with a few unanswered questions, which I mention here as a suggestion for a future deeper analysis of these results: why do some of the peaks of Figure 6.17a split into two peaks in Figure 6.17b and some others do not? Why do the split peaks of Figure 6.17b seem to split even more in Figure 6.17c? Why do negative values appear in the plots of Figure 6.17c? Despite not being able to answer to these questions, I noticed how both effects (reconstructed negative values and splitting of peaks) also appeared in my simulations. Going back to Figure 6.6, one can see how in Figure 6.6a the regions of lower sparsity appear striped in the reconstruction (*i.e.* each column is reconstructed as a series of sharp peaks) and also notice that negative values appear in the plots of Figure 6.6b. My current speculation is that the splitting effect could be a result of the reconstruction algorithm *forcing* a certain degree of sparsity to the reconstructed image, and that negative values might be avoided by imposing a non-negative requirement to the solution. Therefore, as a suggestion for future works, I believe that in order to understand these effects (and then try and correct them to improve the reconstruction) it would be useful to analyse in more details the reconstruction algorithm used.

After performing the compressive experiments on the 0.8 imaging NA set-up, I moved to the 0.3 imaging NA one (see next section). The idea with this second set of experiments was to take advantage of the larger DoF of the 0.3 imaging NA set-up to verify if the same compressive imaging scheme could be used to successfully image a sparse 3D sample over a bigger z-range.

6.5.5 Imaging NA: 0.3

For the experiments with the lower imaging NA set-up, I chose to image a sparse sample of 1 μm fluorescent beads. With respect to the 0.2 μm beads used for the compressive experiments performed on the 0.8 NA set-up, the 1 μm beads give a much stronger signal, thereby helping improve the signal to noise ratio of the acquired images. Using brighter beads was particularly important also because, for the first experiments on this set-up, I decided to use an iris at the back of the imaging objective to mimic the use of an even lower NA objective and obtain a very high DoF. By doing this, I obtained a DoF $\simeq$ 55 μm (equivalent to using an imaging NA = 0.15), with the drawback of losing a lot of the light collected by the imaging objective, resulting in images with a much dimmer signal and a much lower lateral resolution. I decided to compensate the loss of signal using brighter beads, and to ignore the loss of lateral resolution for the moment, since the main aim with this experiments was to check if I could reconstruct the position of beads over an extended z-range, and not to focus on the $x-y$ image quality of the reconstructed 3D volume.

Similarly to what I did for the 0.8 imaging NA experiments, I started by taking a z-stack of the volume of beads, but in this case after changing the last lens before the excitation objective with a cylindrical lens to illuminate the sample with a light-sheet. The z-stack was acquired by moving the sample through the light-sheet using a motorized stage, with a z-resolution of 0.75 μm. Before performing the compressive experiments on the same sample, I identified a set of 9 similarly focused beads within the imaged volume and realigned the sample to focus the chosen beads as well as possible. I acquired a set of compressive images illuminating the sample with the same 61 patterns used for the 0.8 imaging NA experiments. Using the 61 compressive images, I reconstructed the volume of beads, obtaining a 3-dimensional dataset made of N = 121 planes spaced by 0.75 μm, for a total reconstructed z-range of 90 μm (same reconstruction algorithm as for the previous experiments, described in Section 6.4.2).

Figure 6.18a shows the color-coded MIP, along z, of the $x-y$ region of the imaged volume which contains the selected beads (MIP of a 45μm z-stack on the left and of 45 μm of the reconstructed volume on the right). Figure 6.18b shows the relative position of the 9 beads along z, zooming in on a z-range of 45 μm. In order to generate the profiles plotted in Figure 6.18b I selected a square (in x and y) around each of the 9 beads and integrated (either the z-stack or the reconstructed volume) over x and y to get a single vector of N = 121 values for each bead (for a total of 9 vectors for the z-stack and 9 vectors for the reconstructed volume). The two plots of Figure 6.18b show the 61 central values (corresponding to 45 μm) of the 18 obtained vectors (9 in each plot). Separately in each plot, the 9 vectors are normalized to a global maximum.

The peaks in the top plot of Figure 6.18b reflect the z-profile of the light-sheet at the $x-y$ position of each of the 9 beads. To find the z-positions of the beads I fitted each peak with a Gaussian curve and identified the z-position of the bead with the center of the fitted Gaussian (not shown in the figure). The z- positions found analysing the z-stack are shown in both plots of Figure 6.18b as vertical dashed lines (in grey the $\pm$0.25 μm uncertainty which I assigned to the extracted z-positions). The peaks in the bottom plot of Figure 6.18b show the z-positions where the 9 beads were reconstructed at by the compressive scheme. As it can be seen by comparing the position of these peaks with the position of the dashed lines, the compressive reconstruction

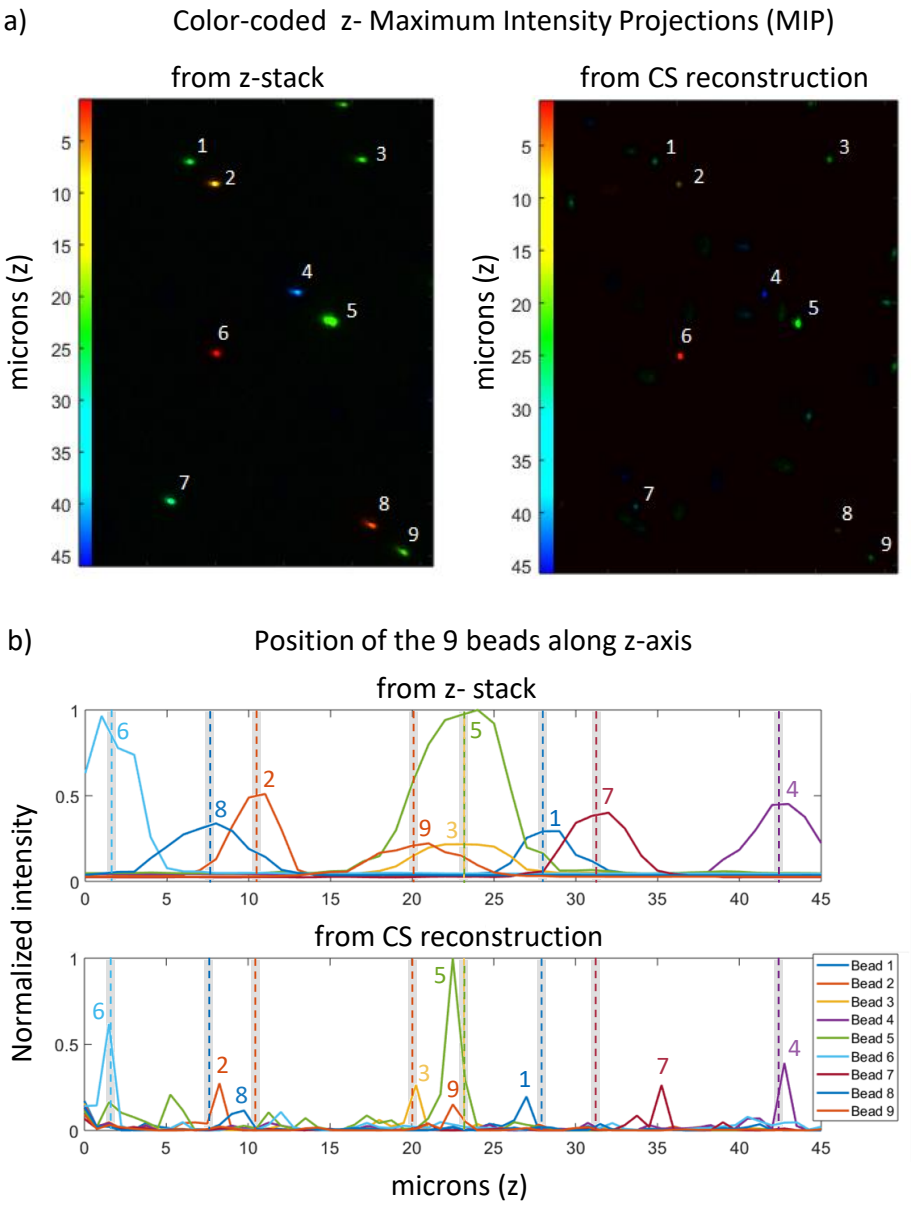

Figure 6.18: *Results of the compressive experiments performed on the 0.3 imaging NA set-up. (a) Colour-coded Maximum Intensity Projection (MIP) along the z-direction (45 µm range) of a z-stack (left) and of a compressive reconstruction (right) of the same volume of fluorescent beads. The z-stack was acquired scanning the volume of beads through a light-sheet with steps of 0.75 µm, while the compressive reconstruction was obtained from M = 61 compressive images and consists of N = 121 planes with z-resolution of 0.75 µm (total z- range 90 µm, only 45 µm selected for the MIP). These MIPs where generated selecting only the central 45 µm of both volumes, and the z-direction was color-coded to show the z-position of the 9 selected beads. (b) z-position of the 9 selected beads as seen from the z-stack (top) and as reconstructed with the compressive imaging scheme (bottom). Each plotted curve was obtained by selecting a square in x and y around the position of a bead, and integrating (either the z-stack or the reconstructed volume) over x and y to get a single vector of N = 121 values (only the 61 central values are shown in this figure). The vertical dashed lines indicate z-position of the beads as extracted from the z-stack in the top plot (in grey the ±0.25 µm uncertainty which I assigned to the extracted z-positions). The peaks in the bottom plot show the z-positions where the 9 beads were reconstructed at by the compressive scheme.*

does not seem to be able to locate all the 9 chosen beads correctly, even though it seems to at least place them in the correct z-region of the volume.

I believe that what could be causing problems to the reconstruction might be the overlapping of signal from out-of-focus beads with the signal from the in-focus beads. As it can be seen in the color-coded MIPs of Figure 6.18a, many beads appear in the reconstructed object (right MIP in the figure) which were not imaged in the 45 μm z-stack (left MIP in the figure). These beads are less in-focus than the 9 beads identified in the z-stack, and in the real sample they are located outside the 90μm reconstructed z-range. The reason why they appear in the reconstructed volume (and in the set of acquired compressed images) is that the illumination patterns used to acquire the compressed images extend beyond a 90 μm z-range, thereby exciting fluorescence in beads which, because of the big DoF of the system, appear as only slightly out-of-focus beads in the acquired images. Regardless of the extent, along z, of the illumination patterns, if the reconstruction algorithm is run to reconstruct a 90 μm z-range, it will try and place everything which appears in the set of compressed images within that z-range. If the fluorescence from these extra beads overlaps (in $x - y$) with the fluorescence from a bead which really is within the reconstructed z-range, the reconstruction does not perform well. Looking at Figure 6.18a, it can be noticed how bead number 7 is very close to two other beads which are in reality located outside the reconstructed z-range, and I believe this could explain why that particular bead is reconstructed in the wrong position. In order to try and solve this problem, it would be useful to restrict the extent along z of the illumination patterns (which on the SLM-SPIM could be done by inserting a vertical slit in the excitation arm or using the SLM to mimic the effect of a slit), or to try and reconstruct a thicker z-range.

6.6 Discussion, conclusions and future works

In this chapter I presented an illumination/image acquisition scheme which can be used to perform 3D compressed imaging using the SLM-SPIM. The final aim of this compressed imaging technique is to reduce the total amount of excitation light delivered to the sample for the acquisition of its 3D image, with respect to what happens when using a traditional light-sheet 3D imaging scheme. The proposed scheme tries to achieve that by reconstructing the image of a 3D sample (made of N planes) acquiring less images than the number of planes (M images with $M < N$). In order to do this, the proposed scheme uses illumination patterns which spread across the whole z-range of the imaged volume, unlike a traditional light-sheet which instead optically sections the sample.

To be able to reconstruct a well focused image of the whole volume using the proposed imaging scheme, the entire imaged z-range needs to be in-focus. In our SLM-SPIM, as in any other light-sheet microscope, the NA of the imaging objective limits the DoF to a few microns (selected to match the thickness of a traditional light-sheet). For the first compressed experiments, I decided to try the proposed compressed imaging scheme on the SLM-SPIM with its original 0.8 imaging NA (experiments presented in Section 6.5.4), knowing that I would only be able to reconstruct an in-focus image across a very limited DoF ($\sim$ 2 μm). To then be able to test the reconstruction algorithm on a bigger z-range, I designed and mounted a separate imaging arm, with a lower imaging NA, which gave a DoF of around 55 μm (objective NA

= 0.3, manually modified to an equivalent NA of $\simeq 0.15$ by the addition and partial closure of an iris behind the imaging objective; experiments presented in Section 6.5.5). Of course, using a lower NA imaging objective also means acquiring images with a lower lateral resolution, which is not ideal. In future works, the next step would therefore be to return to the original 0.8 NA imaging arm (to have a good lateral resolution) but to apply wavefront coding [71] in order to extend its DoF and be able to reconstruct a well focused image over an extended z-range.

Regardless of the chosen imaging NA, in order to successfully image a 3D biological sample with the proposed imaging technique, it is necessary to:

- identify the most appropriate set of illumination patterns (*i.e.* sampling matrix) for the chosen type of sample;
- be able to generate the chosen illumination patterns and be confident that they are well reproduced over the entire imaged z-range;
- be able to perform the compressive reconstruction.

To tackle these aspects, I started by developing and performing optical simulations using Matlab (Section 6.4), and then tried some initial experiments on samples of fluorescent beads embedded in agarose (Section 6.5). Even though I did not get as far as trying and image biological samples, I here want to discuss what was achieved so far, what I learned from that, and what I would suggest as following steps for future works on this imaging technique.

First of all, my simulations showed that, as expected, the imaged sample needs to be sparse along the z-direction in order for the compressed reconstruction to work. As regards the choice of sampling matrix, it would be interesting to try something other than the truncated Fourier matrix I have used so far ($M \times N$ matrix made of the first M rows of a complete $M \times M$ Fourier matrix). One could for example create a similar $M \times N$ sampling matrix selecting M random rows out of an $M \times M$ Fourier matrix. This would mean using a mix of low and high spatial frequency patterns to illuminate the sample, which might help improving the quality of the reconstruction (the set of M images would incorporate high spatial frequency information which is not captured by the truncated Fourier matrix).

Before performing the first experiments, I profiled the chosen illumination patterns (Section 6.5.3). By doing that, I verified that the position of the peaks and valleys of the sinusoidal patterns matched well with what predicted by my simulations across the entire z-range I wanted to image. On the other hand, I noticed two things that would need to be improved: the contrast of the patterns (peak to valley intensity difference, especially in the high spatial frequency patterns) and the absolute peak intensity, which currently varies between patterns and also within each pattern. My first suggestion to a next step would be to take into account the profiled shape of the patterns while performing the reconstruction, and see if that would improve it. One other idea could be to try and improve the shape of the patterns (aiming for better contrast in the fringes and a constant peak intensity between different patterns), which I also believe could improve the quality of the reconstruction.

For the first experiments on fluorescent beads, I acquired a set of $M = N/2$ images, using the same set of M illumination patterns first on the 0.8 NA set-up and later on the 0.3 NA set-up. In both cases, I used the M patterns to reconstruct a z-range of 90 μm. I started by trying a low compression ratio ($k = 2$), with which, according to my simulations, I should have been able to successfully reconstruct a sparse sample of

small beads. For the experiments at $k = 2$, I used the $M = 61$ patterns to reconstruct a volume made of $N = 121$ planes with a z-resolution of 0.75 μm (for a total z-range of 90 μm). Because of the limited DoF of the 0.8 NA imaging arm, even though the reconstructed z-range was equal to 90 μm, I was only able to reconstruct the image of beads located within a much shorter z-range, of the order of $\sim$ 15 μm (as it can be seen from Figure 6.15 and Figure 6.16). Beads located further away from the in-focus plane were seen as too out-of-focus, and the SNR of their image (which would have appeared as a very large disk) was too low for them to be reconstructed by the reconstruction algorithm.

As for the results of my first experiments, using the 0.8 NA imaging arm I was able to reconstruct correctly the z-distribution of the imaged beads with a compression ratio $k = 2$ (Figure 6.16), while the same experiment ran on the 0.3 NA imaging arm did not give as good results (Figure 6.18). As discussed at the end of Section 6.5.5, I believe that the quality of the reconstruction in the experiments on the 0.3 NA imaging arm could be negatively influenced by the combination of the large DoF (obtained by adding and partially closing an iris at the back focal plane of the imaging objective) and the z-extent of the illumination patterns (beyond the reconstructed z-range). Ideally in fact, the illumination patterns should only excite fluorescence within the z-range which one is trying to reconstruct, especially if this z-range is thinner than (or similar to) the DoF of the imaging system. In experiments I ran on the 0.3 NA set-up, a significant quantity of fluorescence excited outside the reconstructed z-range was collected by the acquired images, and this interfered with the correct functioning of the reconstruction where it overlapped (along $x - y$) with the fluorescence from some other in-focus features.

As a suggestion for future works, I would try and improve the quality of the reconstruction by at first concentrating on two aspects: work on the details of the reconstruction algorithm and find the best way to limit the extent of the illumination patterns to the size of the reconstructed z-range. Analysing in more details the reconstruction algorithm would aim at better understanding the origin of a couple of effects which I noticed in my experimental results, namely a splitting (along z) of the reconstructed peaks which identified the positions of the beads, and the appearance of negative intensity values. Limiting the extent of the illumination patterns to the size of the reconstructed z-range would instead improve the signal to noise ratio of the acquired images by eliminating excitation light coming from features of the sample placed outside the reconstructed volume (which can be considered as a source of noise in the acquired images).

7 Conclusions and future works

This thesis presented the SLM-SPIM, a cylindrical-lens-based Selective Plane Illumination Microscope (SPIM) with a phase-only Spatial Light Modulator (SLM) integrated into its excitation arm. The SLM, which is placed in a Fourier plane, permits to move and modify the microscope's light-sheet, making the SLM-SPIM a versatile system able to deliver high quality images by operating in a wide variety of different imaging modalities. The flexibility and performance of the system were demonstrated by imaging samples of fluorescent beads, zebrafish embryos, and optically cleared whole mouse brain samples. This work presented results obtained performing the following imaging techniques: structured illumination and pencil beam scanning to reject out-of-focus light, light-sheet pivoting to reduce shadowing and tiling to obtain a more uniform illumination. The SLM-SPIM presented in this thesis was designed to allow all of these techniques to be employed on an easily reconfigurable optical set-up, compatible with the OpenSPIM design and offering the possibility to choose between three different light-sheets, in thickness and height, which can be selected according to the characteristics of the sample and the imaging technique to be applied.

The flexibility of the SLM-SPIM can also be exploited to try and develop new imaging techniques, and this thesis discussed how the SLM-SPIM was used for preliminary investigations into two novel light-sheet imaging techniques, both of which aim at improving, each in its own way, SPIM's light-efficiency.

The first innovative light-sheet imaging technique presented in this thesis consists of a light-sheet specifically designed to be used while performing tiling. The aim of the proposed new light-sheet is to try and better confine the illumination light, thereby helping reduce the undesired extra photo-bleaching generated by the sample over-excitation typical of the tiling implementation. The initial simulations performed and presented in this thesis seemed to show that, when compared to the use of a normal Gaussian light-sheet, the proposed light-sheet could help decrease photo-bleaching, even though the improvement would probably only be incremental. Nevertheless, experiments were performed on surface-labelled fluorescent beads (which photo-bleached relatively fast) to try an confirm the simulated results.

A first round of experiments was performed imaging a single plane, obtaining results which confirmed what expected from the simulations. The second round of experiments considered thicker imaging volumes (consisting of more than one plane within the sample), and in this case the results obtained were not in good agreement with the predictions from the simulations. The following two possible causes of the observed mismatch between the simulated and experimental results were identified:

- by profiling the proposed light-sheet it was verified that its actual shape did not perfectly match its simulated one. In order to check if this could be the cause of the unexpected experimental results, it would be useful to profile the

sheets more precisely and then run the simulations using the profiled shape of the sheets;

- in the simulations, the process of photo-bleaching was simplified and modelled as a single exponential decay of intensity, only dependent on the amount of excitation light experienced. As it is instead known (and as it also appeared in the experimental data), photo-bleaching is a very complex process and it is not accurately represented by a single exponential decay. If more sophisticated photo-bleaching models were available, the simulations might have more closely matched the experimental results.

To conclude, the current results seem to suggest that, when used for tiling and compared to a Gaussian light-sheet, the proposed modified light-sheet would only give a minimum reduction in photo-bleaching, if any. Nevertheless, the work carried out so far on this new technique could be seen as a good example of how the combination of a simulation tool and a flexible system such as the SLM-SPIM can make it relatively easy to develop and try new imaging techniques.

The second innovative imaging technique discussed in this thesis applies the principles of compressive sensing to try and perform more light-efficient (*i.e.* faster and less photo-damaging) 3D imaging on a light-sheet microscope. Matlab simulations were first performed to test the compressed acquisition scheme and the reconstruction process. The compressed imaging scheme was then tried on the SLM-SPIM, imaging sparse solutions of small fluorescent beads suspended in agarose, first using the SLM-SPIM's original imaging arm (equipped with a 0.8 NA imaging objective) and then using a secondary imaging arm equipped with a 0.3 NA imaging objective (and therefore giving a greater DoF).

On the 0.8 NA imaging arm, using a compression ratio k = N/2 (where N is the number of reconstructed planes), it was possible to correctly reconstruct the z position of a series of beads located within a z-range of $\sim 15\mu$m, a limit which was set by the DoF of the system. As also predicted by my simulations, a fast degradation of the quality of the reconstruction was observed for higher compression ratios. In the experiments on the 0.3 NA imaging objective the reconstruction did not seem to work as well as for the experiments on the 0.8 NA imaging arm. The experimental results obtained so far suggest that the quality of the reconstruction could be improved by working on the following aspects: try to limit the extent of the illumination patterns to the size of the reconstructed z-range, take into account the profiled shape of the patterns while performing the reconstruction, analyse in more detail the reconstruction algorithm used and experiment different sets of illumination patterns.

Overall, both the simulation and the preliminary experimental results obtained for the compressed imaging scheme suggest that, if the sample is sparse enough in the spatial domain, the proposed scheme should make it possible to successfully reconstruct a 3D image of the sample requiring half (or less) of the light-sheet images normally required by the traditional plane-by-plane 3D imaging scheme. This would mean reducing the amount of excitation light delivered to the sample, and possibly also making 3D imaging much faster. Nevertheless, more work should be done not only to make the proposed compressed scheme fully work over the z-range needed for the desired biological application, but also to fairly compare the quality of the reconstructed 3D images with those acquired with the traditional plane-by-plane scheme.

To conclude, the work presented and discussed in this thesis demonstrated that the SLM-SPIM is an extremely versatile and resourceful tool, useful to exploit the variety of possibilities offered by a cylindrical-lens-based light-sheet microscope. As shown in this thesis, the SLM-SPIM can not only be used to perform high quality imaging, but it also offers the flexibility needed to trial new ideas and novel imaging techniques.

Bibliography

[1] Jan Huisken and Didier Y R Stainier. "Selective plane illumination microscopy techniques in developmental biology." In: *Development (Cambridge, England)* 136.12 (2009), pp. 1963–1975.

[2] Donna J Webb and Claire M Brown. "Epi-fluorescence microscopy". In: *Cell Imaging Techniques*. Springer, 2013, pp. 29–59.

[3] José-Angel Conchello and Jeff W Lichtman. "Optical sectioning microscopy." In: *Nature Methods* 2.12 (2005), pp. 920–931.

[4] James Sharpe et al. "Optical projection tomography as a tool for 3D microscopy and gene expression studies". In: *Science* 296.5567 (2002), pp. 541–545.

[5] Angelique Y Louie et al. "In vivo visualization of gene expression using magnetic resonance imaging". In: *Nature Biotechnology* 18.3 (2000), pp. 321–325.

[6] David Huang et al. "Optical coherence tomography". In: *Science* 254.5035 (1991), pp. 1178–1181.

[7] W Jerry Alford, Richfspard D VanderNeut, and Vicent J Zaleckas. "Laser scanning microscopy". In: *Proceedings of the IEEE* 70.6 (1982), pp. 641–651.

[8] Nathan S Claxton, Thomas J Fellers, and Michael W Davidson. "Laser Scanning Confocal Microscopy". In: *Encyclopedia of Medical Devices and Instrumentation* 1979.21 (2006), pp. 1–37.

[9] Martina Rembold et al. "Individual cell migration serves as the driving force for optic vesicle evagination". In: *Science* 313.5790 (2006), pp. 1130–1134.

[10] Fritjof Helmchen and Winfried Denk. "Deep tissue two-photon microscopy". In: *Nature Methods* 2.12 (2005), pp. 932–940.

[11] Philipp J Keller et al. "Reconstruction of zebrafish early embryonic development by scanned light sheet microscopy". In: *Science* 322.5904 (2008), pp. 1065–1069.

[12] Jan Huisken and Didier YR Stainier. "Even fluorescence excitation by multidirectional selective plane illumination microscopy (mSPIM)". In: *Optics Letters* 32.17 (2007), pp. 2608–2610.

[13] Ryosuke Itoh et al. "Light sheet fluorescence microscopy using high-speed structured and pivoting illumination". In: *Optics Letters* 41.21 (2016), pp. 5015–5018.

[14] Florian O Fahrbach and Alexander Rohrbach. "Propagation stability of self-reconstructing Bessel beams enables contrast-enhanced imaging in thick media". In: *Nature Communications* 3 (2012), p. 632.

[15] Thomas A Planchon et al. "Rapid three-dimensional isotropic imaging of living cells using Bessel beam plane illumination". In: *Nature Methods* 8.5 (2011), p. 417.

[16] Omar E Olarte et al. “Image formation by linear and nonlinear digital scanned light-sheet fluorescence microscopy with Gaussian and Bessel beam profiles”. In: *Biomedical Optics Express* 3.7 (2012), pp. 1492–1505.

[17] Tom Vettenburg et al. “Light-sheet microscopy using an Airy beam”. In: *Nature Methods* 11.5 (2014), p. 541.

[18] Eugen Baumgart and Ulrich Kubitscheck. “Scanned light sheet microscopy with confocal slit detection”. In: *Optics Express* 20.19 (2012), pp. 21805–21814.

[19] Jerome Mertz and Jinhyun Kim. “Scanning light-sheet microscopy in the whole mouse brain with HiLo background rejection”. In: *Journal of biomedical optics* 15.1 (2010), p. 016027.

[20] Tobias Breuninger, Klaus Greger, and Ernst HK Stelzer. “Lateral modulation boosts image quality in single plane illumination fluorescence microscopy”. In: *Optics Letters* 32.13 (2007), pp. 1938–1940.

[21] Liang Gao. “Extend the field of view of selective plan illumination microscopy by tiling the excitation light sheet”. In: *Optics Express* 23.5 (2015), pp. 6102–6111.

[22] Henry Siedentopf and Richard Zsigmondy. “Uber sichtbarmachung und größenbestimmung ultramikoskopischer teilchen, mit besonderer anwendung auf goldrubingläser”. In: *Annalen der Physik* 315.1 (1902), pp. 1–39.

[23] Arne H Voie, DH Burns, and FA Spelman. “Orthogonal-plane fluorescence optical sectioning: three-dimensional imaging of macroscopic biological specimens”. In: *Journal of Microscopy* 170.3 (1993), pp. 229–236.

[24] Eran Fuchs et al. “Thin laser light sheet microscope for microbial oceanography”. In: *Optics Express* 10.2 (2002), pp. 145–154.

[25] Jan Huisken et al. “Optical sectioning deep inside live embryos by selective plane illumination microscopy”. In: *Science* 305.5686 (2004), pp. 1007–1009.

[26] Peter A Santi. “Light sheet fluorescence microscopy: a review”. In: *Journal of Histochemistry & Cytochemistry* 59.2 (2011), pp. 129–138.

[27] Jörg G Ritter et al. “High-contrast single-particle tracking by selective focal plane illumination microscopy”. In: *Optics Express* 16.10 (2008), pp. 7142–7152.

[28] Philipp J Keller and Misha B Ahrens. “Visualizing whole-brain activity and development at the single-cell level using light-sheet microscopy”. In: *Neuron* 85.3 (2015), pp. 462–483.

[29] Philipp J Keller, Francesco Pampaloni, and Ernst HK Stelzer. “Life sciences require the third dimension”. In: *Current opinion in cell biology* 18.1 (2006), pp. 117–124.

[30] Michael Weber and Jan Huisken. “Light sheet microscopy for real-time developmental biology”. In: *Current opinion in genetics & development* 21.5 (2011), pp. 566–572.

[31] Eugene Hecht et al. *Optics*. Vol. 5. Addison Wesley San Francisco, 2002.

[32] Dan Hill. “How to Convert FWHM Measurements to 1/e-Squared Halfwidths”. In: *Radiant Zemax Knowledge Base* (2007).

[33] Osamu Shimomura, Frank H Johnson, and Yo Saiga. “Extraction, purification and properties of aequorin, a bioluminescent protein from the luminous hydromedusan, Aequorea”. In: *Journal of cellular and comparative physiology* 59.3 (1962), pp. 223–239.

[34] M Chalfie et al. "Green fluorescent protein as a marker for gene expression". In: *Science* 263.5148 (1994), pp. 802–805.

[35] Daniel J Gage, Tanya Bobo, and Sharon R Long. "Use of green fluorescent protein to visualize the early events of symbiosis between Rhizobium meliloti and alfalfa (Medicago sativa)." In: *Journal of Bacteriology* 178.24 (1996), pp. 7159–7166.

[36] Jeff W Lichtman and José-angel Conchello. "Fluorescence microscopy". In: *Nature Methods* 2.12 (2005), pp. 910–919.

[37] Nathalie B Vicente et al. "Photobleaching correction in fluorescence microscopy images". In: *Journal of Physics: Conference Series*. Vol. 90. 1. IOP Publishing. 2007, p. 012068.

[38] Paula J Cranfill et al. "Quantitative assessment of fluorescent proteins". In: *Nature Methods* 13.7 (2016), pp. 557–562.

[39] Loling Song et al. "Photobleaching kinetics of fluorescein in quantitative fluorescence microscopy". In: *Biophysical journal* 68.6 (1995), pp. 2588–2600.

[40] Daniel B Schmolze et al. "Advances in microscopy techniques". In: *Archives of pathology & laboratory medicine* 135.2 (2011), pp. 255–263.

[41] Ernst Abbe. *Neue Apparate zur Bestimmung des Brechungs-und Zerstreuungs-vermögens fester und flüssiger körper*. Mauke's Verlag (Hermann Dufft), 1874.

[42] Lord Rayleigh. "XXXI. Investigations in optics, with special reference to the spectroscope". In: *The London, Edinburgh, and Dublin Philosophical Magazine and Journal of Science* 8.49 (1879), pp. 261–274.

[43] Omar E Olarte et al. "Light-sheet microscopy: a tutorial". In: *Advances in Optics and Photonics* 10.1 (2018), pp. 111–179.

[44] Dean Wilding et al. "Adaptive illumination based on direct wavefront sensing in a light-sheet fluorescence microscope". In: *Optics Express* 24.22 (2016), pp. 24896–24906.

[45] Runze Li et al. "Selective plane illumination microscopy with structured illumination based on spatial light modulators". In: *Three-Dimensional and Multidimensional Microscopy: Image Acquisition and Processing XXI*. Vol. 8949. International Society for Optics and Photonics. 2014, 89491S.

[46] Mostafa Aakhte, Ehsan A Akhlaghi, and H-Arno J Müller. "SSPIM: a beam shaping toolbox for structured selective plane illumination microscopy". In: *Scientific Reports* 8.1 (2018), p. 10067.

[47] Peter G Pitrone et al. "OpenSPIM: an open-access light-sheet microscopy platform". In: *Nature Methods* 10.7 (2013), p. 598.

[48] Chiara Garbellotto and Jonathan M Taylor. "Multi-purpose SLM-light-sheet microscope". In: *Biomedical Optics Express* 9.11 (2018), pp. 5419–5436.

[49] Christian Maurer et al. "What spatial light modulators can do for optical microscopy". In: *Laser & Photonics Reviews* 5.1 (2011), pp. 81–101.

[50] MP Lee et al. "A multi-modal stereo microscope based on a spatial light modulator". In: *Optics Express* 21.14 (2013), pp. 16541–16551.

[51] Paul Zammit, Andrew R Harvey, and Guillem Carles. "Extended depth-of-field imaging and ranging in a snapshot". In: *Optica* 1.4 (2014), pp. 209–216.

[52] Sean Quirin, Darcy S Peterka, and Rafael Yuste. "Instantaneous three-dimensional sensing using spatial light modulator illumination with extended depth of field imaging". In: *Optics Express* 21.13 (2013), pp. 16007–16021.

[53] Bahaa EA Saleh and Malvin Carl Teich. *Fundamentals of photonics*. New York, NY: John Wiley & Sons, 1991.

[54] Anna Kaufmann et al. "Multilayer mounting enables long-term imaging of zebrafish development in a light sheet microscope". In: *Development* 139.17 (2012), pp. 3242–3247.

[55] Kwanghun Chung et al. "Structural and molecular interrogation of intact biological systems". In: *Nature* 497.7449 (2013), p. 332.

[56] Kevin M Dean and Reto Fiolka. "Uniform and scalable light-sheets generated by extended focusing". In: *Optics Express* 22.21 (2014), pp. 26141–26152.

[57] Qinyi Fu et al. "Imaging multicellular specimens with real-time optimized tiling light-sheet selective plane illumination microscopy". In: *Nature Communications* 7.1 (2016), pp. 1–10.

[58] Kevin M Dean et al. "Deconvolution-free subcellular imaging with axially swept light sheet microscopy". In: *Biophysical journal* 108.12 (2015), pp. 2807–2815.

[59] Philipp J Keller et al. "Fast, high-contrast imaging of animal development with scanned light sheet–based structured-illumination microscopy". In: *Nature Methods* 7.8 (2010), p. 637.

[60] Bo-Jui Chang, Victor Didier Perez Meza, and Ernst HK Stelzer. "csiLSFM combines light-sheet fluorescence microscopy and coherent structured illumination for a lateral resolution below 100 nm". In: *Proceedings of the National Academy of Sciences* 114.19 (2017), pp. 4869–4874.

[61] Mark AA Neil, Rimas Juškaitis, and Tony Wilson. "Method of obtaining optical sectioning by using structured light in a conventional microscope". In: *Optics Letters* 22.24 (1997), pp. 1905–1907.

[62] MAA Neil, R Juškaitis, and T Wilson. "Real time 3D fluorescence microscopy by two beam interference illumination". In: *Optics Communications* 153.1-3 (1998), pp. 1–4.

[63] Benjamin Judkewitz and Changhuei Yang. "Axial standing-wave illumination frequency-domain imaging (SWIF)". In: *Optics Express* 22.9 (2014), pp. 11001–11010.

[64] Philipp J Keller and Ernst HK Stelzer. "Quantitative in vivo imaging of entire embryos with digital scanned laser light sheet fluorescence microscopy". In: *Current opinion in neurobiology* 18.6 (2008), pp. 624–632.

[65] Kristin N Walker and Robert K Tyson. "Wavefront correction using a Fourier-based image sharpness metric". In: *Adaptive Coded Aperture Imaging, Non-Imaging, and Unconventional Imaging Sensor Systems*. Vol. 7468. International Society for Optics and Photonics. 2009, 74680O.

[66] Cyril Bourgenot et al. "3D adaptive optics in a light sheet microscope". In: *Optics Express* 20.12 (2012), pp. 13252–13261.

[67] David L Donoho. "Compressed sensing". In: *IEEE Transactions on information theory* 52.4 (2006), pp. 1289–1306.

[68] Maxime Woringer et al. "Faster and less phototoxic 3D fluorescence microscopy using a versatile compressed sensing scheme". In: *Optics Express* 25.12 (2017), pp. 13668–13683.

[69] Bi-Chang Chen et al. "Lattice light-sheet microscopy: imaging molecules to embryos at high spatiotemporal resolution". In: *Science* 346.6208 (2014), p. 1257998.

[70] Florian O Fahrbach et al. "Rapid 3D light-sheet microscopy with a tunable lens". In: *Optics Express* 21.18 (2013), pp. 21010–21026.

[71] Omar E Olarte et al. "Decoupled illumination detection in light sheet microscopy for fast volumetric imaging". In: *Optica* 2.8 (2015), pp. 702–705.

[72] Laura Marcu, Warren S Grundfest, and Jean-Michel I Maarek. "Photobleaching of arterial fluorescent compounds: Characterization of elastin, collagen and cholesterol time-resolved spectra during prolonged ultraviolet irradiation". In: *Photochemistry and photobiology* 69.6 (1999), pp. 713–721.

[73] Richard G Baraniuk. "Compressive sensing [lecture notes]". In: *IEEE signal processing magazine* 24.4 (2007), pp. 118–121.

[74] Emmanuel J Candès and Michael B Wakin. "An introduction to compressive sampling [a sensing/sampling paradigm that goes against the common knowledge in data acquisition]". In: *IEEE signal processing magazine* 25.2 (2008), pp. 21–30.

[75] Yonina C Eldar and Gitta Kutyniok. *Compressed sensing: theory and applications*. Cambridge university press, 2012.

[76] E. J. Candes and T. Tao. "Near-Optimal Signal Recovery From Random Projections: Universal Encoding Strategies?" In: *IEEE Transactions on Information Theory* 52.12 (2006), pp. 5406–5425.

[77] E. J. Candes, J. Romberg, and T. Tao. "Robust uncertainty principles: exact signal reconstruction from highly incomplete frequency information". In: *IEEE Transactions on Information Theory* 52.2 (2006), pp. 489–509.

[78] Stéphane Mallat. *A wavelet tour of signal processing*. Elsevier, 1999.

[79] Emmanuel Candes and Justin Romberg. "Sparsity and incoherence in compressive sampling". In: *Inverse problems* 23.3 (2007), p. 969.

[80] Emmanuel J Candès and Michael B Wakin. "An introduction to compressive sampling". In: *IEEE signal processing magazine* 25.2 (2008), pp. 21–30.

[81] Michael Lustig, David Donoho, and John M Pauly. "Sparse MRI: The application of compressed sensing for rapid MR imaging". In: *Magnetic Resonance in Medicine: An Official Journal of the International Society for Magnetic Resonance in Medicine* 58.6 (2007), pp. 1182–1195.

[82] Jérôme Bobin, Jean-Luc Starck, and Roland Ottensamer. "Compressed sensing in astronomy". In: *IEEE Journal of Selected Topics in Signal Processing* 2.5 (2008), pp. 718–726.

[83] Moshe Mishali et al. "Xampling: Analog to digital at sub-Nyquist rates". In: *IET circuits, devices & systems* 5.1 (2011), pp. 8–20.

[84] Marco F Duarte et al. "Single-pixel imaging via compressive sampling". In: *IEEE signal processing magazine* 25.2 (2008), pp. 83–91.

[85] M E Gehm and D J Brady. "Compressive sensing in the EO/IR". In: *Applied Optics* 54.8 (2015), pp. C14–C22.

[86] David J Brady et al. "Compressive holography". In: *Optics Express* 17.15 (2009), pp. 13040–13049.

[87] Ori Katz, Yaron Bromberg, and Yaron Silberberg. "Compressive ghost imaging". In: *Applied Physics Letters* 95.13 (2009), p. 131110.

[88] Yuehao Wu et al. "Experimental demonstration of an optical-sectioning compressive sensing microscope (CSM)". In: *Optics Express* 18.24 (2010), pp. 24565–24578.

[89] P Ye et al. "Compressive confocal microscopy: 3D reconstruction algorithms". In: *Emerging Digital Micromirror Device Based Systems and Applications*. Vol. 7210. International Society for Optics and Photonics. 2009, 72100G.

[90] Vincent Studer et al. "Compressive fluorescence microscopy for biological and hyperspectral imaging". In: *Proceedings of the National Academy of Sciences* 109.26 (2012), E1679–E1687.

[91] Martin Weigert et al. "Content-aware image restoration: pushing the limits of fluorescence microscopy". In: *Nature Methods* 15.12 (2018), pp. 1090–1097.

[92] Chinmay Belthangady and Loic A Royer. "Applications, promises, and pitfalls of deep learning for fluorescence image reconstruction". In: *Nature Methods* (2019), pp. 1–11.

[93] Emmanuel Candes and Justin Romberg. "l1-magic: Recovery of sparse signals via convex programming". In: *URL: www. acm. caltech. edu/l1magic/downloads/l1magic. pdf* 4 (2005), p. 14.